COURSE

HEAVY-QUARK PHYSICS AND CP VIOLATION

Jeffrey D. Richman

University of California
Santa Barbara, California 93106, U.S.A.†

† E-mail: richman@charm.physics.ucsb.edu

Photograph of Lecturer

Contents

1. Introduction

I am delighted to present these lectures on the physics of charm and bottom hadrons to this enthusiastic group of graduate students and postdocs here in Les Houches. Why is heavy-quark physics interesting? I hope to show you that we can now address an extraordinarily broad range of issues, ranging from the mysteries of the Cabibbo-Kobayashi-Maskawa (CKM) quark mixing matrix, to the dynamics of the strong and weak interactions, to fascinating rare processes that are sensitive to physics beyond the standard model. In the near future, several new and ongoing experiments will address the driving question of this field: what is the origin of CP violation? So far, CP violation has been observed only as a tiny, part-in-a-thousand effect in kaon decays. There is, as yet, very little empirical evidence to establish that physics within the framework of the standard model—namely, the phase structure of the CKM matrix—is responsible. If the CKM matrix is indeed the source, then we will observe large, CP-violating asymmetries in both B and B_s meson decays. If the expected pattern of CP violation is not observed, then these investigations will provide a window into new physics beyond the standard model.

I was more than a little surprised to discover that nearly all of the members of this audience are theorists. This fact is both intriguing and a little daunting. I have the opportunity to explain the challenges and excitement of building experiments and performing new measurements. At the same time, there is a risk that I will bore you with too many experimental details, or fail to motivate them sufficiently. For some of you, learning how measurements are performed may be something like learning how your sausages are made—you would rather not know. I hope that by the end of these lectures you will at least conclude that the sausages we make are kosher!

The interaction between theory and experiment in heavy-quark physics has been extremely productive, and I will devote a significant part of these lectures to a review of theoretical progress, from the perspective of an experimentalist. I will discuss theory at a fairly simple level, mainly to obtain insights into the key physical ideas, and to help explain the phenomenology that appears in experimental measurements. (For discussions of the more technical theoretical issues, I refer you to the lectures of other speakers at this school, for example, Buras, Manohar, Martinelli, and Wise.)

Experimentalists need to know about theory for several reasons. First, in planning an incisive and coherent set of measurements, it helps greatly to understand the theoretical issues. It is also important to have a sense of how reliable the predictions are and to know the key assumptions that are really being tested. In performing a measurement, one must understand all of the kinematic distributions that describe the processes under study, since both the detection efficiency and the ability to reject backgrounds depend on knowledge of such distributions.

Similarly, theorists should have some knowledge of the strengths and weaknesses of different experiments, as well as a sense of which kinds of measurements are practical and which are not. It is also important for theorists to be aware of assumptions that experimentalists make and to understand the dependence of the measurements on these assumptions. A measured branching fraction, for example, may well depend either on a model for the decay distributions for the signal or on a model describing the background composition. For phenomenologists especially, it is important to be able to communicate with experimentalists, since predictions that are not clearly stated may simply be ignored!

These lectures are unashamedly pedagogical, so I will not aim for the level of impartiality that is customary in a review talk or article. (I have made some recent attempts at such reviews [1,2].) My own work in heavy-quark physics has been mainly on the CLEO experiment, although more recently I have been involved in the construction of the BaBar detector. Many of my examples are from CLEO analyses, both because I am most familiar with them, and because CLEO results are often as good as those from other experiments. When other measurements are better than those of CLEO, however, I will focus on them, especially to show the advantages of different methods.

My goal, then, is to present a balanced and coherent picture of both experiment and theory. The pedagogical approach gives me more freedom to be selective, to spend more time than usual on simple physics arguments, and to present some of my own opinions about the strengths and weaknesses of various measurements. In the process, I hope both to give you a picture of how heavy-flavor physics is done, and to convey my enthusiasm for this field.

I am happy to say that these lectures are destined to become out-of-date in the relatively near future, as experiments provide us with a vast amount of new data. We can therefore expect major advances in nearly all areas of bottom and charm quark physics, and we need young people like you to help explore this new territory.

2. Roadmap and Overview of Bottom and Charm Physics

The physics of bottom and charm hadrons is a broad subject, and it is useful to begin with a roadmap of the main topics and physics issues. Here is an outline of the lectures:

- Introduction to the CKM matrix
- Experimental challenges of b and c physics
- Historical perspective, bumps in the road, and lessons in data analysis
- Leptonic decays of pseudoscalar mesons
- Semileptonic decays and measurements of CKM elements
- Hadronic decays, lifetimes, and rare decays
- CP violation and oscillations

All of the physical processes that I discuss involve underlying weak processes mediated by the W boson, but strong and even electromagnetic interactions play a crucial role as well. The thread that runs through these lectures ties all of these subjects to the quest to understand CP violation.

Although this list is rather long, it is far from complete. For example, I will say very little about baryons (apart from lifetime measurements) or about spectroscopy. The physics of heavy-quark production, including $Z \to b\bar{b}$ and other related electroweak phenomena such as the b forward-backward asymmetry, is entirely absent; these topics could easily be the subject of another series of lectures.

I begin in Section 3 with a short introduction to the CKM matrix and a review of its present status. Because $m_b < m_t$, the b quark must decay into quarks outside its own generation. As a consequence, even the dominant ($b \to c$) decay modes are suppressed by $|V_{cb}|^2 \approx (0.04)^2$, resulting in the long lifetimes of b hadrons, of order 1 ps. In some experiments, these long lifetimes have made distinguishing b hadrons from backgrounds much easier, since separated decay vertices are evident if the b hadron is moving rapidly. B decays provide various ways to measure $|V_{cb}|$ and $|V_{ub}|$, which govern the strengths of $b \to c$ and $b \to u$ transitions. Furthermore, the appearance of the t quark in virtual intermediate states of B and B_s mixing and penguin decay processes allows one to extract $|V_{td}|$ and $|V_{ts}|$. We will also see that phases of the CKM elements, not just their magnitudes, are experimentally accessible and are associated with CP-violating asymmetries. For reasons that I will discuss, the determination of CKM elements is less important in charm physics. Although $|V_{cs}|$ and $|V_{cd}|$ can be determined from charm semileptonic decays, the main focus has been to infer these quantities from unitarity of the CKM matrix and then to use measured branching fractions to test theoretical predictions for the absolute scale of the decay rates.

Section 4 describes the main challenges confronting experiments that study bottom- and charm-quark physics. I compare the strengths and weaknesses of different methods and indicate the kinds of measurements for which each is best suited. Currently, b-physics experiments use three different approaches, all of which involve colliding-beams: $e^+e^- \to \Upsilon(4S) \to B\bar{B}$, $e^+e^- \to Z \to b\bar{b}$, and $p\bar{p} \to b\bar{b}X$. The $\Upsilon(4S)$, a $b\bar{b}$ bound state just above the threshold for producing $B\bar{B}$ pairs, has provided the largest data samples. Over five million $\Upsilon(4S) \to B\bar{B}$ events have been obtained by the CLEO experiment at the Cornell Electron Storage Ring (CESR); this is the largest B sample in the world. The CLEO detector has been upgraded a number of times: CLEO I performed the original observation of B mesons; CLEO II dramatically advanced the field with its CsI calorimeter, which provides superb photon detection; in CLEO II.5, a silicon-vertex detector was added; and CLEO III is now under construction. It will include a new particle-ID system based on a ring-imaging Čerenkov detector. Two new detectors, BaBar at SLAC and Belle at KEK, are now under construction; they will operate at asymmetric-energy e^+e^- machines that will give the $\Upsilon(4S)$ a boost relative to the detector frame, allowing for vertexing of the daughter B mesons. The ARGUS experiment at DESY is no longer in operation, but it also contributed greatly to this field.

The process $e^+e^- \to Z \to b\bar{b}$ has also been used with great effectiveness. Because the energy in this process is so high, a large variety of b hadrons can be produced: B, B_s, b-baryons, as well as radially- and orbitally-excited B mesons. The b hadrons are produced at high momentum ($p \sim 30$ GeV/c), and they move far enough that high-precision vertex detectors help greatly in reconstructing the decay sequences. The LEP experiments ALEPH, DELPHI, OPAL, and L3, as well as the SLD detector at the Stanford Linear Collider (SLC), have performed many investigations of b hadrons, including a comprehensive set of lifetime and mixing measurements. More recently, successful b-hadron lifetime and mixing measurements have been performed by the

CDF experiment at the Fermilab Tevatron $p\bar{p}$ collider. Here again, high-precision vertexing has been essential.

In contrast, high-statistics data on charm particles have been obtained not only by collider experiments such as CLEO, but also by fixed-target spectrometers, mainly at Fermilab. In these experiments, vertex detectors play a crucial role in separating the charm signals from the light-quark background. These fixed-target experiments, beginning with Fermilab E691, provided the first high-precision charm-lifetime measurements. Present Fermilab experiments, such as FOCUS (E831), have accumulated data samples that should yield over one million reconstructed charm decays.

Section 5 surveys some of the main achievements of this field. Many of the most interesting discoveries are quite recent, and there is every expectation that rapid progress will continue. As in any scientific endeavor, however, there have been occasional missteps. In the spirit of the teaching goals of this school, I present some examples of measurements that have not stood the test of time. It is not always clear precisely what lessons should be drawn from such mistakes, but these examples can nevertheless be instructive. I list some guidelines to analyzing data that might help others to avoid these problems.

In the next sections, I discuss the decay modes of charm and bottom mesons, progressing from the simplest to the most complicated processes. Figure 1 shows some of the most important diagrams, which suggest the remarkable variety of phenomena we can observe.

Given that the initial state is a hadronic system, the simplest modes—from a theoretical perspective—are the leptonic decays of charged mesons, discussed in Section 6. In these decays (Fig. 1a), the initial quark and antiquark within the meson annihilate into a virtual W, which then produces a two-body final state consisting of a lepton and its antineutrino. Studies of leptonic decays provide information on meson decay constants, which measure the amplitude for the quark and antiquark to overlap. Sophisticated theoretical methods, such as lattice QCD, are being developed to describe the strong-interaction forces within mesons and to calculate decay constants. We will see that this information is valuable in a wide variety of situations; in particular, it is needed in some cases to extract values of CKM matrix elements. In general, I will not describe the details of data analyses. To give some idea of the difficulties one encounters, however, I have chosen (somewhat arbitrarily) two measurements of $D_s^+ \to \mu^+\nu_\mu$ to describe more fully. The approaches used in these two measurements are quite different.

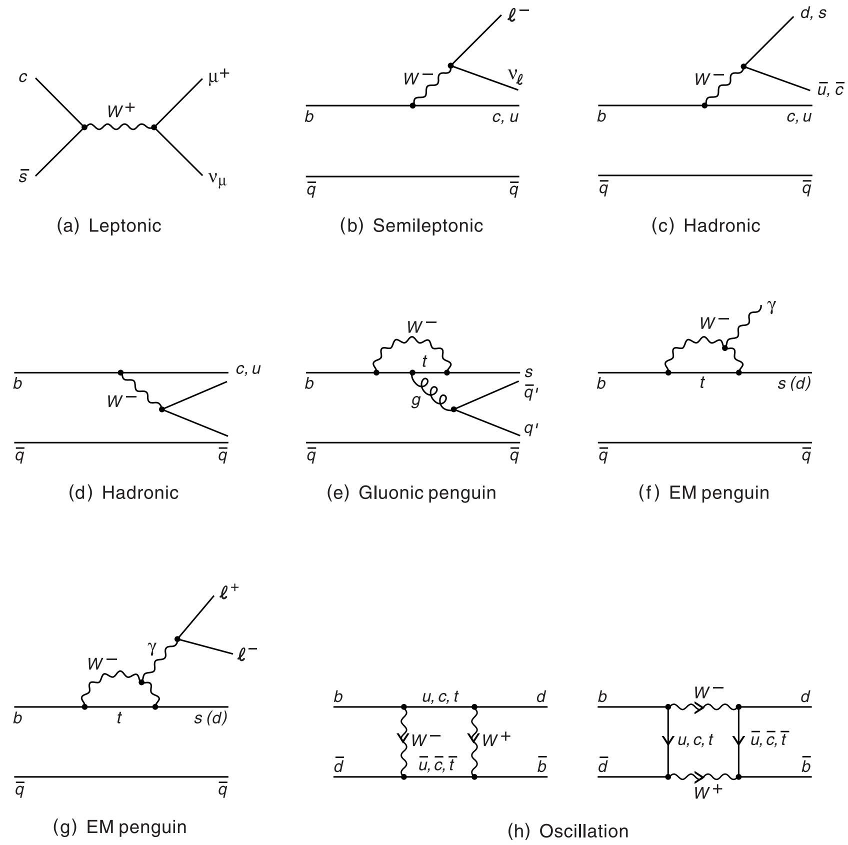

Fig. 1. Diagrams for B and D decays and oscillations: (a) Leptonic decay, (b) Semileptonic decay, (c) hadronic decay (external spectator diagram), (d) hadronic decay (internal spectator diagram), (e) gluonic penguin, (f) radiative penguin with real photon, (g) radiative penguin with dilepton, (h) $B^0\overline{B}^0$ oscillations (mixing). These figures do not show all of the possible decay diagrams, but only the most important ones.

Semileptonic decays (Section 7) are shown in Fig. 1b. These modes are much easier to study experimentally than leptonic decays, mainly because the branching fractions are larger. Theoretical calculations, while difficult, are reliable enough that semileptonic decays provide good measurements of $|V_{cb}|$ and $|V_{ub}|$. As for leptonic decays, the amplitude can be factorized into leptonic and hadronic pieces. However, the final state in semileptonic decay involves at least three particles, so that q^2, the mass squared of the virtual W, is a variable. The hadronic current can be parametrized with a small number of functions of q^2, called form factors; these functions describe the transition of the hadronic system from the initial to the final state. The form factors depend on q^2 because this quantity determines the value of the recoil kick given to the daughter quark of the decaying heavy quark. In some cases, the form factors can be predicted with good precision, as in the case $B \to X_c \ell^- \bar{\nu}$, where X_c denotes a charm meson. Predictions based on heavy-quark effective theory (HQET) and heavy-quark expansions have provided valuable insights into the dynamics of these decays, and have led to more reliable measurements of $|V_{cb}|$. The $B \to X_u \ell^- \bar{\nu}$ decays, where X_u represents a non-charm final state, are used to extract $|V_{ub}|$. The rate and kinematic distributions of these modes are much more difficult to predict, and they are currently a subject of much experimental and theoretical research.

Hadronic decays (Section 8) are the most complicated modes of all. The effects of strong interactions cannot be isolated to a single current, and final-state interactions between the hadronic systems can be significant. Nevertheless, there are special and intriguing phenomena in hadronic decays that, at least in the standard model, cannot occur in leptonic or semileptonic decays. Because there can be more than one decay diagram leading to a given final state, hadronic decays can display a variety of remarkable interference effects. In some cases, these effects give insight into the dynamics of the decay process, while in others they provide a powerful probe of CP-violating phases.

Figures 1c and 1d show the so-called external and internal spectator diagrams for hadronic decay. To a certain extent, the initial-state light quark in these decays can be regarded as a spectator, since it does not play a direct role in the underlying weak process. Generally speaking, the decays that can proceed through the external spectator diagram have rates that are larger than those which must go through the internal spectator diagram. In the latter case, there can be a color mismatch between the quarks produced by the W and the other quarks in the system, suppressing the rate. Interference between the external and internal spectator diagrams has extremely important implications in D^+ decay. The interference in this case is destructive, and it substantially lengthens the D^+ lifetime relative to that of the D^0. We will see that the interference has the opposite sign in B^+ decays, but its effects on the B^+ lifetime are much less significant. Lifetime measurements (Section 8.2) have reached an impressive level of precision and in some cases are raising some interesting theoretical questions.

In Section 8.3, I discuss rare B decays, which have branching fractions of about 10^{-4} or less. Such decays are due to a variety of processes. The spectator diagrams in Figs. 1c and 1d can lead to rare decays through $b \to u$ transitions, which are suppressed by roughly $(|V_{ub}|/|V_{cb}|)^2 \approx 7 \times 10^{-3}$ relative to the dominant $b \to c$ modes. Figure

1e shows a gluonic penguin diagram. This one-loop process involves the emission and reabsorption of the same W, and it leads to an effective flavor-changing neutral current giving $b \to s$ or $b \to d$ transitions. In some cases, the penguin process can interfere with a $b \to u$ spectator decay. Since the CKM phases are different for the two diagrams, the decay rate to a particular final state can be different from that for the CP-conjugate mode, in which the weak phases change sign. For example, one might discover different rates for $\bar{B}^0 \to K^-\pi^+$ and $B^0 \to K^+\pi^-$. CP violation resulting from this type of interference is called direct CP violation and would be extremely interesting to observe. Because it also depends on poorly understood strong phases, however, it will be difficult to use this effect to extract reliable values of the CKM phases. Currently, we have very little experimental data on gluonic penguins, but there should be much more in the relatively near future.

Penguin diagrams can also occur with the emission of a real or virtual photon (Figs. 1f and 1g). The former process has been measured by CLEO for both exclusive and inclusive modes, and more recently there have also been observations from the LEP experiments. Radiative penguin decays are sensitive to physics beyond the standard model, such as supersymmetry, since new, heavy particles can appear in the virtual loops.

In Section 9, I discuss the phenomenon of $B\bar{B}$ oscillations (sometimes called mixing). Figure 1h shows two box diagrams, which lead to the spontaneous oscillation of a B^0 into a $\bar{B}^0$ and vice-versa. (Similar diagrams are responsible for $B_s\bar{B}_s$ oscillations.) The oscillation probability is proportional to $\exp(-t/\tau)\sin^2[(\Delta M\tau/2)(t/\tau)]$, where $\Delta M \approx 0.5\ \mathrm{ps}^{-1}$ is the mass difference between the two neutral B_d mass eigenstates and τ is their (essentially equal) lifetime. The oscillation frequency is sufficiently rapid that an appreciable fraction ($\sim 20\%$) of neutral B mesons oscillate before they decay, and the oscillation probability peaks at about four lifetimes. The frequency is sufficiently slow that the oscillation of rapidly moving B mesons can be directly followed as they propagate through space. There is also great interest in observing B_s oscillations, but their expected rate is about twenty times faster. The probability to decay in the mixed state is essentially maximal (50%), but the structure of B_s oscillations is too fine for present experiments to resolve. From these measurements, one can extract the magnitudes of V_{td} and V_{ts}, which appear because the dominant contributions are due to virtual intermediate states containing t and $\bar{t}$ quarks. An experimental determination of the ratio of B_d to

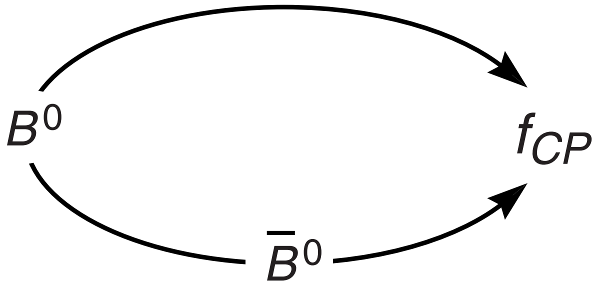

Fig. 2. CP-violating asymmetries result from interference effects involving phases that change sign under the CP operator. The weak phase of the CKM matrix has this property. One way to observe CP violation is to use the interference between the direct decay $B^0 \to f_{CP}$ and the process $B^0 \to \bar{B}^0 \to f_{CP}$. The standard model predicts substantial asymmetries between this process and that in which the initial meson is a $\bar{B}^0$.

B_s oscillation frequencies would help to reduce some of the theoretical uncertainties that arise from hadronic effects.

The subject of CP violation in B decays will open up dramatically in the next few years. I introduce the C and P operators in Sec. 9.1 and briefly discuss the relevance of CP violation to cosmology in Sec. 9.2. All CP-violating effects involve interfering amplitudes, and the various ways in which this can occur are examined in Sec. 9.3 (CP violation in decay), Sec. 9.4 (CP violation in mixing), and Sec. 9.6 (CP violation in the interference between mixing and decay). I have found the subjects of oscillations and CP violation to be quite difficult, and for this reason I include some discussion of the neutral kaon system as well for perspective. Section 9.5 discusses the phenomenology of mixing in these two systems. The major new efforts to study CP violation in the B system are based on the general idea illustrated in Figure 2, which shows that mixing can provide a second amplitude to interfere with a decay to a particular final state. In certain cases, this method can provide information on the CKM phases with little or no uncertainty from strong interaction effects. Experiments using this approach are under construction in the United States, Japan, and Europe; these major efforts will dramatically improve our knowledge of CP violation and the CKM matrix.

Bottom and charm physics involves the study of a large variety of processes, which can be used to measure fundamental parameters of the standard model, to search for effects of physics beyond the standard model, and to probe the dynamics of QCD and the electroweak interactions. Although there are a great many individual physics issues to focus on, it is also important to take a different view and to ask whether we understand bottom and charm physics in a broader sense. Do the measurements fit together? Are there, hiding in the dense forest of B decays, unexpected processes that we are missing?

3. Introduction to the Cabibbo-Kobayashi-Maskawa Matrix and a First Look at CP Violation

In this section, we examine the basic phenomenology of the CKM matrix. We will see that the CKM matrix is not simply an *ad hoc* parametrization of generation-changing quark transitions, but is instead an integral part of the standard model that is closely connected with the generation of quark masses. We briefly review processes that have already constrained the CKM matrix and summarize the current status of these constraints. Many of the quantities discussed later in the paper are defined and explained in this section, including the Wolfenstein parameters A, λ, ρ, and η, and the angles α, β, and γ of the unitarity triangle. Finally, I give a simple example illustrating how CP violation can arise from the CKM matrix.

The standard model successfully accounts for flavor-changing quark transitions in terms of a $V-A$ charged weak current operator $\mathcal{J}^\mu$ that couples to the W-boson according to the interaction Lagrangian

$$\mathcal{L}_{int} = -\frac{g}{\sqrt{2}}(\mathcal{J}^\mu W_\mu^+ + \mathcal{J}^{\mu\dagger} W_\mu^-), \tag{3.1}$$

where for quark transitions

$$\mathcal{J}^\mu = \sum_{i,j} V_{ij} J_{ij}^\mu = \sum_{i,j} \bar{u}_i \gamma^\mu \frac{1}{2}(1-\gamma_5) V_{ij} d_j. \tag{3.2}$$

The V_{ij} are the elements of the CKM matrix, and the indices i and j run over the three quark generations. The field operators u_i $(i = 1, 2, 3)$ annihilate u, c, and t (or create their antiparticles), and the d_j annihilate d, s, and b. The operator W_μ^+ annihilates a W^+ or creates a W^-; the reverse is true for W_μ^-. Thus, the amplitudes for the processes in which a W^- is radiated ($d_j \to W^- u_i$ and $\bar{u}_i \to W^- \bar{d}_j$) are proportional to V_{ij}, whereas the amplitudes for process in which a W^+ is radiated ($u_i \to W^+ d_j$ and $\bar{d}_j \to W^+ \bar{u}_i$) are proportional to V_{ij}^*.

The CKM matrix V can be regarded as a rotation from the quark mass eigenstates, d, s, and b, to a set of new states, d', s', and b', with diagonal couplings to u, c, and t. The standard notation is

$$\begin{pmatrix} d' \\ s' \\ b' \end{pmatrix} = \begin{pmatrix} V_{ud} & V_{us} & V_{ub} \\ V_{cd} & V_{cs} & V_{cb} \\ V_{td} & V_{ts} & V_{tb} \end{pmatrix} \begin{pmatrix} d \\ s \\ b \end{pmatrix} . \tag{3.3}$$

To a first approximation, the CKM matrix is simply the unit matrix, so that the dominant transitions are $u \to d$, $c \to s$, and $t \to b$. In reality, none of the off-diagonal elements is exactly zero, leading to generation-changing transitions between quarks and, as we will see, to the possibility of a CP-violating phase.

The values of CKM matrix elements, like fermion masses, are fundamental input parameters of the standard model and cannot be predicted. In a comprehensive theory of quark flavor—beyond the standard model—these parameters would be explained in terms of other physics or, at the very least, related to a smaller set of constants. Nevertheless, the standard model provides a key insight: the values of both fermion masses and CKM elements originate in the unknown couplings of the fermions to the Higgs field [3]. The detailed discussion of the relationship between the fermion mass matrices and the CKM matrix is beyond the scope of this paper. I will, however, briefly outline the argument as a reminder of how closely related the masses and CKM elements are.

The form of the Yukawa terms in the Lagrangian that couple the Higgs field to the quarks is constrained by $SU(2)_L$ gauge invariance, but this condition does not require the terms to be diagonal in quark flavor:

$$\begin{aligned} \mathcal{L}_{\text{Yukawa}} = \sum_{j,k} [\, & Y_{jk}(\bar{u}_L^j, \bar{d}_L^j) \begin{pmatrix} \phi^0 \\ -\phi^+ \end{pmatrix}^* u_R^k \\ & + \; Y'_{jk}(\bar{u}_L^j, \bar{d}_L^j) \begin{pmatrix} \phi^+ \\ \phi^0 \end{pmatrix} d_R^k + \text{h.c.}], \end{aligned} \tag{3.4}$$

where i and j run over the quark generations, L and R denote left- and right-handed components of the quark fields, and Y_{jk} and Y'_{jk} are the Yukawa couplings. The complex Higgs doublet undergoes spontaneous symmetry breaking:

$$\phi = \begin{pmatrix} \phi^+ \\ \phi^0 \end{pmatrix} \to \frac{1}{\sqrt{2}} \begin{pmatrix} 0 \\ v + H(x) \end{pmatrix} , \tag{3.5}$$

where v is the Higgs vacuum expectation value, and $H(x)$ is the field corresponding to the Higgs particle. After spontaneous symmetry breaking, the Lagrangian becomes

$$\mathcal{L}_{\text{Yukawa}} = \sum_{j,k}[Y_{jk}\bar{u}_L^j u_R^k + Y'_{jk}\bar{d}_L^j d_R^k + \text{h.c.}]\frac{1}{\sqrt{2}}(v + H(x)). \tag{3.6}$$

The terms proportional to v couple the left- and right-handed components of the quark fields and generate the mass terms. To determine the quark mass eigenstates, however, one must diagonalize the mass matrices

$$m_{jk} \equiv \frac{-v}{\sqrt{2}}Y_{jk} \qquad m'_{jk} \equiv \frac{-v}{\sqrt{2}}Y'_{jk}. \tag{3.7}$$

The CKM matrix is a product of unitary matrices that accomplish this task, and it is therefore unitary by construction. The nine fermion masses and four CKM elements are therefore intimately related, and together account for 13 of the 18 standard model parameters. The remaining parameters are the three $SU(3)_C \times SU(2)_L \times U(1)_Y$ gauge coupling constants, the Higgs mass, and the Higgs vacuum expectation value.

The magnitudes of CKM elements are determined largely, but not exclusively, from semileptonic processes. A high-precision value of $|V_{ud}|$ is obtained by comparing the rates for superallowed $0^+ \to 0^+$ nuclear β decays to the muon decay rate. Semileptonic K^0 and K^+ decays are used to extract $|V_{us}|$. The values for $|V_{cs}|$ and $|V_{cd}|$ can be determined using a variety of techniques. The rate of charm production in neutrino interactions with valence quarks in nucleons has been used to determine $|V_{cd}|$. A similar determination of $|V_{cs}|$ is complicated by lack of knowledge regarding the population of $s\bar{s}$ pairs in the nucleon "sea." Alternatively, $|V_{cs}|$ can be determined from the decay $D \to \bar{K}e^+\nu_e$. The magnitudes of the CKM elements for the 2×2 sector governing transitions within the first two generations are [4]

$$\begin{aligned} &|V_{ud}| = 0.9740 \pm 0.0010 \qquad &&|V_{us}| = 0.2196 \pm 0.0023 \\ &|V_{cd}| = 0.224 \pm 0.016 \qquad &&|V_{cs}| = 1.04 \pm 0.16. \end{aligned} \tag{3.8}$$

These values are determined without any assumptions regarding unitarity, a point that we will revisit below.

When a CKM element is determined from a measured decay rate or branching fraction, an absolute scale must be set by theory. If the initial meson with quarks $Q\bar{q}$ is denoted $M_{Q\bar{q}}$, the branching fraction for a semileptonic decay to a hadronic final state $X_{q'q}$ can be written

$$B(M_{Q\bar{q}} \to X_{q'\bar{q}}\ell\nu) = \gamma|V_{q'Q}|^2\tau_M, \tag{3.9}$$

where τ_M is the mean lifetime of M. Experimentalists measure the branching fraction and lifetime, thus determining the decay rate; it falls to theorists to determine γ. A partial exception to this argument is the determination of $|V_{ud}|$, where the overall scale is determined from muon decay. Still, important theoretical corrections are required even in this case. The value for $|V_{cs}|$ given above relies on a theoretical calculation of a D semileptonic transition form factor to set the scale.

For both V_{cd} and V_{cs}, however, one can adopt a different point of view, which is quite important in practice. In this view, we assume that the CKM is unitary, as required in the standard model. Unitarity of the third row and third column implies

$$\sqrt{1-|V_{tb}|^2} = \sqrt{|V_{td}|^2+|V_{ts}|^2} = \sqrt{|V_{ub}|^2+|V_{cb}|^2} \approx 0.04. \tag{3.10}$$

Thus, $|V_{td}|$ and $|V_{ts}|$ must each be less than about 0.04, which implies that

$$\begin{aligned} |V_{ud}|^2 + |V_{cd}|^2 &= 1 - |V_{td}|^2 \approx 1 \\ |V_{us}|^2 + |V_{cs}|^2 &= 1 - |V_{ts}|^2 \approx 1. \end{aligned} \tag{3.11}$$

In other words, if we assume unitarity, the known very small values of $|V_{cb}|$ and $|V_{ub}|$ imply that $|V_{cd}|$ and $|V_{cs}|$ are essentially determined from $|V_{ud}|$, $|V_{us}|$, and Eq. 3.11.

For charm decays, the real aim has therefore not been to determine $|V_{cd}|$ and $|V_{cs}|$, but to use these inferred values so that the *absolute scale* of the form factors can be obtained from experiment. This procedure allows one to check complicated QCD calculations that give the form factor normalizations. This approach cannot be applied to b-hadron decays, where we do not have a comparable check of the theoretical predictions for the factor γ in Eq. 3.9. In B decays, one can measure the *shapes* (q^2 dependences) and *relative sizes* of the form factors, but the overall scale must be determined from theory.

We will see in Sec. 7 that semileptonic decays of B mesons are used to measure $|V_{cb}|$ and $|V_{ub}|$:

$$\begin{aligned} |V_{ub}| &= 0.0033 \pm 0.0008 \\ |V_{cb}| &= 0.0387 \pm 0.0031, \end{aligned} \tag{3.12}$$

where the value for $|V_{cb}|$ is based on the world-average value from $B \to D^*\ell^-\bar{\nu}$ (Table 14) and that for $|V_{ub}|$ is obtained from the CLEO II measurements [5] of $\bar{B} \to \pi\ell^-\bar{\nu}$ and $\bar{B} \to \rho\ell^-\bar{\nu}$ (Eq. 7.96). Thus, $|V_{ub}/V_{cb}| \approx 0.085$.

Information on $|V_{td}|$ and $|V_{ts}|$ can be extracted from $B^0\bar{B}^0$ and $B_s\bar{B}_s$ mixing and from $B \to X_s\gamma$ processes. Using the $B^0\bar{B}^0$ mixing rate, $\Delta M_{B_d} = 0.472 \pm 0.018\ \mathrm{ps}^{-1}$, and other input parameters, the PDG quotes [4]

$$|V_{tb}^* \cdot V_{td}| = 0.0084 \pm 0.0018, \tag{3.13}$$

which shows that V_{td} is of the same order as V_{ub}. If we use the unitarity condition between the second and third columns of the CKM matrix,

$$V_{us}V_{ub}^* + V_{cs}V_{cb}^* + V_{ts}V_{tb}^* = 0, \tag{3.14}$$

and ignore the first term compared to the other two, we find that $|V_{ts}| \approx |V_{cs}V_{cb}^*/V_{tb}^*| \approx |V_{cb}|$, which is borne out by the $B \to X_s\gamma$ measurements.

The current experimental constraint on V_{tb} is very weak. Measurements of semileptonic t decays from CDF and D0 indicate that [6]

$$\frac{|V_{tb}|^2}{|V_{td}|^2 + |V_{ts}|^2 + |V_{tb}|^2} = 0.99 \pm 0.29, \tag{3.15}$$

consistent with the expectation from unitarity of the third column.

Before leaving the subject of the magnitudes of CKM elements, I would like to point out a simple consequence of Eq. 3.9 for the uncertainty on a magnitude. Experimenters generally measure branching fractions, so using this equation involves taking a square root. From the simple propagation of errors, this means that the relative uncertainty on the CKM element is half of that on the branching fraction. If you are impressed by a 5% experimental uncertainty on $|V_{cb}|$, for example, remember that the branching fraction had a 10% uncertainty!

Although we have considered the magnitudes of nine CKM elements, there are only four independent, real parameters needed to specify them in the standard model [3,7,8]. In general, an $n \times n$ unitary matrix has n^2 independent, real parameters. (There are $2n^2$ real parameters but there are n constraints from the normalization of each column and $n(n-1)$ constraints, real plus imaginary, from the orthogonality between each pair of columns. The conditions on the rows do not add additional constraints. One can also see this result by writing $U = \exp(iH)$, where H is a hermitian matrix.) In the CKM matrix, not all of these parameters are physically meaningful, however, because, for n quark generations, $2n-1$ phases can be absorbed by the freedom to select the phases of the quark fields. The number of physical parameters is therefore $n^2-(2n-1) = (n-1)^2$, which gives four parameters for three generations.

Let's examine how this quark rephasing can work [3,9]. We can attach a phase factor to each of the quark operators, so that the current operator becomes

$$\mathcal{J}^\mu = (\, ue^{-i\theta_u}, ce^{-i\theta_c}, te^{-i\theta_t}\,)\, \frac{1}{2}\gamma^\mu(1-\gamma_5) \begin{pmatrix} V_{ud} & V_{us} & V_{ub} \\ V_{cd} & V_{cs} & V_{cb} \\ V_{td} & V_{ts} & V_{tb} \end{pmatrix} \begin{pmatrix} de^{i\theta_d} \\ se^{i\theta_s} \\ be^{i\theta_b} \end{pmatrix}. \tag{3.16}$$

The u, c, and t phases each allow us to multiply a row of the CKM matrix by a phase, while the d, s, and b phases each allow us to multiply a column by a phase. We can therefore select the u, c, and t quark phases so as to make one element in each of the three rows real, say V_{us}, V_{cs}, and V_{ts}. Having made the second column real, we can select the d, s, and b phases so as to make one element in each of the first and third columns real, say V_{ud} and V_{cb}. Thus, with six quarks, we are able to remove five CKM phases; with n quark generations, we can remove $2n-1$ phases.

What degrees of freedom remain in the CKM matrix? We know that an arbitrary $n \times n$ unitary matrix contains n^2 real parameters. If the CKM matrix were merely orthogonal and real, there would be $n^2 - n - \frac{1}{2}n(n-1) = \frac{1}{2}n(n-1)$ independent real rotation parameters. We can summarize the results so far as

- A general unitary matrix has n^2 independent real parameters.
- Of these, $\frac{1}{2}n(n-1)$ are real rotation angles.
- Because we can rephase the quark fields, the number of independent phase factors is therefore $n^2 - \frac{1}{2}n(n-1) - (2n-1) = \frac{1}{2}(n-1)(n-2)$.
- The total number of physical parameters is $(n-1)^2$.

The results for 2, 3, and 4 generations are listed in Table 1. A key conclusion is that there must be at least three generations in order for the CKM matrix to contain a complex phase factor. As we will see, this implies that at least three generations are required for the CKM matrix to produce CP-violating asymmetries.

A standard parametrization for the CKM matrix used by the Particle Data Group [4] is the set of angles $\theta_{12}, \theta_{23}, \theta_{13}$, and δ_{13}, specifying the rotation

$$V = \begin{pmatrix} c_{12}c_{13} & s_{12}c_{13} & s_{13}e^{-i\delta_{13}} \\ -s_{12}c_{23} - c_{12}s_{23}s_{13}e^{i\delta_{13}} & c_{12}c_{23} - s_{12}s_{23}s_{13}e^{i\delta_{13}} & s_{23}c_{13} \\ s_{12}s_{23} - c_{12}c_{23}s_{13}e^{i\delta_{13}} & -c_{12}s_{23} - s_{12}c_{23}s_{13}e^{i\delta_{13}} & c_{23}c_{13} \end{pmatrix}, \tag{3.17}$$

where $c_{12} = \cos\theta_{12}$, $s_{12} = \sin\theta_{12}$, etc. The phase δ_{13} produces CP

Table 1

Degrees of freedom in the CKM matrix as a function of the number n of quark generations.

n (generations)	Total indep. params $(n-1)^2$	Real rot. angles $\frac{1}{2}n(n-1)$	Complex phase factors $\frac{1}{2}(n-1)(n-2)$
2	1	1	0
3	4	3	1
4	9	6	3

violation and would not appear if there were only two generations. This formidable-looking matrix takes on a simpler form if we use the fact that $|V_{ub}| \simeq 0.003$ is very small, so that c_{13} is extremely close to unity. We can then neglect terms proportional to s_{13} relative to terms of order unity, which gives

$$V \approx \begin{pmatrix} c_{12} & s_{12} & s_{13}e^{-i\delta_{13}} \\ -s_{12}c_{23} & c_{12}c_{23} & s_{23} \\ s_{12}s_{23} - c_{12}c_{23}s_{13}e^{i\delta_{13}} & -c_{12}s_{23} & c_{23}c_{13} \end{pmatrix}. \tag{3.18}$$

In this approximation, only V_{ub} and V_{td} carry phases.

Empirically, there is a hierarchy in the magnitudes of CKM elements, which we have already begun to exploit by using the smallness of $|V_{ub}|$. This hierarchy motivates a particular expansion of the CKM matrix, first given by Wolfenstein [10], in the small parameter $\lambda = \sin\theta_C \simeq 0.22$, where θ_C is the Cabibbo angle:

$$V = \begin{pmatrix} V_{ud} & V_{us} & V_{ub} \\ V_{cd} & V_{cs} & V_{cb} \\ V_{td} & V_{ts} & V_{tb} \end{pmatrix} \tag{3.19}$$

$$= \begin{pmatrix} 1-\frac{1}{2}\lambda^2 & \lambda & A\lambda^3(\rho - i\eta) \\ -\lambda & 1-\frac{1}{2}\lambda^2 & A\lambda^2 \\ A\lambda^3(1-\rho-i\eta) & -A\lambda^2 & 1 \end{pmatrix} + \mathcal{O}(\lambda^4). \tag{3.20}$$

The known values of CKM elements can be used to motivate this form, in which only four independent parameters remain: A, λ, ρ, and η. Note that, to $\mathcal{O}(\lambda^4) \approx 10^{-3}$, the 2×2 upper-left portion of the CKM matrix—the matrix associated with Cabibbo rotations of the d- and s-quarks—is constructed to be nearly unitary:

$$(1 - \frac{1}{2}\lambda^2)^2 + \lambda^2 = 1 + \mathcal{O}(\lambda^4) \tag{3.21}$$

in accord with measurements, which give $\sqrt{|V_{ud}|^2 + |V_{us}|^2} = 0.998$. (Of course, exact unitarity of this sector was postulated by Glashow, Iliopoulos, and Maiani to suppress strangeness-changing neutral currents in kaon decays.) Even though $b \to c$ transitions involve only one generation change, the magnitude of V_{cb} is measured to be quite small—about 0.04. As a consequence, the B-meson lifetime is quite long. (Naively, one might have guessed from the magnitude of V_{us} that the amplitude for any one-generation transition would be of order λ, but this is not correct.) Thus, it is natural to write $V_{cb} = A\lambda^2$, where A is a constant of order unity. We also know that $|V_{ub}| \sim 0.003$ or $|V_{ub}/V_{cb}| \sim 0.08$. This suggests that we write $V_{ub} = A\lambda^3(\rho - i\eta)$, where we choose to incorporate the phase in this element (in accord with Eq. 3.18). From the unitarity of the third column, the magnitude of V_{tb} is equal to unity up to corrections of $\mathcal{O}(\lambda^4)$. The orthogonality of the second and third columns then gives $V_{ts} \simeq -V_{cb} = -A\lambda^2$. Finally, orthogonality between the third and first columns specifies

$$A\lambda^3(\rho - i\eta)(1) + A\lambda^2(-\lambda) + 1 \cdot V_{td}^* = 0 + \mathcal{O}(\lambda^4), \tag{3.22}$$

or $V_{td} = A\lambda^3(1 - \rho - i\eta)$. This parametrization is very convenient for understanding how various measurements constrain the CKM matrix and is completely adequate for our purposes. For discussions in which higher accuracy is required, the expansion can be carried out further, as discussed by Buras and Fleischer [11,12].

By applying the orthogonality condition to the first and third columns, we can obtain a useful relation between the two smallest elements of the CKM matrix, V_{ub} and V_{td}:

$$V_{ud}V_{ub}^* + V_{cd}V_{cb}^* + V_{td}V_{tb}^* = 0, \tag{3.23}$$

in which each term in the sum is of order λ^3. This relation, which has been emphasized by Bjorken and Chau and Keung [13], can be represented by a triangle in the complex plane (Fig. 3). In the parametrization given above, V_{cd}, V_{cb}, and V_{tb} are all real, and by using $V_{ud} \simeq V_{tb} \simeq 1$ and $V_{cd} < 0$ we obtain

$$\frac{V_{ub}^*}{|V_{cd}V_{cb}|} + \frac{V_{td}}{|V_{cd}V_{cb}|} = 1. \tag{3.24}$$

In terms of the Wolfenstein parameters given in Eq. 3.20, the coordinates of the vertices of the triangle are (0,0), (1,0), and (ρ, η).

From Eq. 3.20, it is also easy to see that measurements of $|V_{cb}|$ and $|V_{ub}|$ provide the constraints

$$|V_{cb}/V_{us}|^2 = A \qquad \text{and} \qquad |V_{ub}^*/V_{cd}V_{cb}| = \sqrt{\rho^2 + \eta^2}. \tag{3.25}$$

Thus, measurements of $|V_{cb}|$ essentially determine A. The constraint from $|V_{ub}|$ defines a circle in the (ρ, η) plane; when errors are taken

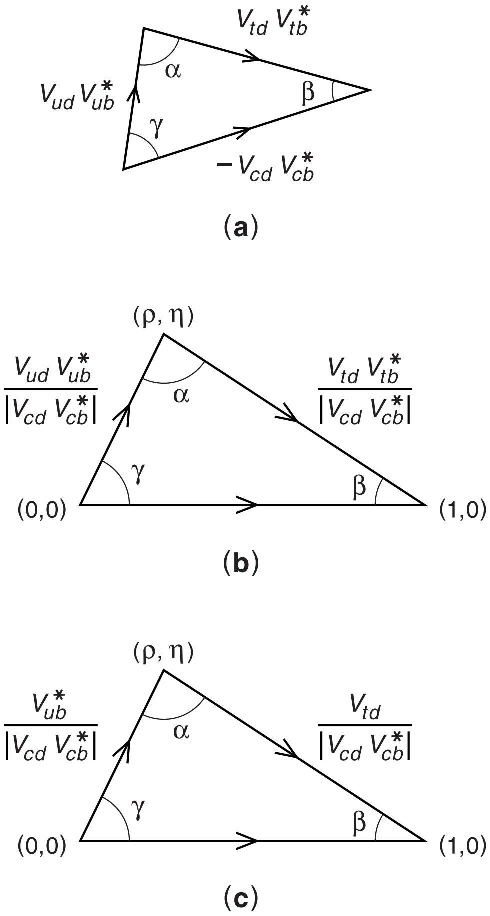

Fig. 3. The CKM unitarity triangle: (a) shows the orthogonality condition between the first and third columns of the CKM matrix; the orientation of the triangle is arbitrary and depends on phase convention. (b) shows a rescaled version of the triangle in which each side has been divided by the $|V_{cd}V_{cb}^*|$, so that the base has unit length. The base has also been aligned with the real axis by choice of phase convention. (c) shows a commonly used labeling resulting from the approximation $V_{ud} = V_{tb} = 1$. In the Wolfenstein parametrization, the upper vertex of the triangle has coordinates (ρ, η). All CP-violating amplitudes in the standard model are proportional to the area of the triangle.

into account this constraint becomes an annulus. The equations that describe constraints from $B^0\bar{B}^0$ and $B_s\bar{B}_s$ mixing are given in Sec. 9.5 (Eq. 9.108). Since the mixing rates are dominated by virtual $t\bar{t}$ intermediate states, $B^0\bar{B}^0$ measurements constrain

$$|V_{td}|^2 = A^2\lambda^6[(1-\rho)^2 + \eta^2]. \tag{3.26}$$

A particular value of $|V_{td}|$ corresponds to a circle centered at the point $(\rho = 1, \eta = 0)$. Figure 4 shows the separate constraints on the location of the point (ρ, η) from $|V_{ub}|$ (from $B \to X_u \ell^- \bar{\nu}$), $|V_{td}|$ (from $B^0\bar{B}^0$ mixing) and $|\epsilon_K|$ (from CP violation in the neutral K system). This figure is meant to illustrate the way in which the individual constraints enter; a much more carefully constructed plot of the combined constraint, taking into account correlations, is discussed below.

What information do we obtain from $B_s\bar{B}_s$ mixing? From Eq. 9.108, we see that the mixing rate determines $|V_{ts}|$, which is essentially the same as $|V_{cb}|$. The real value of the $B_s\bar{B}_s$ mixing measurement, however, is that it allows us to reduce the uncertainties that affect the determination of $|V_{td}|$. The ratio of $B^0\bar{B}^0$ to $B_s\bar{B}_s$ mixing rates determines

$$\frac{\Delta M_d}{\Delta M_s} = \frac{|V_{td}|^2}{|V_{ts}|^2}\frac{M_{B_d}}{M_{B_s}}\frac{f_{B_d}^2 B_{B_d}}{f_{B_s}^2 B_{B_s}}. \tag{3.27}$$

The ratios of the decay and bag constants in this equation are much easier to predict than their individual values, so measurements or even limits on $B_s\bar{B}_s$ mixing are extremely valuable.

We digress briefly to discuss the constraint on the unitarity triangle from ϵ_K. To a good approximation [12,14],

$$\epsilon_K = \frac{e^{i\pi/4}}{\sqrt{2}\Delta M_K}\,\mathrm{Im}\, M_{12}, \tag{3.28}$$

where a small ($\approx 2\%$) correction term proportional to $\mathrm{Re}\, M_{12}$ has been ignored and

$$\begin{aligned} M_{12} = \frac{G_F^2 M_W^2}{12\pi^2} f_K^2 B_K M_K \times [&(V_{cs}V_{cd}^*)^2 \eta_1 S_0(x_c) + (V_{ts}V_{td}^*)^2 \eta_2 S_0(x_t) \\ &+ (V_{cs}V_{cd}^*)(V_{ts}V_{td}^*)\eta_3 S_0(x_c, x_t)], \end{aligned} \tag{3.29}$$

where $x_i = m_i^2/M_W^2$ $(i = c, t)$, f_K is the K decay constant, and B_K is a phenomenological bag constant parametrizing non-perturbative QCD effects. The factors $\eta_1 = 1.38 \pm 0.20$, $\eta_2 = 0.57 \pm 0.01$, and $\eta_3 = 0.47 \pm 0.04$ are relatively well-known QCD corrections that depend on the heavy-quark masses. The functions $S_0(x)$ and $S_0(x_c, x_t)$ are given by

$$\begin{aligned} S_0(x) &= \frac{4x - 11x^2 + x^3}{4(1-x)^2} - \frac{3x^3 \ln x}{2(1-x)^3} \\ S_0(x_c, x_t) &= x_c\left[\ln\frac{x_t}{x_c} - \frac{3x_t}{4(1-x_t)} - \frac{3x_t^2 \ln x_t}{4(1-x_t)^2}\right], \end{aligned} \tag{3.30}$$

where in the last expression only the linear terms in $x_c \ll 1$ have been kept. The largest uncertainty in using these relations has been in the value of B_K. However, the precision and reliability of lattice QCD calculations have improved significantly over the past few years, and the value $B_K = 0.75 \pm 0.15$ is commonly used [11].

To derive the constraint in the (ρ, η) plane, we need to express the CKM elements in Eq. 3.29 in terms of ρ and η and then take the imaginary part. The term from the $t\bar{t}$ intermediate state gives

$$\begin{aligned} \mathrm{Im}[(V_{ts}V_{td}^*)^2] &= \mathrm{Im}\{[-A\lambda^2 A\lambda^3(1-\rho+i\eta)]^2\} \\ &= 2A^4\lambda^{10}\eta(1-\rho). \end{aligned} \tag{3.31}$$

This result shows that for ρ well away from 1, the extraction of $|\epsilon_K|$ depends on

$$A^4 = \frac{|V_{cb}|^4}{\lambda^8}. \tag{3.32}$$

Thus, the relative uncertainty in $|V_{cb}|$ is magnified by as much as a factor of four when it propagates into the uncertainty on $|\epsilon_K|$. The term from the ct intermediate state gives $\mathrm{Im}(V_{cs}V_{cd}^*)(V_{ts}V_{td}^*) = A^2\lambda^6\eta$ and is therefore less sensitive to $|V_{cb}|$. The evaluation of $\mathrm{Im}(V_{cs}V_{cd}^*)^2$ requires use of the $\mathcal{O}(\lambda^5)$ correction to the imaginary part of V_{cd}; in other words, one has to carry out the expansion of the Wolfenstein parametrization to higher order. This expansion is discussed in Buras and Fleischer [12], with the result $\Delta V_{cd} = -iA^2\lambda^5\eta$; this implies $\mathrm{Im}(V_{cs}V_{cd}^*)^2 = -2A^2\lambda^6\eta$. With these results, one can show that the measurement of $|\epsilon_K|$, together with the value of $|V_{cb}|$, yields the hyperbolic constraint curves shown in Fig. 4.

A very careful analysis of the CKM constraints has been performed by Grossman, Nir, Plaszczynski, and Schune [15]. This analysis takes into account the non-gaussian nature of the model-dependent errors on $|V_{ub}|$, $f_{B_d}\sqrt{B_{B_d}}$, B_K, and $f_{B_s}^2 B_{B_s}/f_{B_d}^2 B_{B_d}$. The combined constraint is shown in Fig. 5a without the measured limit on B_s mixing and in Fig. 5b with the limit incorporated.

One can show that in order for CP violation to be permitted in the standard model, the area of the unitarity triangle must be nonzero. In particular, V_{ub} and V_{td} must be nonzero and complex relative to $V_{cd}V_{cb}$. More quantitatively, the interference terms that produce CP violation are proportional to the quantity [3]

$$J_{\mathrm{CP}} = |\mathrm{Im}(V_{ij}V_{il}^*V_{kj}^*V_{kl})|; \qquad i \neq k, \mathrm{J} \neq l, \tag{3.33}$$

where no sums are implied. What is this equation telling us? The term $z_1 = V_{ij}V_{il}^*$ is one term in the sum of terms that gives the inner product

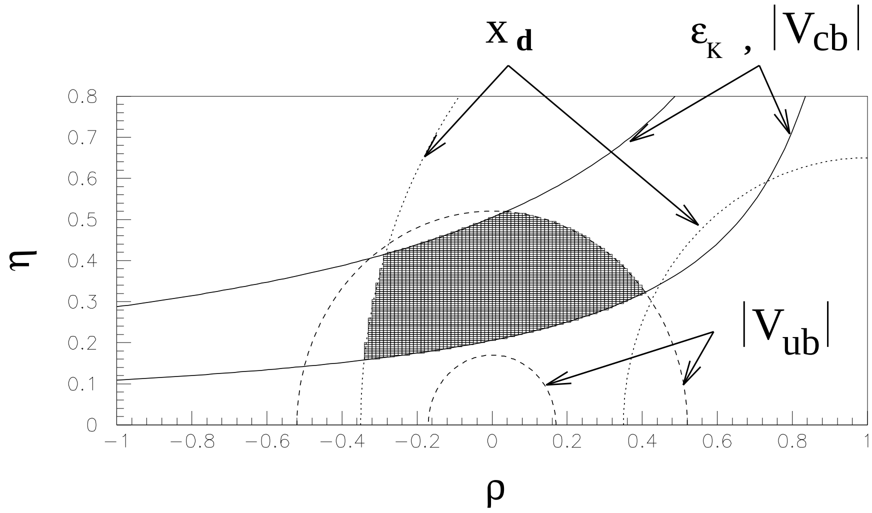

Fig. 4. Individual constraints on the (ρ, η) plane arising from measurements of $|V_{ub}|$, $B^0\bar{B}^0$ mixing ($|V_{td}|$), CP violation in kaon decays (ϵ), and $|V_{cb}|$. It is important to recognize that the hyperbolic curves derived from CP violation in kaon decays also depend on $|V_{cb}|$. The bands shown correspond to 1.5σ. The proper calculation of the overlap region, however, must take into account correlations. This is done in Fig. 5, which also uses more recent values of all input quantities. From Ref. [1].

between column j and column l. Similarly, $z_2^* = V_{kj}^* V_{kl}$ is the complex conjugate of another one of these terms. Using polar coordinates it is easy to show that the quantity $\mathrm{Im}(z_1 z_2^*)$ is proportional to the sine of the angle between z_1 and z_2; in fact, the result is twice the area of the triangle of which z_1 and z_2 are two sides. This quantity gives a measure of CP-violating interference terms that is independent of the overall orientation of unitarity triangle constructed from the inner product between columns j and l. In the Wolfenstein parametrization,

$$J_{\mathrm{CP}} \simeq A^2 \eta \lambda^6, \tag{3.34}$$

so $\eta \neq 0$ is required for CP violation.

It is worth remembering that there are in fact six CKM unitarity triangles: three from inner products between the columns and three from inner products between the rows. It can be shown [3] that all of these triangles have the same area. The three triangles corresponding to inner products between the columns represent the relations

$$\begin{aligned} &V_{ud}V_{us}^* + V_{cd}V_{cs}^* + V_{td}V_{ts}^* = 0 \\ &V_{ud}V_{ub}^* + V_{cd}V_{cb}^* + V_{td}V_{tb}^* = 0 \\ &V_{us}V_{ub}^* + V_{cs}V_{cb}^* + V_{ts}V_{tb}^* = 0. \end{aligned} \tag{3.35}$$

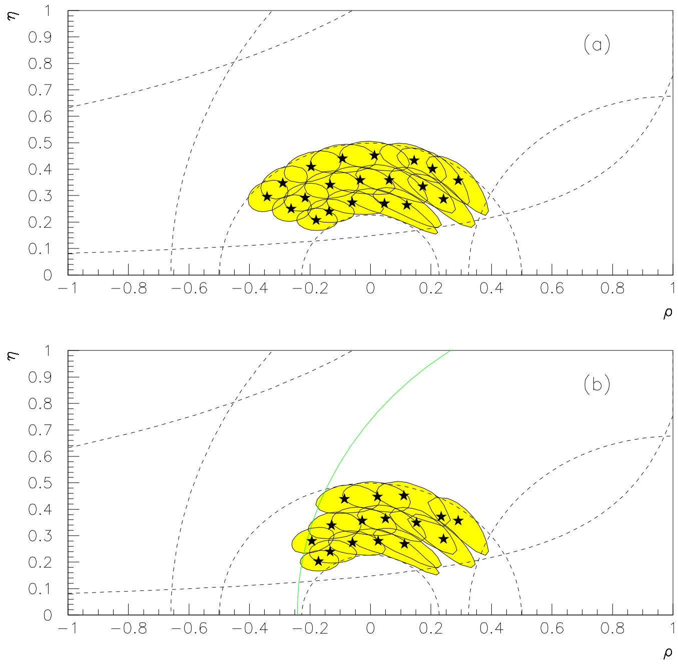

Fig. 5. Current constraints on the (ρ, η) plane (a) without $B_s\bar{B}_s$ mixing information and (b) with $B_s\bar{B}_s$ mixing information included. This analysis incorporates non-gaussian errors on various model-dependent quantities. The allowed region (shaded) corresponds to 95% C.L. Figure provided by M.-H. Schune.

We can count powers of λ to get a rough feeling for the appearance of these triangles:

$$\begin{aligned} \mathcal{O}(\lambda) + \mathcal{O}(\lambda) + \mathcal{O}(\lambda^5) &= 0 \\ \mathcal{O}(\lambda^3) + \mathcal{O}(\lambda^3) + \mathcal{O}(\lambda^3) &= 0 \\ \mathcal{O}(\lambda^4) + \mathcal{O}(\lambda^2) + \mathcal{O}(\lambda^2) &= 0. \end{aligned} \tag{3.36}$$

The triangles are clearly very different: the (column 1)$\times$(column 2)* triangle has two long sides of order λ and one very short side of order λ^5, while the (column 1)$\times$(column 3)* triangle is special in that all three sides have lengths of order λ^3. It is crucial, however, to remember that all of these triangles have the same area, and it is not hard to verify Eq. 3.34. What does this area correspond to? Factors like $[(V_{ub}V_{us}^*)(V_{tb}V_{ts}^*)^*]$ are associated with *interference terms* between first-order weak amplitudes. For example, for $\bar{B}^0 \to K^-\pi^+$ there could be a tree amplitude $A_1 \propto (V_{ub}V_{us}^*) \sim [(A\lambda^3)\lambda]$ from a $b \to uW^-$,

$W^- \to \bar{u}s$ decay and and a penguin amplitude $A_2 \propto (V_{tb}V_{ts}^*) \sim A\lambda^2$ from a $b \to t \to s$ transition with the emission and reabsorption of a W^-. (See Fig. 1.) Equation 3.34 is telling us that the product of of CKM factors for all such interference term are the same.

In a measurement, however, it is not the size of the interference term by itself that matters, but the size of the interference term relative to the rate for the process. For two interfering amplitudes A_1 and A_2, the asymmetry between a process and its CP conjugate is of the form

$$\mathcal{A}_{CP} = \frac{|A_1 + A_2|^2 - |\bar{A}_1 + \bar{A}_2|^2}{|A_1 + A_2|^2 + |\bar{A}_1 + \bar{A}_2|^2}, \tag{3.37}$$

where $\bar{A}_1$ and $\bar{A}_2$ are the amplitudes for the CP conjugate process. The numerator gives the interference term, while the denominator contains the squares of the magnitudes of the individual amplitudes as well. In some sense, the strategy for CP studies is to find situations in which the denominator is not much bigger than the numerator ($\propto A^2\eta\lambda^6$)! This is precisely what can happen with interference terms based on (column 1)$\times$(column 3)*: all sides of the triangle are $\mathcal{O}(\lambda^3)$, so the denominator itself is proportional to λ^6. We can therefore have asymmetries of order unity. In contrast, the squashed shape of the triangle relevant to the neutral kaon system means that the denominator will be large (λ^2) compared to the numerator in that case.

Further discussion of the connection between complex elements of the CKM matrix and CP violation can be found at the end of this section, in Sec. 9, and in Sec. 12.

We will see that the angles α, β, and γ can be extracted from CP violating asymmetries in B and B_s decays. Using the result $z_2/z_1 = (|z_2|/|z_1|)\exp i(\theta_2 - \theta_1)$, where $z_1 = |z_1|\exp(i\theta_1)$ and $z_2 = |z_2|\exp(i\theta_2)$, we can relate the terms in Eq. 3.23 to the angles of the unitarity triangle shown in Fig. 3. For example, from the upper-left and upper-right sides of the triangle we have

$$\frac{V_{ub}^*V_{ud}/|V_{ub}^*||V_{ud}|}{V_{tb}^*V_{td}/|V_{tb}^*||V_{td}|} = e^{i(\pi-\alpha)}, \tag{3.38}$$

or

$$\frac{V_{tb}^*V_{td}/|V_{tb}^*||V_{td}|}{V_{ub}^*V_{ud}/|V_{ub}^*||V_{ud}|} = -e^{i\alpha}, \qquad \alpha = \arg\left[-\frac{V_{tb}^*V_{td}}{V_{ub}^*V_{ud}}\right]. \tag{3.39}$$

The upper-right and lower sides give

$$\frac{(-V_{cb}^*V_{cd})/|V_{cb}^*||V_{cd}|}{V_{tb}^*V_{td}/|V_{tb}^*||V_{td}|} = e^{i\beta}, \qquad \beta = \arg\left[-\frac{V_{cb}^*V_{cd}}{V_{tb}^*V_{td}}\right]. \tag{3.40}$$

Finally, the upper left and lower sides give

$$\frac{V_{ub}^* V_{ud}/|V_{ub}^*||V_{ud}|}{(-V_{cb}^* V_{cd})/|V_{cb}^*||V_{cd}|} = e^{i\gamma}, \qquad \gamma = \arg\left[-\frac{V_{ub}^* V_{ud}}{V_{cb}^* V_{cd}}\right]. \tag{3.41}$$

In our discussion of CP violation, we will encounter the quantities

$$\begin{aligned}
\mathrm{Im}\left(\frac{V_{tb}^* V_{td}}{V_{tb} V_{td}^*}\frac{V_{ub} V_{ud}^*}{V_{ub}^* V_{ud}}\right) &= \sin 2\alpha \\
\mathrm{Im}\left(\frac{V_{cb}^* V_{cd}}{V_{cb} V_{cd}^*}\frac{V_{tb} V_{td}^*}{V_{tb}^* V_{td}}\right) &= \sin 2\beta \\
\mathrm{Im}\left(\frac{V_{ub}^* V_{ud}}{V_{ub} V_{ud}^*}\frac{V_{cb} V_{cd}^*}{V_{cb}^* V_{cd}}\right) &= \sin 2\gamma.
\end{aligned} \tag{3.42}$$

In the conventional parametrization of the CKM matrix, V_{ud}, V_{cd}, V_{cb}, and V_{tb} are real and $V_{cb} < 0$ so that

$$\frac{V_{td}}{V_{ub}^*} = -\frac{|V_{td}|}{|V_{ub}|}e^{i\alpha}, \qquad V_{td} = |V_{td}|e^{-i\beta}, \qquad V_{ub}^* = |V_{ub}|e^{i\gamma} \tag{3.43}$$

and

$$\begin{aligned}
\sin 2\alpha &= \mathrm{Im}\left(\frac{V_{ub} V_{td}}{V_{ub}^* V_{td}^*}\right) \\
\sin 2\beta &= \mathrm{Im}\left(\frac{V_{td}^*}{V_{td}}\right) \\
\sin 2\gamma &= \mathrm{Im}\left(\frac{V_{ub}^*}{V_{ub}}\right).
\end{aligned} \tag{3.44}$$

We can also connect α, β, and γ with the Wolfenstein parameters ρ and η. From Fig. 3 we have

$$\begin{aligned}
\tan\alpha &= \frac{\eta}{\eta^2 - \rho(1-\rho)}, \qquad \tan\beta = \frac{\eta}{1-\rho}, \\
\tan\gamma &= \frac{\eta}{\rho}.
\end{aligned} \tag{3.45}$$

I want to briefly discuss an example of CP violation, since the central idea is quite simple, and there are several interesting observations that we can already make. We will compare the decay rates for $\bar{B}^0(b\bar{d}) \to \pi^+\pi^-$ and $B^0(\bar{b}d) \to \pi^+\pi^-$. Each of these processes has a contribution from a tree diagram, with amplitudes

$$\begin{aligned}
A_T(\bar{B}^0 \to \pi^+\pi^-) &= aV_{ub}V_{ud}^* \\
A_T(B^0 \to \pi^+\pi^-) &= aV_{ub}^*V_{ud}.
\end{aligned} \tag{3.46}$$

For simplicity, we ignore the penguin contribution to the decay. The coefficient a contains a lot of complicated physics, including final-state interactions, and it is in general a complex number. However, a is not conjugated in going from B^0 to $\bar{B}^0$. (The relation between the two amplitudes in Eq. 3.46 is treated much more carefully in Sec. 9 and in the Appendix.) If these were the only amplitudes present, there would be no CP asymmetry, since the magnitudes of the amplitudes are the same. In fact, the factor $V_{ub}V_{ud}^*$ is just one side of the unitarity triangle, and its orientation depends on the CKM phase convention. You can make a single amplitude point anywhere you want! To produce a CP asymmetry, we need another amplitude to generate an interference term, and a second amplitude is generated from mixing. A proper treatment of mixing requires an analysis of the coupled $B^0\bar{B}^0$ system and the calculation of the mass eigenstates. A great simplification arises from the fact that the intermediate state in mixing is dominated by $t\bar{t}$. The total amplitudes included both the tree diagram and mixing are derived in Sec. 9.6 and are of the form

$$\begin{aligned} A(\bar{B}^0 \to \pi^+\pi^-) &= aV_{ub}V_{ud}^* + b\frac{V_{tb}V_{td}^*}{V_{tb}^*V_{td}}V_{ub}^*V_{ud} \\ A(B^0 \to \pi^+\pi^-) &= aV_{ub}^*V_{ud} + b\frac{V_{tb}^*V_{td}}{V_{tb}V_{td}^*}V_{ub}V_{ud}^*. \end{aligned} \tag{3.47}$$

In fact, there can be different overall phases multiplying these expressions, but they do not affect the physical results. (See the discussion in Sec. 9 and in the Appendix.) The difference in decay rates is proportional to

$$\begin{aligned} |A(\bar{B}^0 &\to \pi^+\pi^-)|^2 - |A(B^0 \to \pi^+\pi^-)|^2 \\ &= ab^*(V_{ub}V_{ud}^*)(V_{ub}V_{ud}^*)\frac{V_{tb}^*V_{td}}{V_{tb}V_{td}^*} \\ &\quad + a^*b(V_{ub}^*V_{ud})(V_{ub}^*V_{ud})\frac{V_{tb}V_{td}^*}{V_{tb}^*V_{td}} \\ &\quad - ab^*(V_{ub}^*V_{ud})(V_{ub}^*V_{ud})\frac{V_{tb}V_{td}^*}{V_{tb}^*V_{td}} \\ &\quad - a^*b(V_{ub}V_{ud}^*)(V_{ub}V_{ud}^*)\frac{V_{tb}^*V_{td}}{V_{tb}V_{td}^*} \\ &= 4\,\mathrm{Im}(ab^*)\,\mathrm{Im}\left[(V_{ub}^*V_{ud})^2\frac{V_{tb}V_{td}^*}{V_{tb}^*V_{td}}\right] \end{aligned} \tag{3.48}$$

There are several observations to make regarding this result. First, to obtain a nonzero difference between the decay rates, we require $\mathrm{Im}(ab^*) \neq 0$. If we write $a = |a|\exp(i\theta_a)$ and $b = |b|\exp(i\theta_b)$, then the condition $\mathrm{Im}(ab^*) = |a||b|\sin(\theta_a - \theta_b) \neq 0$ implies that a and b must be noncollinear in the complex plane. While the phases associated with a and b do not reverse sign under the CP operation, they must nevertheless still be present to produce a CP asymmetry. In Sec. 9, we will see how the role of this "strong phase" is filled in the inteference between mixing and decay. Similarly, the imaginary part of the CKM factors in Eq. 3.48 is proportional to the sine of twice the angle between the two complex numbers $z_1 = V_{ub}^* V_{ud}$ and $z_2 = V_{tb}^* V_{td}$. The angle between z_1 and z_2 is $\pi - \alpha$, where α is shown in Fig. 3. Thus, the asymmetry between the rates for $\bar{B}^0 \to \pi^+\pi^-$ and $B^0 \to \pi^+\pi^-$ probes $\sin 2\alpha$. You can also see explicitly in Eq. 3.48 that, because the CKM elements for B^0 decay are the complex conjugates of those for $\bar{B}^0$ decay, the two terms proportional to ab^* do not cancel and the two terms proportional to a^*b do not cancel, except for the case in which the unitarity triangle collapses to a straight line. Thus, to produce a CP-violating asymmetry, we require the presence of both the CP violating phases from the CKM elements and the non-CP violating phases from a and b.

We note also that the angle between $z_1 = V_{ub}^* V_{ud}$ and $z_2 = V_{tb}^* V_{td}$ is defined using only the first and third generations: one does not need all three generations to be present *in a given process* to produce a CP asymmetry: two complex numbers are sufficient to define an angle, and with three generations the angle can be nonzero! One might then wonder specifically how CP asymmetries are excluded in a world with just two generations. Let's consider the analogous situation for $K^0 \to \pi^+\pi^-$ decay assuming that the third generation is missing. Then, ignoring penguins as before, the interference between direct decay and mixing followed by decay gives

$$\begin{aligned} A(\bar{K}^0 \to \pi^+\pi^-) &= aV_{us}V_{ud}^* + b\frac{V_{cs}V_{cd}^*}{V_{cs}^*V_{cd}}V_{us}^*V_{ud} \\ A(K^0 \to \pi^+\pi^-) &= aV_{us}^*V_{ud} + b\frac{V_{cs}^*V_{cd}}{V_{cs}V_{cd}^*}V_{us}V_{ud}^*. \end{aligned} \tag{3.49}$$

and

$$\begin{aligned} &|A(\bar{K}^0 \to \pi^+\pi^-)|^2 - |A(K^0 \to \pi^+\pi^-)|^2 \\ &\qquad = 4\,\mathrm{Im}(ab^*)\,\mathrm{Im}[(V_{us}^*V_{ud})^2\frac{V_{cs}V_{cd}^*}{V_{cs}^*V_{cd}}]. \end{aligned} \tag{3.50}$$

But, with only two generations, unitarity gives

$$V_{us}^* V_{ud} + V_{cs}^* V_{cd} = 0. \qquad (3.51)$$

Thus, the CKM factor in Eq. 3.50 is real, and there can be no CP asymmetry. Here the unitarity constraint Eq. 3.51 is telling us that the two complex numbers are collinear; this is how the equations know that there are only two generations.

Finally, this example gives us insight as to why simple phase rotations of the quark fields cannot somehow be confused with CP violation. We have seen that when a quark field is multiplied by a phase factor, an entire row or column of the CKM matrix is effectively multiplied by this phase factor. Thus, every term in the inner product between two rows or two columns is multiplied by the phase factor, and the entire unitarity triangle rotates. The angles between the sides of the triangle do not change, and it is those angles that enter into CP asymmetries.

4. Experimental Challenges and Approaches in Heavy-Quark Physics

Experimentalists have used a wide variety of techniques to study the physics of bottom and charm hadrons. The most important challenges are straightforward to state:

- How can we produce and detect millions of b and c hadrons?
- How can we distinguish events containing b and c hadrons from other processes?
- How can we extract the maximum information from each event?

The answers to these questions are not simple. In each case, creativity, compromise, and technological innovation come into play, and there are often many different approaches that can succeed. This section describes the experimental environments and compares their advantages and disadvantages.

Table 2 summarizes some of the important features of current b experiments and the accelerators at which they operate. Although the Υ states were discovered in a fixed-target experiment at Fermilab in 1977, all successful b-hadron experiments have been performed in colliding-beam machines. Currently, three main approaches are used: $e^+e^- \to \Upsilon(4S) \to B\bar{B}$, $e^+e^- \to Z \to b\bar{b}$, and $p\bar{p} \to b\bar{b}X$. The CLEO experiment at the Cornell Electron Storage Ring (CESR) [16] has the largest b-hadron data sample, with over 5 million $\Upsilon(4S) \to B\bar{B}$ events.

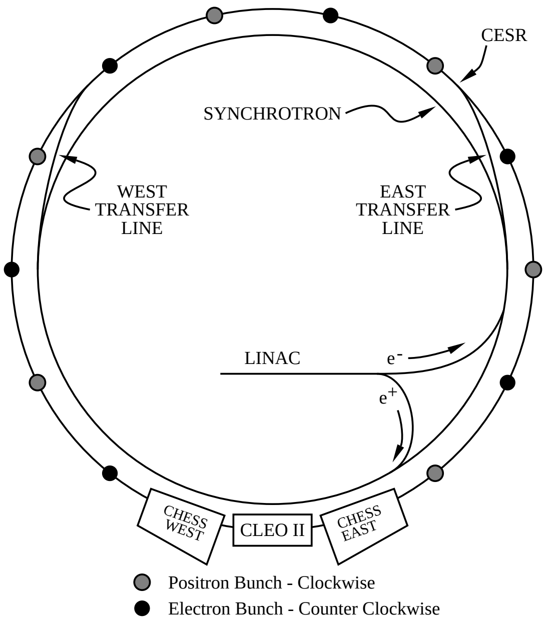

Fig. 6. The CESR machine consists of three main parts: a linear accelerator, which brings the beams to an energy of about 200 MeV; a synchrotron, which further accelerates the beams to 5 GeV; and the storage ring itself. The e^+e^- collisions take place at an interaction point surrounded by the CLEO detector. The circumference of CESR is only 768 m, and the ring is located underneath a playing field at Cornell University.

Most of the CLEO analyses discussed in this paper use 3 million events or less, however, since the data processing is relatively slow. The CESR ring is fairly small by present standards: its circumference is 768 m, and it roughly fits under one of the playing fields at Cornell University. It now has the highest luminosity of any collider in the world, $\mathcal{L} = 5 \times 10^{32}$ cm^{-2}s^{-1}. Figure 6 shows the main features of CESR.

One of the most important advances in achieving high luminosities in storage rings is multibunch operation, which allows higher total beam currents to be stored. At present, CESR operates with 18 bunches of electrons and 18 bunches of positrons. Table 3 shows a dramatic increase in the number of stored bunches with two new machines, KEKB in Japan (5000 bunches/beam) and PEP-II at SLAC (1658 bunches/beam). Two new detectors, Belle [18] at KEK and BaBar [17] at SLAC, are now being constructed by international collaborations and should begin operation at these machines in 1999.

Table 2

Comparison of existing experiments studying b-hadron physics. The production cross section at the Z is expressed as a function of $R_b = \sigma(Z \to b\bar{b})/\sigma(Z \to \text{hadrons}) \approx 0.22$. The number of b events available at the Tevatron experiments is very large, of order 10^9, but this number cannot be directly compared with the e^+e^- data samples, because it is only possible to trigger on a small fraction of the decays, as discussed in the text. (The quantity specified for CDF is the number of b hadrons rather than the number of $b\bar{b}$ pairs.) The luminosity quoted for CESR is the peak value at the beginning of a run, while others are typical values or averages.

Machine ($b\bar{b}$ Production)	Detectors	$\mathcal{L}$ ($\text{cm}^{-2}\text{s}^{-1}$)	$\sigma_{b\bar{b}}$ (nb)	$\sigma_{b\bar{b}}$ $/\sigma_{\text{had}}$	$\beta\gamma$	$N(b\bar{b})$ $(/10^6)$
CESR ($e^+e^- \to \Upsilon(4S) \to B\bar{B}$)	CLEO II	5×10^{32}	1.05	0.26	0.06	5.1
LEP ($e^+e^- \to Z \to b\bar{b}$)	ALEPH, DELPHI, OPAL, L3	2×10^{31}	$30 \times R_b$	0.22	6	0.9
SLC ($e^+e^- \to Z \to b\bar{b}$)	SLD	$(1-2) \times 10^{30}$	$30 \times R_b$	0.22	6	0.08
Tevatron ($p\bar{p} \to b\bar{b}X$)	CDF, D0	2×10^{31}	50 μb	0.001	≥ 2	[600]

Table 3

Comparison of e^+e^- accelerators now under construction that will operate at the $\Upsilon(4S)$. CESR3 is an upgrade to the existing machine. These machines are expected to begin operation in 1999.

Machine	Circum. (m)	E_{beam} (GeV)	$\mathcal{L}$ ($\text{cm}^{-2}\text{s}^{-1}$)	bunches /beam	beam sep. method	bunch sep. (m)	$\beta\gamma$
CESR3	768	5.3×5.3	2×10^{33}	45	2.5 mr xing angle	4.2	0.06
KEKB	3016	8.0×3.5	1×10^{34}	5000	22 mr xing angle	0.6	0.42
PEP II	2219	9.0×3.1	3×10^{33}	1658	magnetic	1.26	0.56

Multibunch operation has a number of complications. The fields left behind in the accelerator by one bunch can interact with a subsequent bunch, leading to instabilities, which must somehow be kept under control. There must also be a mechanism to prevent collisions of bunches at points other than at the designated interaction point. The methods for avoiding these so-called parasitic collisions have a major impact on the accelerator, the interaction region, and the detector design.

In CESR, the beams are stored within a single ring of magnets and radio-frequency cavities. This is possible because the beams have the same energy but are travelling in opposite directions. To avoid parasitic collisions, the beams must be put into slightly different orbits. For many important measurements of CP violation, however, it is necessary to have unequal beam energies, so that the center of mass of the $B\bar{B}$ system moves with respect to the detector and the asymmetries can be measured as a function of the relative B decay times. This is the motivation for building the KEKB and PEP-II accelerators, (Table 3), which are now under construction. The need for unequal beam energies led to two separate rings; this feature in turn allows a vast increase in the number of bunches.

Still, there is the problem of how to prevent parasitic collisions near the interaction region in a two-ring machine. In PEP-II, for example, the bunch separation is only 1.26 m; the first parasitic crossing would occur at only half this distance from the interaction point! Figure 7 shows a top-view of the PEP-II interaction region. The trajectories of the beams are separated by permanent dipole magnets (B1) placed very close to the interaction point. The beam separation comes at a price: a large flux of synchrotron photons sprays off the beams during the bends. These photons must be intercepted by carefully placed masks. Furthermore, the magnets also occupy valuable space that could be used to add more detector elements. At PEP II, the forward region is extremely valuable: due to the boost, 90 degrees in the $\Upsilon(4S)$ frame corresponds to only 61 degrees to the beam axis in the detector frame. The KEKB machine uses a completely different approach: the beams do not collide head-on, but instead enter with a crossing angle of 22 mrad. In CESR3 (an upgrade to the symmetric-energy CESR machine), there are relatively few bunches and a larger bunch spacing, so that a crossing angle of only 2.5 mrad is sufficient to solve the problem.

In these high-current storage rings, the quality of the vacuum, especially near the interaction point, is crucial. Coulomb scattering or bremsstrahlung of the beam particles from residual gas molecules in the beam pipe can lead to electromagnetic showers and enormous backgrounds in the detector. Thus, high luminosity can be achieved, but not without great attention to its consequences for backgrounds in the detector and for radiation damage to detector components.

For experimenters, the three techniques used to produce b hadrons offer different advantages and disadvantages. A distinctive feature of running at the $\Upsilon(4S)$ is that, because its mass is only about 20 MeV above that for a $B^0\bar{B}^0$ or B^+B^- pair, no additional pions are produced, nor are any other types of b hadrons, which are too heavy. As a consequence, in a symmetric-energy machine such as CESR, the energy of each B meson is equal to the beam energy. When computing the invariant mass of a set of particles X_α, assumed to come from the process

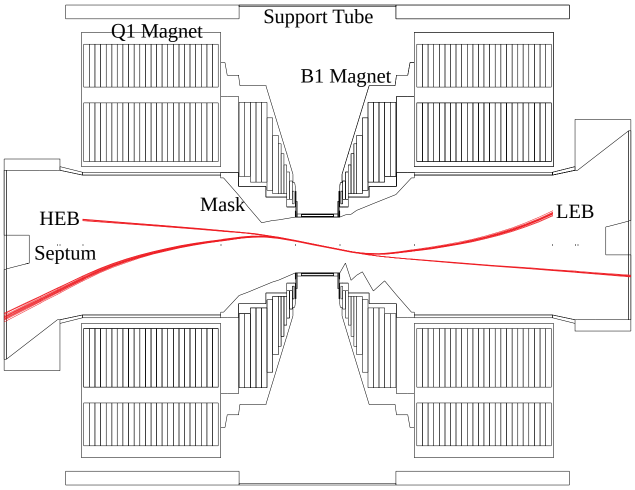

Fig. 7. The interaction region of the new PEP-II machine is complicated by the need to avoid parasitic crossings of the closely spaced beam bunches. In this view from above, the detector is not shown and the scale transverse to the beam direction is expanded by a factor of ten relative to the scale along the beam direction. The 9 GeV electron beam (HEB) enters from the left, while the 3.1 GeV positron beam (LEB) enters from the right. After interacting, the beams are separated by permanent dipole magnets (B1) that start at about 20 cm on either side of the interaction point. The space on the beam pipe between the magnets is occupied by a five-layer silicon vertex detector (not shown). The drift chamber is located outside the support tube.

$B \to X_1 X_2 ... X_n$, one can therefore impose the constraint $E_B = E_{\rm beam}$:

$$m_B = \sqrt{E_{\rm beam}^2 - (\sum_{\alpha=1}^{n} \mathbf{p}_\alpha)^2}. \tag{4.1}$$

In analyses of hadronic decays, this technique gives a mass resolution of $\sigma_{M_b} \approx 3$ MeV, about a factor of ten better than the resolution without the constraint (see Sec. 8). Before using this constraint, it is important to verify that the measured energy of the candidate system is consistent with the beam energy within resolution:

$$\Delta E = \sum_{\alpha=1}^{n} \sqrt{m_\alpha^2 + |\mathbf{p}_\alpha|^2} - E_{\rm beam} \approx 0. \tag{4.2}$$

The best approach is to look at the m_B distribution both for events with $\Delta E \approx 0$ and for sidebands with $\Delta E < 0$ and $\Delta E > 0$. For a two-body decay to low-mass particles (such as $B \to \pi\pi$), m_B and ΔE essentially measure the difference and sum of the momenta:

$$m_B = \sqrt{E_{\rm beam}^2 - (\mathbf{p}_1 + \mathbf{p}_2)^2} \simeq \sqrt{E_{\rm beam}^2 - (|\mathbf{p}_1| - |\mathbf{p}_2|)^2}$$

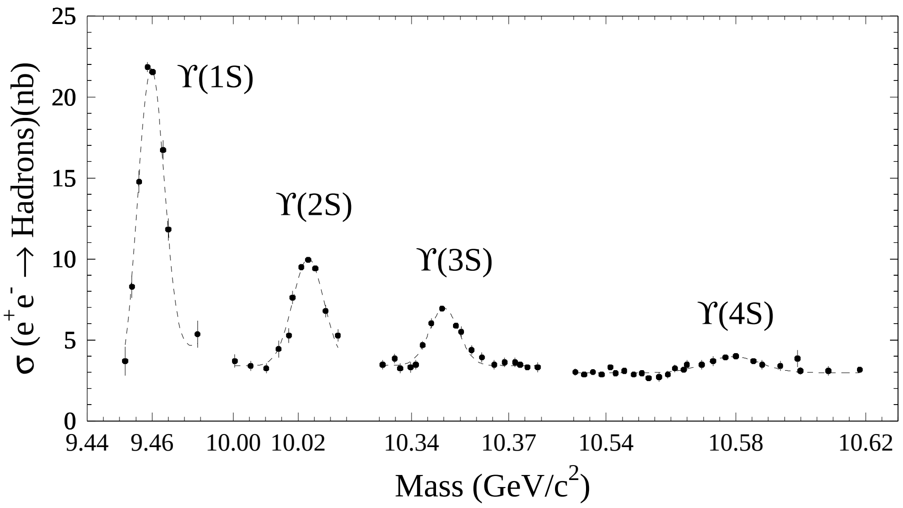

Fig. 8. The hadronic cross section vs. center-of-mass energy in the Υ energy region. The $\Upsilon(4S)$, at 10.58 GeV, is the third radial excitation of the ground state. It has sufficient mass to decay into $B^0\bar{B}^0$ or B^+B^- pairs, which results in its larger width. The continuum events underneath the $\Upsilon(4S)$ typically have a two-jet topology, which allows them to be distinguished from the much more isotropic distribution of tracks in $\Upsilon(4S) \to B\bar{B}$ decays.

$$\Delta E = \sqrt{m_1^2 + \mathbf{p}_1^2} + \sqrt{m_2^2 + \mathbf{p}_2^2} - E_{\text{beam}} \simeq (|\mathbf{p}|_1 + |\mathbf{p}|_2) - E_{\text{beam}}, \quad (4.3)$$

where we have used the fact that the B mesons move very slowly in the $\Upsilon(4S)$ rest frame, so the momentum vectors of the daughter hadrons are nearly back-to-back.

Figure 8 shows the hadronic cross section in the Υ energy region, measured by the CLEO detector at CESR. The $\Upsilon(4S)$ is a rather modest resonance; it is much broader than the lighter Υ's because the $B\bar{B}$ channel is open. The $\Upsilon(4S)$ cross section is 1.05 nb, and there is an additional 3 nb contribution to the total hadronic cross section from continuum (nonresonant $e^+e^- \to q\bar{q}$, $q = u, d, s, c$) events. Still, this gives the most favorable signal-to-backgound ratio of any environment, and there is a positive side: both $e^+e^- \to c\bar{c}$ and $e^+e^- \to \tau^+\tau^-$ events are interesting in themselves.

Two strategies are used to deal with continuum background at the $\Upsilon(4S)$. First, many of these events can be removed from the data sample with a relatively simple selection cut based on overall event shape, which characterizes the distribution of particle momentum vectors. In continuum events, the particles are generally collimated into two back-to-back jets; in contrast, the distribution of tracks in $\Upsilon(4S) \to B\bar{B}$ events is much more isotropic. The spherical topology of $\Upsilon(4S)$ events is due to the very low B momentum in the $\Upsilon(4S)$ rest frame, $p \approx 325$ MeV$/c$. Although useful for separating $B\bar{B}$ events from continuum, the spherical event shape has a disadvantage. The decay products of the two B mesons overlap in space, making it more difficult to associate the correct tracks with each other and resulting in combinatorial backgrounds. The second strategy for dealing with the continuum background is to measure it. CLEO spends one-third of its time running at a center-of-mass energy about 60 MeV below the $\Upsilon(4S)$. Each analysis performed at the $\Upsilon(4S)$ is also performed on the continuum sample, providing a direct measurement of this backgound contribution.

A particular strength of the CLEO detector, shown in Fig. 9, is its ability to measure both charged tracks and photons with very good precision. The momentum of charged particles is determined from the track curvature in a 1.5 T magnetic field. The high value of the magnetic field helps to provide good momentum resolution for "stiff" tracks from low-multiplicity modes such as $B \to \pi^+\pi^-$. It has the disadvantage that low-momentum tracks can curl multiple times, complicating the pattern recognition for the hits in the drift chamber. Measurements of the "soft pion" from the ubiquitous $D^{*+} \to D^0\pi^+$ decay can suffer from this problem. The electromagnetic calorimeter, constructed from 7800 CsI crystals, can detect photons down to energies of about 30 MeV with high efficiency. The resolution is $\sigma_E/E \approx 4\%$ for a 100 MeV photon and 2% for a 2 GeV photon (relevant for $B \to K^*\gamma$); a typical π^0 mass resolution is $\sigma_{\pi^0} \approx 6$ MeV$/c^2$. Since electrons or positrons also produce electromagnetic showers, the CsI calorimeter also provides a powerful tool for electron detection and measurement. This device adds enormously to the detector's capability for reconstructing exclusive final states, and both BaBar and Belle are using similar technology for their calorimeters. Figure 10 shows a $B \to K^*\gamma$ decay observed in the CLEO detector.

The process $e^+e^- \to Z \to b\bar{b}$ has complementary advantages and disadvantages to running at the $\Upsilon(4S)$. The b and $\bar{b}$ quarks hadronize into a wide variety of particles. The fractions for the different species of hadrons are [20]

$$\begin{aligned} f_{B^+} = f_{B_d^0} &= (39.05^{+1.2}_{-1.4})\% \\ f_{B_s^0} &= (10.6^{+1.4}_{-1.3})\%, \\ f_{b\text{-baryon}} &= (11.3^{+2.5}_{-2.1})\%. \end{aligned} \tag{4.4}$$

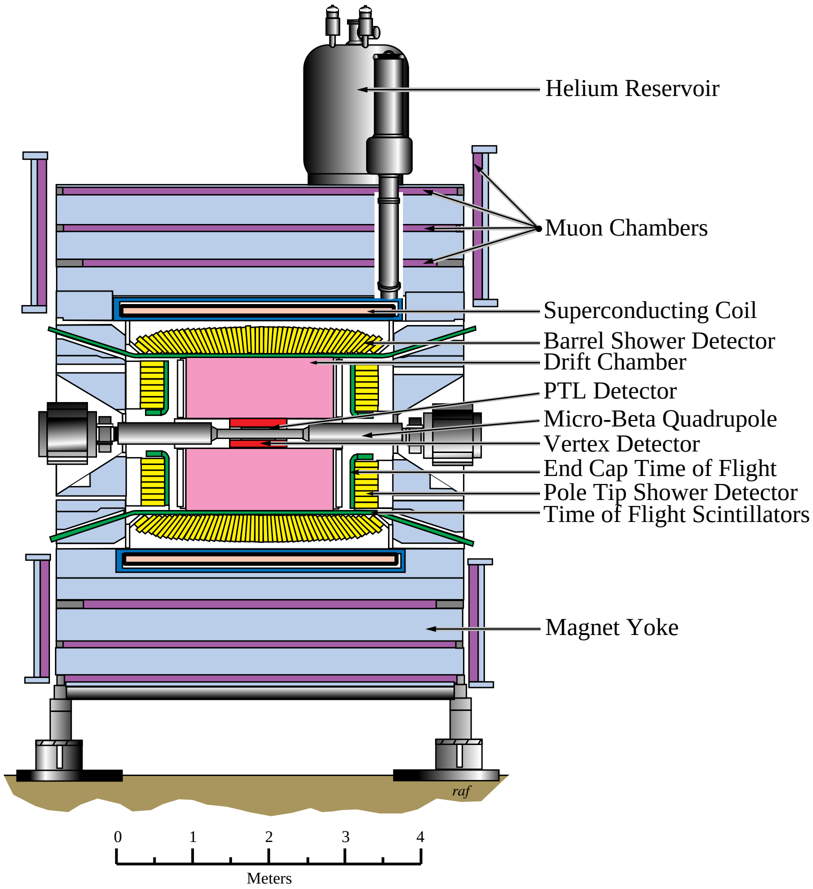

Fig. 9. The CLEO II Detector. The beam pipe, which runs left-to-right, is surrounded by tracking chambers that measure the trajectories of charged particles. Outside of the drift chamber are time-of-flight scintillators and the CsI crystal calorimeter (labelled shower detectors), and a 1.5 T superconducting coil. A three-layer silicon vertex detector (not shown) was installed in 1996. This recent upgrade is called CLEO II.5, and will be followed by the major CLEO III upgrade [19] in 1999.

These particles are both produced directly from the $b\bar{b}$ pair and as decay products of various types of excitations of the ground state b hadrons. Unlike the $\Upsilon(4S)$, there are accompanying lighter particles, so that the b hadrons do not have a fixed momentum, although there is a peak around 30 GeV/c. Since $Z \to b\bar{b}$ events are jet-like, there is

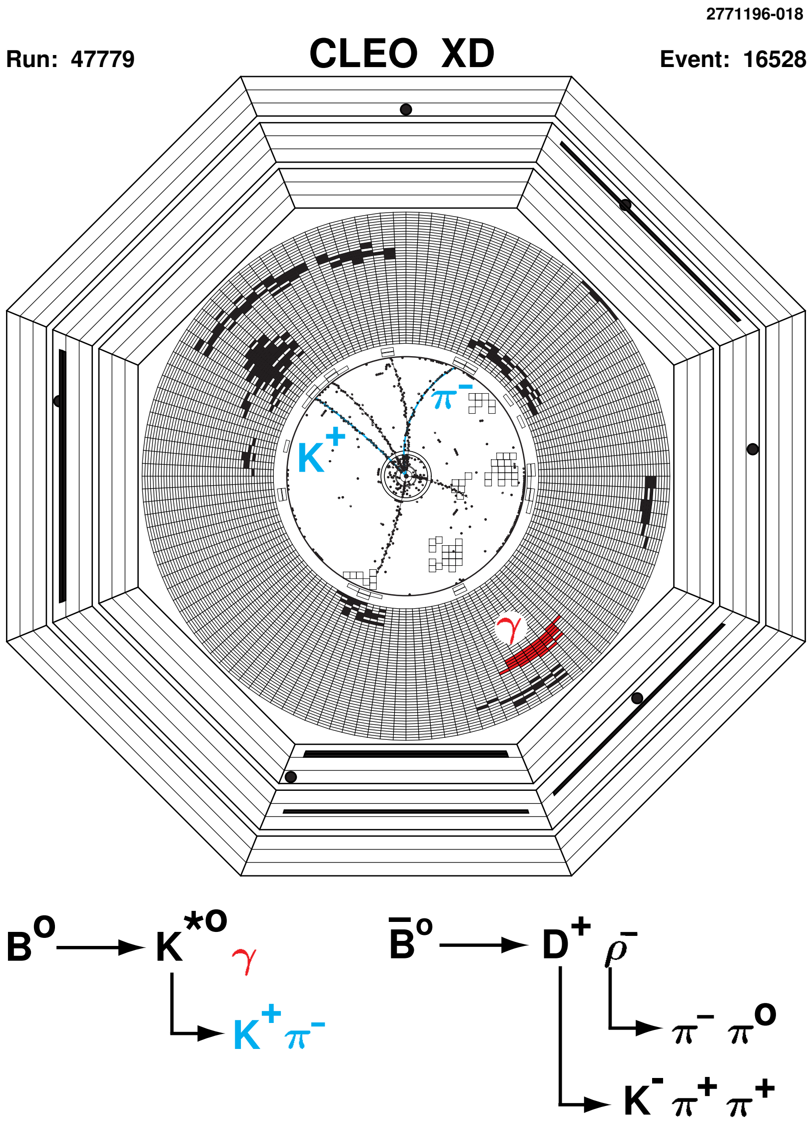

Fig. 10. The decay $B^0 \to K^{*0}\gamma$, $K^{*0} \to K^+\pi^-$ observed in the CLEO II detector. The curved tracks in the drift chamber are shown in xy projection (perpendicular to the beam axis), whereas the clusters in the CsI calorimeter are shown in perspective as if looking into a barrel. The outermost detectors, which only have noise hits in this event, are muon chambers.

very little confusion between the decay products of the two b hadrons, in contrast to the situation at the $\Upsilon(4S)$.

Although Z decays provide access to many different types of b hadrons, it is not a simple matter to determine the production rates of individual species with high precision. This introduces an uncertainty in the normalization of branching fractions and related quantities such as CKM elements. For that matter, it has not been fully established empirically that $B(\Upsilon(4S) \to B^0\bar{B}^0) = B(\Upsilon(4S) \to B^+B^-) = 0.5$, although this equality is usually assumed and is expected from the nearly identical values of the B^- and B^0 masses. Some $\Upsilon(4S)$ analyses incorporate a systematic error due to the uncertainty in the $B^0\bar{B}^0$ and B^+B^- production fractions. In general, it is always worth paying attention to how an experiment normalizes its branching fractions and to understand what assumptions, if any, are present.

Table 2 and Table 3 compare the relativistic boost factors in different experimental environments. The highest momentum b-hadrons, with $\beta\gamma \approx 6$, are produced at the Z. The typical distance of the b decay vertex from the interaction point is $\beta\gamma c\tau_B \approx 2.9$ mm. Although the b hadrons still decay within the beam pipe, the decay vertex can be clearly resolved by extrapolating tracks measured with high-precision silicon vertex detectors, which are placed just outside the beam pipe. The use of such devices has resulted in a very successful b physics program at LEP. Figure 11 shows tracks in a $Z \to b\bar{b}$ decay detected by the DELPHI vertex detector. Compare this to the CLEO event (Fig. 10), where the decay products of the two B mesons are not collimated into jets. The typical B decay length in CLEO is only 30 μm, which is too small to be resolved. However, vertexing of charm hadrons produced in B decays can still be very useful. The asymmetric B factories give a boost $\beta\gamma \approx 0.6$, ten times larger than that at CLEO and a tenth of the boost at LEP. The typical B decay length is about 0.25 mm, and vertexing will be extremely important.

The CDF experiment at the Tevatron (Fermilab) has demonstrated that certain b physics measurements can be performed successfully in the hadron-collider environment. The process $p\bar{p} \to b\bar{b}X$ produces an enormous number of b hadrons, since $\sigma_{b\bar{b}} \approx 50$ μb. However, most of these events cannot be written to tape, because $\sigma(b\bar{b})/\sigma_{\mathrm{inelastic}} = 10^{-3}$, and they cannot be distinguished by the triggers, which initiate detector readout, from the large number of uninteresting background events. The triggers for selecting b-hadron events are based on leptons. The inclusive single-lepton trigger selects [21] b hadrons with a typical $p_T \sim 20$ GeV/c, while the $J/\psi \to \ell^+\ell^-$ trigger gives a typical $p_T \sim 10$ GeV/c, where p_T is the momentum transverse to the beam axis. The b-hadron p_T spectrum is peaked at the low end, so the triggers select only a small fraction of decays even for these modes. In spite of these difficulties, there are a number of excellent b physics studies at

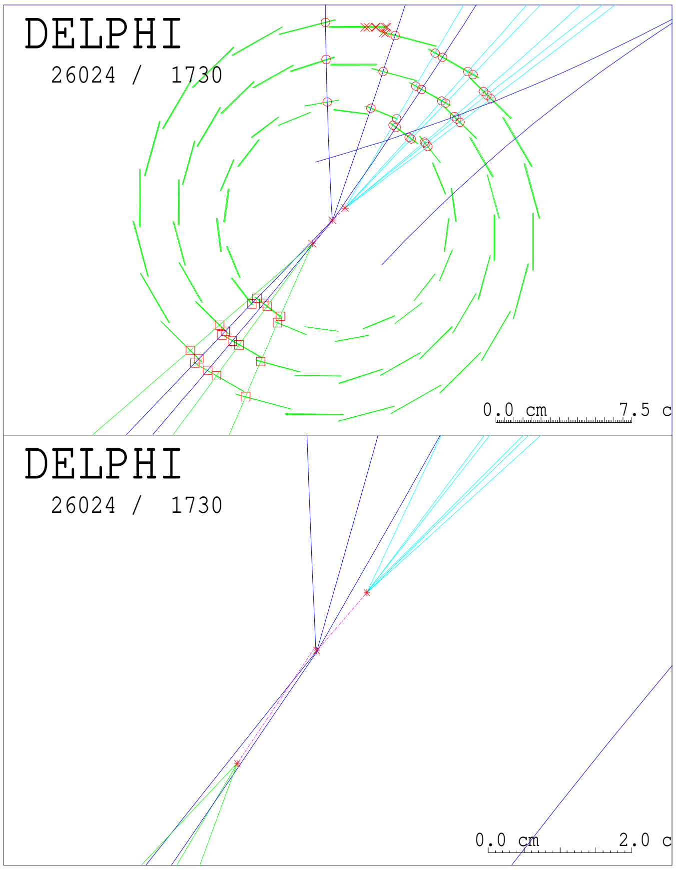

Fig. 11. A $Z \to b\bar{b}$ event observed in the DELPHI vertex detector. The decay products of the b hadrons are highly collimated into jets. The vertex detector surrounds the beam pipe, and by extrapolating tracks back to their intersection points it is possible to identify decay vertices and determine their locations. Figure used with permission.

CDF, especially in the area of lifetime measurements. The enormous production rate allows the use of hadronic decay modes, which typically give the smallest systematic uncertainties. The CDF experiment also has a good chance to observe CP violation in the decay $B^0 \to J/\psi K_s$.

Measurements of charm hadron decays have been performed both in e^+e^- colliding-beam experiments such as CLEO and at fixed-target experiments. The challenge for fixed-target experiments is to suppress a very large background from light-quark production. In photoproduction experiments, where a high-energy photon is incident on a nuclear target, the charm cross section is typically 0.5 μb, or 0.5% of the total cross section [1]. In hadroproduction experiments, where a proton is incident on a nuclear target, the charm production cross section is higher but represents even less of the total cross section. For proton momenta in the range 400 GeV/c to 800 GeV/c the charm cross section is 20 μb to 40 μb, while the total cross section is 1000 times greater [22]. To suppress the backgrounds, fixed-target experiments exploit the relative long charm-hadron lifetimes (10^{-13} s to 10^{-12} s), which, together with a large boost factor, enable charm particles to travel measurable distances from the primary production point. Silicon vertex detectors again play a key role in distinguishing signal events from backgrounds. Examples of such fixed-target charm experiments are E831 (an upgraded version of the E687 photoproduction experiment) and E791 (hadroproduction) at Fermilab. The E831 experiment, shown in Fig. 12, expects to reconstruct over a million reconstructed charm decays from its current data sample.

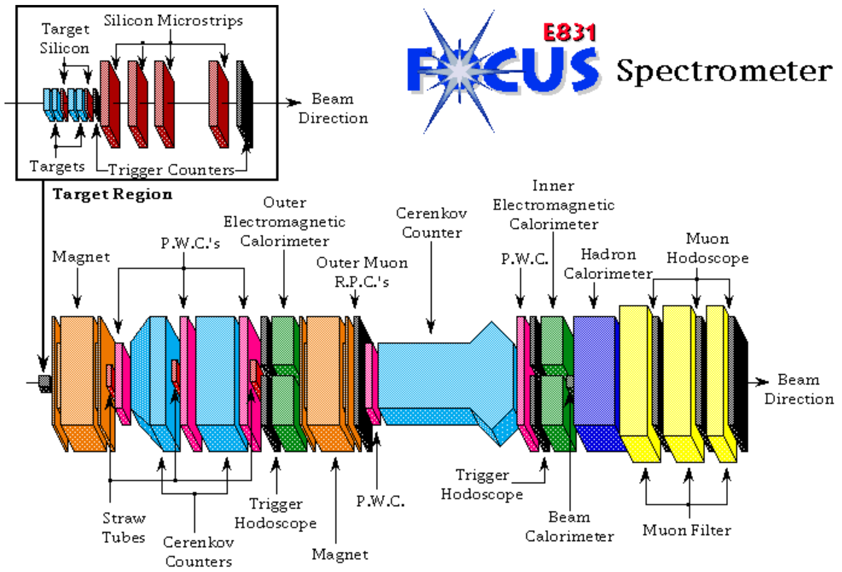

Fig. 12. The FOCUS (E831) fixed-target charm experiment at Fermilab. The photon beam enters from the left. Note the planes of the silicon-strip detectors in the segmented target. Figure used with permission.

Fixed-target experiments have not yet been able to obtain useful samples of b-hadrons because the cross sections are too low at the energies of presently available beams. The HERA-B experiment, now under construction at DESY (Hamburg), will be able to study CP violation in the decay $B^0 \to J/\psi K_S^0$, as well as B_s mixing and a variety of other processes. The experiment has a novel configuration: 820 GeV protons from the HERA proton synchrotron are incident upon a wire target that is mounted internally to the accelerator beam pipe. The target consists of short pieces of wire ($\Delta z \simeq 0.5$ mm along the beam direction), providing a well-defined primary-vertex location. The wires will be inserted into the halo of the proton beam, which extends out a few millimeters from the beam axis. The detector itself is a 20-meter-long spectrometer that covers the angular range 10–200 milliradians. It will begin operation in the relatively near future.

The longer-term future will bring several additional experiments with the capability to measure CP violation. These include the LHC experiments Atlas and CMS, as well as the dedicated B-physics experiment LHC-B. At Fermilab, the BTeV experiment is now being designed to use forward-production of b-hadrons at the Tevatron.

5. Historical Perspective, Bumps in the Road, and Lessons in Data Analysis

5.1. *A very short history of heavy-quark physics*

Table 4 lists some of the most important achievements in bottom and charm quark physics. I have included not only discoveries, but also important technological advances and milestones. The ARGUS experiment, which is no longer in operation, made numerous discoveries, including $B^0\bar{B}^0$ mixing. The experiment ran at the DORIS e^+e^- storage ring at DESY from 1982 to 1992, accumulating about 210,000 $\Upsilon \to B\bar{B}$ events. Theorists might argue that my selection of historical highlights is biased toward experimental results. In any case, the development of heavy-quark effective theory starting around 1989 has had an enormous effect on the field.

5.2. *Bumps in the road: case studies*

Experiments in bottom and charm physics have produced an enormous number of measurements, and it is not surprising that some of them have not stood the test of time. At the risk of offending some of my colleagues, who I hope will appreciate the pedagogical goals of these lectures, I will examine some of these measurements here. I have restricted myself to experiments studying b physics—these provide

Table 4
A brief history of charm and bottom physics.

1974	Discovery of J/ψ (Brookhaven and SLAC)
1975–1985	Exploration of $c\bar{c}$ spectroscopy; theoretical studies of QCD potential
1976	Discovery of the D meson (SLAC)
1977	Discovery of the $\Upsilon(1S)$ (FNAL)
1983	Discovery of the B meson (Cornell)
1985	Precision measurements of $\tau(D^+)$ and $\tau(D^0)$ in high-rate fixed-target charm experiments using silicon-strip detectors (FNAL)
1987	Discovery of $B^0\bar{B}^0$ mixing (DESY)
1987	First discussions of asymmetric B factories
1989	Heavy Quark Effective Theory (Isgur, Wise, and many others); provides new methods for extracting $\|V_{cb}\|$
1993	Discovery of B_s and Λ_b (CERN)
1993	Discovery of $B \to X_u \ell^- \bar{\nu}$ (Cornell and DESY); showed that $\|V_{ub}\| \neq 0$
1993-1994	Discovery of radiative penguin decays $B \to K^*\gamma$ and $B \to X_s\gamma$ inclusive decay (Cornell)
1997	Discovery of $B \to K\pi$ and other rare hadronic modes (Cornell)
1997	Fixed-target charm experiments approaching 10^6 reconstructed charm decays (FNAL)
1997	CESR reaches $\mathcal{L} = 4.0 \times 10^{32}\ \mathrm{cm^{-2}s^{-1}}$

plenty of examples—and at the end of this section, I will try to draw some lessons from them.

In 1983, the CLEO collaboration published the paper [23] "Observation of Exclusive Decay Modes of b-flavored Mesons." Because this study provided the first measurement of the B-meson mass, it can be regarded [24] as the discovery of the B. At the time, it was not universally accepted that it would even be possible to reconstruct such decays, so the analysis opened the door to exclusive B physics. For a detailed discussion of the CLEO I analysis, as well as an historical perspective, see Stone [25].

There were, however, already two indications that b-flavored hadrons were being produced at the $\Upsilon(4S)$: the large width of the $\Upsilon(4S)$ compared to that of the $\Upsilon(1S)$, $\Upsilon(2S)$, and $\Upsilon(3S)$ resonances and the observation of high-energy leptons associated with $\Upsilon(4S)$ decays. The reconstruction of specific exclusive final states was quite difficult, both because B branching fractions are small, and because the dominant modes lead to charm mesons, which themselves can be easily reconstructed only in a relatively small fraction of their decay modes.

The difficulties were particularly formidable in the CLEO I detector,

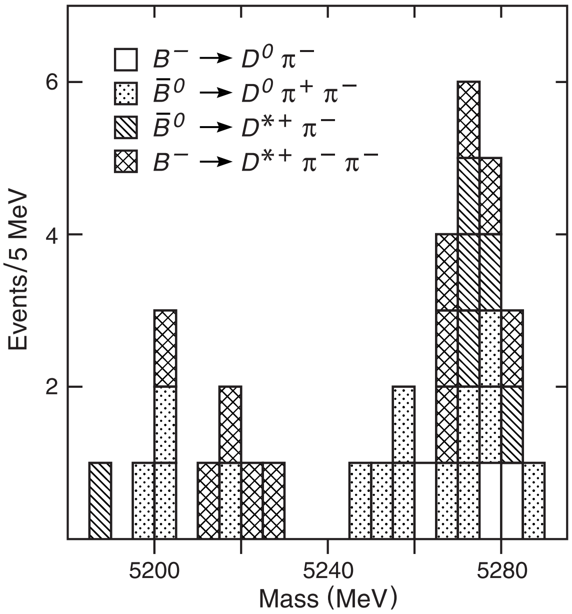

Fig. 13. CLEO I: In the original observation of exclusive B decays, several decay modes were summed to get sufficient sensitivity.

which was not able to reconstruct modes with π^0s and which also had poor efficiency for reconstructing low-momentum charged pions. In the CLEO I analysis, the only D decay mode used was $D^0 \to K^-\pi^+$, which has a branching fraction of about 4%. In such situations—when an experiment is attempting to discover a new particle—it is often the case that there are too few events in any single decay mode to establish a signal. The experimenters must resort to summing signals over a variety of final states to obtain sufficient sensitivity to claim an observation.

Figure 13 shows the B mass distributions for four low-multiplicity modes. The $\bar{B}^0$ and B^- masses were obtained from a fit in which the B energy, D mass, and D^* mass were constrained to known values, leading to a B-candidate mass distribution that peaks somewhat below 5.28 GeV$/c^2$. These decays (conjugate modes are implied), along with the number of events assigned in the CLEO I analysis and the projected numbers based on the recent estimates by Stone [25], are:

(i) $B^- \to D^0\pi^-$ (2 events; 3 projected),

(ii) $\bar{B}^0 \to D^0\pi^+\pi^-$ (5 events, 0 projected),

(iii) $B^- \to D^{*+}\pi^-\pi^-$ (6 events, 1/3 projected),

Table 5

CLEO I and current B branching fractions. To make a precise comparison the CLEO I values needed to be renormalized to take into account different assumptions on $\Upsilon(4S)$, D^*, and D branching fractions. The $\bar{B}^0 \to D^0\pi^+\pi^-$ decay is now known to be dominated by $D^{*+}\pi^-$; this branching fraction is counted twice in the right-hand column, giving what amounts to an upper limit for the sum.

Mode	CLEO I branching fraction (%)	PDG 97 branching fraction (%)
$B^- \to D^0\pi^-$	4.2 ± 4.2	0.53 ± 0.05
$B^- \to D^{*+}\pi^-\pi^-$	4.8 ± 3.0	0.21 ± 0.06
$\bar{B}^0 \to D^0\pi^+\pi^-$	13 ± 9	dominated by $D^{*+}\pi^-$
$\bar{B}^0 \to D^{*+}\pi^-$	2.6 ± 1.9	0.26 ± 0.04
Sum	24.6 ± 10.5	1.26 ± 0.10

(iv) $\bar{B}^0 \to D^{*+}\pi^-$ (5 events, 1 projected).

In most cases, the number of events observed in CLEO I is far higher than the projected number.

Table 5 compares the 1983 CLEO I branching fractions with current values from the Particle Data Book. The CLEO I measurements are roughly a factor of 10 higher than present values. Given that the CLEO I signal was 18 events, current data indicate that there should only have been a few events from the modes listed. To make a precise comparison it is important to check for differences between assumed values of input branching fractions. For example, CLEO used $B(\Upsilon(4S) \to B^0\bar{B}^0) = 0.40 \pm 0.02$ and $B(\Upsilon(4S) \to B^+B^-) = 0.60 \pm 0.02$, whereas we now assume 0.50 for both values. In addition, CLEO used the value $B(D^0 \to K^-\pi^+) = (3.0 \pm 0.6)\%$; the current value [4] is $(3.82 \pm 0.12)\%$.

The CLEO paper contains an important qualification, which to some extent explains the extremely large values measured for the branching fractions: "If a B decay contains a low-energy particle that escapes detection, the remaining particles from that B may still be consistent with the beam-energy constraint and give an acceptable fit." The paper states that this problem affects $B^- \to D^0\pi^-$ and $\bar{B}^0 \to D^0\pi^+\pi^-$ but not $B^- \to D^{*+}\pi^-\pi^-$ and $\bar{B}^0 \to D^{*+}\pi^-$, so only the latter two processes are used in the B mass determination. CLEO obtained the masses

$$\begin{aligned} M_{B^+} &= (5270.8 \pm 2.3 \pm 2.0)\ \mathrm{MeV}/c^2, \\ M_{B^0} &= (5274.2 \pm 1.9 \pm 2.0)\ \mathrm{MeV}/c^2, \end{aligned} \tag{5.1}$$

which can be compared with the current PDG values

$$\begin{aligned} M_{B^+} &= (5278.9 \pm 1.5)\ \mathrm{MeV}/c^2, \\ M_{B^0} &= (5279.8 \pm 1.6)\ \mathrm{MeV}/c^2. \end{aligned} \tag{5.2}$$

The CLEO I and current values of the masses are consistent to within about 2σ.

It can be very difficult to determine what problems might be present in a study performed many years ago. Stone [25] has recently examined the CLEO I analysis. It is likely that the difficulty is precisely the one discussed in the CLEO paper: kinematic fitting to the wrong decay hypothesis, sweeping modes with missed low-energy particles into the signal. Although this problem was recognized, it appears that its impact on the analysis was underestimated. It is interesting that similar problems affected the Mark III measurement of D branching fractions [26]; the problems were recognized and corrected in a reanalysis of the same data [27].

The situation in which very weak signals in several modes are combined to establish a statistically significant signal is inherently fraught with the possibility of mishap. This, of course, is often the situation in which we find ourselves in measurements with discovery potential. With very low statistics signals, it is important to distinguish between (1) the statistical uncertainty on the central value of the measurement and (2) the probability that the observed events is due to background. For a small number of events, the relative statistical error on the signal is very large $(1/\sqrt{N})$, but if the background is known to be much smaller, the significance of the signal can still be very high. Just because a signal has only a few events is not reason to dismiss it: you need to know the size of the background and its uncertainty as well. However, small signals present great difficulties because it is extremely easy to overlook or underestimate the contributions of small background sources. In addition, the usual checks that one performs on the signal by examining various kinematic distributions are only marginally useful, putting even more reliance on correct determination of the background.

Figure 52 (in Sec. 8) shows a recent set of mass plots for hadronic decays from the CLEO II. The contrast with Fig. 13 is enormous. The integrated luminosity at the $\Upsilon(4S)$ used in the 1997 CLEO II analysis is 3.1 fb^{-1}, compared with only 40.7 pb^{-1} in 1983. The CLEO II detector is also vastly superior to CLEO I. B physics has come a long way, but it had to start somewhere!

My second example also comes from another low-statistics measurement [28,29], in this case performed by the Crystal Ball experiment after it was moved from the SPEAR ring at SLAC to the DORIS ring at DESY. The Crystal Ball was a spherical array of about 700 NaI(Tl) crystals, and it had earlier performed detailed studies of charmonium

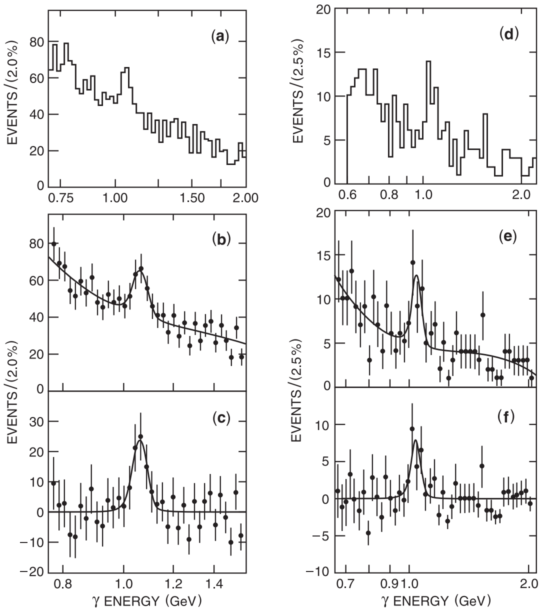

Fig. 14. Initial evidence from the Crystal Ball for the process $\Upsilon(1S) \to \gamma\zeta(8.3)$. The plots on the left and right are for high- and low-multiplicity final states, respectively. Within each group, the figures are (a) photon energy spectrum, (b) fitted photon energy spectrum, and (c) photon energy spectrum after background subtraction. No signals were present in a subsequent data sample. Figure used with permission.

states by observing the spectrum of photons from transitions between these states.

At the 1984 summer conference at SLAC, the Crystal Ball collaboration presented a paper [28], "Evidence for a Narrow Massive State in the Radiative Decays of the Upsilon." The new particle, called the $\zeta(8.3)$, was apparently produced in the radiative decay $\Upsilon(1S) \to \gamma\zeta(8.3)$. It was conceivable, although considered unlikely, that the $\zeta(8.3)$ could be a non-standard-model Higgs particle. There was simply no obvious explanation for the $\zeta(8.3)$. The Crystal Ball detector did not have a magnetic field, and it had only minimal charged-particle tracking detectors, so the signal was established almost entirely on the basis of the recoil photon spectrum rather than by reconstructing a $\zeta(8.3)$ mass peak. Still, some basic properties of the charged-tracks and event topology could be determined, and the events were divided into two samples: $\zeta(8.3) \to$ multi-hadrons and $\zeta(8.3) \to 2$ low-multiplicity jets. These two event samples were said to be statistically independent.

The evidence for the $\zeta(8.3)$ was based on peaks in the photon-energy spectra in the two event samples. The spectrum for the multi-hadron mode, shown in Fig. 14(a), had a 4.2σ peak, while the low-multiplicity jet sample had a peak with a statistical significance of 3.3σ. The significance for the combined signal was over 5σ, a frequently used threshold for claiming a new effect. The mass and width were measured to be

$$\begin{aligned} M(\zeta) &= (8322 \pm 8 \pm 24)\ \mathrm{MeV}/c^2 \\ \Gamma(\zeta) &< 80\ \mathrm{MeV}/c^2 \quad 90\%\ \mathrm{C.L.} \end{aligned} \tag{5.3}$$

The signal was obtained in a sample of 100 K $\Upsilon(1S)$ decays. Although the Crystal Ball collaboration presented the $\zeta(8.3)$ in conference papers, they did not publish the result in a journal. Instead, they accumulated a second sample of 200 K $\Upsilon(1S)$ decays to verify the signal. In this new sample, there were (-29 ± 29) events at the expected mass in the high-multiplicity sample, and the claim was retracted. The CUSB collaboration at CESR also searched for a signal and found none.

It appears [30] that the peak was the combination of two things: (1) a random statistical fluctuation and (2) enhancement of this fluctuation by the tuning of event selection cuts on the data. There is very little that we can do about large statistical fluctuations: if we look at enough histograms, there are bound to be some. The Crystal Ball adopted one approach to the problem of tuning cuts on the data; they analyzed a second data sample using the same cuts. In my view, it is far preferable to use Monte Carlo events for defining event selection criteria, a point that I discuss in the following section.

My last example is the claim for the first observation of the exclusive semileptonic decay $B^- \to \rho^0 \ell^- \bar{\nu}$ from the ARGUS collaboration. This rare decay mode provides a method to measure the magnitude of V_{ub}, one of the smallest and least well-measured elements of the CKM matrix. The first evidence for $b \to u$ transitions was based on CLEO and ARGUS measurements of the inclusive lepton-energy spectrum beyond the $B \to X_c \ell^- \bar{\nu}$ endpoint, where X_c represents a final state with charm. The theoretical uncertainties associated with extracting $|V_{ub}|$ from the endpoint measurement are large, so there was great interest in measuring $|V_{ub}|$ in a different way.

At the 1991 Lepton-Photon Conference, the ARGUS collaboration presented [31] the results of a search for $B^- \to \rho^0 \ell^- \bar{\nu}$. The method was to select events with a moderately high energy lepton, $E_\ell > 1.5$ GeV, imposing various kinematic requirements for consistency with the semileptonic decay of a B meson, and then to plot the mass spectrum of the $\pi^+\pi^-$ candidates. Figure 15 shows this distribution, with a peak at the ρ^0 mass. This signal led to the branching

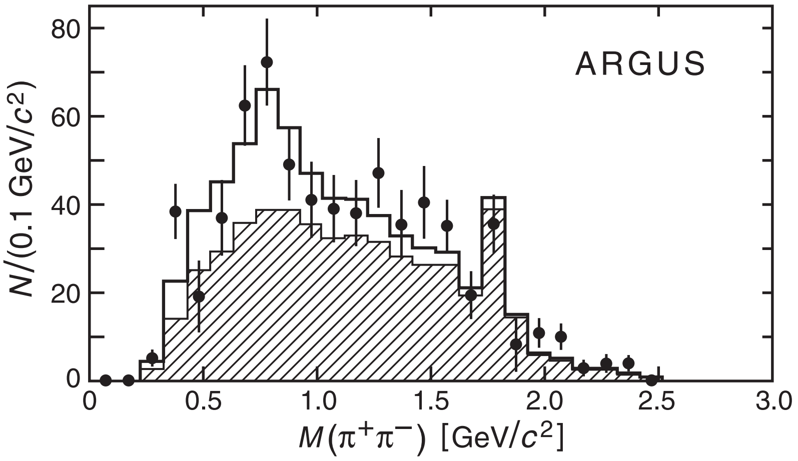

Fig. 15. Evidence from ARGUS for $B^- \to \rho^0 \ell^- \bar{\nu}$ presented at the 1991 Lepton-Photon Conference. The points with error bars are the continuum-subtracted data; the histogram is the overall fit, and the background from $b \to c$ decays is represented by the shaded region. (Used with permission and drawn from Ref. [31].)

fraction measurement

$$B(B^- \to \rho^0 \ell^- \bar{\nu}) = (1.13 \pm 0.36 \pm 0.27) \times 10^{-3}. \tag{5.4}$$

One of the most difficult aspects of the measurement was the determination of the shape of the background under the ρ peak. The dominant contribution is from semileptonic decay to charm final states, $B \to X_c \ell^- \bar{\nu}$, but there can be smaller contributions from various $B \to X_u \ell^- \bar{\nu}$ processes. Compounding this difficulty is the fact that the ρ is a very broad state ($\Gamma \approx 150$ MeV$/c^2$) and, with low statistics, it is difficult to distinguish it from a combinatorial $\pi^+\pi^-$ backgound that often peaks in roughly the same mass region. CLEO eventually presented a limit [32] that excluded the ARGUS central value, but a signal was not found until significantly later [5], because the branching fraction was far below that claimed by ARGUS. The CLEO II measurement is

$$B(\bar{B}^0 \to \rho^+ \ell^- \bar{\nu}) = (2.5 \pm 0.4^{+0.5}_{-0.7} \pm 0.5) \times 10^{-4}, \tag{5.5}$$

where the errors are statistical, systematic, and estimated model-dependence, respectively. Since

$$\Gamma(\bar{B}^0 \to \rho^+ \ell^- \bar{\nu}) = 2\Gamma(B^- \to \rho^0 \ell^- \bar{\nu}) \tag{5.6}$$

by isospin, the CLEO II result is effectively 1/10 that of ARGUS. The ARGUS result was never published in a journal. Statistically, the ARGUS measurement was marginal; some might argue that, given its large uncertainty, it was consistent with the CLEO II result. However, assuming that the CLEO II branching fraction is correct, the probability for ARGUS to observe any signal in their data sample was extremely low. One interesting aspect of the ARGUS analysis was the rather low value of the lepton-energy cut. As we will see, this mode is expected from rather general considerations to have a very hard lepton-energy spectrum. Thus, a useful test of the signal would have been to apply a much higher value of the cut to see if the signal was enhanced relative to the background.

5.3. Some rules for data analysis

• **Never determine your event-selection criteria using the data sample that you will use to measure your signal.** It is very easy to exploit statistical fluctuations in the data sample, biasing the signal upwards. Usually, the best approach is to tune cuts on a Monte Carlo sample used solely for this purpose. If the Monte Carlo doesn't perfectly describe the distributions of the signal, your cuts might not be optimal. However, they will not be biased, which is much more important. If a data sample is used to tune cuts, it should not be used to measure the size of the signal or to determine the level of backgound. Thus, the first steps of an analysis should be (1) make rough estimates and map out the main issues and strategies, (2) write event generators and simulate the analysis. The first step should not be to look at the data! As for most rules, there are exceptions to this one, and with extreme care one can develop event-selection cuts based on the data. An interesting example is the Brookhaven E787 search for $K^+ \to \pi^+\nu\bar{\nu}$ [33].
• **Don't use more cuts than you need.** A simple analysis is easier to understand, check, duplicate, and present.
• **Always check to see whether your signal is robust as you vary your cuts.** If there are systematic variations in the size of your signal (after background subtraction and efficiency correction), then you might not understand your background composition, the kinematic distributions of your signal, or the detector response.
• **Look at all the distributions you can think of for your signal and compare them with what you expect.** For example, angular distributions can often be predicted; they can build your confidence in the signal or even be used to improve its significance by cutting or fitting.
• **Look at the distributions of the events that your cuts ex-**

clude. Try to select event samples with little or no signal contribution to check your understanding of the background.
• **When possible, use data rather than Monte Carlo events to measure efficiencies and background levels.** This is particularly important for quantities that depend sensitively on the particle interactions with the detector (resolutions, misidentification probabilities, lepton detection efficiencies).
• **Do not use Monte Carlo events blindly; find out where the information came from that went into the Monte Carlo code.** The Monte Carlo may do well in predicting the background in someone else's analysis, but it may never have been checked for the modes or region of phase space relevant to your analysis.
• **Be careful not to underestimate the systematic errors associated with ignorance of (1) the signal efficiency, (2) background composition, and (3) background shapes.** For example, the signal efficiency is usually sensitive to the signal decay distributions, which are not always perfectly known. In some cases, however, the uncertainties in these distributions are not evaluated or even recognized.

Good luck!

6. Leptonic Decays

6.1. Introduction to leptonic decays

Leptonic decays provide a clean way to probe the strong interactions that bind the quark-antiquark system in the initial-state meson, simply because there are no strong interactions in the final state to complicate the interpretation of the decay-rate measurement. I'll begin by posing a few questions related to leptonic decays:
• Which charm and bottom mesons have the largest leptonic branching fractions? Which modes are experimentally accessible now?
• Why are the leptonic branching fractions of charm and bottom mesons so small compared to those of the π^+ and K^+?
• How can leptonic decays be separated from the much larger semileptonic backgrounds?
• What are the dominant systematic errors in the best leptonic decay measurements?
• How precise are current predictions for decay constants? What kinds of theoretical uncertainties affect these predictions?

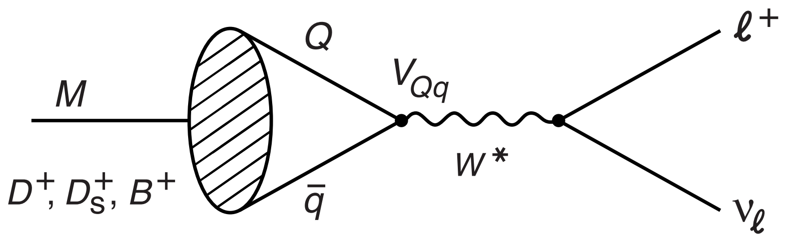

Fig. 16. Feynman diagram for leptonic decay.

• What are the effects of radiative corrections in charm and bottom leptonic decays?

Figure 16 shows a Feynman diagram for leptonic decay. The initial meson, of mass M and four-momentum p, contains a $Q\bar{q}$ pair that meets at a point, annihilating via a virtual W into a lepton and a neutrino. The CKM element V_{Qq} (or V_{Qq}^*) enters at the annihilation vertex. The four-momentum q_μ of the W is fixed: $q_\mu = p_\mu$ and $q^2 = M^2$. This situation contrasts with that in semileptonic decay, where q_μ varies depending on the kinematic configuration, and q^2 can take on a broad range of positive values. (In scattering processes, $q^2 \leq 0$.) Experimentally, one observes only the lepton directly; in favorable situations, the four-momentum of the neutrino can be inferred from the missing momentum in the event.

Because the lepton-neutrino system cannot interact strongly with the initial state, the matrix element can be factorized into the product of hadronic and leptonic currents:

$$\mathcal{M} = \frac{G_F}{\sqrt{2}} V_{Qq} \langle 0|J_\mu|M\rangle \bar{u}(k,\sigma)\gamma^\mu(1-\gamma_5)v(p,s), \tag{6.1}$$

where the leptonic current is written out in terms of Dirac spinors. For the case of pseudoscalar meson decay, there is only one four-vector that can be used to construct the hadronic current, namely p_μ, the four-vector of the initial meson. The current operator J_μ has a $V - A$ form but, as we show in the appendix (Sec. 11), only the matrix element of the axial-vector part of the current contributes. The hadronic current can then be written as

$$\langle 0|\bar{q}\gamma_\mu\gamma_5 Q|P(p)\rangle = i f_M p_\mu, \tag{6.2}$$

where f_M denotes the meson decay constant. It is remarkable that all of the effects of the strong interactions can be parametrized in terms of this single quantity, which measures the amplitude for the Q and $\bar{q}$ quarks to have zero separation. In fact, in a non-relativistic meson, where both quarks are heavy, the decay constant can be related in a very simple way [34] to the wave function at the origin: $f_M^2 M = 12|\psi(0)|^2$.

Using Eq. 6.1 and Eq. 6.2, it is simple to calculate the leptonic decay rate for a pseudoscalar meson, ignoring radiative corrections:

$$\Gamma(M_{Q\bar{q}} \to \ell^- \bar{\nu}) = \frac{G_F^2}{8\pi} |V_{qQ}|^2 f_M^2 M m_\ell^2 \left(1 - \frac{m_\ell^2}{M^2}\right)^2, \tag{6.3}$$

where f_M is the decay constant, V_{qQ} is the CKM matrix element, and m_ℓ and M are the masses of the lepton and the decaying charged meson $M_{Q\bar{q}}$, respectively.

If we start with a vector-meson, the hadronic current must be proportional to its polarization vector ϵ_μ, giving

$$\langle 0|\bar{q}\gamma_\mu\gamma_5 Q|V(\epsilon)\rangle = f_M V_{Qq} M_V \epsilon_\mu. \tag{6.4}$$

In practice, it is very difficult to observe the leptonic decay of a vector meson, because this weak process is overwhelmed in rate by strong or electromagnetic decays to the pseudoscalar meson, for example $D^* \to D\pi$ or $D^* \to D\gamma$. Nevertheless, knowledge of both pseudoscalar and vector-meson decay constants have important applications, as we will now see.

Figure 17 shows several situations in which decay constants are involved. In Fig. 17a, a B^- meson decays into a two-body hadronic final state. In Sec. 8, we will analyze this process in the framework of the factorization approximation; roughly speaking, this means that the upper and lower vertices can be considered separately. The quark-antiquark pair produced by the W is created at a point, and the amplitude for the pair to produce a particular meson is therefore proportional to the meson decay constant. In contrast, the process by which the daughter charm quark and the spectator quark form a D or D^* meson is quite different, since the quark-antiquark pair is not produced at a point, or even on a distance scale that is small compared to the size of the meson. We will later use transition form factors from semileptonic decay to analyze the physics at the lower vertex.

Figure 17b shows an extremely important application of decay constants: the processes of $B^0\bar{B}^0$ and $B_s\bar{B}_s$ mixing, which can be used to extract the magnitudes of the CKM elements V_{td} and V_{ts}. We will see in Sec. 9.5 that the oscillation frequency is proportional to f_B^2. Even though it appears that exchange of W bosons could lead to a spatial separation of the b and $\bar{d}$ quarks, the short range of the W means that this separation is negligible on the scale of the size of the B meson.

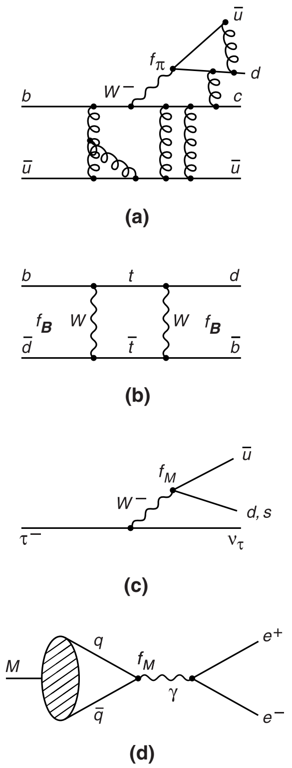

Fig. 17. Processes in which meson decay constants are involved: (a) hadronic decay, (b) $B^0\bar{B}^0$ oscillations, (c) τ decay, and (d) neutral vector meson decay to lepton pairs. The gluons shown in (a) are simply a reminder that processes involving hadrons are very complicated.

Figure 17c shows the decay of a τ lepton. Because the leptonic current is known, this process can be used to determine f_M for kinematically accessible mesons produced at the upper vertex. The rate for the τ decay is given by [35]

$$\Gamma(\tau^- \to M^-\nu_\tau) = \frac{m_\tau^3}{16\pi} G_F^2 |V_{ij}|^2 f_M^2 (1 - \frac{M^2}{m_\tau^2})(1 - b_M \frac{M^2}{m_\tau^2}), \qquad (6.5)$$

where $b_M = 0$ for $J = 0$ and $b_M = 2$ for $J = 1$. Decay constants for neutral vector mesons can be determined from the electromagnetic process shown in Fig. 17d. Again, the decay constant enters because the q and $\bar{q}$ must meet at a point.

As a result of the factor m_ℓ^2 in Eq. 6.4, leptonic decay of a pseudoscalar meson is forbidden in the limit $m_\ell \to 0$. As m_ℓ increases, the leptonic rate also increases to a maximum value and then falls again to zero as m_ℓ approaches M. Both vector (γ_μ) and axial-vector ($\gamma_5\gamma_\mu$) couplings at a vertex favor decays in which the final-state fermion and antifermion have opposite helicities; the more relativistic the fermions, the stronger the effect, hence the dependence on m_ℓ. This effect is sometimes called helicity suppression, and it is a particular consequence of helicity conservation. The effects of helicity conservation are ubiquitous in particle physics; we will meet them again, for example, in the discussion of kinematic distributions for semileptonic decays. A well-known application of Eq. 6.4 is charged-pion decay, where

$$\frac{\Gamma(\pi^+ \to e^+\nu_e)}{\Gamma(\pi^+ \to \mu^+\nu_\mu)} \approx 10^{-4}. \tag{6.6}$$

For D_s^+ decay, Eq. 6.4 gives

$$\begin{aligned}\Gamma(D_s^+ \to e^+\nu_e) : \Gamma(D_s^+ \to \mu^+\nu_\mu) : \Gamma(D_s^+ \to \tau^+\nu_\tau)\\ \approx 10^{-5} : 1 : 10.\end{aligned} \tag{6.7}$$

To understand this effect, it is important to distinguish between chirality and helicity. The left- and right-handed chiral projections of a spin-1/2 field are defined by $\psi_L = P_L\psi$ and $\psi_R = P_R\psi$, where $P_L = (1-\gamma_5)/2$ and $P_R = (1+\gamma_5)/2$. These operators satisfy $P_L^2 = P_L$, $P_R^2 = P_R$, and $P_R + P_L = 1$, the usual conditions on projection operators. The field operator ψ either destroys a fermion or creates an antifermion, while $\overline{\psi}$ does the reverse. The operator ψ_L either destroys a left-handed chirality fermion or creates a right-handed antifermion. Each chiral projection is a mixture of both negative and positive helicity states, but in the relativistic limit, the left-handed chiral projection of a spin-1/2 particle is purely helicity $\lambda = -1/2$, while the right-handed chiral projection is purely helicity $\lambda = +1/2$.

It is easy to show that a vector- or axial-vector current involving a fermion field ψ can be decomposed as

$$\overline{\psi}\Gamma^\mu\psi = \overline{\psi}_L\Gamma^\mu\psi_L + \overline{\psi}_R\Gamma^\mu\psi_R, \tag{6.8}$$

where L and R are used to indicate *chiral* projections, and Γ_μ represents either a vector or an axial-vector coupling. As a consequence, in a t-channel process, a left-handed chirality fermion in the initial state couples only to a left-handed fermion in the final state, and right-handed to right-handed. If a fermion and antifermion (not necessarily of the same type) are either produced or annihilated with a vector or axial-vector coupling, Eq. 6.8 implies that they must have opposite chirality. In the relativistic limit, these statements about chirality translate directly in statements about helicity. Figure 18 illustrates these effects of helicity conservation.

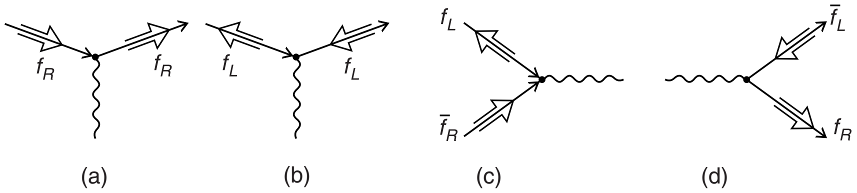

Fig. 18. Helicity conservation in various situations. In (a) and (b), helicity is conserved in a t-channel scattering process: a helicity $-1/2$ fermion is scattered into a helicity $-1/2$ final state and similarly for helicity $+1/2$. The spin vector rotates along with the momentum vector. The same effect implies that helicity $-1/2$ fermions couple to helicity $+1/2$ antifermions, and vice-versa, as shown in (c) and (d). These statements apply to vertices with vector or axial-vector couplings and are exact in the limit of zero fermion masses.

Another physical effect is that in processes like $e^+e^- \to \Upsilon(4S)$ or $e^+e^- \to Z$, the vector particles cannot have a spin projection zero along the beam axis. In W-mediated weak decays, these considerations apply, but there is the additional effect that P_L picks out only one of the two possible ways to satisfy the helicity-conservation constraints by forcing the W's daughter fermion to be left-handed and the daughter antifermion to be right-handed.

We now return to leptonic decay. Fig. 19 shows two decay configurations in which the neutrino has negative helicity. The lepton and neutrino helicities are equal in Fig. 19a and opposite in Fig. 19b. If the decaying meson has spin 0, however, the opposite-helicity configuration is forbidden by angular momentum conservation, since there would be nonzero angular momentum along the decay axis. (Note that in calculating angular momentum quantized along a two-body decay axis, we don't have to worry about orbital-angular momentum: since $\mathbf{L} = \mathbf{r} \times \mathbf{p}$, there can't be any such contribution.) The decay can only proceed through the configuration shown in Fig. 19a, but this is helicity suppressed. In the limit of zero lepton masses, the requirements of helicity conservation and angular momentum conservation are in direct conflict, and the decay is forbidden, except for the mitigating effects of radiative corrections.

We can use Eq. 6.4 to give us an idea which leptonic decays of charm and bottom hadrons would be easiest to search for. Note first of all that the dependence on the CKM element is crucial:

$$\begin{aligned}
&\Gamma(D^+ \to \ell^+\nu_\ell) \propto |V_{cd}|^2 \approx (0.22)^2 \\
&\Gamma(D_s^+ \to \ell^+\nu_\ell) \propto |V_{cs}|^2 \approx (0.97)^2 \\
&\Gamma(B^+ \to \ell^+\nu_\ell) \propto |V_{ub}|^2 \approx (0.003)^2.
\end{aligned} \tag{6.9}$$

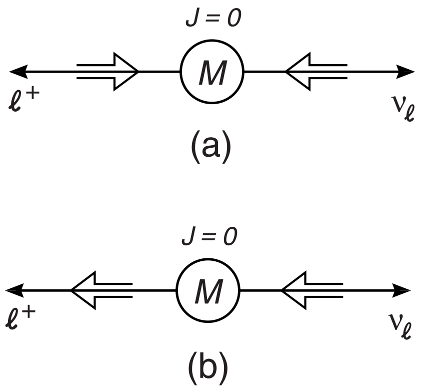

Fig. 19. Leptonic decay of a pseudoscalar meson: (a) Configuration allowed by angular momentum conservation but suppressed by the axial-vector coupling (b) configuration forbidden by angular momentum conservation but favored by the axial-vector coupling.

Table 6

Predictions for leptonic branching fractions of the D^+,D_s^+, and B^+ under the assumption that f_D, f_{D_s}, and f_B are all equal to 200 MeV. For comparison, the measured values of the π^+ and K^+ leptonic branching fractions are included.

	$B(e\nu)$	$B(\mu\nu)$	$B(\tau\nu)$
D^+	8.2×10^{-9}	3.5×10^{-4}	9.2×10^{-4}
D_s^+	7.5×10^{-8}	0.0032	0.031
B^+	7.5×10^{-12}	3.2×10^{-7}	7.1×10^{-5}
π^+	1.2×10^{-4}	99.99%	
K^+	1.6×10^{-5}	63.5%	

The D_s^+ should have the most accessible leptonic decays, since they are CKM favored. It is unfortunate that B^+ leptonic decay is highly suppressed, since we would like to use it to measure f_B, which is needed for B mixing calculations. It will probably be some time before leptonic B decays are observed.

Table 6 lists the predictions of Eq. 6.4 for the leptonic branching fractions for the D^+, D_s^+, and B^+, under the assumption that $f_D = f_{D_s} = f_B = 200$ MeV. For comparison, I also list the measured leptonic branching fractions for the π^+ and K^+ mesons. As expected, the modes $D_s^+ \to \mu^+\nu_\mu$ and $D_s^+ \to \tau^+\nu_\tau$ have the largest branching fractions; the advantage of the relatively large branching fraction for $D_s^+ \to \tau^+\nu_\tau$ is partly offset by the difficulty in reconstructing the τ^+ decay.

At first glance, it is startling that

$$B(D_s^+ \to \mu^+\nu_\mu) \ll B(K^+ \to \mu^+\nu_\mu). \tag{6.10}$$

Even though the assumed value f_{D_s} used in Table 6 may not be quite right, the dramatic difference in the D_s^+ and K^+ leptonic branching fractions will not change if we use any value within the measured or expected range. What happens to f_M as the meson mass increases? An asymptotic scaling law, which can be derived from HQET [36], predicts that

$$f_M^2 \cdot M \to \text{constant (for large } M). \tag{6.11}$$

Note that this factor appears in the leptonic decay rate formula, Eq. 6.4. In contrast, the total decay rate for a heavy meson is proportional to M^5, so the leptonic branching fraction becomes small. If we compare rates instead of branching fractions, we have

$$\begin{aligned}
\Gamma(K^+ \to \mu^+\nu_\mu) &= 5.13 \times 10^7 \text{ s}^{-1} \\
\Gamma(D_s^+ \to \mu^+\nu_\mu) &= 6.9 \times 10^9 \text{ s}^{-1} \\
\Gamma(D_s^+ \to \tau^+\nu_\mu) &= 6.6 \times 10^{10} \text{ s}^{-1},
\end{aligned} \tag{6.12}$$

which shows that the leptonic decay *rate* is in fact higher for the D_s^+ than for the K^+.

6.2. Measurements of leptonic decays

Imagine that you are given a large sample of events containing a mix of charm hadrons, moving at high momentum. The sample also contains a large number of events without charm particles. How would you find a signal for D_s^+ leptonic decay?

The most conspicuous problem is that the only directly observed particle from the decay is the lepton. At best, the neutrino can be inferred from the missing momentum vector, assuming that the initial D_s^+ momentum is somehow known and the detector is very nearly hermetic. If there is no such estimate of the neutrino momentum, then the D_s^+ mass peak cannot be observed. In this case, the signal must be established by some other technique. Even if the neutrino momentum can be estimated, the resolution is not as good as that for a directly measured particle. The D_s^+ mass peak will be broader than for a hadronic decay, making it more difficult to distinguish the signal from backgrounds. Another problem is that there are plenty of leptons around from other sources, in particular, from charm semileptonic decays. Given these difficulties, and the small branching fractions, it is

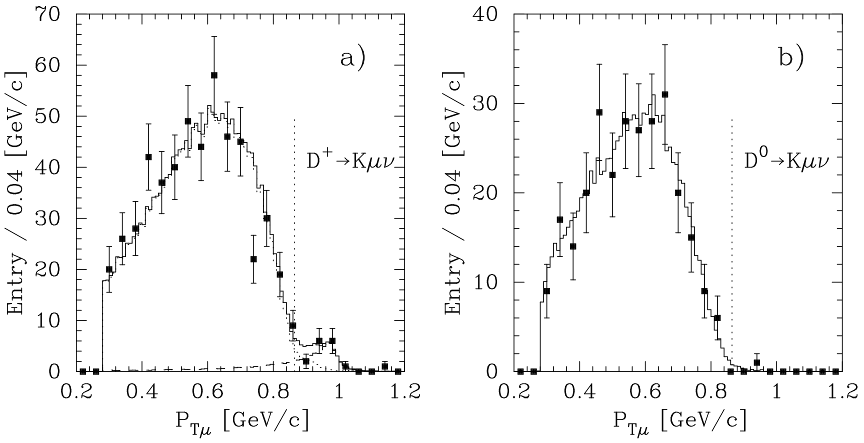

Fig. 20. Observation of D_s^+ leptonic decay from the E653 experiment at Fermilab. The left-hand figure (a) shows the distribution of p_{T_μ} (muon momentum transverse to the D_s^+ direction) for the sample of one-prong kinks. The dominant source of events is semileptonic D^+ decay, but there is an excess of events at high p_{T_μ}; this excess is attributed to leptonic decay. The right-hand figure (b) shows the p_{T_μ} spectrum for two-prong vees.

not surprising that current measurements of leptonic branching fractions do not have high precision. Nevertheless, steady progress is being made, and in this section we examine some of the measurements.

One way to get additional information about the decay is to observe not just the charged lepton, but also the D_s^+ itself before it decays. A leptonic decay would then produce a "kink" in the trajectory of a charged track, since the muon recoils against an unobserved neutrino. In most experiments, it is not possible to observe the kink, because the D_s^+ decays before it ever reaches a detector. Figure 20 shows data from the E653 experiment [37] at Fermilab, which had the ability to observe such kinks. The charm hadrons are produced by the interactions of a high-energy π^- beam incident on a photographic-emulsion target. The target is followed by 18 planes of silicon-strip detectors and a magnetic spectrometer. To analyze the events, the emulsion must first be removed from the experiment. It is then processed and scanned for kinks and other topologies, such as vees, which are due to neutral particles decaying into a pair of oppositely charged tracks. The kinks and vees are identified in the emulsion, while the silicon-vertex detectors serve to link the tracks found in emulsion with those in the spectrometer, where the momenta are measured.

The observation of a kink, however, is not sufficient to identify a leptonic decay. The semileptonic process, $D^+ \to \bar{K}^0\mu^+\nu_\mu$, for example, can produce an identical topology. To separate leptonic decays from this background, E653 measures the momentum, $p_{T\mu}$, of the muon perpendicular to the parent particle's direction. The distribution of $p_{T\mu}$ for tracks in the kink sample is shown in Fig. 20a. The dominant source of events is $D^+ \to \bar{K}^0\mu^+\nu_\mu$, which produces a broad spectrum in $p_{T\mu}$. The signal has a much narrower $p_{T\mu}$ distribution peaked at about half the D_s^+ mass; this peak is largely beyond the endpoint for the semileptonic decay. Beyond the nominal endpoint, there are 23 ± 6 events above the semileptonic background, but there is still an small contamination, estimated to be 4.5 events, from $D^+ \to \mu^+\nu_\mu$.

Given the small size of the signal, it is important to demonstrate that it is not simply an artifact related to the background. Figure 20b shows the $p_{T\mu}$ distribution for the sample of vees (two oppositely charged tracks emerging from a common vertex point). There is a large contribution from $D^0 \to K^-\mu^+\nu_\mu$, which produces a $p_{T\mu}$ spectrum similar to that from $D^+ \to \bar{K}^0\mu^+\nu_\mu$. As expected, there is no excess beyond the semileptonic endpoint in this sample.

In the E653 experiment, it is not possible to determine the total number of D_s^+ decays, so the leptonic signal is normalized relative to the signal for $D_s^+ \to \phi\pi^+$, which is the best measured D_s^+ decay mode. Unfortunately, this branching fraction is quite poorly known, $B(D_s^+ \to \phi\pi^+) = (3.6 \pm 0.9)\%$, and this 25% uncertainty propagates into all D_s^+ branching fractions. The problem of normalizing signals is quite important, and we will return to it in our discussion of hadronic decays.

Currently, the largest $D_s^+ \to \mu^+\nu_\mu$ signal is from a recent CLEO II measurement [38], which uses about 5×10^6 $e^+e^- \to c\bar{c}$ events produced at $\sqrt{s} = M(\Upsilon(4S))$ or 60 MeV below. These events typically have a two-jet topology, and the fragmentation of the charm quark leads not only to D and D_s production, but also to D^* and D_s^*. Rather than simply searching for $D_s^+ \to \mu^+\nu_\mu$, the CLEO analysis exploits the constraints provided by the decay sequence $D_s^{*+} \to \gamma D_s^+$, $D_s^+ \to \mu^+\nu_\mu$. The momentum of the neutrino is inferred—somewhat crudely—from the missing momentum, and it is used to reconstruct D_s^+ and D_s^{*+} masses. Because the neutrino momentum, p_ν, is used to compute both quantities, the error on p_ν tends to cancel when the difference between the reconstructed masses is computed:

$$\Delta M = M(\mu^+\nu_\mu\gamma) - M(\mu\nu_\mu). \tag{6.13}$$

The resolution on ΔM is reasonably good, with $\sigma \approx 16$ MeV/c^2, and the signal is ultimately identified as a peak in the ΔM distribution. This procedure is analogous to measurements that use the reconstructed $D^* - D$ mass difference when studying certain D decays.

A second key idea in the CLEO analysis is to use events with electrons to measure the dominant component of the background. Because $D_s^+ \to e^+\nu_e$ is negligible (due to helicity suppression), we can assume that events passing the analysis cuts but which have electrons instead of muons must be due to background processes. The backgounds in this analysis are due to three main sources:

(i) semileptonic processes (primarily $D \to K\ell^+\nu$, $D \to \pi\ell^+\nu$ and $D_s \to \eta\ell^+\nu$);

(ii) leptonic processes: (a) signal events in which the wrong photon is selected; (b) $D_s^+ \to \mu^+\nu_\mu$ decays for which the D_s^+ did not come from D_s^{*+} decay, but was produced directly; and (c) $D^+ \to \mu^+\nu_\mu$, which is Cabibbo suppressed; and

(iii) events in which a hadron has been misidentified as a muon.

The semileptonic backgrounds have nearly the same rates to the e and μ channels, so the electron sample can be used to measure the semileptonic contamination of the muon sample. The leptonic and misidentification backgrounds are very different in the e and μ samples and must be studied in a different way.

The problem of hadrons being misidentified as muons is quite significant, and it is the source of one of the most important systematic errors in the analysis. In fact, this "fake rate" is now thought to have been underestimated in the original CLEO II analysis of this mode, resulting in a value of f_{D_s} that was too large. Muons in the $D_s^+ \to \mu^+\nu_\mu$ analysis are required to have momenta $p_\mu > 2.4$ GeV/c. This value is relatively high, and it greatly suppresses background from semileptonic decays, while still retaining 33% of the signal events. At such high momenta, however, hadrons are more likely to penetrate the steel absorber in front of the muon detectors, thus appearing to be muons. To estimate the number of such occurrences, one can study tracks "tagged" as π^+ or K^+ mesons by virtue of being reconstructed in mass peaks, for example, from $K_s \to \pi^+\pi^-$ and $D^{*+} \to D^0\pi^+$, $D^0 \to K^-\pi^+$. Such processes serve to identify the daughter hadrons simply by kinematics. The revised misidentification rates used in the new CLEO II analysis are based on a sample of 10,000 such events; this study found that the probability for a π^+ to fake a μ^+ signature is $(0.65 \pm 0.08)\%$.

Figure 21 shows the ΔM mass difference distribution for the CLEO II measurement (a) before background subtraction and (b) after sub-

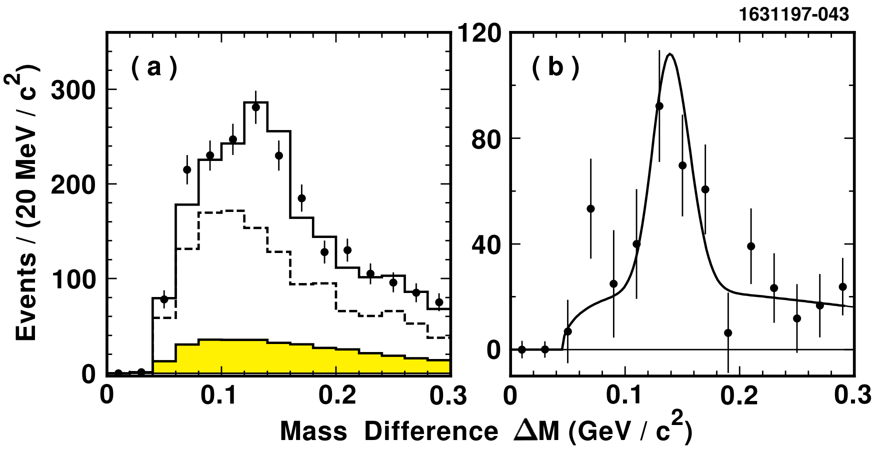

Fig. 21. CLEO II signal for $D_s^+ \to \mu^+\nu$. The left hand plot (a) shows the ΔM mass difference for D_s^{*+} candidates for muon data (points with error bars), electron data (dashed histogram), and the additional background due to the excess of muon fakes over electron fakes (shaded region). The solid histogram is the overall fit. The two background contributions are not summed in this figure. The right-hand figure (b) shows the ΔM distribution for muon events after the backgrounds estimated from the electron sample and from the excess of muon fakes over electron fakes have been subtracted. There remains some combinatorial background and background from $D^+ \to \mu^+\nu_\mu$. The signal contains 182 ± 22 events.

traction of all but leptonic backgrounds, which are taken into account in the fit. The background peaks in the same region as the signal, which itself is not overwhelming. Nevertheless, this signal is by far the most significant yet observed by any experiment. The CLEO II analysis gives

$$\frac{\Gamma(D_s^+ \to \mu^+\nu_\mu)}{\Gamma(D_s^+ \to \phi\pi^+)} = 0.173 \pm 0.021 \pm 0.031, \tag{6.14}$$

where the first error is statistical and the second is systematic. When computing the actual branching fraction and f_{D_s}, there is a large additional uncertainty from the error on the branching fraction for the $D_s^+ \to \mu^+\nu_\mu$ normalization mode, as discussed above. Improvement in the precision of this key branching fraction is extremely desirable.

Table 7 lists f_{D_s} measurements from various experiments. Both the published value of f_{D_s} and a corrected value are included. The corrected values are obtained from the CLEO II paper, in which the results are renormalized to a common set of branching fractions. The LEP experiments L3 and OPAL have also measured f_{D_s} using $D_s^{*+} \to D_s^+\gamma$, $D_s^+ \to \tau^+\nu_\tau$. The L3 signal [41] is shown in Fig. 22; it has 15.6 ± 6.0 events and gives $f_{D_s} = 309 \pm 58 \pm 33 \pm 38$ MeV, while the

Table 7

Measurements of f_{D_s} from $D_s^+ \to \mu^+\nu_\mu$ decay. The corrected values use a common set of branching fractions as described in the CLEO paper. The first error is statistical, the second systematic, and the third is the uncertainty due to the error on the branching fraction for the normailizing mode $D_s^+ \to \phi\pi^+$. Values of f_{D_s} obtained from $D_s^+ \to \tau^+\nu_\tau$ are given in the text.

Experiment	Observed Evts.	Published f_{D_s} (MeV)	Corrected f_{D_s} (MeV)
WA75 [39]	6	$232 \pm 45 \pm 20 \pm 48$	$238 \pm 47 \pm 21 \pm 48$
BES [40]	3	$430^{+150}_{-130} \pm 40$	same
E653 [37]	$23.2 \pm 6.0^{+1.0}_{-0.9}$	$194 \pm 35 \pm 20 \pm 14$	$190 \pm 34 \pm 20 \pm 26$
CLEO II [38]	182 ± 22	-	$280 \pm 17 \pm 25 \pm 34$

Table 8

Values of decay constants for various charged and neutral mesons: f_π and f_K are from the Particle Data Book [4], while the others are from Neubert and Stech [113]. The decay constants for neutral vector mesons V are obtained from the rate for $V \to e^+e^-$.

Decay Constant	Value (MeV)
f_{π^+}	$130.7 \pm 0.1 \pm 0.36$
f_{K^+}	$159.8 \pm 1.4 \pm 0.44$
f_{ρ^+}	208 ± 1
$f_{K^{*+}}$	214 ± 7
$f_{a_1^+}$	229 ± 10
f_ϕ	237 ± 4
$f_{J/\psi}$	405 ± 14

Delphi signal [42] has 10.8 ± 5.4 events (including both $D_s^+ \to \tau^+\nu_\tau$ and $D_s^+ \to \mu^+\nu_\mu$) and gives $f_{D_s} = 330 \pm 95$ MeV. Values of decay constants for other charged and neutral mesons are listed in Table 8.

The correct calculation of an experimental average of the f_{D_s} values requires some work, due to a number of correlated systematic errors. I have computed one such average [2], $f_{D_s} = (241 \pm 21 \pm 30)$ MeV, where the first error combines the statistical and most of the systematic uncertainties, and the second error is due to the uncertainty from the overall normalization of D_s^+ branching fractions. For a recent review of leptonic decay results, see the paper by Nippe [43], who obtains the average value $f_{D_s} = (251 \pm 31)$ MeV. Nippe uses $B(D_s^+ \to \phi\pi^+) = (3.7 \pm 0.7)\%$ rather than the value $(3.6 \pm 0.9)\%$ (see PDG97 [4]), which

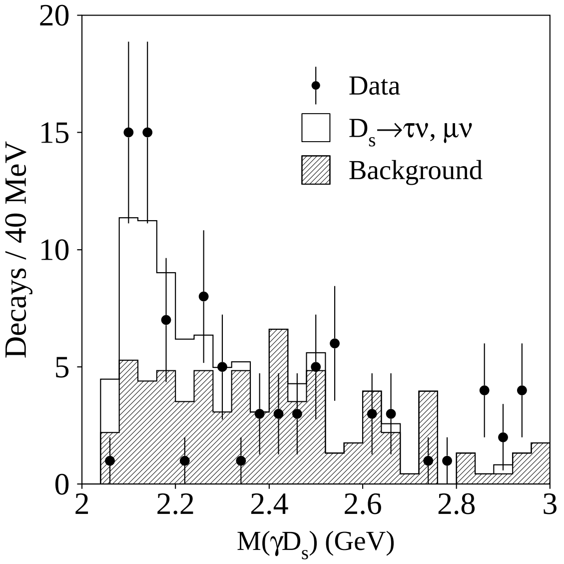

Fig. 22. L3 signal for $D_s^{*+} \to D_s^+\gamma$, $D_s^+ \to \tau^+\nu_\tau$. The points with error bars are the data, the hatched region represents the Monte Carlo estimate for the background, and the open histogram shows the fitted signal.

is used in Ref. [2].

Searches for $B(B^+ \to \tau^+\nu)$ are not yet sensitive to rates at the level predicted by the standard model. The current limit (from LEP experiments [43]) is $B(B^+ \to \tau^+\nu_\tau) < 5.7 \times 10^{-4}$ (90% C.L.).

Because helicity suppression plays such a key role in leptonic decays, it is interesting to see whether the emission of a photon can substantially affect the decay rates. We might expect photon radiation to mitigate the effects of helicity suppression when $\ell^- = e^-$ or $\ell^- = \mu^-$; there should be little overall increase in the rate for $\ell^- = \tau^-$, since there is much less helicity suppression in that case. Estimates of these effects are model dependent and have been discussed by several authors. For example, Atwood, Eilam, and Soni [44] find that the dominant contribution comes from photon radiation from the light quark in the meson and that $B(B^+ \to \ell^+\nu\gamma) \approx 3.5 \times 10^{-6}$, essentially independent of the species of lepton. The $\ell^+\nu\gamma$ rate is large relative to the purely leptonic rate for $\ell^+ = \mu^+$ but not for $\ell^+ = \tau^+$:

$$\frac{B(B^+ \to \mu^+\nu_\mu\gamma)}{B(B^+ \to \mu^+\nu_\mu)} \simeq 16,$$

$$\frac{B(B^+ \to \mu^+ \nu_\mu \gamma)}{B(B^+ \to \tau^+ \nu_\tau,\ \tau^+ \to \mu^+ \nu_\mu \bar{\nu}_\tau)} \simeq 0.4. \tag{6.15}$$

The effect on D_s^+ decays is very small:

$$\frac{B(D_s^+ \to \mu^+ \nu_\mu \gamma)}{B(D_s^+ \to \mu^+ \nu_\mu)} \simeq 5.9 \times 10^{-3}. \tag{6.16}$$

CLEO has obtained [45] the limits $B(B^+ \to \mu^+ \nu \gamma) < 5.2 \times 10^{-5}$ and $B(B^+ \to e^+ \nu \gamma) < 2.0 \times 10^{-4}$, both at 90% C.L. These results demonstrate how difficult it will be to make precision measurements of leptonic decays, but progress will be possible at the new B factories.

6.3. Lattice calculations of leptonic decay constants

The calculation of heavy-meson decay constants using lattice QCD have been progressing steadily, and they may have even reached the point where experimentalists should start taking them seriously! These numerical calculations of hadron properties are based on computer simulations using a discrete space-time lattice. Because the limiting resource is computing power, certain approximations are made. First, the space-time volume is typically divided into 16^3 to 48^3 spatial lattice sites and 32 to 100 time intervals. To contain a meson, the lattice must have a spatial length of 1.5 fm or more, which means that the spacing a is typically between 0.1 fm and 0.05 fm. For numerical reasons, lattice calculations are performed using imaginary time it rather than t, and excited states must be allowed to decay away (e^{-Et}), leaving a configuration that corresponds to a sufficiently pure ground state. This is why the number of time intervals on the lattice is typically larger than the number of lattice sites along a spatial dimension. Many lattice groups calculate their results for a series of values of a and then extrapolate to $a = 0$, the so-called continuum limit. This extrapolation is a significant source of uncertainty. A second limitation of lattice calculations is that until recently, they have been performed in the so-called quenched approximation. In this model of hadron dynamics, the interactions occur between valence quarks and gluons only; there are no virtual-quark loops. We are now seeing the first attempts to include quark loops, and there are some rough estimates of how big these loop-related effects are.

At the *7th International Conference on Heavy Flavor Physics*, Claude Bernard gave a talk [46] that clarified many points regarding the history of lattice calculations. He argued that there have been three (overlapping) eras: ancient history (roughly 1988–1994); the middle ages (roughly 1992–1997); and the modern era, which we appear to just be entering. Many of the calculations performed in the ancient era were simply wrong. Some were affected by poorly understood lattice artifacts; in others, the ground-state meson was not sufficiently isolated from its excited states in the calculation. Improvements were made during the middle ages, but here again, the calculations suffered from such limitations as no extrapolation to $a = 0$ and no estimates of the quenching error. Calculations in the modern era are characterized by detailed estimates of all uncertainties, at least within the quenched approximation. The implication of all of this is that there is no point in making enormous tables listing all of the lattice calculations, since many of them are known to be wrong, at least by the experts. I have therefore listed some of the most recent results, most of which are declared to be "modern" in Bernard's talk.

Ideally, lattice predictions come with three errors: a statistical error, a systematic error within the quenched approximation (often dominated by the $a \to 0$ extrapolation), and an estimate of the quenching error. Figure 23 shows preliminary results from a calculation of f_B from the MILC collaboration [47] as a function of the lattice spacing. Two possible points at $a = 0$ are used to estimate an error associated with the extrapolation to the continuum limit. Table 9 lists some of the recent lattice results. There seems to be a consensus that f_B is significantly below 200 MeV, at least in the quenched approximation. Two significant statements can be made about this approximation. First, loops are expected to increase f_B, so the corrected values should be somewhat higher than the quenched results. Second, based on the studies of the MILC collaboration, which has performed some calculations with loops, such effects are not expected to be dramatic, possibly bringing up their result by 13 MeV, which is only a 5% shift.

The lattice predictions of f_{D_s} are consistent, within errors, with the experimental averages discussed in the previous section. It is clear, however, that both experiment and theory need to improve the precision of these results.

7. Semileptonic Decays

7.1. Introduction to semileptonic decays

Semileptonic decays, due to their simplicity, provide an excellent laboratory in which to measure $|V_{cb}|$ and $|V_{ub}|$. These processes also allow us to study the effects of nonperturbative QCD interactions on the

Table 9

Some recent results on decay constants from lattice calculations. The errors are statistical, systematic within the quenched approximation, and (for the MILC result) an estimate of the uncertainty due to the quenched approximation. The MILC, JLQCD, and FNAL results are reviewed by Bernard [46]; the Ali Khan *et al.* results are from Ref. [48].

Group	f_B (MeV)	f_{B_s}/f_B	f_{D_s} (MeV)
MILC	$153(10)(^{+36}_{-13})(^{+13}_{-0})$	$1.10(2)(^{+5}_{-3})(^{+3}_{-2})$	$199(8)(^{+40}_{-10})(^{+10}_{-0})$
JLQCD	$163(12)(^{+13}_{-16})$	-	$213(11)(^{+12}_{-8})$
FNAL	166(10)(28)	1.17(4)(3)	215(7)(30)
Ali Khan *et al.*	147^{+17}_{-20}	$1.20(^{+6}_{-4})$	

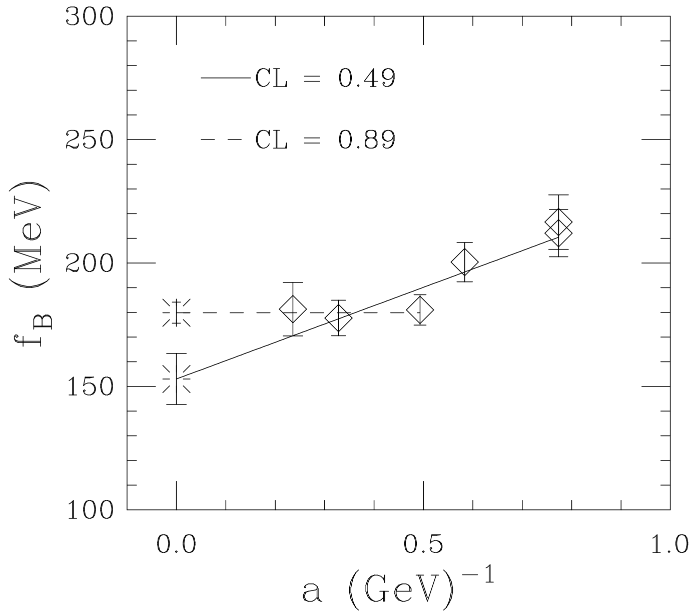

Fig. 23. Lattice calculation of f_B from the MILC collaboration as a function of lattice spacing a. Two possible extrapolations to the continuum limit $a = 0$ are shown. The uncertainty on the extrapolation is based on the difference between these two values. Figure provided by R. Sugar.

weak-decay process. These goals may sound contradictory: how can we measure standard-model parameters if complicated hadronic effects are present?

We can untangle the effects of strong interactions on semileptonic decays for a number of reasons. First, it is important to recognize that although such effects are difficult to calculate, they are isolated to the hadronic current. As a consequence, the effect of strong interactions can be rigorously parametrized in terms of a small number of form factors, which are functions of the Lorentz-invariant quantity q^2, the square of the mass of the virtual W. Thus, we have a solid starting point for understanding how strong interactions affect the decay. Second, the difficulty in understanding these effects is quite dependent on the decay mode. For $b \to c\ell^-\bar{\nu}$ decays, the large masses of both the b and c quarks provide the key to reliable theoretical predictions based on heavy-quark effective theory (HQET) for exclusive decays and heavy-quark expansions for inclusive decays. Third, it has been recognized that in different regions of the three-body phase space for semileptonic decay, the strong interactions play a very different role. Thus, by focusing on the particular kinematic configurations in which the hadronic system is least disturbed by the decay, it has been possible to reduce the uncertainties associated with hadronic effects. These considerations have led to major advances in the reliable determination of $|V_{cb}|$.

Heavy-quark symmetry helps in two major ways in $b \to c\ell^-\bar{\nu}$ decays. First, it relates different form factors to each other, reducing the number of independent functions that need to be understood. Second, it tells us the value ("normalization") of the form-factors when the daughter charm hadron has zero momentum with respect to the parent b hadron, the so-called zero-recoil configuration. The zero-recoil point corresponds to the maximum value of q^2:

$$\begin{aligned} q^2 &= (p_B - p_{D^*})^2 = (E_B - E_{D^*})^2 - (\mathbf{p}_B - \mathbf{p}_{D^*})^2 \\ &= (m_B - m_{D^*})^2, \end{aligned} \tag{7.1}$$

where we have used the decay $\bar{B} \to D^*\ell^-\bar{\nu}$ as an example. In the heavy-quark symmetry limit ($m_b \to \infty$ and $m_c \to \infty$), the hadronic system is undisturbed by the replacement of one very heavy quark by another. Since the b and c quark masses are not truly infinite, there are corrections to predictions based on the heavy-quark symmetry limit, but they are relatively small. *Heavy-quark symmetry cannot give us the actual q^2 dependence of the form factors, since this depends on the complexities of the strong interactions. The symmetry only relates the q^2 dependence of the different form factors to each other and gives the normalization at zero recoil.* The three form factors for $\bar{B} \to D^*\ell^-\bar{\nu}$ and the single form factor for $\bar{B} \to D\ell^-\bar{\nu}$ all become directly related, in the heavy-quark symmetry limit, to a single form factor, the Isgur-Wise function.

Significant challenges in understanding semileptonic decays remain, however. The problems are particularly difficult in $b \to u\ell^-\bar{\nu}$ decays. While the determination of $|V_{ub}|$ is improving, both experimentally and theoretically, there are still large uncertainties. Due to the small value of the u-quark mass, the zero-recoil configuration in $b \to u\ell^-\bar{\nu}$ decays does not provide a solid normalization point. Furthermore, the small mass of the daughter meson results in a large accessible range in q^2, over which there can be considerable variation of the form factors.

Although $|V_{cb}|$ has been measured with reasonably good precision, further improvements are highly desirable, because some tests of the CKM framework are highly sensitive to the value of $|V_{cb}|$. For example, to determine the constraint in the $\rho - \eta$ plane arising from measurements of the CP-violating quantity $|\epsilon_K|$ measured in neutral K decays, one needs the quantity $A^4 \propto |V_{cb}|^4$ (see Sec. 3). This dependence on $|V_{cb}|$ means that the relative uncertainty on $|V_{cb}|$ is magnified by a factor of four. Thus, a quantitative understanding of the effects of strong interactions on the underlying weak decay is essential for extracting precise values of CKM elements and for testing the CKM framework of CP violation.

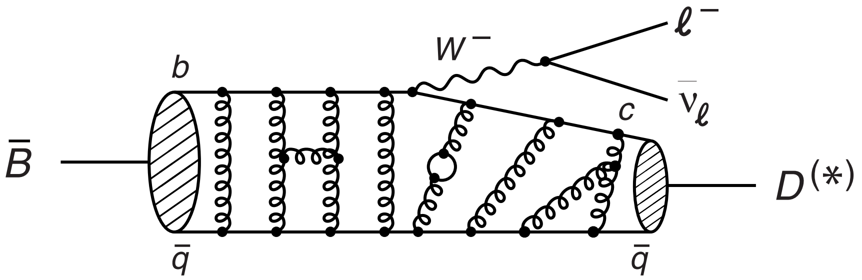

Fig. 24. Semileptonic decay of a B meson. The complicated effects of the strong interactions can be rigorously parametrized by a small number of form factors, which are functions of q^2, the square of the mass of the virtual W. The recoil velocity of the hadronic system is directly related to q^2.

Figure 24 shows the diagram for the semileptonic decay of a $\bar{B}$ meson. The large number of gluons is meant to suggest the complexity of non-perturbative strong-interaction effects. Unlike leptonic decays, the quantity q^2, the square of the mass of the virtual W, is not a constant, but varies as a function of the kinematic configuration. We will see that there are two key variables that enter into the description of the decay: q^2 and E_ℓ, the lepton energy. To understand semileptonic decays, it is very often useful to analyze the dynamics at several representative values of q^2. For each value, we can think of the semileptonic decay $M \to X\ell^-\bar{\nu}$ as proceeding in two steps: (1) the two-body decay $M \to XW(q^2)$ and (2) the two-body decay $W(q^2) \to \ell^-\bar{\nu}$. I will present a simple, physical picture of semileptonic decays that is centered on understanding the role of q^2, the $V-A$ coupling, meson quantum numbers, and simple dynamical considerations.

The discussion of semileptonic decays is divided into several sections, covering the dynamics of semileptonic decay, a brief introduction to HQET, inclusive $b \to c$ and $b \to u$ semileptonic decays, form factor predictions, and measurements of exclusive decays. To conclude this introduction, I offer a list of questions to ponder:

• How do the strong interactions affect semileptonic decay in different kinematic regions? What is the general behavior of the form factors? How does this behavior differ among different semileptonic processes?
• What determines the shape of the lepton-energy spectrum? Why is the shape of the spectrum different for bottom and charm decays?
• What determines the shape of the observed q^2 distribution? Why is this distribution completely different for $\bar{B} \to D\ell^-\bar{\nu}$ and $B \to D^*\ell^-\bar{\nu}$?
• What role does the $V-A$ structure of the weak current play in different processes? Does this role depend on the quantum numbers of the hadrons?
• What does heavy-quark effective theory tell us about semileptonic decays?
• If P is a pseudoscalar meson and V is the vector meson with the same quark content, what is the value of the ratio $\Gamma(M \to V\ell^-\bar{\nu})/\Gamma(M \to P\ell^-\bar{\nu})$? (Hint: it's not generally three!) What determines the relative populations of the helicity states of V?
• How are the observed decay distributions related to form factors?
• What have experiments told us about form factors? How much do form factors typically vary over the allowed kinematic range? How do the results compare with theoretical predictions?
• Given the presence of an unobserved neutrino, how are semileptonic decays identified?
• What are the best methods for determining $|V_{cb}|$ and $|V_{ub}|$? Which uncertainties dominate in each case: experimental or theoretical?
• What can we learn from the semileptonic branching fraction (as opposed to the semileptonic rate)? Are the values of the semileptonic branching fractions in B and D decay understood?

Review articles on semileptonic decays have been written by Richman and Burchat [1] and by Neubert [36]. The latter article contains extensive information on HQET.

7.2. Dynamics of semileptonic decay

I will begin with a qualitative picture of the dynamics of the semileptonic decay $M \to X\ell^-\bar{\nu}$, where M is a pseudoscalar meson (a D or B) containing a heavy quark. We will focus on decays in which the hadronic system X is a single meson, since such processes dominate the D and B semileptonic decay rates. In semileptonic D decays, the known resonant exclusive modes come fairly close to saturating the inclusive semileptonic rate, and multibody, nonresonant final states have not been observed. In B decays, the two modes $\bar{B} \to D\ell^-\bar{\nu}$ and $\bar{B} \to D^*\ell^-\bar{\nu}$ account for about two-thirds of the semileptonic rate. Part of the remainder is to due to D^{**} production, but there is still a little room for nonresonant final states.

A powerful tool for describing the dynamics of semileptonic decay is the Dalitz plot, which maps the probability for different kinematic configurations over the allowed region of phase space. Figure 25 is based on a Monte Carlo simulation of a sample of $\bar{B} \to D^*\ell^-\bar{\nu}$ decays, which we have generated using HQET-based form-factor parameters given by Neubert [36]. (These predicted values are quite similar to those measured by CLEO [49]; this measurement is discussed below in the section on exclusive semileptonic decays.) In this plot, each point represents a single $\bar{B} \to D^*\ell^-\bar{\nu}$ decay. Because Dalitz-plot variables (energies or squared masses) are used, *phase space is uniform over the plot*, so that a constant matrix element would give a uniformly distributed set of points. In this section we will analyze the physical significance of different Dalitz-plot regions and qualitatively explain the pattern shown in Fig. 25.

For Dalitz-plot variables, we have chosen E_ℓ, the energy of the lepton measured in the rest frame of the initial meson M (whose mass is also labeled M), and q^2, the variable mass-squared of the W:

$$q^2 = m_W^2 = (p_\ell + p_{\bar{\nu}})^2 = (P - p_X)^2 = M^2 + {m_X}^2 - 2ME_X, \qquad (7.2)$$

where P is the four-momentum of M and E_X is the energy of X in the M-meson rest frame. This result is simply an equation from two-body decay kinematics ($M \to XW$), and it shows that E_X *is linearly related to* q^2. Traditionally, form factors have been parametrized in terms of q^2, but in our discussion of HQET, we will use an alternate form based on four-velocities rather than four-momenta. The form factors are then written in terms of

$$w \equiv v \cdot v_X = \frac{P}{M} \cdot \frac{p_X}{m_X} = \frac{E_X}{m_X} = \gamma_X = \frac{M^2 + m_X^2 - q^2}{2Mm_X}. \qquad (7.3)$$

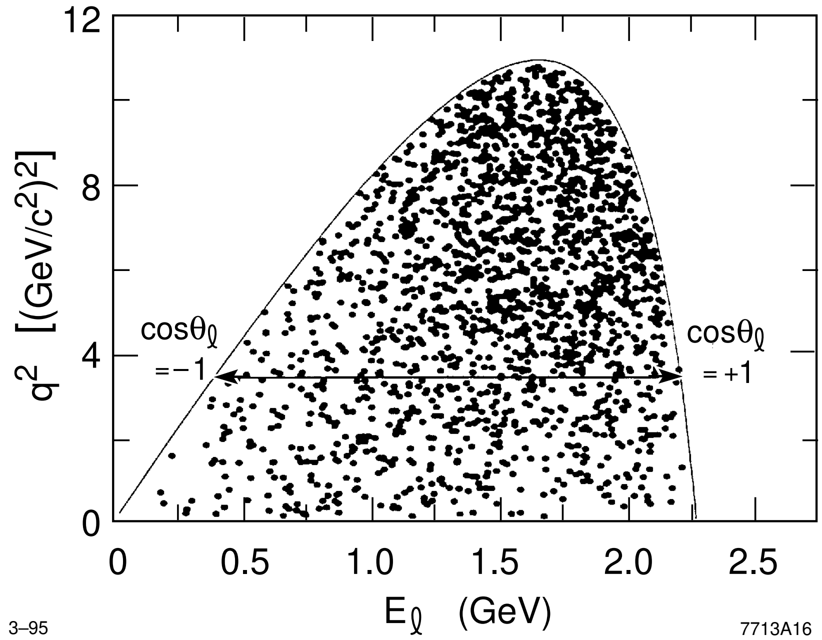

Fig. 25. A Monte Carlo simulation of the Dalitz plot for the process $\bar{B} \to D^* \ell^- \bar{\nu}$, using HQET-based form factors from Neubert [36]. Because Dalitz-plot variables are used, equal-sized areas in the allowed region correspond to equal amounts of available phase space. The form factors are largest at high q^2, which increases the density of points towards the top of the plot. At a fixed value of q^2, the range in lepton energies from left to right corresponds to the variation of $\cos\theta_\ell$, where θ_ℓ is the polar angle of the lepton in the W rest frame, from -1 to $+1$ (see Fig. 28). The increase in density across the Dalitz plot from left to right can be traced to the $\cos\theta_\ell$ distribution, which is asymmetric due to the $V-A$ coupling. This coupling enhances the amplitude for the negative-helicity state of the W relative to the positive-helicity state. Special cases occur at $q^2_{\rm max}$, where the W (or the D^*) is unpolarized, and at $q^2 = 0$, where it is in a pure helicity zero state.

This quantity is just the relativistic gamma factor of the daughter meson in the rest frame of the parent meson, and it has a minimum value of one. The literature contains a number of different names for this quantity, including ω and y.

Two key semileptonic decay configurations are shown in Fig. 26. The initial $\bar{B}$ meson, which contains a b-quark and a spectator quark $\overline{q}$, is shown in Fig. 26a, while the configurations for $q^2 = q^2_{\rm max}$ and $q^2 = q^2_{\rm min}$ are shown in Figs. 26b and 26c.

The maximum value of q^2 occurs when E_X is minimized: $E_X = m_X$ and $w = E_X/m_X = 1$ (Fig. 26b). At $q^2_{\rm max}$, the virtual W is as heavy as it can possibly be, and there is no kinetic energy. Both the W and the daughter meson X are produced at rest in the parent-meson rest frame. We have seen above that $q^2_{\rm max} = (M - m_X)^2$ at zero recoil; the

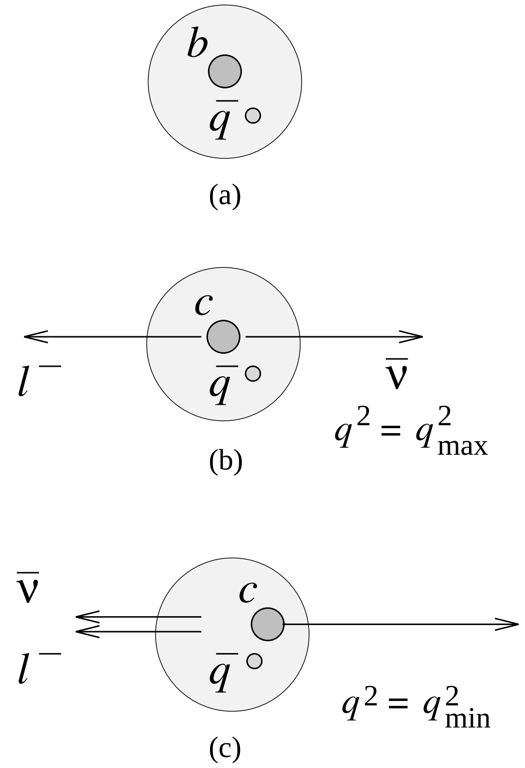

Fig. 26. Kinematic configurations for the semileptonic decay of a B meson: (a) B meson before decay; (b) decay configuration for $q^2 = q^2_{\text{max}}$ (zero recoil), where the form factors are largest for producing a D or D^* meson in the final state; and (c) configuration for $q^2 = q^2_{\text{min}}$, where the form factors are smallest.

W therefore decays into a back-to-back lepton and neutrino, each of which has energy $E \approx \sqrt{q^2}/2$, ignoring the lepton mass.

The minimum value of q^2 (the lightest the $\ell^-\bar{\nu}$ system can be) is $q^2_{\text{min}} = m^2_\ell$, which is zero to a good approximation for electrons or muons. This value occurs whenever the lepton and the neutrino are collinear (Fig. 26c). The recoil energy of the hadronic system, E_X, is maximized when q^2 is minimized (Eq. 7.2), so at q^2_{min}, the hadronic system X recoils fast in the opposite direction. The value of w corresponding to $q^2_{\text{min}} = 0$ is

$$w_{\text{max}} = \frac{M^2 + m_X^2}{2Mm_X}. \tag{7.4}$$

Table 7.2 lists the ranges in q^2 and w for a number of important semileptonic decays. For $\bar{B} \to D\ell^-\bar{\nu}$ and $\bar{B} \to D^*\ell^-\bar{\nu}$ the range is very modest: $\Delta w = 0.5 - 0.6$. For $\bar{B} \to \pi\ell^-\bar{\nu}$, the range is very large, $\Delta w \approx 18$,

Table 10

Ranges of q^2 and w for semileptonic decays of charm and bottom mesons. The variable w is the relativistic factor γ_X for the daughter meson X, as measured in the rest frame of the parent meson. Note that $w_{\max}$ is the γ factor at maximum recoil velocity, which occurs at the mimimum value of q^2, $q^2_{\min} \approx 0$.

Decay	$q^2_{\max} \approx \Delta q^2$ (GeV$^2/c^4$)	$\Delta w = \Delta\gamma = \gamma_{\max} - 1$
$D \to \pi\ell^+\nu$	2.97	5.70
$D \to \bar{K}\ell^+\nu$	1.87	1.01
$D \to \rho\ell^+\nu$	1.20	0.42
$D \to \bar{K}^*\ell^+\nu$	0.94	0.28
$\bar{B} \to \pi\ell^-\bar{\nu}$	26.4	17.9
$\bar{B} \to \rho\ell^-\bar{\nu}$	20.3	2.51
$\bar{B} \to D\ell^-\bar{\nu}$	11.7	0.59
$\bar{B} \to D^*\ell^-\bar{\nu}$	10.7	0.50

and the pion becomes very relativistic. We therefore expect a larger variation of the form factors over phase space for this decay.

For a given lepton energy E_ℓ, the allowed range of q^2 is given by

$$(m_\ell^2 \approx 0) \leq q^2 \leq 2ME_\ell + \frac{2{m_X}^2 E_\ell}{2E_\ell - M}, \tag{7.5}$$

which defines the boundary of the Dalitz plot.

Both q^2 and E_ℓ are experimentally accessible, although it may not be completely obvious how one measures q^2. Broadly speaking, there are two possible approaches. In an exclusive process (where X is a particular hadronic final state), one can measure q^2 by identifying X or its decay products, measuring the energy of X, and transforming the energy to the rest frame of the decaying particle M. Equation 7.2 is then used to compute q^2. The determination of the M rest frame (which is also needed to determine E_ℓ) cannot be taken for granted, because there is an unobserved particle, the neutrino. In fixed-target charm experiments, q^2 is determined only up to a quadratic ambiguity, because the charm-meson direction, but not its energy, is determined by high-resolution tracking detectors. For B mesons produced in the process $\Upsilon(4S) \to B\bar{B}$, the B is produced nearly at rest in the $\Upsilon(4S)$ frame ($\beta\gamma \approx 0.06$). In symmetric-energy e^+e^- machines the $\Upsilon(4S)$ is at rest in the detector frame, while in asymmetric-energy machines there is a boost, as discussed in Sec. 4.

A second approach to measuring q^2 can be used with hermetic detectors. With sufficient care, the missing-momentum vector of an event can, to a good approximation, be associated with the neutrino. Then, q^2 can be calculated from the lepton and neutrino momenta. This approach suffers from poorer resolution, both because particles besides the neutrino, such as K_L's, may not be observed, and because in colliding-beam detectors the component of the missing momentum along the beam direction is not always well measured. Nevertheless, this procedure can work, and in principle it can be applied to inclusive decays, where the X system is not explicitly reconstructed.

Let's now consider qualitatively how the Dalitz plot variables q^2 and E_ℓ are related to the underlying physics of the decay. Distributions of these variables are determined by two effects: the dynamics of the formation of the hadronic system X and the spin structure of the decay. We now analyze these effects, starting with the variable q^2.

To compare the decay dynamics in different regions of q^2, we refer again to Fig. 26. At high q^2, when the lepton and the neutrino are produced nearly back-to-back (Fig. 26b), the daughter meson receives only a very small momentum kick.* For processes in which the daughter-quark mass accounts for most of the meson mass ($\bar{B} \to D^{(*)}\ell^-\bar{\nu}$), the daughter quark itself also receives very little recoil kick at q^2_{max}. A heavy, static source of color field at the center of the meson is replaced by a color source of a different flavor, but the color field is not changed. Relativistic effects, which depend on the mass of the heavy quark, become negligible. For example, the color magnetic moment of the heavy quark is proportional to $1/m_Q$, so only the color "electric" field is important. Thus, the so-called light degrees of freedom—the spectator quark and the gluons—are least disturbed at q^2_{max}. These observations are among the key ideas in HQET, which we will discuss further in the anaysis of exclusive semileptonic decays.

In low-q^2 configurations, the daughter quark q' recoiling against the W receives a large kick and initially moves rapidly with respect to the spectator quark $\bar{q}$. For the daughter and spectator quarks to form a bound state, gluons must be exchanged in order to transfer momentum to the light degrees of freedom of the meson. The larger the recoil, the stronger the suppression resulting from this effect. As a consequence, the $q^2 = 0$ configuration is typically the least favorable for the formation of a meson. (There are, however, important spin-related effects

* This situation contrasts with that in a scattering process, where the minimum kick occurs at $q^2 = 0$. In a scattering process this is, however, still the highest value of q^2, which is either negative or zero.

that can change this conclusion; we will discuss these effects later in this section.) Theoretical calculations are usually difficult at low q^2, because the hadronic system is highly disturbed, and it is at $q^2 = 0$ that one might expect significant production of nonresonant final states to occur, in analogy to QCD jets.

Thus, we have three key observations:

• For processes in which both the initial and final quarks are both heavy compared with the strong interactions that bind the mesons (typified by $\Lambda_{\rm QCD}$), the spectator quark and the gluons are almost completely undisturbed at $q^2 \approx q^2_{\rm max}$. At $q^2_{\rm max}$, calculations of the decay rate for $b \to c\ell^-\bar{\nu}$ have relatively small uncertainties (3% to 5%), while those for $b \to u\ell^-\bar{\nu}$ are still quite difficult.

• Even if the daughter quark is light, the zero-recoil configuration is generally still the most favorable one for the formation of a low-mass meson.

• Decay modes with a large accessible range in q^2 are expected to have a correspondingly large decrease in the amplitude as q^2 decreases from $q^2_{\rm max}$ to $q^2_{\rm min} \approx 0$. This variation of the amplitude with q^2 is parametrized by form factors.

We can see the suppression of the rate as q^2 decreases in Fig. 25: the density of points is highest at the top of the Dalitz plot and becomes significantly smaller toward the bottom. We note, however, that the actual *probability distribution* of q^2 does not peak at $q^2_{\rm max}$ but somewhat below, because at $q^2_{\rm max}$ *the amount of phase space goes to zero.*

We also need to consider the consequences of angular momentum conservation, which directly affect the distributions of both q^2 and E_ℓ. These effects are strongly dependent on the spin of the daughter meson. The first step is to show that the W behaves like a spin-1 particle. From our discussion of helicity conservation in Sec. 6, we know that, due to the $V - A$ coupling, the lepton and neutrino spins point in the same direction in the W frame, in the limit that the lepton has a zero mass. These effects give an angular-momentum projection of $J_z = -1$ along the ℓ^- direction in a $W^- \to \ell^-\bar{\nu}$ decay or $J_z = +1$ along the ℓ^+ direction in a $W^+ \to \ell^+\nu$ decay. Because there is one unit of spin angular momentum along the decay axis, and orbital angular momentum cannot cancel it ($\mathbf{L} = \mathbf{r} \times \mathbf{p}$), the W cannot behave like a spin-0 particle, even though it is virtual. This argument holds in the limit that we can neglect the mass of the charged lepton. More formally, we will see that certain form factors cannot significantly affect the decay unless the charged lepton is heavy, as for $\ell = \tau$. We can therefore imagine that the first step of semileptonic decay is $M \to XW$, where

W is a spin-1 particle.

Now, if both M and X are pseudoscalar particles ($B \to D\ell^-\bar{\nu}$, $B \to \pi\ell^-\bar{\nu}$, $D \to K\ell^-\bar{\nu}$, $D \to \pi\ell^-\bar{\nu}$), then the decay cannot conserve angular momentum unless there is one unit of orbital angular momentum to cancel the spin angular momentum of the W. The decays $D \to KW$ or $B \to DW$ are therefore P-wave processes, whereas $D \to K^*W$ can occur in an S, P, or D-wave. As a consequence, the decay rate when X is a pseudoscalar meson contains a factor $|\mathbf{p}_X|^3$ (one power of $|\mathbf{p}_X|$ from phase space, two more from the amplitude squared).

As can be seen from Eq. 7.2, $|\mathbf{p}_X| = 0$ at $q^2 = q^2_{\rm max}$, so the factor suppresses the rate at high q^2, where the large form factor values would ordinarily lead to a large decay rate. Alternatively, one can easily see that such a decay must be forbidden at $q^2_{\rm max}$, because the back-to-back lepton-neutrino system has one unit of angular momentum along its line of flight, and this angular momentum cannot be cancelled by the daughter pseudoscalar meson. In terms of w, we have

$$|\mathbf{p}_X| = m_X\sqrt{w^2-1}, \tag{7.6}$$

so that the $|\mathbf{p}_X|^3$ factor greatly increases the probability for large values of w. If Fig. 25 were made for $\bar{B} \to D\ell^-\bar{\nu}$ rather than for $\bar{B} \to D^*\ell^-\bar{\nu}$, the density of points in the upper region would be significantly reduced. The dramatic result of the P-wave decay can be seen in the CLEO II data for $B \to D\ell^-\bar{\nu}$. Figure 27a shows the strong suppression of the decay rate for small D momenta resulting from the $\mathbf{p}_D^3$ factor. Figure 27b shows the behavior of the decay *amplitude* as a function of w, after the P-wave and phase space factors are divided out. The modest increase in the rate towards small w are due to the form factor, which describes the nonperturbative QCD effects discussed in connection with Fig. 26. In this decay, the form factor effects are nearly overwhelmed by effects of angular momentum conservation.

Finally, we note that the q^2 distribution will be different if the final-state meson has orbital excitation; under such circumstances the typical value of q^2 can be pushed significantly lower.

Having discussed the physics that controls the q^2 distribution, we turn now to the factors that influence the distribution of E_ℓ. We can see directly from the Dalitz-plot boundary in Fig. 25 that if phase space were populated uniformly, the lepton-energy spectrum would be peaked toward the high end. However, the lepton-energy spectrum is strongly affected by three aspects of the dynamics: (1) the $V-A$ coupling, (2) the quantum numbers of the particle X, and (3) the distribution in q^2. We now consider each of these in turn.

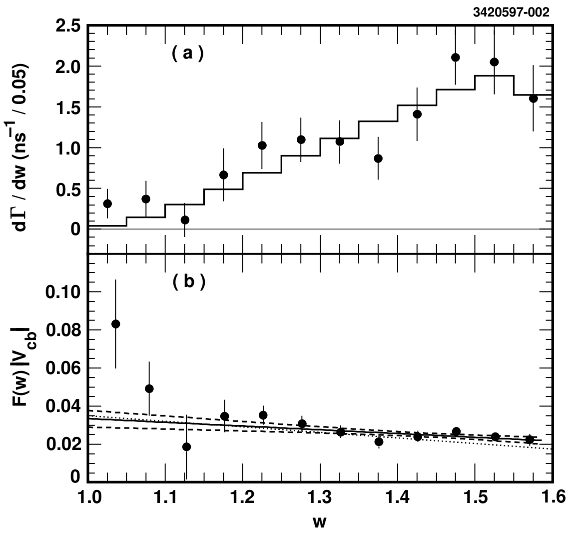

Fig. 27. CLEO II analysis of $B \to D\ell^-\bar{\nu}$: (a) the distribution of the rate $d\Gamma/dw$ of $w = E_D/m_D$, which ranges from 1 (zero recoil) to about 1.6 (maximum recoil). The points with error bars are the background-subtracted, efficiency-corrected data, and the histogram is the best fit assuming a linear dependence of the form factor on w. The P-wave nature of the decay suppresses the rate at low recoil. (b) the w dependence of the *amplitude* after the P-wave dependence has been divided out; the remaining w dependence is due to the form factor, which favors decay configurations at low values of w (high q^2). The solid line is the best fit; the dashed lines show the slopes allowed within the statistical errors on the fit. The dotted line is the superimposed curve from the corresponding fit in the $\bar{B} \to D^*\ell^-\bar{\nu}$ analysis.

A direct consequence of the $V - A$ coupling is that the charged lepton and the neutrino share the available energy differently for charm and bottom decays. The processes $b \to c\ell^-\bar{\nu}$ and $b \to u\ell^-\bar{\nu}$ produce c- and u-quarks that are predominantly helicity $\lambda = -1/2$ in association with a charged lepton that is almost purely helicity $\lambda = -1/2$. The decays $c \to s\ell^+\nu$ and $c \to d\ell^+\nu$ also produce predominantly $\lambda = -1/2$ s- and d-quarks, but they are in association with a charged lepton that is almost purely $\lambda = +1/2$. As a result, the collinear configuration in which the charged lepton recoils against the daughter quark and the neutrino—the configuration leading to the highest lepton energy—is allowed for b-quark decays but forbidden by angular momentum conservation for c-quark decays. Thus, in the case of b (or $\bar{b}$) decay, the lepton-energy spectrum peaks at a higher energy than the neutrino spectrum; the reverse is true for c decays.

The argument we have given ignores the quantum numbers of the meson X, but these are quite important in determining the lepton-energy spectrum in an exclusive decay. In particular, the $V - A$ effect described above is important when X is a spin-1 particle but is masked when X has spin 0. These effects are best understood by relating, via a Lorentz transformation, the distribution of E_ℓ (in the rest frame of the parent meson, M) to the angular distribution of the charged lepton in the W rest frame. We define the angle θ_ℓ (Fig. 28) as the polar

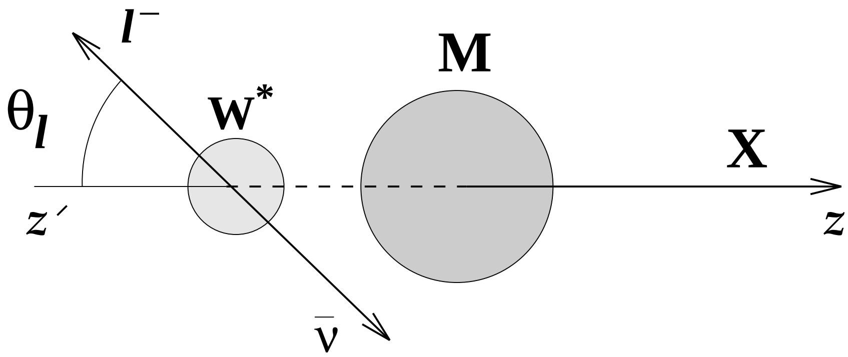

Fig. 28. The polar angle θ_ℓ is defined in the rest frame of the virtual W (denoted here as W^*), in which the charged lepton and the neutrino are back-to-back. The angle is measured with respect to the axis z' pointed opposite to the momentum vector of X, the daughter meson. Due to the Lorentz boost between the W and M rest frames, leptons with small values of θ_ℓ have higher energy in the M rest frame than leptons with large values of θ_ℓ, at fixed q^2.

angle of the lepton in the W rest frame, with respect to the direction of the W momentum vector in the M rest frame. (In the M rest frame, $\mathbf{p}_W = -\mathbf{p}_X$.) Ignoring the charged-lepton mass, its energy in the W rest frame is simply $E_\ell^{[W]} = \frac{1}{2}\sqrt{q^2}$. However, leptons going forward (along $\mathbf{p}_W$) in the W rest frame are given a higher energy in the M rest frame, due to the boost, than those going backward. From the Lorentz transformation to the M rest frame,

$$E_\ell = \frac{1}{2}[(E_\ell^{\max} + E_\ell^{\min}) + (E_\ell^{\max} - E_\ell^{\min}) \cos\theta_\ell], \tag{7.7}$$

where

$$E_\ell^{\max,\min} = \frac{1}{2M}\left[\frac{1}{2}(M^2 + q^2 - m_X^2) \pm M|\mathbf{p}_X|\right] \tag{7.8}$$

and

$$|\mathbf{p}_X| = \sqrt{\frac{(M^2 - q^2 + m_X{}^2)^2}{4M^2} - m_X{}^2}. \tag{7.9}$$

As q^2 increases, the lepton energy tends to increase as well, because

$$\frac{1}{2}(E_\ell^{\max} + E_\ell^{\min}) = \frac{(M^2 + q^2 - m_X{}^2)}{4M}. \tag{7.10}$$

The range of lepton energies observed in the M rest frame, however, decreases as q^2 increases, because $(E_\ell^{\max} - E_\ell^{\min}) = |\mathbf{p}_X| = |\mathbf{p}_W|$ decreases as the boost becomes smaller. (The width of the Dalitz plot at a fixed q^2 is just the two-body phase space factor for $B \to XW(q^2)$.) At $q^2 = q^2_{\max}$, the W and the X system are each at rest in the M rest frame and E_ℓ is the same for all angles θ_ℓ. Both of these features—the increase in $\frac{1}{2}(E_\ell^{\max} + E_\ell^{\min})$ with q^2 and the diminishing range in lepton energies—are simply phase space effects and can be seen directly from the shape of the Dalitz-plot boundary in Fig. 25.

It is clear that to predict the observed lepton-energy spectrum, one must understand the physics underlying the distribution of $\cos\theta_\ell$. I will digress to show how easy it is to calculate angular distributions for two-body decays; we will then apply the results to the process $W \to \ell^- \bar{\nu}$. Consider the decay $A_{J,M} \to B_{\lambda_B} C_{\lambda_C}$, where J is the spin of A, M is its spin projection along an arbitrary z axis, and λ_B and λ_C are the helicities of B and C, respectively. We consider final states in which B and C have definite (and opposite) linear momenta, which we specify in the rest frame of A, as well as the definite helicities λ_B and λ_C. In the helicity formalism [50,51], such states are called two-particle plane-wave helicity states. The amplitude for this process is

$$\mathcal{M} = \langle \mathbf{p}_B = \mathbf{p}_f, \lambda_B; \mathbf{p}_C = -\mathbf{p}_f, \lambda_C | U | A_{J,M} \rangle, \tag{7.11}$$

where the operator U is the operator that propagates the initial state though the interaction to the final-state particles. Because particles B and C have equal and opposite momenta in the rest frame of A, we can characterize the final state by the direction $\hat{n}(\theta,\phi)$ of the decay axis with respect to the z-axis (spin-quantization axis of A), by the magnitude of either particle's momentum, and by the helicities λ_B and λ_C. Thus (suppressing $|\mathbf{p}_f|$ because it is fixed)

$$\mathcal{M} = \langle \theta, \phi, \lambda_B, \lambda_C | U | A_{J,M} \rangle. \tag{7.12}$$

The probability distribution $dN/d\cos\theta d\phi$ is proportional to $|\mathcal{M}|^2$. It is important to plot angular distributions as a function of $\cos\theta$ and ϕ rather than θ and ϕ since phase space is proportional to $d\Omega = d\cos\theta d\phi$. The use of θ will not give a wrong answer, but it will introduce a physically meaningless Jacobian that will make the plots more difficult to interpret.

The key idea of the helicity formalism is that rotational invariance of the helicities ($\lambda = \mathbf{s} \cdot \mathbf{p}$) allows one to define a set of two-particle basis states $|j, m, \lambda_B, \lambda_C\rangle$ that have definite total angular momentum j, angular momentum projection m, and helicities λ_B and λ_C. We can then exploit conservation of angular momentum by inserting a complete set of these states into Eq. 7.12:

$$\begin{aligned}
\mathcal{M} &= \sum_{j,m} \langle \theta, \phi, \lambda_B, \lambda_C | j, m, \lambda_B, \lambda_C \rangle \langle j, m, \lambda_B, \lambda_C | U | A_{J,M} \rangle \\
&= \sum_{j,m} \langle \theta, \phi, \lambda_B, \lambda_C | j, m, \lambda_B, \lambda_C \rangle \delta_{jJ} \delta_{mM} A_{\lambda_B \lambda_C} \\
&= \langle \theta, \phi, \lambda_B, \lambda_C | J, M, \lambda_B, \lambda_C \rangle A_{\lambda_B \lambda_C} \\
&= \text{constant} \times D^{J*}_{M,\Delta\lambda}(\phi, \theta, -\phi) A_{\lambda_B \lambda_C}, \qquad (7.13)
\end{aligned}$$

where $\Delta\lambda = \lambda_B - \lambda_C$, and $D^{J*}_{M,\lambda}(\phi, \theta, -\phi)$ are the rotation operators

$$D^{J*}_{M,\Delta\lambda}(\phi, \theta, -\phi) = e^{i(M-\Delta\lambda)\phi} d^J_{M,\Delta\lambda}(\theta). \qquad (7.14)$$

The angle θ is the polar angle of $\mathbf{p}_B$ with respect to the spin quantization axis of A; ϕ is the azimuthal angle about this axis. The so-called helicity amplitudes $A_{\lambda_B \lambda_C}$ can be different for each set of possible helicities, but they contain no angular dependence. The last step in the derivation is where most of the work is; the original derivation is in the paper by Jacob and Wick. All of the ϕ dependence is contained in phase factors, which, for a single non-sequential two-body decay, disappear when the square of the amplitude is computed. (If the helicities are specified in the final state, there is no coherence between their amplitudes.) The functions $d^J_{m_1,m_2}(\theta)$ are listed in a table of the Particle Data Book on the same page as the Clebsch-Gordon coefficients. A useful identity is $d^j_{m',m}(\theta) = (-1)^{m-m'} d^j_{m,m'}(\theta) = d^j_{-m,-m'}(\theta)$.

We will need the following d-functions:

$$\begin{aligned}
d^1_{-1,-1}(\theta) &= \frac{(1+\cos\theta)}{2} \qquad d^1_{1,-1}(\theta) = \frac{(1-\cos\theta)}{2} \\
d^1_{0,-1}(\theta) &= \frac{-\sin\theta}{\sqrt{2}}. \qquad (7.15)
\end{aligned}$$

Let's apply these results to semileptonic decay. To do this, we need to specify the quantization axis for the spin of the W. (The W corresponds to the parent particle A in the discussion above.) This axis is taken to be the momentum direction of the W in the B rest frame or, equivalently, the direction opposite to that of the daughter hadron. The quantum number M in the formulas above then corresponds to the helicity of the W, and the polar angle of the lepton, θ_ℓ, is measured in the W frame with respect to the direction of the W momentum in the B frame.

The $dN/d\cos\theta_\ell$ distribution is connected to both the $V-A$ couplings and to the quantum numbers of X. In b- or c-quark semileptonic decay, the daughter-quark helicity is predominantly $\lambda = -1/2$. If this quark combines with the spectator quark to form a pseudoscalar meson, as in $\bar{B} \to D\ell^-\bar{\nu}$, $\bar{B} \to \pi\ell^-\bar{\nu}$, or $D \to \bar{K}\ell^+\nu$, the helicity information is lost, since the helicity of the meson must be zero. Because the initial meson has spin zero, angular momentum conservation along the decay axis forces the W to have helicity zero as well. This means that $M = 0$ in Eq. 7.13. The helicity difference for the $\ell^-\bar{\nu}$ system is $\Delta\lambda = \lambda_\ell - \lambda_{\bar{\nu}} = -1$. We therefore use $d^1_{0,-1}(\theta)$, which gives

$$\frac{dN}{d\cos\theta_\ell} \propto \sin^2\theta_\ell. \tag{7.16}$$

This result is model independent and holds for all values of q^2. If you think you have discovered a new signal of the form $P \to P'\ell^-\bar{\nu}$, where P and P' are pseudoscalars, it is always a good idea to check the angular distribution of the lepton in the W rest frame!

If, however, the daughter quark and the spectator form a spin-1 meson, as in $D \to \bar{K}^*\ell^+\nu$, $\bar{B} \to D^*\ell^-\bar{\nu}$, or $\bar{B} \to \rho\ell^-\bar{\nu}$, then the helicity information of the daughter quark is not lost. It is manifested as a higher probability for the vector meson to have helicity $\lambda = -1$ than $\lambda = +1$. Roughly speaking, a rapidly recoiling $\lambda = -1/2$ daughter quark can combine with the spectator quark to form a $\lambda = -1$ or $\lambda = 0$ meson, as shown in Fig. 29. (This description is not appropriate when the daughter quark is nonrelativistic, or when the W is massless, as discussed below.) The probabilities for different vector-meson helicities also apply to the W, because to conserve angular momentum along the decay axis, the helicities of the W and the vector meson must be the same.

The predominance of $\lambda_W = -1$ over $\lambda_W = +1$ affects the lepton spectrum differently for $\bar{B}$ and D decays. In $\bar{B}$ decay, the process $W^- \to \ell^-\bar{\nu}$ produces a $\lambda = -1/2$ charged lepton and a $\lambda = 1/2$ antineutrino. For $\lambda_W = -1$ the angular distribution of the lepton is

$$dN/d\cos\theta_\ell \propto |d^1_{-1,-1}(\theta_\ell)|^2 \propto (1+\cos\theta_\ell)^2, \tag{7.17}$$

so the leptons tend to go forward in the W frame and are boosted to higher energy in the $\bar{B}$ frame. For $\lambda_W = +1$ the angular distribution

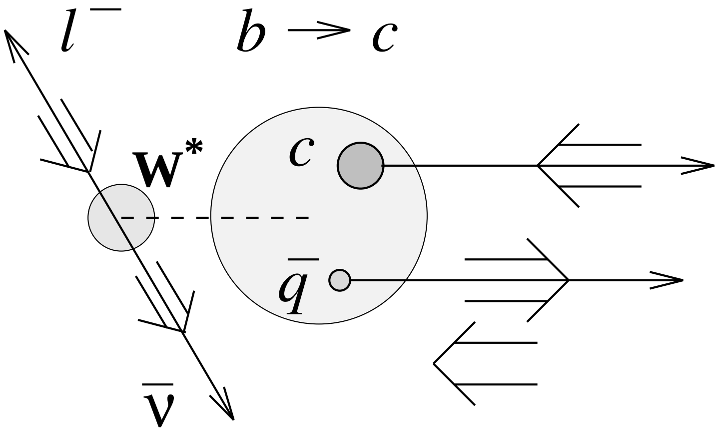

Fig. 29. In B semileptonic decay, the $V-A$ coupling at the $b \to c$ (or $b \to u$) vertex produces a c quark that is predominantly helicity $\lambda = -1/2$. In the simple model shown here, the helicity of the meson X is then determined by whether the c quark combines with a spectator quark that has $\lambda = +1/2$ or $\lambda = -1/2$. If X is a spin-zero meson, only $\lambda = 1/2$ spectator quarks can contribute. If X has spin 1, both helicities of the spectator quark contribute, leading to X helicities of $\lambda = 0$ and $\lambda = -1$, but not $\lambda = +1$. It is easy to see that this $V-A$ effect, combined with overall angular momentum conservation, results in a harder energy spectrum for the charged lepton than for the neutrino, as observed in the rest frame of M.

is

$$dN/d\cos\theta_\ell \propto |d^1_{+1,-1}(\theta_\ell)|^2 \propto (1-\cos\theta_\ell)^2, \tag{7.18}$$

so the leptons tend to go backwards in the W frame and are boosted to lower energy in the $\bar{B}$ frame. Since $\lambda_W = -1$ tends to predominate over $\lambda_W = +1$ in $\bar{B}$ decays to a spin-1 particle (D^*, ρ), the lepton spectrum is harder than the neutrino spectrum. If we switched from a $\bar{B}$ to a B, the helicities of both the daughter quark and the charged lepton would reverse, and the angular distribution would be the same.

For D decay, the $c \to s$ or $c \to d$ transition again produces a hadron with more $\lambda = -1$ than $\lambda = +1$, but the lepton is positively charged and has $\lambda = +1/2$. Again, to conserve angular momentum, the W spin projection must cancel that of the daughter hadron, so it has more $\lambda = -1$ than $\lambda = +1$. Since the $W^+ \to \ell^+\nu$ decay produces a $\lambda = +1/2$ charged lepton and $\lambda = -1/2$ neutrino, the lepton angular distribution for $\lambda_W = -1$ is

$$dN/d\cos\theta_\ell \propto |d^1_{-1,+1}(\theta_\ell)|^2 \propto (1-\cos\theta_\ell)^2 \tag{7.19}$$

which leads to a softer boosted energy spectrum for the lepton than the neutrino.

Finally, the lepton-energy spectrum is affected by the q^2 distribution. If q^2 is forced to be high by the behavior of the form factors, E_ℓ will also tend to be large (see Eq. 7.10). Conversely, in decays in which X is a spin-0 particle, the P-wave effect suppresses high q^2-decays, softening the lepton-energy spectrum.

The simplified arguments we have made do not hold at $q^2 = q^2_{\text{max}}$ or at $q^2 = 0$. At q^2_{max}, the daughter vector meson is at rest. Its helicity is therefore undefined, and both the vector meson and the W are unpolarized. As a result, the $\cos\theta_\ell$ distribution becomes uniform at high q^2. At small values of q^2, the lepton and neutrino become parallel in the M rest frame, and their combined spin projection along their direction of motion is zero. The helicity ± 1 components are absent, and there is no lepton forward-backward asymmetry in the W frame. The helicity of the vector meson must also be zero in this configuration.

We now summarize our understanding of the Dalitz plot for $\bar{B} \to D^* \ell^- \bar{\nu}$ in Fig. 25. It is useful to refer also to Fig. 30, which shows the contributions to the rate from the different helicities as a function of w. Near the top of the Dalitz plot, where q^2 is large, the D^* is moving very slowly and is nearly unpolarized: $\lambda = -1$, 0, and $+1$ are present in approximately equal amounts. The distribution of $\cos\theta_\ell$ is then uniform because the W is also unpolarized. The form factors are largest in this region, accounting for the high density of points. As q^2 decreases, the $\lambda = -1$ component of the D^* begins to dominate over the $\lambda = +1$ component, which explains the excess of points on the right side of the Dalitz plot compared with the left side. At the lowest value of q^2, the charged lepton and the neutrino are parallel in the lab frame, leading to maximum D^* recoil, and both the D^* and W are forced into a pure $\lambda = 0$ state. There is no asymmetry in the $\cos\theta_\ell$ distribution at $q^2 = 0$: its distribution at this edge of phase space is $dN/d\cos\theta_\ell \propto \sin^2\theta_\ell$. This effect can be seen in Fig. 25 in the depletion of points at high and low lepton energies for small values of q^2.

7.3. Heavy quark effective theory and semileptonic decays

In the last few years, a new theoretical approach known as heavy quark effective theory (HQET) has emerged for analyzing so-called heavy-light mesons (mesons containing one heavy and one light quark), as well as baryons containing a heavy quark and two light quarks. Many authors have contributed to the development of HQET, whose history

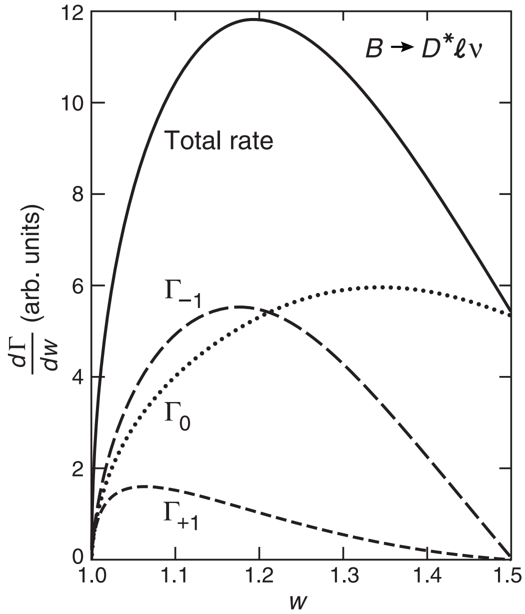

Fig. 30. Contributions to the rate in $B \to D^* \ell^- \bar{\nu}$ from different D^* (or W) helicities. The zero recoil configuration is at $w = 1$ ($q^2_{\rm max}$), while maximum recoil occurs at $w \approx 1.5$ ($q^2 \approx 0$). At intermediate values of w, the $V - A$ coupling produces more rate into the $\lambda = -1$ state than into $\lambda = +1$.

is traced in the extensive review by Neubert [36]. A number of the separate ideas underlying HQET emerged over a long period and can be found in the papers of, among others, Shuryak [52], Nussinov and Wetzel [53], and Voloshin and Shifman [54,55]. Two papers by Isgur and Wise [56,57] played a major role in synthesizing and extending this development, and they are among the most frequently cited papers in particle physics over the last few years. This work led to a rapid expansion in the study of HQET; among the key papers are those of Eichten and Hill [58,59], Falk *et al.* [60], Grinstein [61], and Georgi [62]. Many reviews of this subject are also available, such as those by Wise [63–65], Bigi, Shifman, and Uraltsev [66], Grinstein [67], Mannel [68,69], and Neubert [36,70]. If you perform a literature search using SPIRES (http://www-spires.slac.stanford.edu/FIND/hep) or with the Los Alamos preprint server (http://xxx.lanl.gov/) you will be rewarded with an avalanche of papers by these and many other authors.

A simple argument [71] indicates that within a hadron containing a heavy quark, the heavy quark moves nonrelativistically. The momentum of the heavy quark, $\mathbf{p}_{\rm Q}$, must balance that of the light constituents of the hadron, $\mathbf{p}_{\text{light}}$:

$$|\mathbf{p}_{\text{Q}}| = |\mathbf{p}_{\text{light}}| \sim \Lambda_{\text{had}} \sim \Lambda_{\text{QCD}}, \tag{7.20}$$

where $\Lambda_{\text{had}} \sim 0.2 - 0.3$ GeV is a typical hadronic interaction scale. In the proton, for example, we have $\Lambda_{\text{had}} \approx m_P/3 \approx 330$ MeV. In heavy-light hadrons, the typical momentum transfer between the light constituents and the heavy quark is Λ_{had}, but the associated *velocity transfer* to the heavy quark is very small:

$$|\mathbf{v}_{\text{Q}}| = \frac{|\mathbf{p}_{\text{Q}}|}{m_{\text{Q}}} \sim \frac{\Lambda_{\text{had}}}{m_{\text{Q}}}, \tag{7.21}$$

so that in the limit $m_{\text{Q}} \gg \Lambda_{\text{had}}$, the heavy quark behaves essentially as a stationary source of a color field. The velocity of the hadron and the heavy-quark become the same. Furthermore, the heavy quark's spin, which interacts with the system through a color magnetic moment proportional to $1/m_{\text{Q}}$, also decouples from the dynamics in this limit.

In the heavy-quark limit, the actual value of the mass of the heavy quark therefore becomes irrelevant. The configuration of the light constituents of a heavy-light hadron is not affected by the replacement of a heavy quark $Q(v_Q, s)$ with another heavy quark $Q'(v_Q, s')$, where the heavy quarks have the same four-velocity v_Q but different flavors Q and Q' and different spins s and s'. Thus, instead of describing the form-factor variation of the semileptonic decay $M \to X\ell^-\bar{\nu}$ in terms of the square of the four-momentum transfer, q^2, HQET calculations use the square of the four-velocity transfer, $(v - v')^2 = 2(1 - v \cdot v')$, where v and v' are the four velocities (p_μ/m) of the initial and final hadrons.

We have already seen that, in the rest frame of the initial hadron, $v \cdot v'$ has a simple physical interpretation:

$$v \cdot v' = \gamma_X = \frac{1}{\sqrt{1 - \beta_X^2}}, \tag{7.22}$$

where β_X is the velocity of the final state hadron (Eq. 7.3) The quantity $v \cdot v'$, which is often called w or y in the literature, is dimensionless and ranges from $\gamma_X = 1$ at minimum recoil to the maximum value $(M^2 + m_X^2)/(2Mm_X)$. It is linearly related to q^2 by

$$w \equiv v \cdot v' = \frac{M^2 + {m_X}^2 - q^2}{2Mm_X} \tag{7.23}$$

or

$$v \cdot v' - 1 = \frac{q^2_{\text{max}} - q^2}{2Mm_X}. \tag{7.24}$$

Since the typical mass scale for the light constituents within the hadron is $\Lambda_{\rm had}$, the square of the four-momentum transferred to these constituents during the decay must be $\sim \Lambda_{\rm had}^2(v-v')^2$, independent of the heavy quark mass.

The heavy-quark symmetry limit provides a good description of a real physical system if the light constituents have sufficiently small momenta that they cannot probe distance scales of the order $1/m_Q$. Since the momentum transfer to the light constituents has the typical scale $\Lambda_{\rm had}(v\cdot v'-1)$, this condition is equivalent to the statement $(v\cdot v'-1) \ll m_Q/\Lambda_{\rm had}$. If this condition is violated in a certain region of phase space, then the quark under consideration cannot be regarded as heavy.

In practice, the heavy-quark symmetry limit is the starting point for an expansion in the general framework of HQET. In HQET, the properties and decays of hadrons containing a heavy quark are analyzed in terms of a systematic expansion in the variable E/m_Q, where E can be due to a number of QCD effects such as the kinetic energy of the heavy quark or the chromomagnetic interaction energy. (At each order in $1/m_Q$, there is an associated perturbative expansion in the strong coupling constant α_s.) In contrast to calculations based on hadron models, the HQET expansion is derived directly from the fundamental theory of QCD. Although the terms in the expansion can be difficult to evaluate, the systematic and rigorous nature of HQET means that uncertainties are easier to identify and estimate than those for calculations based on hadron models.

For the expansion to be useful, the higher-order terms must be small, at least in the regions of phase space of interest. The decays best suited to treatment using HQET involve $b\to c\ell^-\bar\nu$ transitions, since both the initial- and final-state hadrons contain a heavy quark. Examples of such decays are $\bar B\to D\ell^-\bar\nu$, $\bar B\to D^*\ell^-\bar\nu$, and $\Lambda_b\to\Lambda_c\ell^-\bar\nu$. Note that compared with $\Lambda_{\rm had}$, the strange quark cannot be regarded as heavy, since $m_s\simeq 0.3\ \mathrm{GeV}/c^2$. Thus, HQET is not applicable to charm semileptonic decays.

7.4. Inclusive semileptonic decay and $|V_{cb}|$

In the inclusive approach to semileptonic decays, one considers the sum over all possible final-state hadrons, ignoring the detailed breakdown among the individual decay modes that contribute to the semileptonic rate. Experimentally, it is necessary to observe only the lepton, eliminating the difficulty of reconstructing what are often very complex decay sequences of the daughter hadrons. Theoretical calculations of inclusive properties have certain advantages of simplicity as well, since calculations in which the heavy quark is assumed to decay as a free particle (with the light quark acting merely as a spectator) provide a good starting point for predictions. Recently, there has been great interest in refining calculations for b-hadron semileptonic decays using heavy-quark expansions. It has been shown that spectator-model predictions correspond to the lowest-order term in such expansions [72,73].

The inclusive semileptonic branching fraction is defined by

$$\mathcal{B}_{\rm SL} = \frac{\sum_X \Gamma(M \to X\ell^-\bar{\nu})}{\Gamma(M \to \text{all})}, \tag{7.25}$$

where ℓ is either an electron or a muon, but not both. For precise measurements, it may be necessary to correct for the slightly smaller phase space available in the muon mode or for radiative effects, which are larger in the electron mode. Because the τ-lepton mass is large, the case $\ell = \tau$ is treated separately. Often, the branching fraction measured by experiments is an average over more than one species of heavy hadron, M, because measurements of the lepton alone are not sufficient to distinguish between different types of hadrons carrying the same heavy quark.

Inclusive measurements of leptons can provide a remarkable amount of information:

- $\mathcal{B}_{\rm SL}$ can be used to determine what fraction of the semileptonic rate can be accounted for by known exclusive channels and thus help to determine whether there are additional exclusive modes to be discovered.
- An important application of $\mathcal{B}_{\rm SL}$ is that it can be used to compute the total semileptonic decay width: $\Gamma_{\rm SL} = \mathcal{B}_{\rm SL}/\tau_M$, where τ_M is the measured lifetime of the hadron M. In B decays, one can compare the inclusive semileptonic decay width to theoretical calculations to determine $|V_{cb}|$. The measurement of $|V_{cb}|$ using this method has attracted much interest, because $\mathcal{B}_{\rm SL}$ and τ_B have been measured with very good precision, and theorists believe that the theoretical uncertainties can also be made very small.
- The lepton-energy spectrum contains important information about which modes contribute. For example, the lepton-energy spectrum from the set of decays $B \to X_u\ell^-\bar{\nu}$, where X_u is a non-charm hadron, extends to a higher energy than the spectrum from decays $B \to X_c\ell^-\bar{\nu}$, where X_c is a charm hadron. One can therefore measure the semileptonic rate in the endpoint region of the lepton-energy spectrum to measure $|V_{ub}|$.

• In B decays it is of interest to know if there are any large unexpected contributions to the hadronic rate, for example, from gluonic penguin processes. We can use $\mathcal{B}_{\rm SL}$ to calculate the ratio between the hadronic rate and the semileptonic rate. Since the semileptonic rate can be calculated with good precision, $\mathcal{B}_{\rm SL}$ effectively provides a constraint on the hadronic rate.
• Separate measurements of $\mathcal{B}_{\rm SL}$ for $Q\bar{u}$ and $Q\bar{d}$ mesons allow one to extract the ratio of the lifetimes of the charged and neutral mesons. For example, in D-meson decays,

$$\begin{aligned}\frac{\tau_+}{\tau_0} &= \frac{\Gamma(D^0 \to \text{all})}{\Gamma(D^+ \to \text{all})} = \frac{\Gamma(D^0 \to \text{all})}{\Gamma(D^0 \to X\ell^+\nu)} \frac{\Gamma(D^+ \to X\ell^+\nu)}{\Gamma(D^+ \to \text{all})} \\ &= \mathcal{B}^+_{\rm SL}/\mathcal{B}^0_{\rm SL}, \end{aligned} \tag{7.26}$$

where we have assumed that the charged and neutral D-mesons have the same semileptonic partial widths. This assumption is expected to be very good, since the two mesons differ only in the isospin of the light quark. (There will be a very small difference because, for example, $\Gamma(D^+ \to (\pi^0 + \eta + \eta')\ell^+\nu)$ is not exactly the same as $\Gamma(D^0 \to \pi^-\ell^+\nu)$.)
• Decays to leptons are also used simply as a means to determine the flavor of the decaying heavy quark. In measurements of CP violation and mixing, one uses the fact that $b \to \ell^-$ while $\bar{b} \to \ell^+$.

In b-hadron decay, the challenge for inclusive measurements is to determine what part of the observed lepton-momentum spectrum is due to leptons from b decay (primary leptons) and what part is due to leptons from charm decay (secondary leptons) or other sources (misidentified hadrons, photon conversions, J/ψ decays, etc.). A standard technique (which has now been surpassed) is to fit the observed lepton-momentum spectrum to a sum of the shapes expected for primary and secondary decays, after subtracting backgrounds from other sources. Thus, a large part of the effort (and uncertainty) in the analysis is in the determination of these shapes.

Figure 31 shows the electron and muon data from CLEO II [1,74,75], which has the largest event sample. The muon spectrum cuts off below 1.3 GeV/c due to the iron absorber in front of the muon detectors, but the electron spectrum is measured down to 0.6 GeV/c. Backgrounds from continuum processes, $\psi \to \ell^+\ell^-$, photon conversions, π^0 Dalitz decays, and $B \to X\tau^-\bar{\nu}_\tau$ decays have been subtracted. The electron spectrum has been radiatively corrected according to the prescription of Atwood and Marciano [76], so the electron and muon data can be directly compared.

It is clear from Fig. 31 that it is not trivial to extract the contribution

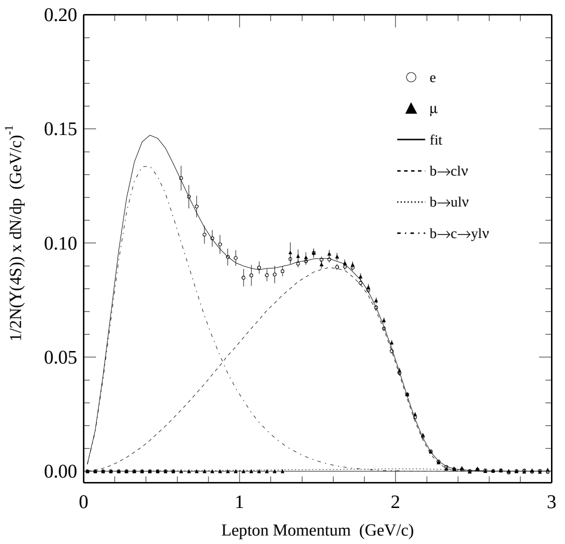

Fig. 31. CLEO II inclusive single-lepton analysis. Although the spectrum can be measured extremely well, the difficulty is to extract the contributions from primary (dashed curve) and secondary (dot-dashed curve) leptons. The uncertainty in the shapes of these spectra produces the dominant systematic error in the measurement. In the fit shown above, the shape of the primary-lepton spectrum is obtained from the ACCMM inclusive model. An alternative method using dileptons avoids this problem.

to the spectrum from semileptonic B decays. In fact, the main limitation of using the inclusive single-lepton spectrum to measure $\mathcal{B}_{\rm SL}$ is that it is necessary to fit the spectrum to shapes that describe the contributions from primary ($b \to \ell^-$ and charge conjugate) and secondary ($b \to c \to \ell^+$ and charge conjugate) contributions. The primary lepton spectrum is usually described by models, and the uncertainty in the predicted shapes produces the dominant uncertainty in the measurement. For this reason, we turn to an alternative measurement technique for measuring $\mathcal{B}_{\rm SL}$.

The ARGUS collaboration [77] introduced a method, based on charge correlations in dilepton events, that allows one to separate the contributions of primary and secondary leptons without relying on model-dependent shapes. This technique, which has now been used by CLEO [78] as well, substantially reduces the need for models in the determination of $\mathcal{B}_{\rm SL}$.

The first step is to require that one lepton (the "tagging lepton") have high momentum, so that it must nearly always be primary. For example, with $p_\ell > 1.4$ GeV$/c$, only about 2.8% of these leptons are secondary. The lepton spectrum extracted is that for the other lepton in the event, for which no such cut is applied.

Assuming that the tagging lepton is always primary (a small correction for secondary tags must be made), there are three possibilities for the other lepton. These possibilities and the corresponding lepton charge correlations are, assuming no $B^0\bar{B}^0$ mixing,

- the other lepton is primary and is produced in the decay of the other B meson, resulting in opposite-sign leptons ($\ell^+\ell^-$);
- the other lepton is secondary and is produced in the decay chain of the other B meson, resulting in same-sign leptons ($\ell^+\ell^+$ or $\ell^-\ell^-$); or
- the other lepton is secondary and is produced in the decay chain of the same B meson in the event, resulting in opposite-sign leptons ($\ell^+\ell^-$).

Thus, if one can eliminate events corresponding to the third scenario, then a lepton with charge opposite to that of the tag must be primary, whereas a lepton with the same charge as the tag must be secondary. This discussion ignores mixing, but the $B^0\bar{B}^0$ mixing rate is well measured, and it is not difficult to correct for this effect.

If primary and secondary leptons are from the decay chain of the same B meson (the third case listed above), there is a strong angular correlation, resulting from momentum conservation, such that they tend to be in opposite hemispheres. In contrast, leptons from different B mesons have uncorrelated angular distributions, since the two B's are produced essentially at rest relative to each other. By requiring both leptons to be in the *same* hemisphere, events in which the two leptons come from the decay chain of a single B meson are effectively removed.

With these analysis cuts, a lepton whose charge is opposite to that of the tagging lepton must be primary, while one with the same charge as the tagging lepton must be secondary (up to the mixing correction). One can therefore separately measure the number of primary and secondary leptons in each momentum bin. Figure 32 shows the primary and secondary electron-momentum spectra obtained from the CLEO II analysis. There is a lower cutoff in the electron identification efficiency, however, and a small extrapolation, based on models, is required to obtain the total semileptonic rate. In the CLEO II measurement, the minimum momentum in the measurement is 0.6 GeV/c, and the measured branching fraction above this cutoff is model independent, giving $B(\bar{B} \to X\ell^-\bar{\nu}, p > 0.6\ \mathrm{GeV}/c) = (9.85 \pm 0.16 \pm 0.40)\%$. The extrapolation to zero momentum amounts to only $(6.1 \pm 0.5)\%$ of the semileptonic rate. The central value of this extrapolation fraction is based on the average of the ACCMM and the ISGW** predictions and the error is based on the difference between these two models.

Table 11

Measurements of the inclusive semileptonic branching fraction. The CLEO II and ARGUS measurements are averaged over the $\bar{B}^0$ and B^-, while the LEP measurements are averaged over the b hadrons produced in $Z \to b\bar{b}$. Full references to these measurements are given in Ref. [2].

Experiment	$\mathcal{B}(b \to q\ell^-\bar{\nu})$ (%)
ARGUS	$9.7 \pm 0.5 \pm 0.4$
CLEO II	$10.49 \pm 0.17 \pm 0.43$
$\Upsilon(4S)$ avg.	10.23 ± 0.39
ALEPH	$11.01 \pm 0.23 \pm 0.28 \pm 0.11$
DELPHI	$11.06 \pm 0.39 \pm 0.19 \pm 0.12$
L3	$10.85 \pm 0.12 \pm 0.43$
OPAL	$10.5 \pm 0.6 \pm 0.4 \pm 0.3$
Z avg.	$10.95 \pm 0.13 \pm 0.29$

The ISGW** is a modified version of the ISGW model in which the $B \to D^{**}\ell^-\bar{\nu}$ branching fraction is allowed to float.

Table 11 lists the values of $\mathcal{B}_{\rm SL}$ obtained from the ARGUS, CLEO II dilepton analyses, as well as those measured at LEP. In computing the LEP average, I assumed [2] a common systematic of 0.25% (absolute). The discrepancy between $\Upsilon(4S)$ and LEP measurements is not very large, but the LEP results have always been systematically somewhat higher, even though the presence of b baryons should very slightly decrease the semileptonic branching fraction.

We now show how $|V_{cb}|$ is extracted from the semileptonic rate, following the review of Gibbons [79]. The analysis assumes that the average B lifetimes at the $\Upsilon(4S)$ are $\langle\tau_B\rangle = (1.59 \pm 0.04)$ ps, while the average b-hadron lifetime at the Z is $\langle\tau_b\rangle = (1.55 \pm 0.02)$ ps. In the $1/m_Q$ expansion [80–82]

$$\Gamma = \Gamma_0 \left[1 - a_1 \left(\frac{m_c^2}{m_b^2}\right)\frac{\alpha_s}{\pi} + \frac{a_{np}}{m_b^2} + \mathcal{O}\left(\alpha_s^2, \frac{\alpha_s}{m_b^2}, \frac{1}{m_b^3}\right)\right] \tag{7.27}$$

where the a_1 term parametrizes perturbative QCD corrections, a_{np}/m_b^2 parametrizes non-perturbative corrections, which are small, and

$$\Gamma_0 = \frac{G_F^2 m_b^5}{192\pi^3}|V_{cb}|^2 z_0\left(\frac{m_c^2}{m_b^2}\right). \tag{7.28}$$

The function $z_0(x)$ is the phase-space factor

$$z_0(x) = 1 - 8x^2 + 8x^6 - x^8 - 24x^4 \ln x. \tag{7.29}$$

The calculations of Ball *et al.* and Shifman *et al.* give

$$\begin{aligned} \Gamma/|V_{cb}|^2 &= (43.2 \pm 4.2)\ \mathrm{ps}^{-1} && \text{Ball } et\ al.\ [83] \\ \Gamma/|V_{cb}|^2 &= (41.3 \pm 4.0)\ \mathrm{ps}^{-1} && \text{Shifman } et\ al.\ [84] \\ \Gamma/|V_{cb}|^2 &= (42.3 \pm 4.2)\ \mathrm{ps}^{-1} && \text{Combined} \end{aligned} \tag{7.30}$$

The combined value is the average of the two predictions, but the error is the larger of the two stated errors, which are essentially the same.

Next we correct the measurements of $\mathcal{B}_{\mathrm{SL}}$ by subtracting a small amount $b \to u\ell^-\bar{\nu}$ transitions. An inclusive prediction by Rosner [85] gives

$$\begin{aligned} \frac{\mathcal{B}(B \to X_u\ell^-\bar{\nu})}{\mathcal{B}(B \to X_c\ell^-\bar{\nu})} &= (1.85 \text{ to } 2.44)\left|\frac{V_{ub}}{V_{cb}}\right|^2 \\ &= (1.5 \pm 1.0)\%, \end{aligned} \tag{7.31}$$

where the experimental error has been included. The final value from the $\Upsilon(4S)$ measurements is

$$|V_{cb}| = (3.87 \pm 0.09 \pm 0.19) \times 10^{-2}, \tag{7.32}$$

where the first error is experimental and the second theoretical. Note that the 10% theoretical uncertainty in the rate translates into a 5% uncertainty in $|V_{cb}|$, an impressive achievement. The value from the LEP experiments is

$$|V_{cb}| = (4.06 \pm 0.07 \pm 0.20) \times 10^{-2}. \tag{7.33}$$

This value is consistent with that obtained at the $\Upsilon(4S)$, and its errors are comparable. It is not clear to me, however, to what extent model-dependent systematic errors are included in the LEP results.

7.5. Lepton-endpoint region in semileptonic B decay and $|V_{ub}|$

The determination of $|V_{ub}|$ is one of the most important and challenging measurements in B physics. The curve in Fig. 31 representing the $b \to u\ell^-\bar{\nu}$ rate shows clearly how little these processes perturb the total spectrum below the endpoint region. As we have just seen in Eq. 7.31, over all lepton energies, simple free-quark models predict that $\Gamma(b \to u\ell^-\bar{\nu})/\Gamma(b \to c\ell^-\bar{\nu}) \approx 1.5\%$. The key to measuring $|V_{ub}|$

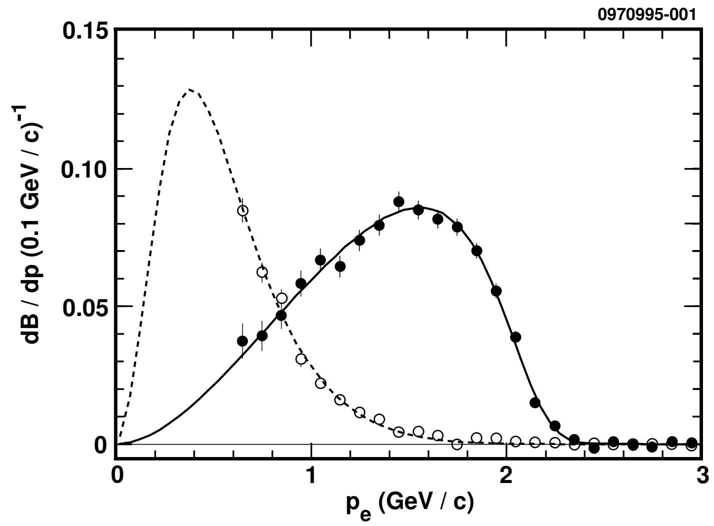

Fig. 32. CLEO II lepton momentum spectrum (electrons) from B decays based on the dilepton charge-correlation analysis. The solid point with error bars are the primary lepton spectrum ($\bar{B} \to X e \bar{\nu}$); the open circles with error bars are the secondary lepton spectrum $\bar{B} \to X_c \to Y e \nu$. The curves show the best fit to the modified ISGW model, which has 23% $\bar{B} \to D^{**} \ell^- \bar{\nu}$.

is to take advantage of the large lepton momenta made accessible by the small mass of the daughter u quark. By working in the region at and beyond the lepton-momentum-spectrum endpoint for $B \to X_c \ell^- \bar{\nu}$ processes, one gains enormously in sensitivity to $B \to X_u \ell^- \bar{\nu}$ decays.

Although the advantages of working in this endpoint region ($2.3 < p_\ell < 2.6$ GeV/c) are decisive, there are also disadvantages. The major difficulty is the need to convert the measured rate for this tiny portion of phase space into a value of $|V_{ub}|$. This calculation can be performed using either inclusive or exclusive models, but both have substantial uncertainties.

We turn now to the measurement of the rate in the endpoint region. Although the measurement is properly described as "inclusive," the analysis is rather different from that of the inclusive lepton spectrum described above. The reason is that continuum processes produce high-momentum leptons, which constitute an enormous background unless suppressed by kinematic cuts. The signal efficiency of these cuts is much more sensitive to the shapes of kinematic distributions (especially to that of q^2) than the very loose cuts used in the analysis of the inclusive lepton spectrum. This sensitivity introduces another source of model dependence into the results, beyond the overall scale γ_{thy}.

The primary characteristic used to remove continuum events is event topology: continuum events are usually much more jet-like than $\Upsilon(4S) \to B\bar{B}$ events, which are quite spherical. In the CLEO II measurement [86], which has the highest statistics, the event shape is described quantitatively using the variable $R_2 = H_2/H_0$, where the H_i are Fox-Wolfram moments [87]. The R_2 variable ranges from 0 (completely spherical) to 1 (completely jetlike); for the endpoint analysis CLEO requires $R_2 < 0.2$. Even with continuum suppression cuts, a significant continuum background remains. Fortunately, it can be directly measured by running just below the $\Upsilon(4S)$ resonance and performing the same analysis.

Figure 33 shows the CLEO lepton-momentum spectrum (including both electrons and muons) in the endpoint region. In the upper plot, for which the stricter cuts were used, the $b \to u\ell^-\bar{\nu}$ yields in the two bins are $43.0 \pm 10.2 \pm 6.7$ events ($2.4 < p_\ell < 2.6$ GeV/c) and $64.3 \pm 11.4 \pm 4.4$ events ($2.3 < p_\ell < 2.4$ GeV/c), with a total of $107 \pm 15 \pm 11$ events. Prior to the observation of the exclusive $\bar{B} \to \rho\ell^-\bar{\nu}$ and $\bar{B} \to \pi\ell^-\bar{\nu}$ signals, these yields (and those from a similar ARGUS analysis) were the only evidence that $|V_{ub}|$ is nonzero. The corresponding yields with the looser, less model-dependent cuts are $128.4 \pm 26.3 \pm 15.3$ events and $98.1 \pm 23.6 \pm 14.9$ events. The data sample used for this analysis contains only 955,000 $\Upsilon(4S) \to B\bar{B}$ events, so a substantial improvement will be possible when the full CLEO data sample (5 million events) is used.

The $B \to X_u\ell^-\bar{\nu}$ signal is normalized to the $B \to X_c\ell^-\bar{\nu}$ rate in the endpoint region. Thus, the analysis determines $|V_{ub}/V_{cb}|$. For the ACCMM (inclusive) model, the value is $|V_{ub}/V_{cb}| = 0.076 \pm 0.008$, while for the ISGW model (sum of exclusive modes) the value is $|V_{ub}/V_{cb}| = 0.101 \pm 0.010$. We will compare these results with those of the exclusive measurements in the following section.

7.6. Form factors and kinematic distributions for exclusive semileptonic decay; HQET predictions and the Isgur-Wise function

In this section we examine the connections between form factors and observable kinematic distributions in exclusive semileptonic decays. Although the formalism may seem complicated at first, the connections turn out to be fairly simple. We also write the form factors and decay distributions using the standard HQET formalism, which, while completely general, allows one to easily identify the behavior in the heavy-quark symmetry limit. The relationship between various observable form factors and the Isgur-Wise function is also discussed. All

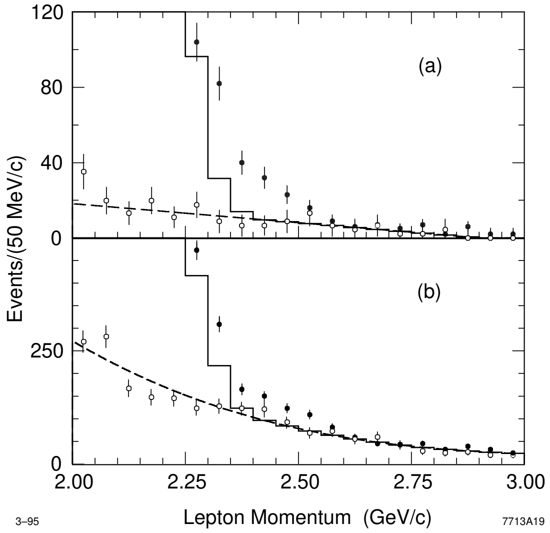

Fig. 33. Inclusive end-point spectrum in B decays from CLEO II. The upper plot (a) is from the analysis with tighter cuts; the lower plot (b) is from the analysis with looser cuts. Efficiencies in the latter analysis have less sensitivity to models, but the backgrounds are larger. In both plots, the solid points with error bars are the data taken at the $\Upsilon(4S)$, while the open circles with error bars represent the continuum background level, which is measured using data taken below the $\Upsilon(4S)$. The histogram shows the total background prediction,which includes both continuum and $\bar{B} \to X_c \ell^- \bar{\nu}$. The excess of observed events over this total background is interpreted as evidence for $\bar{B} \to X_u \ell^- \bar{\nu}$ decays.

of these ideas will be used in Sec. 7.7, where we present the results of measurements of exclusive semileptonic decays.

The matrix element for the semileptonic decay $M_{Q\bar{q}} \to X_{q'\bar{q}} \ell^- \bar{\nu}$ can be written as the product of a hadronic and a leptonic current:

$$\begin{aligned}\mathcal{M}(M_{Q\bar{q}} \to X_{q'\bar{q}} \ell^- \bar{\nu}) = \langle X_{q'\bar{q}} | \bar{q}' \frac{-ig}{2\sqrt{2}} V_{q'Q} \gamma_\mu (1-\gamma_5) Q | M_{Q\bar{q}} \rangle \\ \times P^{\mu\nu}(q) \bar{u}_\ell \frac{-ig}{2\sqrt{2}} \gamma_\nu (1-\gamma_5) v_\nu \qquad (7.34)\end{aligned}$$

where the operator Q annihilates the quark Q (or creates $\bar{Q}$) and the W propagator is given by

$$P^{\mu\nu}(q) = \frac{i(-g^{\mu\nu} + q^\mu q^\nu / M_W^2)}{q^2 - M_W^2} \simeq i \frac{g^{\mu\nu}}{M_W^2}. \qquad (7.35)$$

The last expression for the propagator is appropriate when the energies are much less than M_W. We have used the form of the CKM element $V_{q'Q}$ appropriate to the case in which a W^- is emitted (*e.g.*, V_{cb} or V_{ub}); if a W^+ were emitted, as in $c \to s$ or $c \to d$, the form of the CKM element is $V_{Qq'}^*$ (*e.g.*, V_{cs}^* or V_{cd}^*), but the absolute magnitude is taken in the end in any case. We therefore have the phenomenological form for the matrix element

$$\mathcal{M}(M_{Q\bar{q}} \to X_{q'\bar{q}}\ell^-\bar{\nu}) = -i\frac{G_F}{\sqrt{2}} V_{q'Q} L^\mu H_\mu, \tag{7.36}$$

where $G_F/\sqrt{2} = g^2/8M_W^2$. The leptonic current is exactly known

$$L^\mu = \bar{u}_\ell \gamma^\mu (1-\gamma_5) v_\nu, \tag{7.37}$$

and the hadronic current is given by

$$H_\mu = \langle X_{q'\bar{q}} | \bar{q}' \gamma_\mu (1-\gamma_5) Q | M_{Q\bar{q}} \rangle. \tag{7.38}$$

We can use Lorentz invariance to construct the hadronic current from the available four-vectors, which are momenta and spin-polarization vectors. The Lorentz vector or axial-vector quantities thus formed have Lorentz-invariant coefficients (form factors) that are functions of q^2. We will consider two main classes of exclusive semileptonic decay: $P \to P'\ell\nu$, where both P and P' are pseudoscalar particles, and $P \to V\ell\nu$, where V is a vector particle.

In the case of a $P(Q\overline{q}) \to P'(q'\overline{q})\ell\nu$ decay, there are only two independent four vectors, which we can take to be $p+p'$ and $q = p - p'$. For these quantum numbers, the hadronic current H^μ has no contribution from the matrix element of the axial-vector current (as discussed in the appendix) and can be written [36,88]

$$\langle P'(p')|V^\mu|P(p)\rangle = F_1(q^2)\left[(p+p')^\mu - \frac{M^2 - m_{P'}^2}{q^2} q^\mu\right] + F_0(q^2)\frac{M^2 - m_{P'}^2}{q^2} q^\mu, \tag{7.39}$$

where $V^\mu = \overline{q}'\gamma^\mu Q$ and $F_0(0) = F_1(0)$, so there is no singular behavior at $q^2 = 0$. The form factors $F_0(q^2)$ and $F_1(q^2)$ can be associated with the exchange of particles with quantum numbers $J^P = 0^+$ and $J^P = 1^-$, respectively [88]. Another common way to write the current is

$$\langle P'(p')|V^\mu|P(p)\rangle = f_+(q^2)(p+p')^\mu + f_-(q^2)(p-p')^\mu, \tag{7.40}$$

where $f_+(q^2) = F_1(q^2)$ and

$$F_0(q^2) = f_+(q^2) + \frac{q^2}{M^2 - m_{P'}^2} f_-(q^2). \tag{7.41}$$

In practice, these expressions for the currents simplify, because the terms proportional to q^μ are nearly always negligible, both here and for the case $P \to V\ell\nu$. The reason is that in the limit $m_\ell \to 0$, $q^\mu L_\mu = 0$, where L_μ is the lepton current. Thus, $P \to P'\ell\nu$ is, to a very good approximation, described by only one form factor $F_1(q^2)$ when $\ell = e$ or μ:

$$\langle P'(p')|V^\mu|P(p)\rangle = F_1(q^2)(p+p')^\mu. \tag{7.42}$$

The differential decay rate for $P \to P'\ell\nu$ can now be calculated, giving

$$\frac{d\Gamma}{dq^2} = \frac{G_F^2|V_{q'Q}|^2 p_{P'}^3}{24\pi^3}|f_+(q^2)|^2, \tag{7.43}$$

where Q and q' are the initial and final state quarks in the underlying transition $Q \to q'\ell\nu$. The momentum $p_{P'}$ is the magnitude of the three-momentum of the final-state meson P' in the rest frame of P. It is a function of q^2 (see Eq. 7.9). In fact, the dominant q^2 dependence usually arises not from the falloff of the form factor as q^2 decreases, but from the $p_{P'}^3$ term, which enhances the rate at *low* q^2. We have integrated over all decay angles to obtain Eq. 7.43; as we have seen in Eq. 7.16, however, the lepton angular distribution in the W frame is not isotropic but is $dN/d\cos\theta_\ell \propto \sin^2\theta_\ell$. The leptons tend to come out perpendicular to the W direction.

Many different methods have been applied to the difficult problem of calculating the form factors. Quark-model calculations estimate meson wave functions and use them to compute the matrix elements that appear in the hadronic currents. These integrals are performed by analyzing the decay at a particular value of q^2, either $q^2 = 0$ or $q^2 = q^2_{\rm max}$. One perspective is that the hadronic system is least disturbed at high q^2, so $q^2_{\rm max}$ is where the integrals are most naturally evaluated. Historically, however, the convention in charm decays has been to specify the form factors at $q^2 = 0$. The variation of the form factors with q^2 is determined as a separate step in the calculation. In fact, this variation is usually assumed to have a very simple form. Because the physics being described is nonperturbative, none of these phenomenological forms should be taken too seriously at a fundamental level, although they often do reasonably well in describing the data. One approach, used in the WSB [88] and KS [89] models, is called "nearest pole dominance," which has its origin in vector-dominance ideas. Here, the q^2 dependence of a form factor f_i is assumed to have the form

$$f_i(q^2) = \frac{f_i(0)}{\left(1 - \frac{q^2}{m^2_{\rm pole}}\right)^n}\ , \tag{7.44}$$

where n is an integer, usually one for mesons. The pole mass m_{pole} is the mass of the lowest-lying $Q\overline{q}'$ meson with the quantum numbers appropriate to a given part of the hadronic current. Thus, for a $D \to \bar{K}^* \ell^+ \nu$ decay, the quark transition is $c \to s$, so the pole mass for the vector form factor is equal to $m_{D_s^*}$.

In the last few years, much effort has gone into lattice calculations of semileptonic form factors. Some of the lattice predictions for D semileptonic decays are discussed in the following section.

The form factors used in HQET are somewhat different from those described above because, in the limit of very heavy quark masses, the four-velocities of the hadrons, rather than their four-momenta, are the appropriate quantities to use. The hadronic current for $P \to P'\ell\nu$ is expressed [36,56,57,90,91] in terms of HQET form factors $h_+(v \cdot v')$ and $h_-(v \cdot v')$:

$$\begin{aligned} &\langle P'(v')|\, V^\mu \,|P(v)\rangle \\ &\qquad = \sqrt{M m_{P'}}\Big[h_+(v\cdot v')(v+v')^\mu + h_-(v\cdot v')(v-v')^\mu\Big], \end{aligned} \tag{7.45}$$

The differential decay rate is then

$$\begin{aligned} \frac{d\Gamma(P \to P'\ell\nu)}{dw} = \frac{G_F^2|V_{cb}|^2}{48\pi^3}&(m_P + m_{P'})^2 m_{P'}^3 (w^2-1)^{3/2} \\ &\times \left|h_+(w) - \frac{m_P - m_{P'}}{m_P + m_{P'}} h_-(w)\right|^2. \end{aligned} \tag{7.46}$$

We will see that in the heavy-quark symmetry limit, $h_+(w) \to \xi(w)$, where $\xi(w)$ is the Isgur-Wise function, while $h_-(w) \to 0$.

For the process $P(Q\overline{q}) \to V(q'\overline{q})\ell\nu$, where V is a vector meson, each term in the current must be linear in the polarization vector, ε, of the vector meson. (Actually, the complex conjugate is used since V is an outgoing particle.) The polarization vector transforms as a Lorentz axial-vector: under parity the time-like component reverses but the space-like components are unchanged. The simplest term in the hadronic current is essentially just ε^* multiplied by a function $A_1(q^2)$, which is called an axial-vector form factor. The contribution from the term associated with this form factor, unlike others, does not go to zero as the vector-meson momentum $|\mathbf{p}'|$ goes to zero, and it dominates the rate at high q^2. Another term that can be written is proportional to $\epsilon^{\mu\nu\alpha\beta}\varepsilon^*_\nu p'_\alpha p_\beta$, which transforms as a Lorentz four-vector. For $\mu = 0$, $\nu = 1$, $\alpha = 2$, $\beta = 3$, this term transforms into itself under parity; for $\mu = 1$, $\nu = 0$, $\alpha = 2$, $\beta = 3$ it transforms into minus itself. This term multiplies a function $V(q^2)$, which is called a vector form factor. The most general form for the current is [36,88]

$$\langle V(p',\varepsilon)|V^\mu - A^\mu|P(p)\rangle = \frac{2i\epsilon^{\mu\nu\alpha\beta}}{M+m_V}\varepsilon^*_\nu p'_\alpha p_\beta V(q^2)$$
$$-(M+m_V)\varepsilon^{*\mu}A_1(q^2) + \frac{\varepsilon^*\cdot q}{M+m_V}(p+p')^\mu A_2(q^2)$$
$$+2m_V\frac{\varepsilon^*\cdot q}{q^2}q^\mu A_3(q^2) - 2m_V\frac{\varepsilon^*\cdot q}{q^2}q^\mu A_0(q^2), \tag{7.47}$$

where $V^\mu = \overline{q}'\gamma^\mu Q$, $A^\mu = \overline{q}'\gamma^\mu\gamma_5 Q$, and

$$A_3(q^2) = \frac{M+m_V}{2m_V}A_1(q^2) - \frac{M-m_V}{2m_V}A_2(q^2), \tag{7.48}$$

with $A_0(0) = A_3(0)$. Again, terms proportional to q^μ only play an important role for the case $\ell = \tau$. Thus, $P \to V\ell\nu$ is essentially described by three form factors: $A_1(q^2)$, $V(q^2)$, and $A_2(q^2)$:

$$\langle V(p',\varepsilon)|V^\mu - A^\mu|P(p)\rangle = \frac{2i\epsilon^{\mu\nu\alpha\beta}}{M+m_V}\varepsilon^*_\nu p'_\alpha p_\beta V(q^2)$$
$$-(M+m_V)\varepsilon^{*\mu}A_1(q^2) + \frac{\varepsilon^*\cdot q}{M+m_V}(p+p')^\mu A_2(q^2). \tag{7.49}$$

The form factors A_1, A_2, and V are dimensionless and relatively real, since CP is conserved in these decays and there are no final-state strong interactions [92]. (Possible CP violating effects in semileptonic B decays due to physics beyond the standard model are discussed in [93].) We can therefore take them to be real. $A_1(q^2)$ and $A_2(q^2)$ can be associated with the exchange of a particle with quantum numbers $J^P = 1^+$, whereas $V(q^2)$ is associated with $J^P = 1^-$. We will see later (Eq. 7.60 and Eq. 7.59) that A_1 contributes to all three helicity components of the final-state vector meson (or the W^*), A_2 contributes only to the helicity-zero component, and $V(q^2)$ contributes only to the helicity ± 1 components.

In terms of HQET form factors, the hadronic current is

$$\langle V(v',\varepsilon)|(V^\mu - A^\mu)|P(v)\rangle = \sqrt{Mm_V}\Big[ih_V(v\cdot v')\,\epsilon^{\mu\nu\alpha\beta}\,\varepsilon^*_\nu\,v'_\alpha\,v_\beta$$
$$-\,h_{A_1}(v\cdot v')\,\varepsilon^{*\mu}\,(v\cdot v'+1) + h_{A_2}(v\cdot v')\,v^\mu\,\varepsilon^*\cdot v$$
$$+\,h_{A_3}(v\cdot v')\,v'^\mu\,\varepsilon^*\cdot v\Big]. \tag{7.50}$$

Heavy-quark symmetry does not predict the w (or q^2) dependence of the form factors, but it does relate the form factors to each other, reducing the number of independent unknown functions. In the heavy-quark symmetry limit (for example, $m_b,\ m_c \to \infty$ in $b \to c\ell^-\bar{\nu}$),

$$h_+(w) = h_V(w) = h_{A_1}(w) = h_{A_3}(w) = \xi(w), \tag{7.51}$$

where $\xi(w)$, the Isgur-Wise function, is a common form factor for decays into pseudoscalar and vector mesons. These states are in the same HQET multiplet, because they differ only in the relative spin orientations of the quarks. Furthermore, in the heavy-quark symmetry limit,

$$h_-(w) = h_{A_2}(w) = 0. \tag{7.52}$$

The Isgur-Wise function can also be regarded as the form factor (in the heavy-quark symmetry limit) for the elastic scattering of the meson by a current that gives a kick to the heavy quark. The form factor gives the amplitude that the meson remains intact through the scattering process.

Nonperturbative methods, such as lattice QCD or QCD sum rules, are needed to calculate the long-range, soft-gluon strong interactions that the Isgur-Wise function describes. In the key decay mode $\bar{B} \to D^*\ell^-\bar{\nu}$, however, the range of $v \cdot v' = \gamma_{D^*}$ is fairly small, 1 to 1.5. A Taylor explansion of ξ about $w = v \cdot v' = 1$ is expected to work well over most of this region:

$$\xi(w) \approx 1 - \rho^2\,(w-1) + \mathcal{O}[(w-1)^2]. \tag{7.53}$$

At zero recoil ($w = v \cdot v' = \gamma_X = 1$), the light constituents of the meson are essentially undisturbed by the heavy-quark decay. In the heavy-quark symmetry limit, there is then a complete overlap between the initial and final meson wave functions, and the value of the Isgur-Wise function is known, $\xi(1) = 1$. This result, which must be modified to take into account the finite quark masses, is of great practical importance for measuring $|V_{cb}|$.

In the short Δw range for $\bar{B} \to D^*\ell^-\bar{\nu}$ and $\bar{B} \to D\ell^-\bar{\nu}$, the shape of the Isgur-Wise function is thus characterized primarily by the slope ρ^2. Although ρ^2 is difficult to calculate, it must be positive and is expected to be roughly in the range 0.5 to 2.0. The primary theoretical tools used to determine the Isgur-Wise function are QCD sum rules, which are based on quark-hadron duality, and lattice QCD, in which a computer calculation is performed using a discrete space-time lattice.

A major theoretical effort has been undertaken to evaluate corrections to the heavy quark symmetry limit for various processes. In general, the largest corrections are from terms of order $1/m_b$, $1/m_c$, which can be estimated in the framework of HQET. At the zero recoil point, $w = 1$, the two form factors h_{A_1} and h_+ are protected against $1/m_Q$ corrections. As w increases, however, all of the heavy-quark symmetry relations are subject to significant symmetry-breaking corrections. These results have major implications for the determination of $|V_{cb}|$, since h_{A_1} is the only form factor governing the rate at zero recoil for $\bar{B} \to D^*\ell^-\bar{\nu}$. The practical application of this result is discussed in Sec. 7.7.

The HQET form factors are related to the traditional form factors F_1, V, A_1, and A_2 by [90,36]

$$\begin{aligned} RF_1(q^2) &= h_+(w) - \Big(\frac{M - m_{P'}}{M + m_{P'}}\Big)\, h_-(w), \\ R^*\,V(q^2) &= h_V(w), \\ R^{*-1}A_1(q^2) &= \frac{w+1}{2}\, h_{A_1}(w), \\ R^*A_2(q^2) &= h_{A_3}(w) + \frac{m_V}{M}\, h_{A_2}(w), \end{aligned} \tag{7.54}$$

where we have explicitly written $m_{P'}$ and m_V instead of m in order to distinguish between the different masses for the final-state mesons. The constants R and R^* are given by

$$R = \frac{2\sqrt{Mm_{P'}}}{M + m_{P'}} \qquad \text{and} \qquad R^* = \frac{2\sqrt{Mm_V}}{M + m_V}. \tag{7.55}$$

The heavy-quark symmetry limit has not yet been imposed on Eq. 7.54: it is generally valid.

We can use these results to show how the traditional form factors F_1, V, A_1, and A_2 are themselves related to the Isgur-Wise function in the heavy-quark symmetry limit. For $P \to P'\ell\nu$ we have

$$F_1(q^2) = R^{-1}\xi(w), \tag{7.56}$$

and for $P \to V\ell\nu$ we have (also in the heavy-quark symmetry limit)

$$V(q^2) = A_2(q^2) = \frac{A_1(q^2)}{\left[1 - \frac{q^2}{(M+m_V)^2}\right]} = R^{*-1}\,\xi(w). \tag{7.57}$$

Four independent kinematic variables completely describe the semileptonic decay $P \to V\ell\nu$, where the vector meson decays to two pseudoscalars, $V \to P_1P_2$. The four variables most commonly used are q^2 or w and the three angles shown in Fig. 34. The angle θ_ℓ is measured in the W^* (or $\ell\nu$) rest frame, where the lepton and the neutrino are back to back: it is the polar angle between the charged lepton and the direction opposite to that of the vector meson. The angle θ_V is measured in the rest frame of the vector meson, where the pseudoscalars P_1 and P_2 are back to back. In this frame, θ_V is the polar angle between one of these mesons, say, P_1, and the direction of the vector meson in the parent meson's rest frame. Although either P_1 or P_2 can be chosen for this definition, one must be careful to use a consistent choice for the angle χ, which we define to be the azimuthal angle between the projections of the momenta of the lepton and P_1 in the plane perpendicular to the decay axis.

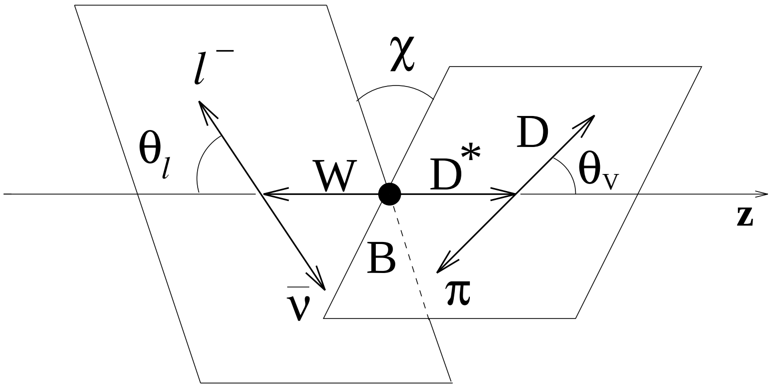

Fig. 34. Definition of the angles θ_V, θ_ℓ, and χ in the decay $\bar{B} \to D^* \ell^- \bar{\nu}$. (These angles are used for any $P \to V \ell \nu$ in which the vector meson decays into two pseudoscalars.) The lepton and neutrino are drawn back to back because they are shown in the W^* rest frame. Similarly, the D and the π are shown in the D^* rest frame. The angle θ_ℓ is thus measured in the W rest frame, while θ_V is measured in the D^* rest frame. The azimuthal angle χ is measured between the W and D^* decay planes. In the literature, the angle θ_ℓ is sometimes defined as the direction between the charged lepton and the recoiling vector meson, measured in the $\ell\nu$ rest frame.

The differential decay rate for $P(Q\bar{q}) \to V(q'\bar{q})\ell^-\bar{\nu}$, $V \to P_1 P_2$ can be expressed in terms of these four kinematic variables q^2, θ_ℓ, θ_V and χ [94,89]:

$$\frac{d\Gamma(P \to V\ell\nu,\ V \to P_1 P_2)}{dq^2\, d\cos\theta_V\, d\cos\theta_\ell\, d\chi} = \frac{3}{8(4\pi)^4} G_F^2 |V_{q'Q}|^2 \frac{p_V q^2}{M^2} \mathcal{B}(V \to P_1 P_2)$$
$$\times \{(1-\eta\cos\theta_\ell)^2 \sin^2\theta_V |H_+(q^2)|^2$$
$$+ (1+\eta\cos\theta_\ell)^2 \sin^2\theta_V |H_-(q^2)|^2$$
$$+ 4\sin^2\theta_\ell \cos^2\theta_V |H_0(q^2)|^2$$
$$- 4\eta\sin\theta_\ell(1-\eta\cos\theta_\ell)\sin\theta_V\cos\theta_V\cos\chi\, H_+(q^2)H_0(q^2)$$

$$+ 4\eta \sin\theta_\ell (1 + \eta\cos\theta_\ell)\sin\theta_V \cos\theta_V \cos\chi\, H_-(q^2) H_0(q^2)$$
$$- 2\sin^2\theta_\ell \sin^2\theta_V \cos 2\chi\, H_+(q^2) H_-(q^2)\}. \qquad (7.58)$$

The amplitudes for helicities 0, +1, and −1 are proportional to $H_0(q^2)$, $H_+(q^2)$ and $H_-(q^2)$. Because the parent meson has spin zero, the vector meson and the W^* must have the same helicity. The detailed dynamics of the hadronic current are described by the variation of these helicity amplitudes with q^2, which we have not yet specified. The magnitude of the three-momentum of V in the rest frame of P, p_V, is a function of q^2 (see Eq. 7.9). The factor η is equal to +1 for B decays and −1 for D decays. It is this factor that leads to the different lepton-energy distributions for bottom and charm decays. Note that the angle θ_ℓ is defined with respect to the direction of the virtual W in the parent rest frame; this accounts for the sign differences between our formula and certain others in the literature [92], which use $\pi - \theta_\ell$.

The joint distribution given in Eq. 7.58 incorporates the $V-A$ structure of the leptonic current, as well as the assumption that the mass of the charged lepton can be neglected. In general, there is a fourth helicity amplitude corresponding to the time-like helicity component of the virtual W, but its contribution is negligible when the lepton mass is small. The differential decay rate formula for finite lepton mass is given, for example, in Ref. [89]. Eq. 7.58 also assumes that the daughter meson is a narrow resonance; if this is not the case, a Breit-Wigner line shape should be included.

The helicity amplitudes can, in turn, be related to the two axial-vector form factors, $A_1(q^2)$ and $A_2(q^2)$, and the vector form factor, $V(q^2)$, which appear in the hadronic current (Eq. 7.47):

$$H_0(q^2) = \frac{1}{2m_V\sqrt{q^2}}[(M^2 - m_V^2 - q^2)(M + m_V)A_1(q^2)$$
$$-4\frac{M^2 p_V^2}{M + m_V} A_2(q^2)] \qquad (7.59)$$

and

$$H_\pm(q^2) = (M + m_V)A_1(q^2) \mp \frac{2Mp_V}{M + m_V} V(q^2). \qquad (7.60)$$

We note that while A_2 contributes only to H_0 and V contributes only to $H_\pm$, A_1 contributes to all three helicity amplitudes. At high q^2 (small p_V), each of the helicity amplitudes is dominated by A_1.

We can also relate the helicity amplitudes to the set of form factors defined in HQET. Since this result is applicable mainly to the decay

$\bar{B} \to D^* \ell^- \bar{\nu}$, we write the result with the relevant masses:

$$H_0(w) = (m_B - m_{D^*}) \sqrt{\frac{m_B m_{D^*}}{q^2(w)}} (w+1)\, h_{A_1}(w) \times \Big[1 + \big(\frac{w-1}{1-r}\big)(1 - R_2(w))\Big] \tag{7.61}$$

and

$$H_\pm(w) = (m_B - m_{D^*}) \sqrt{\frac{m_B m_{D^*}}{q^2(w)}} (w+1)\, h_{A_1}(w) \times \frac{\sqrt{1 - 2wr + r^2}}{1-r} \Big[1 \mp \sqrt{\frac{w-1}{w+1}} R_1(w)\Big], \tag{7.62}$$

where $r = m_{D^*}/m_B$. The terms $w \pm 1$ are related to q^2 by

$$w \pm 1 = \frac{(m_B \pm m_{D^*})^2 - q^2}{2 m_B m_{D^*}}. \tag{7.63}$$

The form factor ratios $R_1(w)$ and $R_2(w)$ are given by

$$\begin{aligned} R_1(w) &\equiv \frac{h_V(w)}{h_{A_1}(w)} = \left[1 - \frac{q^2}{(M+m_V)^2}\right] \frac{V(q^2)}{A_1(q^2)} \\ R_2(w) &\equiv \frac{h_{A_3}(w) + (m_V/M) h_{A_2}(w)}{h_{A_1}(w)} \\ &= \left[1 - \frac{q^2}{(M+m_V)^2}\right] \frac{A_2(q^2)}{A_1(q^2)}. \end{aligned} \tag{7.64}$$

These results are general and are not restricted to the heavy-quark symmetry limit. Using Eq. 7.51 and Eq. 7.52 (or Eq. 7.54 and Eq. 7.57) we see that *in the heavy-quark symmetry limit* $R_1(w) = 1$ *and* $R_2(w) = 1$, *independent of* w. Recent measurements from CLEO, discussed in the following section, have shown that these ratios are indeed close to unity for $\bar{B} \to D^* \ell^- \bar{\nu}$. From inspection of Eq. 7.61 and Eq. 7.62, it is clear that as $w \to 1$, H_0 and $H_\pm$ are governed by $h_{A_1}(w)$.

Figure 35 shows a prediction for the $\bar{B} \to D^* \ell^- \bar{\nu}$ and $\bar{B} \to D \ell^- \bar{\nu}$ form factors from an HQET-based calculation by Neubert. All of the form factors associated with these decays are expected to have essentially the same shape.

Many experiments have measured ratios of the traditional form factors

$$r_V = \frac{V(q^2)}{A_1(q^2)} \qquad \text{and} \qquad r_2 = \frac{A_2(q^2)}{A_1(q^2)}. \tag{7.65}$$

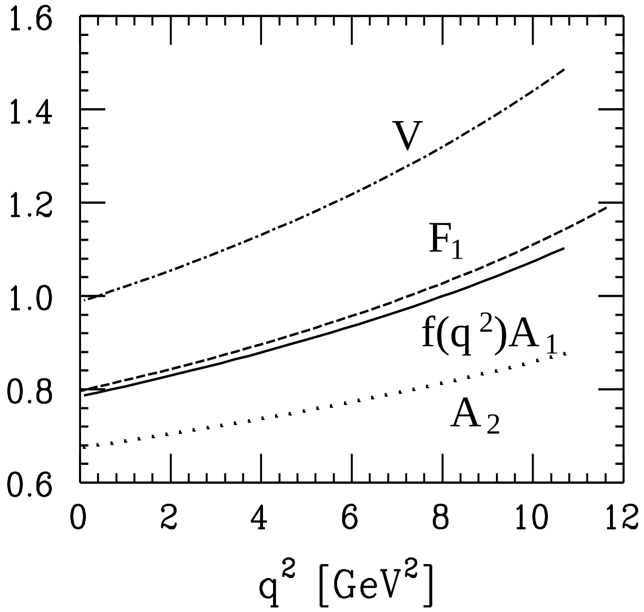

Fig. 35. The q^2 dependence of form factors in $\bar{B} \to D\ell^-\bar{\nu}$ and $\bar{B} \to D^*\ell^-\bar{\nu}$ according to an HQET-based calculation by Neubert. The curves represent V (dot-dashed), F_1 (dashed), $f(q^2)A_1$ where $f(q^2) = [1 - q^2/(m_B + m_{D^*})]^{-1}$ (solid), and A_2 (dotted). From [36], with permission from M. Neubert.

These quantities are usually assumed to be constant in the fit. However, in the heavy-quark symmetry limit, it is not r_V and r_2 that should be approximately q^2 independent, but R_1 and R_2. For charm decays, this consideration is not especially relevant, since the heavy-quark symmetry limit is not expected to hold, even approximately. For B decays, however, the ratios R_1 and R_2 are preferred.

In the real world, the heavy-quark symmetry limit does not apply, and it is therefore of great interest to know how large the symmetry-breaking corrections are. Neubert's (model-dependent) estimate of these corrections for $\bar{B} \to D^*\ell^-\bar{\nu}$ gives [36]

$$R_1 \approx 1.3 \qquad \text{and} \qquad R_2 \approx 0.8. \tag{7.66}$$

Neubert argues that HQET predicts unambiguously that R_1 for $\bar{B} \to D^*\ell^-\bar{\nu}$ must be significantly larger than unity, whereas the prediction for R_2 is less certain [36,95] In reality, both R_1 and R_2 are expected to have a mild q^2 (or w) dependence

$$\begin{aligned} R_1(w) &= 1.35 - 0.22(w-1) + 0.09(w-1)^2 \\ R_2(w) &= 0.79 + 0.15(w-1) - 0.04(w-1)^2. \end{aligned} \tag{7.67}$$

Thus, symmetry breaking affects both the equality of the form factors at $w = 1$ and the equality of their slopes. It is important to remember that a typical value of $w - 1$ in $\bar{B}^0 \to D^{*+}\ell^-\bar{\nu}$ is about 0.25, so the predicted variation of R_1 and R_2 with w is rather small. Thus, the observed behavior of the form factors should be similar to that predicted in the heavy-quark symmetry limit. Ideally, we would measure the w dependence of all three form factors and determine whether the ratios predicted in Eq. 7.67 are correct. We will discuss the $\bar{B} \to D^*\ell^-\bar{\nu}$ form-factor measurements in the following section.

It is interesting to analyze the w or q^2 dependence of each term contributing to the differential rate. All of the w dependence resides in the H_iH_j terms multiplied by the factor $p_V q^2$, which form the coefficients of the angular terms in Eq. 7.58. The momentum can be expressed in terms of w by

$$p_V = |\mathbf{p}_{D^*}| = m_{D^*}\sqrt{w^2 - 1}. \tag{7.68}$$

Fig. 36 shows the w dependence of these coefficients, using as inputs the form factors measured by CLEO for the decay $\bar{B}^0 \to D^{*+}\ell^-\bar{\nu}$. Recall from Eq. 7.23 that the minimum value, $w = 1$, corresponds to $q^2 = q^2_{\max}$, where the hadronic system has zero recoil velocity in the parent meson's rest frame. There is no phase space for this configuration, which explains why all of the curves in Fig. 36 go to zero at $w = 1$. However, as $w \to 1$, the rates from the three possible helicities contribute equally, because both the daughter meson and the virtual W are stationary in the parent rest frame. As we discussed at the end of Sec. 7.2, this forces these particles to be unpolarized.

As w increases, we see that the H_-^2 term quickly begins to dominate over the H_+^2 term. This result is expected from the $V - A$ nature of the W couplings, which leads to a higher probability for the vector meson (and the virtual W) to have helicity $\lambda = -1$ than $\lambda = +1$. (See Sec. 7.2 and Fig. 29.) This effect also produces a larger value for the interference term H_0H_- than for H_0H_+ at all values of q^2 except the endpoints. The CLEO measurements discussed in Sec. 7.7 show clear effects in the correlation between χ and $\cos\theta_V$ due to this interference term.

At the other extreme, $w = w_{\max} \approx 1.5$ or $q^2 = 0$, the recoil velocity is maximum. The lepton and neutrino momenta are parallel in the rest frame of P, and their combined spin projection along their direction of motion is zero. Hence, only the H_0^2 combination contributes in this limit. This point is also evident from inspection of Eq. 7.60 and Eq. 7.59, which show that $p_V q^2 H_0^2$ remains finite as $q^2 \to 0$, whereas both $p_V q^2 H_+^2$ and $p_V q^2 H_-^2$ go to zero. It is also instructive to exam-

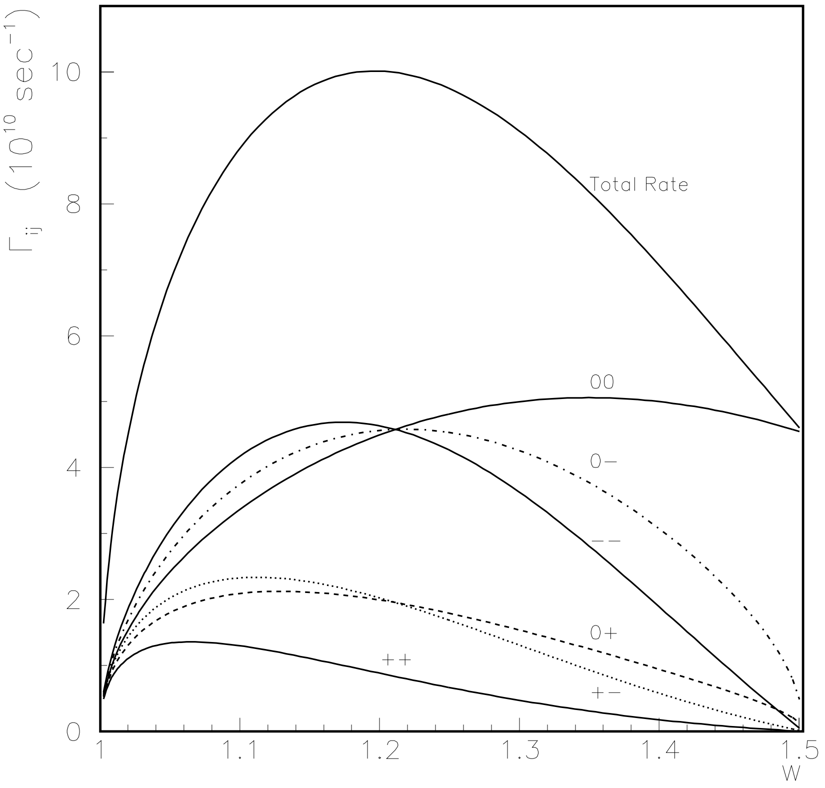

Fig. 36. The predicted w-dependence of different helicity combinations in the decay $\bar{B} \to D^* \ell^- \bar{\nu}$. The curves show the quantities $\Gamma_{ij} = \frac{G_F^2 |V_{cb}|^2 p_V q^2}{96\pi^3 M^2} H_i(q^2) H_j(q^2)$, $i, j = +, -, 0$, which appear as coefficients of the angular factors in Eq. 7.58. We have assumed $R_1 = 1.3$ and $R_2 = 0.8$, with a linear w dependence (slope=$\rho^2 = 1.0$) for h_{A_1}. The overall scale is also determined by $|V_{cb}| = 0.04$. The solid lines correspond to the terms that contribute to the total decay rate: Γ_{ij}, $i = j$. The terms Γ_{ij}, $i \neq j$, do not contribute to the total decay rate because the angular functions that they multiply in Eq. 7.58 integrate to zero. The D^* helicity can only be zero at maximum recoil ($w = 1.5$); as w decreases, both helicity -1 and $+1$ contribute, but helicity -1 dominates due to the $V - A$ coupling. At minimum D^* recoil, all three helicities contribute equally, but phase space goes to zero.

ine the dependence of Eq. 7.58 on the form factors themselves via the helicity amplitudes (Eq. 7.59 and Eq. 7.60). When the recoil of the hadronic system is small ($w \approx 1$) the terms proportional to $V(q^2)$ and $A_2(q^2)$ can be neglected compared with those proportional to $A_1(q^2)$, which appear in all the helicity amplitudes. As a consequence, the A_1 form factor dominates the rate at large values of q^2.

Since the form factor $A_1(q^2)$ appears in all three helicity amplitudes (Eqs. 7.60 and 7.59) and typically dominates the rate, it is natural to use the new variables $r_V \equiv V/A_1$ and $r_2 \equiv A_2/A_1$ or in HQET, R_1 and R_2 defined in Eq. 7.64.

It is common to report the values of certain other integrated observables that can be derived from the form factors. These are $\bar{A}_{\rm FB}$, the forward-backward asymmetry of the lepton in the W rest frame,

$$\bar{A}_{\rm FB} = \frac{\int_0^1 \frac{d\Gamma}{d\cos\theta_\ell} d\cos\theta_\ell - \int_{-1}^0 \frac{d\Gamma}{d\cos\theta_\ell} d\cos\theta_\ell}{\int_{-1}^1 \frac{d\Gamma}{d\cos\theta_\ell} d\cos\theta_\ell} = \frac{3}{4}\frac{(\Gamma_- - \Gamma_+)}{(\Gamma_L + \Gamma_T)}, \tag{7.69}$$

and $\bar{A}_{\rm pol}$, which is related to the ratio of longitudinal to transverse polarization of the vector meson:

$$\bar{A}_{\rm pol} = \frac{2\int p_V q^2 |H_0|^2 dq^2}{\int p_V q^2 (|H_-|^2 + |H_+|^2) dq^2} - 1 = 2\frac{\Gamma_L}{\Gamma_T} - 1, \tag{7.70}$$

where

$$\Gamma_i = \frac{G_F^2 |V_{cb}|^2}{96\pi^3} \int dq^2 p_V \frac{q^2}{{m_B}^2} |H_i(q^2)|^2, \tag{7.71}$$

and

$$\Gamma_L = \Gamma_0 \qquad\qquad \Gamma_T = \Gamma_+ + \Gamma_- . \tag{7.72}$$

We can easily see which form factors these observables are sensitive to by examining the expressions for the helicity amplitudes, Eq. 7.59 and Eq. 7.60. Since the only difference between H_+ and H_- is the sign of the coefficient of $V(q^2)$, it is clear that the difference $\Gamma_- - \Gamma_+$ is proportional to an integral over $V(q^2)$. Thus, $\bar{A}_{\rm FB}$ provides a measurement of r_V (or R_1 in the HQET picture). In contrast, the ratio of longitudinal to transverse polarization is almost completely controlled by r_2 (or R_2 in the HQET version). Roughly speaking, then, r_V (or R_1) is determined from the $\cos\theta_\ell$ distribution and the $\cos\theta_V$ vs. χ correlation, whereas r_2 or (R_2) is determined from the $\cos\theta_V$ and q^2 distributions.

7.7. *Exclusive semileptonic decay, $|V_{cb}|$, and $|V_{ub}|$*

The subject of exclusive semileptonic decays has changed dramatically over the past several years. Huge data samples at CLEO, LEP, and the fixed-target charm experiments at Fermilab have led to vastly improved measurements of both branching fractions and decay distributions. The experimental sensitivity has also allowed the observation of

CKM-suppressed modes, although the statistical uncertainties are still fairly large. In the case of B mesons, the observation of $\bar{B} \to \pi \ell^- \bar{\nu}$ and $\bar{B} \to \rho \ell^- \bar{\nu}$ represents major milestones in the effort to measure $|V_{ub}|$. Impressive theoretical progress has also been made, and predictions based on HQET, lattice QCD, and other methods have put the subject on a much more solid foundation.

There is a vast literature on this subject. For a theoretical perspective, I particularly recommend the papers describing the ISGW [96] and ISGW2 [97] models, which have played a major role in the development of this subject. Experimentalists have found the ISGW models to be extremely useful because all of the form factors are predicted for a wide variety of modes. Neubert has written a comprehensive review [36] of HQET, which contains much information regarding semileptonic decays. Richman and Burchat [1] have written a review of leptonic and semileptonic decays.

Table 12 lists the branching fractions for exclusive semileptonic decays of D^0, D^+, $\bar{B}^0$, and B^- mesons. Have a look at this table and see what observations you can make. Here are some of my conclusions:

• The branching fractions for the CKM-favored modes ($c \to s$ and $b \to c$) are relatively large. In fact, $B \to D^* \ell^- \bar{\nu}$ has the largest branching fraction of any exclusive B decay.

• There is a remarkable difference between the vector-to-pseudoscalar (V/P) ratios for the CKM-favored D and B decays:

$$\frac{B(D \to K^* \, \mathrm{e}^+ \, \nu_e)}{B(D \to K \, \mathrm{e}^+ \, \nu_e)} \approx 0.55 \qquad \frac{B(B \to D^* \, \mathrm{e}^- \, \bar{\nu}_e)}{B(B \to D \, \mathrm{e}^- \, \bar{\nu}_e)} \approx 2.5 \tag{7.73}$$

• The sizes of $|V_{cd}|^2/|V_{cs}|^2$ and $|V_{ub}|^2/|V_{cb}|^2$ can be crudely estimated from

$$\frac{B(D^+ \to \rho^0 \, \mathrm{e}^+ \, \nu_e)}{B(D^+ \to \bar{K}^{*0} \, \mathrm{e}^+ \, \nu_e)} \approx \frac{0.25\%}{4.8\%} \approx 0.05 \sim \frac{|V_{cd}|^2}{|V_{cs}|^2}$$

$$\frac{B(\bar{B}^0 \to \rho^+ \, \mathrm{e}^- \, \bar{\nu}_e)}{B(\bar{B}^0 \to D^{*+} \, \mathrm{e}^- \, \bar{\nu}_e)} \approx \frac{0.025\%}{4.6\%} \approx 0.005 \sim \frac{|V_{ub}|^2}{|V_{cb}|^2}, \tag{7.74}$$

where differences in phase space and in the form factors are ignored.

• The uncertainties on the branching fractions for the CKM-suppressed $\rho e \nu$ and $\pi e \nu$ modes are quite large, both in B and in D decays, and we do not yet have good measurements of the V/P ratios. The ratios do not appear to be large, however. (See the discussion later in this section on $\bar{B} \to \rho(\pi) \ell^- \bar{\nu}$ for more details on this case.)

• The only mode so far observed to an orbitally-excited state is $B^- \to D_1^0 \ell^- \bar{\nu}$, which has a substantial branching fraction.

For semileptonic decays, there is a vast amount of information be-

Table 12

Measured branching fractions for exclusive D and B meson decays. All values are given in % and confidence levels are at 90%. The results for $B^- \to D_1^0 e^- \bar{\nu}$ and $B^- \to D_2^{*0} e^- \bar{\nu}$ assume that $B(D_1^0 \to D^{*+}\pi^-) = 67\%$ and $B(D_2^{*0} \to D^{*+}\pi^-) = 20\%$. The D_1 is a P-wave charm meson ($L = 1$ relative orbital angular momentum between the c and the light quark); the orbital angular momentum and the light-quark spin S_q are (to a very good approximation) coupled to give $j = L + S_q = 3/2$. The D_2^* is the $j = 3/2$ state with total $J = 2$. Both states are narrow, since they must decay in a D wave, in contrast to the two $j = 1/2$ states, which can decay in an S wave. The large difference between the D^0 and D^+ branching fractions is due to $\tau_{D^+}/\tau_{D^0} \simeq 2.5$. All B branching fractions in the table are from CLEO [101,102,5,108]. Recent world averages for B semileptonic branching fractions are given in Drell [103]. The $D \to K^{(*)} e\nu$ branching fractions are taken from the Particle Data Book [4], and the $D \to \pi e\nu$ and $D \to \rho e\nu$ branching fractions are my averages based on CLEO, E653, E791, E687, and Mark III measurements.

D^0	D^+	$\bar{B}^0$	B^-
$K^- e^+ \nu_e$ 3.63 ± 0.20	$\bar{K}^0 e^+ \nu_e$ 6.7 ± 0.9	$D^+ e^- \bar{\nu}_e$ $1.87 \pm 0.15 \pm 0.32$	$D^0 e^- \bar{\nu}_e$ $1.95 \pm 0.15 \pm 0.34$
$K^{*-} e^+ \nu_e$ 2.01 ± 0.33	$\bar{K}^{*0} e^+ \nu_e$ 4.8 ± 0.5	$D^{*+} e^- \bar{\nu}_e$ $4.56 \pm 0.32 \pm 0.40$	$D^{*0} e^- \bar{\nu}_e$ $5.37 \pm 0.56 \pm 0.67$
			$D_1^0(2420) e^- \bar{\nu}_e$ $0.56 \pm 0.12 \pm 0.09$
			$D_2^{*0}(2460) e^- \bar{\nu}_e$ < 0.8
$\pi^- e^+ \nu_e$ 0.37 ± 0.07	$\pi^0 e^+ \nu_e$ 0.31 ± 0.15	$\pi^+ e^- \bar{\nu}_e$ $(1.8 \pm 0.4 \pm 0.3 \pm 0.2) \times 10^{-2}$	$\pi^0 e^- \bar{\nu}_e$
$\rho^- e^+ \nu_e$ -	$\rho^0 e^+ \nu_e$ 0.25 ± 0.03	$\rho^+ e^- \bar{\nu}_e$ $(2.5 \pm 0.4^{+0.5}_{-0.7} \pm 0.5) \times 10^{-2}$	$\rho^0 e^- \bar{\nu}_e$

yond that conveyed by a table of branching fractions. The additional information is contained in the kinematic distributions and their correlations, which we will examine in this section.

Let's begin with the decays $P \to P'\ell\nu$, where both P and P' are pseudoscalars. From Eq. 7.43, we can see that the q^2 distribution is sensitive not only to the square of the form factor, but also to the p^3 factor arising from the P-wave decay and phase space.

CLEO has observed [98] a signal of about 2700 events in the decay $\bar{D}^0 \to K^- e^+ \nu_e$. The analysis uses over two million $e^+e^- \to c\bar{c}$ events produced in the continuum. The method is to study the decay sequence $D^{*+} \to D^0 \pi^+_{\rm soft}$, $D^0 \to K^- e^+ \nu_e$, in which the signal appears as a peak near zero in the distribution of the reconstructed mass difference $\Delta M =$

$M(K^-\ell^+\pi^+_{\rm soft}) - M(K^-\ell^+)$. Thus, the neutrino four-vector is simply ignored, resulting in a degradation of the ΔM resolution. Nevertheless, the backgrounds are sufficiently low that the q^2 distribution is quite clean, as shown in Figure 37.

As expected from the p_K^3 factor, there is a dramatic decrease in the rate as q^2 increases. The remaining q^2 dependence is in fact very mild and there is as yet very little experimental sensitivity to the curvature. To parametrize the q^2 dependence of the form factors one can use, for example, an exponential form

$$f_+(q^2) = f_+(q^2_{\rm max})e^{-\alpha(q^2_{\rm max}-q^2)} = f_+(0)e^{\alpha q^2} \tag{7.75}$$

or a pole form:

$$f_+(q^2) = \frac{f_+(0)}{1 - q^2/M^2_{\rm pole}}. \tag{7.76}$$

For charm decays, it is traditional to quote form factors at $q^2 = 0$, whereas in $b \to c$ decays, where HQET is applicable, it is more appropriate to give their values at $q^2_{\rm max}$. Figure 38 shows explicitly how the q^2 dependence of the decay rate depends on p_K^3 and the square of the form factor.

The CLEO II data shown in Fig. 37 give [98]

$$\begin{aligned} \alpha &= (0.29 \pm 0.04 \pm 0.06)\ \text{GeV}^{-2} \\ M_{\rm pole} &= (2.00 \pm 0.12 \pm 0.18)\ \text{GeV}. \end{aligned} \tag{7.77}$$

for the exponential and pole forms, respectively. The world-average value of $M_{\rm pole}$ is given in the review by Ryd [99]:

$$M_{\rm pole} = (1.91 \pm 0.09)\ \text{GeV}. \tag{7.78}$$

The expected value of the pole mass for $D \to K\ell^+\nu$ is $M_{D_s^*} = 2.1$ GeV, which is roughly consistent with the measured value. The CLEO II data, together with the D^0 lifetime and the value of $|V_{cs}|$ determined from unitarity, give

$$f_+(0) = 0.76 \pm 0.02 \pm 0.02, \tag{7.79}$$

where the exponential form was used in the integration of the form factor.

The E687 experiment [100] has sufficient sensitivity in the $D \to K\mu\nu$ mode to obtain a rough measurement of the f_- form factor, which only enters for nonzero lepton mass. With 1900 $D \to K\mu\nu$ events, the result is

$$\frac{f_-(0)}{f_+(0)} = -1.3^{+3.6}_{-3.4} \pm 0.6, \tag{7.80}$$

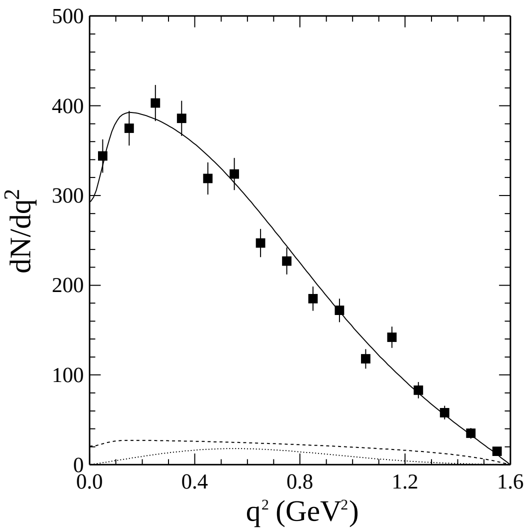

Fig. 37. The q^2 distribution for $D^0 \to K^- \, e^+ \, \bar{\nu}$ measured by CLEO. The points with error bars are the data, the solid curve is the fit to signal plus background, the dashed curve is combinatorial background, and the dotted curve is the background from $D^+ \to \bar{K}^0 \ell^+ \nu$ decays. The dip near $q^2 = 0$ is due to resolution effects.

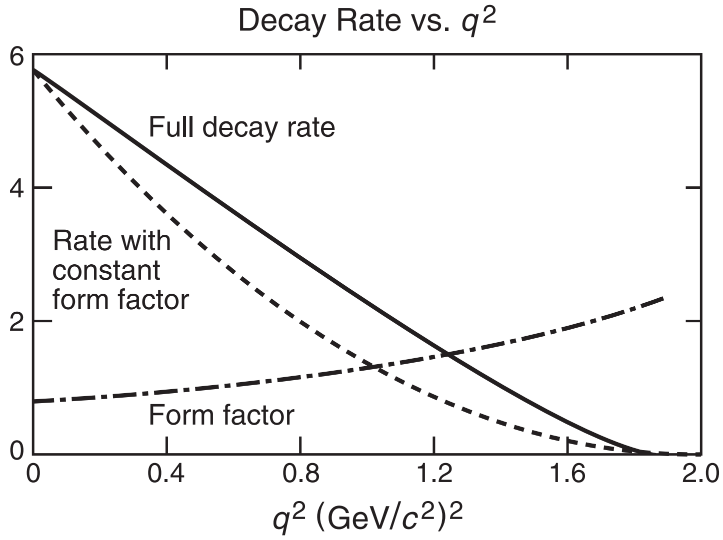

Fig. 38. The q^2 dependence for $D \to K \ell^+ \nu$ is dominated by the p^3 factor arising from the P-wave nature of the amplitude. The solid line shows the full q^2 dependence, the dashed line shows the dependence if the form factor were constant, and the dot-dashed line shows the dependence arising from the squared form factor only. The scale of the vertical axis is arbitrary.

which shows how difficult it is to probe the f_- form factor!

The importance of these results is that we can determine the absolute normalization of the form factor, because $|V_{cs}|$ is independently known from unitarity of the CKM matrix (see Sec. 3). We will use $f_+(0)$ below when we examine the mysteriously small value of the vector-to-pseudoscalar ratio in charm semileptonic decay.

The analogous process in B decays is $\bar{B} \to D\ell^-\bar{\nu}$. Before the development of HQET, many people felt that from a theoretical standpoint, this mode was preferable to $\bar{B} \to D^*\ell^-\bar{\nu}$ for measuring $|V_{cb}|$. The reason was that $\bar{B} \to D\ell^-\bar{\nu}$ depends on only one form factor, while $\bar{B} \to D^*\ell^-\bar{\nu}$ depends on three. At that time, the values of $|V_{cb}|$ were extracted from the *total rate*, which depends on all of the form factors involved in the decay. Experimentally, however, larger backgrounds make it more difficult to measure $\bar{B} \to D\ell^-\bar{\nu}$ than $\bar{B} \to D^*\ell^-\bar{\nu}$. It appeared that the optimal mode for theorists was different from the optimal mode for experimentalists, a situation that occurs all too often!

This picture changed completely with the development of HQET. If we consider $\bar{B} \to D^*\ell^-\bar{\nu}$ at zero recoil, only *one* form factor, $h_{A_1}(w)$, is involved (in the original basis of form factors, $A_1(q^2)$ is the only one contributing at zero recoil). This result can be seen from Eq. 7.61 and Eq. 7.62 (set $w = 1$ and there won't be any dependence on $R_1(w)$ or $R_2(w)$) or from Eq. 7.59 and Eq. 7.60 (set $p_V = p_{D^*} = 0$). Furthermore, the $h_{A_1}(w)$ form factor has no $1/m_Q$ corrections at zero recoil, a result known as Luke's theorem. In contrast, $\bar{B} \to D\ell^-\bar{\nu}$ is suppressed at zero-recoil by the p_D^3 factor, and there are leading $1/m_Q$ corrections. For these reasons, together with its experimental advantages of higher rate and lower background, $\bar{B} \to D^*\ell^-\bar{\nu}$ has become the preferred mode for extracting $|V_{cb}|$. Nevertheless, we should try to measure the CKM elements in as many ways as possible. In addition, it is important to compare the form factor slopes in $\bar{B} \to D\ell^-\bar{\nu}$ and $\bar{B} \to D^*\ell^-\bar{\nu}$ to see if they are essentially identical, as expected in HQET. In the following discussion, I will present results for $\bar{B} \to D\ell^-\bar{\nu}$ and $\bar{B} \to D^*\ell^-\bar{\nu}$ more or less in parallel, since the form factors for these modes are related in HQET, and both are used to extract $|V_{cb}|$.

Figure 39 shows the signals for $B^- \to D^0\ell^-\bar{\nu}$ and $\bar{B}^0 \to D^+\ell^-\bar{\nu}$ in a CLEO II analysis [101]. This measurement used a technique in which the momentum of the neutrino is estimated from the missing momentum in the event. One can then compute ΔE and the beam-energy constrained B mass for each candidate, as discussed in Sec. 4 (Eq. 4.1 and Eq. 4.2). From Fig. 39 it is clear that there is a lot of background, which must be determined with great care. The histograms show that the dominant backgrounds are quite different for the two modes. Why? The $D^0\ell^-\bar{\nu}$ mode has more background from $D^*\ell^-\bar{\nu}$, since all D^{*0} decays and about two-thirds of D^{*+} decays produce D^0's. This problem is therefore much less severe for the $D^+\ell^-\bar{\nu}$ mode, but here there is more combinatorial background, since the D^+ is reconstructed in the three-body decay $D^+ \to K^-\pi^+\pi^+$.

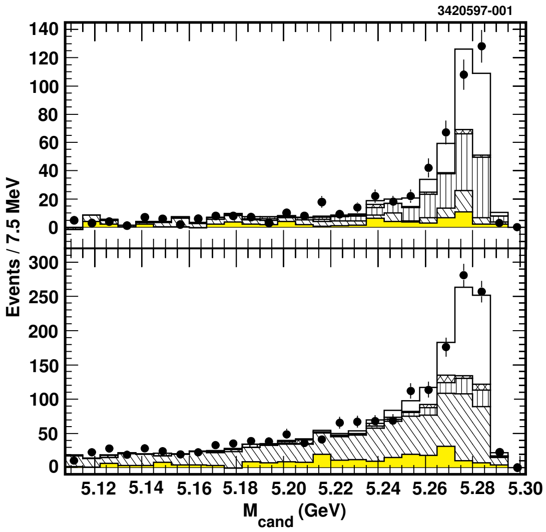

Fig. 39. CLEO II analysis of $\bar{B} \to D\ell^-\bar{\nu}$. The upper figure shows $B^- \to D^0\ell^-\bar{\nu}$, while the lower one shows $\bar{B}^0 \to D^+\ell^-\bar{\nu}$. The points with error bars are the data, the shaded region is the background from continuum events and events with fake leptons, the diagonal hatch region is the combinatoric background, the vertical hatch is the $\bar{B} \to D^*\ell^-\bar{\nu}$ background, and the crosshatch region is $\bar{B} \to D^{**}\ell^-\bar{\nu}$ and other backgrounds. From Ref. [101].

We have already seen the mild w dependence of the $\bar{B} \to D\ell^-\bar{\nu}$ form factor in Fig. 27. Experimentally, there is very little sensitivity to any w dependence beyond the linear term of the Taylor expansion of the form factor about the zero-recoil point. In the HQET basis, $\bar{B} \to D\ell^-\bar{\nu}$ depends on both $h_+(w)$ and $h_-(w)$ (Eq. 7.46), where $h_+(w) \to \xi(w)$ and $h_-(w) \to 0$ in the heavy-quark symmetry limit. The combination of these form factors that appears in Eq. 7.46 can be written as a new function $\mathcal{F}_D(w)$, which also goes to $\xi(w)$ in the heavy-quark symmetry limit:

$$\frac{d\Gamma(\bar{B} \to D\ell^-\bar{\nu})}{dw} = \frac{G_F^2|V_{cb}|^2}{48\pi^3}(m_B + m_D)^2(m_D\sqrt{w^2-1})^3\mathcal{F}_D^2(w), \tag{7.81}$$

where $p_D(w) = m_D\sqrt{w^2-1}$. For $\bar{B} \to D^*\ell^-\bar{\nu}$ we can integrate Eq. 7.58 over all of the angular variables to obtain, in the HQET form-factor basis [36],

$$\frac{d\Gamma(\bar{B} \to D^*\ell^-\bar{\nu})}{dw} = \frac{G_F^2|V_{cb}|^2}{48\pi^3}(m_B - m_D^*)^2 m_{D^*}^3\sqrt{w^2-1}(w+1)^2 \times \left[1 + \frac{4w}{w+1}\frac{m_B^2 - 2wm_Bm_{D^*} + m_{D^*}^2}{(m_B - m_{D^*})^2}\right]\mathcal{F}_{D^*}^2(w), \tag{7.82}$$

where

$$\mathcal{F}_{D^*}(w)^2 = |h_{A_1}(w)|^2\left[1 + \frac{4w}{w+1}\frac{m_B^2 - 2wm_Bm_{D^*} + m_{D^*}^2}{(m_B - m_{D^*})^2}\right]^{-1}\sum_{i=0,\pm1}|\tilde{H}_i(w)|^2 \tag{7.83}$$

and

$$|\tilde{H}_0(w)|^2 = \left[1 + \left(\frac{w-1}{1-r}\right)(1 - R_2(w))\right]^2$$
$$|\tilde{H}_\pm(w)|^2 = \frac{1 - 2wr + r^2}{(1-r)^2}\left[1 \mp \sqrt{\frac{w-1}{w+1}}R_1(w)\right]^2, \tag{7.84}$$

where $r = m_{D^*}/m_B$. (See Eq. 7.61 and Eq. 7.62.) Recall that in the heavy-quark symmetry limit $R_1(w) = R_2(w) = 1$, but that there are corrections to this result in the real world. Thus, the function $\mathcal{F}_{D^*}(w)$ has a rather complicated relationship to the individual form factors. We note that when $R_1(w) = R_2(w) = 1$,

$$\sum_{i=0,\pm1}|\tilde{H}_i(w)|^2 = \left[1 + \frac{4w}{w+1}\frac{m_B^2 - 2wm_Bm_{D^*} + m_{D^*}^2}{(m_B - m_{D^*})^2}\right], \tag{7.85}$$

which explains why this term is explicitly factored out in Eq. 7.82. Measurements of the w distribution by itself are sensitive to $\mathcal{F}_{D^*}(w)$, whereas measurements of the full, correlated kinematic distribution can extract information on all three form factors, as we will see below.

Because the hadronic system is essentially undisturbed at zero recoil, the overlap integral of the initial and final mesons is essentially unity. This statement corresponds to the unit normalization of the Isgur-Wise function, $\xi(1) = 1$. For finite masses, the form factors at zero recoil are computed in the framework of the HQET expansion in $1/m_Q$:

$$\mathcal{F}_D(1) = 0.98 \pm 0.07,$$
$$\mathcal{F}_{D^*}(1) = 0.93 \pm 0.03, \tag{7.86}$$

which are indeed close to unity. The calculation of these values and the understanding of their uncertainties represent a major theoretical effort over the last few years.

In this approach, we need to know the rate at zero recoil ($w = 1$), so that Eq. 7.81 and Eq. 7.82 can be used to extract $|V_{cb}|$. Unfortunately, there is no rate at zero recoil, because phase space goes to zero! This can be seen from Fig. 25 or from Fig. 30. (The width of the physical region of the Dalitz plot in Fig. 25 is equal to the momentum of the daughter hadron in the B rest frame.) As we have seen, $\bar{B} \to D\ell^-\bar{\nu}$ is further suppressed in the zero recoil region by the P-wave effect, which gives the p_D^2 part of the p_D^3 in Eq. 7.81. For these reasons, experiments have had to measure the rate at zero recoil by performing an extrapolation using the full range in w. Since the shape of $\mathcal{F}(w)$ is not known, the extrapolation introduces an additional uncertainty. Fortunately the range in w for both $\bar{B} \to D\ell^-\bar{\nu}$ and $\bar{B} \to D^*\ell^-\bar{\nu}$ is quite modest, $\Delta w = 0.5 - 0.6$ (see Table 7.2), and the form factors are expected to have a nearly linear dependence on w over this range. A common approach is to write $\mathcal{F}(w)$ as a Taylor expansion about the zero-recoil point:

$$\mathcal{F}(w) = \mathcal{F}(1)\left[1 - \hat{\rho}^2(w-1) + \hat{c}(w-1)^2 + ...\right]. \tag{7.87}$$

The notation $\hat{\rho}^2$ is meant to distinguish this slope from ρ^2, the slope of the true Isgur-Wise function (which corresponds to the heavy-quark symmetry limit) and from the slopes of the individual form factors. (For example $\rho^2_{A_1}$ is the slope of the h_{A_1} form factor.) There are different expansion coefficients for $\mathcal{F}_D(w)$ and $\mathcal{F}_D^*(w)$. The $d\Gamma/dw$ distribution are usually fit under various assumptions to explore the sensitivity to the shape of the extrapolation function. Sometimes theoretical predictions are also used to limit the size of the quadratic coefficient $\hat{c}$.

Figure 40 shows the CLEO II measurements [102] of the w distributions for $\bar{B}^0 \to D^{*+}\ell^-\bar{\nu}$ and $B^- \to D^{*0}\ell^-\bar{\nu}$ *before* acceptance corrections are applied. The low detection efficiency for the soft π^+ from $D^{*+} \to D^0\pi^+$ strongly affects the distribution for $\bar{B}^0 \to D^{*+}\ell^-\bar{\nu}$ near $w = 1$. Recall from Sec. 4 that, due to the high magnetic field (1.5 T), such soft pions do not travel very far out into the detector, but instead spiral around multiple times in the inner layers. (The new silicon vertex detector should help to significantly improve this efficiency.) By correcting for the detection efficiency, one can extract the w-dependence of $\mathcal{F}_{D^*}(w)$, as shown in Fig. 41. The extrapolations to $w = 1$ assuming linear and quadratic forms are shown.

The values of $\mathcal{F}(1)|V_{cb}|$ and $\hat{\rho}^2$ measured by CLEO II, ARGUS, and

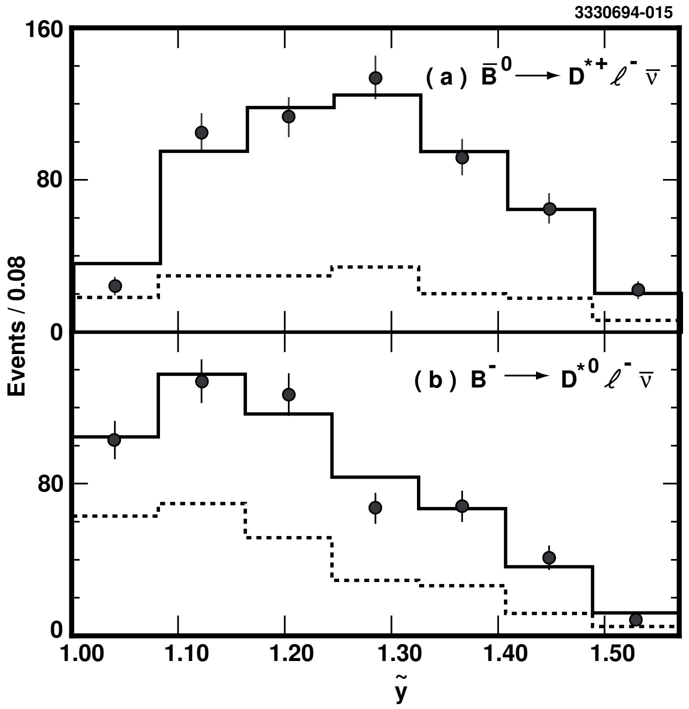

Fig. 40. CLEO II analysis of $\bar{B} \to D^* \ell^- \bar{\nu}$, showing (a) the w distribution (rate) for $\bar{B}^0 \to D^{*+} \ell^- \bar{\nu}$, where the detection efficiency is poor for low values of w, and (b) the w distribution for $B^- \to D^{*0} \ell^- \bar{\nu}$, where the efficiency is better at low w. The variable plotted is called $\tilde{y}$, to emphasize that there is some smearing of the measured quantity due to resolution effects, including the unknown direction of the B meson. (The B momentum is, however, small at the $\Upsilon(4S)$.) The points with error bars are the data, the solid-line histogram shows the best fit (which takes into account acceptance corrections), and the dashed-line histogram shows the contribution from backgrounds. From Ref. [102].

the LEP experiments have been compiled by Drell [103] and are listed in Table 13. (ARGUS was the first experiment to use this technique.) The spread in the values of $\hat{\rho}^2$ is quite large and shows that we have a lot more work to do on this mode. Still, the values of $|V_{cb}|$ are reasonably consistent. The separate averages computed by Drell for $\bar{B} \to D \ell^- \bar{\nu}$ and $\bar{B} \to D^* \ell^- \bar{\nu}$ are listed Table 14.

What measurements allow us to test the predictions of HQET? With data from semileptonic decay, there are essentially two approaches: (1) comparison of the different form factors governing $\bar{B} \to D^* \ell^- \bar{\nu}$ with each other and (2) comparison of $\bar{B} \to D \ell^- \bar{\nu}$ with $\bar{B} \to D^* \ell^- \bar{\nu}$. We can see from Table 14 that the values of $\hat{\rho}^2$ for the two modes are consistent within errors. Figure 34 shows the decay angles that, together with q^2,

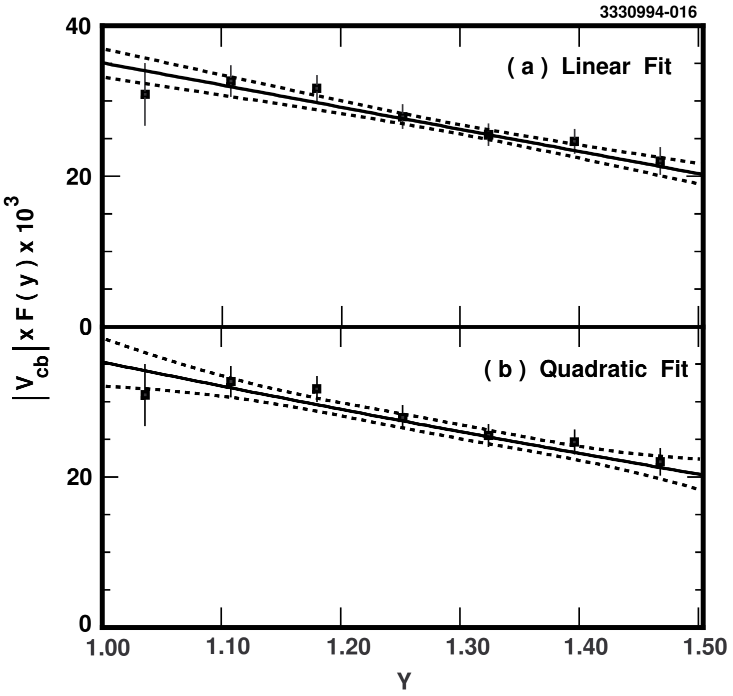

Fig. 41. CLEO II analysis of $\bar{B} \to D^* \ell^- \bar{\nu}$, showing the form factor dependence on the measured value of w. This is not a plot of the rate, but of the amplitude. The data from $\bar{B}^0 \to D^{*+} \ell^- \bar{\nu}$ and $B^- \to D^{*0} \ell^- \bar{\nu}$ have been combined. The upper histogram (a) shows a linear fit to the data, while the lower histogram (b) shows a quadratic fit. The solid lines are the best fit and the dashed lines show the curves allowed within the statistical errors. From Ref. [102].

Table 13
Measurements of $\mathcal{F}(1)|V_{cb}|$ and $\hat{\rho}^2$ using $\bar{B} \to D^* \ell^- \bar{\nu}$ and $\bar{B} \to D \ell^- \bar{\nu}$. From Ref. [103].

Mode	Experiment	$\mathcal{F}(1)\lvert V_{cb}\rvert/10^{-2}$	$\hat{\rho}^2$
$\bar{B} \to D^* \ell^- \bar{\nu}$	ALEPH	$3.21 \pm 0.18 \pm 0.19$	$0.31 \pm 0.17 \pm 0.08$
	DELPHI	$3.69 \pm 0.21 \pm 0.22$	$0.782 \pm 0.187 \pm 0.036$
	OPAL	$3.26 \pm 0.17 \pm 0.22$	$0.42 \pm 0.17 \pm 0.05$
	CLEO	$3.52 \pm 0.19 \pm 0.18$	$0.84 \pm 0.12 \pm 0.08$
	ARGUS	$3.92 \pm 0.39 \pm 0.28$	$1.17 \pm 0.24 \pm 0.06$
$\bar{B} \to D \ell^- \bar{\nu}$	ALEPH	$2.82 \pm 0.68 \pm 0.65$	$-0.05 \pm 0.53 \pm 0.38$
	CLEO	$3.42 \pm 0.44 \pm 0.49$	$0.61 \pm 0.21 \pm 0.13$

are used in the CLEO II measurement [104] of the individual $\bar{B} \to D^* \ell^- \bar{\nu}$ form factors. The form factors are measured by performing a

Table 14

Average values for $|V_{cb}|$ and $\hat{\rho}^2$ from $\bar{B} \to D^*\ell^-\bar{\nu}$ and $\bar{B} \to D\ell^-\bar{\nu}$. The similar values observed for $\hat{\rho}^2$ for the two modes are expected from HQET. From Ref. [103].

Mode	$\lvert V_{cb}\rvert/10^{-2}$	$\hat{\rho}^2$
$\bar{B} \to D^*\ell^-\bar{\nu}$	3.87 ± 0.31	0.71 ± 0.11
$\bar{B} \to D\ell^-\bar{\nu}$	3.94 ± 0.50	0.66 ± 0.19

joint, four-dimensional maximum likelihood fit to these variables. The analysis is performed using $\bar{B}^0 \to D^{*+}\ell^-\bar{\nu}$, where $D^{*+} \to D^0\pi^+$ and $D^0 \to K^-\pi^+$ or $D^0 \to K^-\pi^+\pi^0$. These modes are fairly clean, with a total of 779 signal events over about 161 background events. The D^* signals for the two channels are shown in Fig. 42.

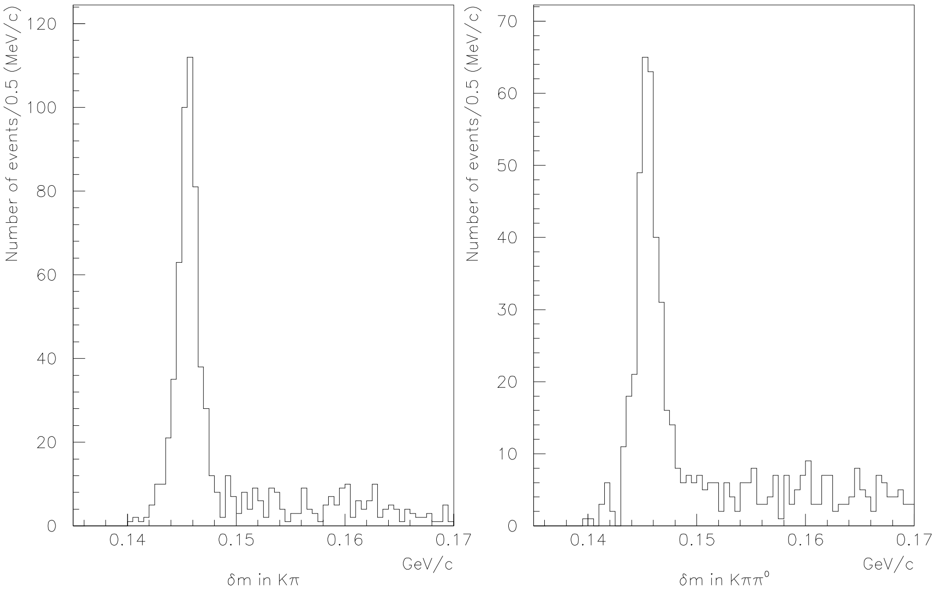

Fig. 42. D^* signals from the CLEO II measurement of the $\bar{B}^0 \to D^{*+}\ell^-\bar{\nu}$ form factors. The figures show the signals in the distributions of the reconstructed $D^* - D$ mass difference $\delta M = (M(K^-\pi^+\pi_s^+) - M(K^-\pi^+))$ (left) and $\delta M = (M(K^-\pi^+\pi^0\pi_s^+) - M(K^-\pi^+\pi^0))$ (right).

Figure 43 shows some of the fit projections for the combined $\bar{B} \to D^*\ell^-\bar{\nu}$ modes. The two upper histograms compare the distributions of

$\cos\theta_V$ in the lower and upper half of the q^2 range. Although acceptance effects, which are taken into account in the fit, gradually reduce the efficiency as $\cos\theta_V$ increases, it is apparent that in the lower q^2 range there is a strong forward-backward-peaking component. At low q^2, the lepton and antineutrino become collinear, with zero net spin along their common direction, forcing the D^* also to have zero helicity. This effect produces a distribution $dN/d\cos\theta_V \propto \cos^2\theta_V$. In contrast, at very high q^2, the D^* is nearly at rest and unpolarized, producing a $\cos\theta_V$ distribution that is uniform, apart from acceptance effects. The lower two histograms show distributions of the azimuthal angle χ for the lower and upper range of $\cos\theta_V$. The correlation between these histograms arises from an interference term proportional to the difference between negative and positive helicity amplitudes, multiplied by the zero helicity amplitude. The observed upward slope of the first histogram (c) and the downward slope of the second histogram (d) are consistent with either $(V-A)(V-A)$ or $(V+A)(V+A)$ couplings, which cannot be distinguished. However, the observed correlation rules out a mixed coupling $(V \mp A)(V \pm A)$.

The fit determines $R_1(w=1)$ and $R_2(w=1)$, as well as the dimensionless form factor slope $\rho^2_{A_1}$ of h_{A_1}. (Since the true form of $h_{A_1}(w)$ is not known, several different functions are tried in addition to a simple linear function with slope $\rho^2_{A_1}$.) Table 15 compares the measured values for $R_1(1)$ and $R_2(1)$ obtained from the combined fit to $\bar{B}^0 \to D^{*+}\ell^-\bar{\nu}$ and $B^- \to D^{*0}\ell^-\bar{\nu}$ with theoretical predictions from Neubert [36], Close and Wambach [105], and the ISGW2 model [97]. Within errors, the measurements are in good agreement with the predictions, and they follow the expected pattern $R_1(1) > 1$ and $R_2(1) < 1$.

In summary, we can say that $R_1(1)$ and $R_2(1)$ are quite consistent with HQET predictions (they are actually consistent with the heavy quark symmetry limit $R_1 = R_2 = 1$ itself), as are the relative sizes of form factor slopes for $\bar{B} \to D\ell^-\bar{\nu}$ and $\bar{B} \to D^*\ell^-\bar{\nu}$. With larger data samples, we can expect substantial improvements in these measurements.

We turn now to measurements of the $D \to K^*\ell^+\nu$ branching fraction and form factors and to the question of the $B(D \to K^*\ell^+\nu)/B(D \to K\ell^+\nu)$ ratio. There has been a long struggle, both experimental and theoretical, to understand the physics of these modes and the low value of the vector-to-pseudoscalar ratio. The $D \to K^*\ell^+\bar{\nu}$ form factors have been measured by several experiments; Fig. 44 shows the distributions from a recent analysis [106] from the E791 charm-hadroproduction ex-

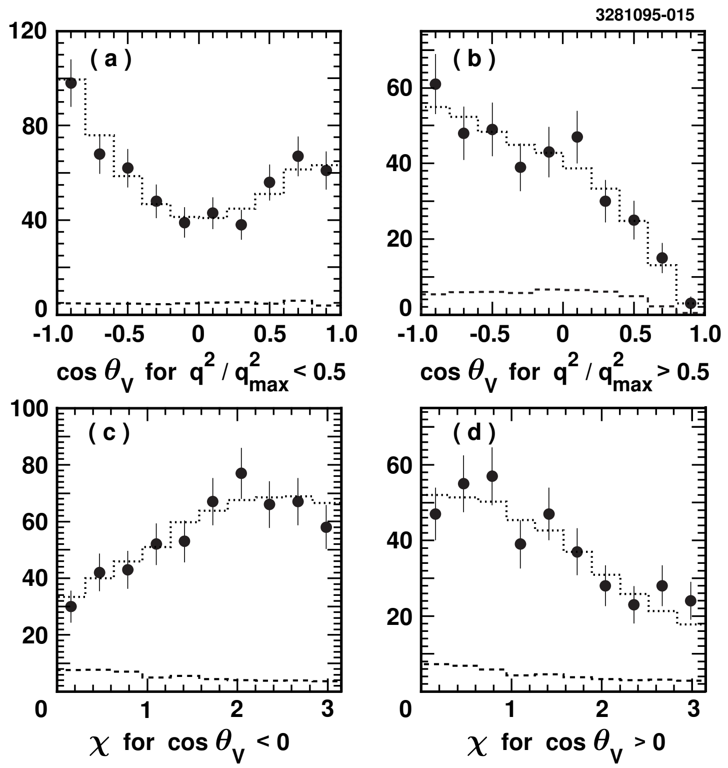

Fig. 43. Distributions of $\cos\theta_V$ and χ in the CLEO II measurement of the $\bar{B} \to D^*\ell^-\bar{\nu}$ form factors. The histograms show (a) $\cos\theta_V$ for the lower half of the q^2 range, (b) $\cos\theta_V$ for the upper half of the q^2 range, (c) χ for the lower half of the $\cos\theta_V$ range, and (d) χ for the upper half of the $\cos\theta_V$ range. The points with error bars are the data; the solid histogram is the fit, including backgrounds; and the dashed line is the contribution from backgrounds. The interpretation of these histograms is discussed in the text. From Ref. [104].

periment at Fermilab. The event sample consists of approximately 3000 $D^+ \to \bar{K}^{*0}e^+\nu_e$, $\bar{K}^{*0} \to K^-\pi^+$ decays, and the kinematic distributions studied are analogous to those measured for $\bar{B} \to D^*\ell^-\bar{\nu}$ (see Fig. 34). Given that HQET is not expected to be applicable to this decay, it is appropriate to fit for the form factor ratios r_V and r_2 (Eq. 7.65) rather than the HQET-motivated ratios R_1 and R_2. The tradition in charm physics is to quote r_V and r_2 at $q^2 = 0$. The E791 measurements are the most precise so far, giving

$$r_V = \frac{V(0)}{A_1(0)} = 1.84 \pm 0.11 \pm 0.08$$

$$r_2 = \frac{A_2(0)}{A_1(0)} = 0.71 \pm 0.08 \pm 0.09. \tag{7.88}$$

Table 15

CLEO II measurements of form factor ratios for $\bar{B} \to D^* \ell^- \bar{\nu}$ and comparison with theoretical predictions. The fit also yields the slope of the form factor $h_{A_1}(w)$ at $w = 1$: $\rho^2_{A_1} = 0.91 \pm 0.15 \pm 0.06$. The value obtained for this slope is sensitive to the shapes assumed for the form factors, but the values of R_1 and R_2 are relatively insensitive.

	$R_1(w=1)$	$R_2(w=1)$
CLEO II	$1.18 \pm 0.30 \pm 0.12$	$0.71 \pm 0.22 \pm 0.07$
Neubert	1.3 ± 0.1	0.8 ± 0.2
Close & Wambach	1.15	0.91
ISGW2	1.27	1.01

Table 16

Comparison of form factors for $D^+ \to K^{*0} e^+ \nu_e$ measured by E791 with ISGW2 model predictions.

	$A_1(0)$	$A_2(0)$	$V(0)$
E791	0.58 ± 0.03	0.41 ± 0.06	1.06 ± 0.09
	$A_1(q^2_{\max})$	$A_2(q^2_{\max})$	$V(q^2_{\max})$
E791	0.68 ± 0.04	0.48 ± 0.08	1.35 ± 0.12
ISGW2	0.70	0.94	1.52

Using the measured rate and the value of $|V_{cs}|$ determined from unitarity, the absolute scale of the form factors can be determined, and the values are given in Table 16, along with predictions from the ISGW2 model.

Figure 45 shows a comparison [107] of the experimental averages for the $D \to K \ell^+ \nu$ and $D \to K^* \ell^+ \nu$ form factors at $q^2 = 0$ with theoretical predictions from lattice calculations. There is good agreement between theory and experiment on the single form factor $f_+(0)$ for $D \to K \ell^+ \nu$. (The value of $|V_{cs}|$ determined from unitarity is used to set the scale.) In contrast, the more precise predictions for the $D \to K^* \ell^+ \nu$ form factors, in particular $A_1(0)$ (which is the most important one for the overall rate), tend to be higher than what is measured. We can conclude that at some level the overall rate for $D \to K \ell^+ \nu$ is understood, but that the rate for $D \to K^* \ell^+ \nu$ is lower than expected. It will be interesting to see how this puzzle is ultimately resolved.

The measurement of exclusive $B \to X_u \ell^- \bar{\nu}$ decays is one of the major goals of B physics. With improvements in lattice QCD and

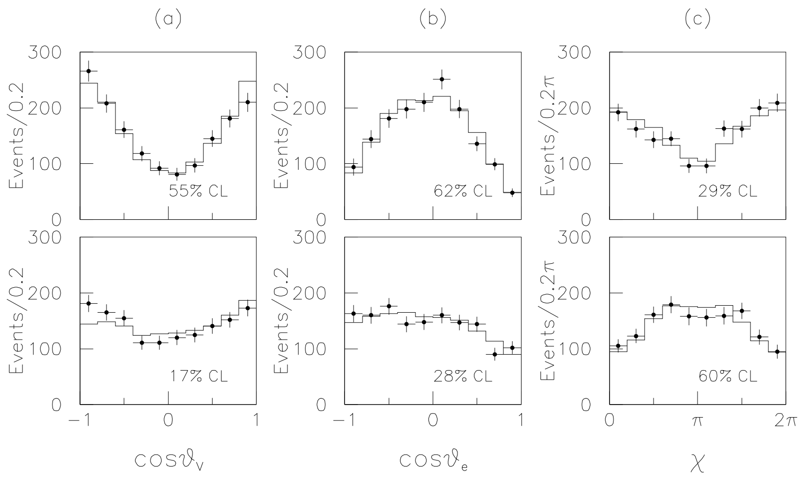

Fig. 44. E791 $D \to K^* \ell^+ \nu$ analysis. The points with error bars are the data and the histograms are the best-fit predictions, which incorporate acceptance effects. The plots are (a) $\cos\theta_V$ for $q^2/q^2_{\max} \leq 0.5$ (upper), and $q^2/q^2_{\max} > 0.5$ (lower); (b) $\cos\theta_e$ for $q^2/q^2_{\max} \leq 0.5$ (upper), and $q^2/q^2_{\max} > 0.5$ (lower); and (c) χ for $\cos\theta_V \leq 0$ (upper) and $\cos\theta_V > 0$ (lower). The low q^2 region has a larger fraction of helicity zero, which is manifested as a larger forward-backward peaking component of K's from $K^* \to K\pi$ ($\cos\theta_V$). We also see a dramatic change in the lepton-energy distribution: at low q^2, the leptons tend to come out at 90 deg to the W direction; at higher q^2 they are more backward peaked, in contrast to the situation in B decays, where the forward peaking leads to a hard lepton spectrum. The azimuthal angle χ shows a strong dependence on $\cos\theta_V$. Figure used with permission.

other theoretical methods, the uncertainties in predicting the rate for exclusive $B \to X_u \ell^- \bar{\nu}$ modes should become smaller than those for the inclusive endpoint spectrum, and hence provide a more precise value of $|V_{ub}|$.

For $B \to X_u \ell^- \bar{\nu}$ decays, unlike $B \to X_c \ell^- \bar{\nu}$, model predictions indicate that the rate should be distributed over many exclusive channels, with no dominant modes. The hadronic system X_u can range over much of the light-quark hadron spectrum, including radially excited and P-wave mesons. However, this picture is somewhat modified for the lepton-spectrum endpoint region, where the backgrounds from $B \to X_c \ell^- \bar{\nu}$ are suppressed and experimental sensitivity is best. In this region, theoretical models indicate that a small number of exclusive decays are dominant: $B^- \to \rho^0 \ell^- \bar{\nu}$, $\bar{B}^0 \to \rho^+ \ell^- \bar{\nu}$, $B^- \to \omega \ell^- \bar{\nu}$, $\bar{B}^0 \to \pi^+ \ell^- \bar{\nu}$ and $B^- \to \pi^0 \ell^- \bar{\nu}$. A key prediction, which is essentially model independent, is that the lepton spectra for the decays to final states with vector mesons are expected to peak at very high energy,

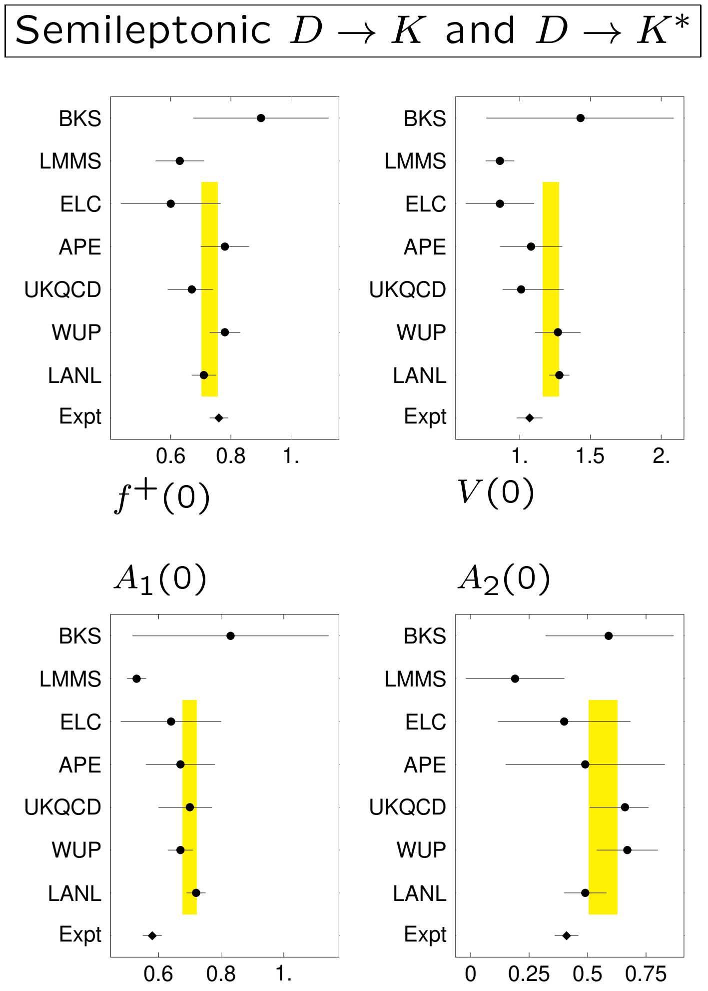

Fig. 45. Comparison of experimental average values with lattice predictions for $D \to K\ell^+\nu$ ($f^+(0)$) and $D \to K^*\ell^+\nu$ ($A_1(0)$, $A_2(0)$, and $V(0)$) form factors. (Figure provided by J. Flynn.)

as discussed in Sec. 7.2. Figure 46 shows predictions for lepton-energy and q^2 distributions from a calculation in which lattice results are used to constrain a form factor model. Figure 47 shows the results of a calculation by Ball [109] of the $\bar{B} \to \rho\ell^-\bar{\nu}$ form factors and a comparison with lattice results. There is considerable variation of some of the form factors over the q^2 range, especially in comparison with those from $\bar{B} \to D^*\ell^-\bar{\nu}$.

The rates for $B^- \to \rho^0\ell^-\bar{\nu}$ and $\bar{B}^0 \to \rho^+\ell^-\bar{\nu}$ are connected by

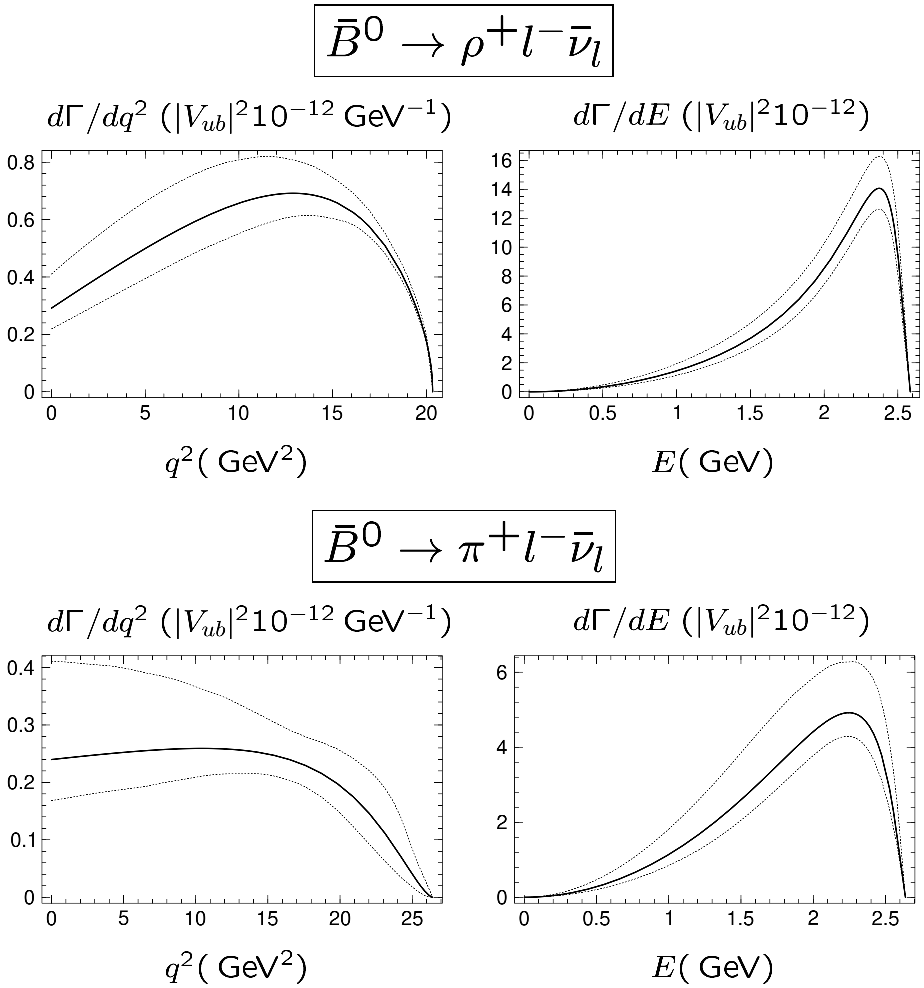

Fig. 46. Predictions for E_ℓ and q^2 distributions for $\bar{B} \to \rho\ell^-\bar{\nu}$ and $\bar{B} \to \pi\ell^-\bar{\nu}$. These curves are based on a calculation in which lattice results are used to constrain a form factor model. Note the sharply peaked lepton-energy spectrum for $B \to \rho\ell^-\bar{\nu}$. The solid curves are the central-value predictions, while the dotted curves are allowed within one-sigma errors. Figure provided by J. Flynn.

isospin symmetry, since the B^- and $\bar{B}^0$ have the same space and spin wave functions in this limit, as do the ρ^0 and ρ^+. A simple way to see this is to note that the ρ^0 flavor-wave function is $(1/\sqrt{2})(u\bar{u} - d\bar{d})$, while that for the ρ^+ is $u\bar{d}$. For $B^- \to \rho^0\ell^-\bar{\nu}$ decay, the flavor wave-function projection of the daughter $u\bar{u}$ system onto the ρ^0 therefore gives $1/\sqrt{2}$ in the amplitude, whereas for $\bar{B}^0 \to \rho^+\ell^-\bar{\nu}$, the projection

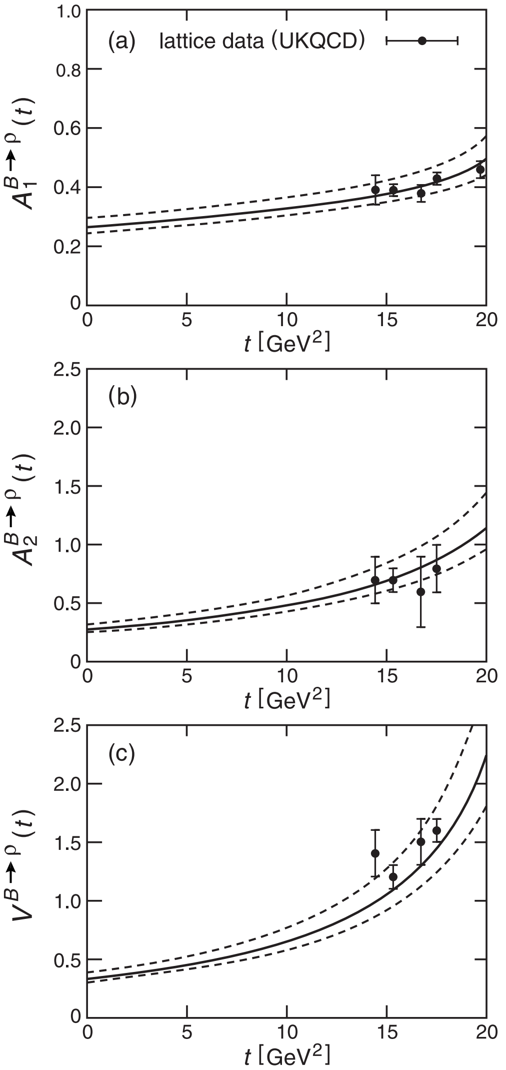

Fig. 47. Calculation of the form factors with $t = q^2$ for $\bar{B} \to \rho\ell^-\bar{\nu}$ by P. Ball using line-cone sum rules (curves) and by the UKQCD lattice collaboration (points with error bars). The variation with q^2 is especially dramatic for the V form factor. Figure provided by P. Ball.

of the daughter $u\bar{d}$ system onto the ρ^+ gives unity. Isospin symmetry tells us that in all other respects the decays are the same. Although the rate for $B^- \to \omega\ell^-\bar{\nu}$ cannot be related to these by a flavor symmetry, it is expected in the quark model to be approximately equal to that for $B^- \to \rho^0\ell^-\bar{\nu}$. Thus,

$$\Gamma(\bar{B}^0 \to \rho^+\ell^-\bar{\nu}) = 2\Gamma(B^- \to \rho^0\ell^-\bar{\nu}) \approx 2\Gamma(B^- \to \omega\ell^-\bar{\nu})$$

$$\Gamma(\bar{B}^0 \to \pi^+\ell^-\bar{\nu}) = 2\Gamma(B^- \to \pi^0\ell^-\bar{\nu}) \tag{7.89}$$

In reality, there may be a small amount of isospin violation due to $\rho^0-\omega$ mixing, so these relationships may be affected to some extent [110,111].

The CLEO II measurement [5] of $\bar{B} \to \pi\ell^-\bar{\nu}$ and $\bar{B} \to \rho\ell^-\bar{\nu}$ is unusual in that it relies on the very good solid-angle coverage (hermeticity) of the detector to associate the neutrino momentum with the missing momentum in the event:

$$(E_\nu, \mathbf{p}_\nu) = (|\mathbf{p}_{\text{miss}}|, \mathbf{p}_{\text{miss}}), \tag{7.90}$$

where

$$\mathbf{p}_{\text{miss}} = \sum_\alpha \mathbf{p}_\alpha. \tag{7.91}$$

Here the index α runs over the charged tracks and neutral clusters detected in the calorimeter. Although it might appear obvious that the neutrino momentum should be identified with the missing momentum, there are a great many effects that can contribute to missing momentum other than a neutrino, such as undetected K_L^0s or mismeasured tracks. To achieve good resolution on the neutrino four momentum, a detailed understanding of these effects is required, as we will discuss below.

Using the neutrino four vector, one proceeds as in a hadronic analysis. As discussed in Sec. 4 (Eq. 4.2 and Eq. 4.1), we define ΔE, the energy difference between the candidate B decay products and the beam energy

$$\Delta E = (E_\nu + E_\ell + E_\pi) - E_{\text{beam}}, \tag{7.92}$$

and m_B, the beam-energy constrained mass:

$$M_B = [E^2_{\text{beam}} - (|\mathbf{p}_\nu + \mathbf{p}_\ell + \mathbf{p}_\pi|^2)]^{1/2}. \tag{7.93}$$

Signal events are expected to have $\Delta E \approx 0$ and m_B peaking at the B mass. The real question is what resolution can be achieved in these quantities, and at what expense in detection efficiency.

Although the identification of neutrino momentum with the missing momentum in the event has been used in many other experiments, in particular at hadron colliders, the CLEO II analysis is able to take the method a step further by carefully selecting events such that the neutrino momentum is measured well. Events are required to have only one lepton to ensure that only one neutrino is present, and events with large missing mass (for example, from undetected K_L^0s) are removed by requiring $M^2_{\text{miss}}/2E_{\text{miss}} < 300$ MeV. With these and other cuts to suppress spurious tracks and clusters, the resolution on ΔE is 110 MeV (about 5%), the resolution on the neutrino direction is about 6deg, and the resolution on the beam-energy constrained mass is 7.5 MeV/c^2. The cuts required to achieve good resolution result in rather low signal efficiencies: $\epsilon = 1.5\%$ for $\bar{B}^0 \to \rho^+\ell^-\bar{\nu}$ and $\epsilon = 2.3\%$ for $\bar{B}^0 \to \pi^+\ell^-\bar{\nu}$.

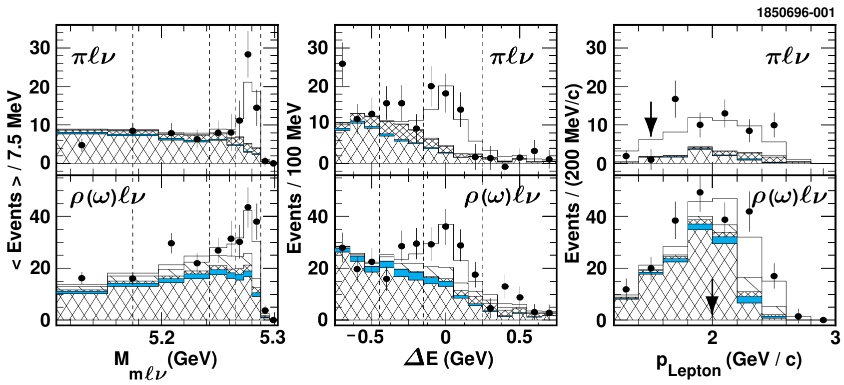

Fig. 48. CLEO II analysis of exclusive $\bar{B} \to X_u\ell^-\bar{\nu}$ decays. The histograms show the beam-energy constrained mass of the candidate $\bar{B} \to m\ell^-\bar{\nu}$ decay products (left), the ΔE distribution (middle), and the lepton-energy distribution (right). The upper plots are for the $\bar{B} \to \pi\ell^-\bar{\nu}$ channel, while the lower plots are for the combined vector-meson (ρ^0, ρ^+, and ω) channels. The points with error bars are the data after subtraction of continuum background and fake-lepton events. The coarse crosshatch, grey, and unshaded components are $b \to cX$, $b \to H_u\ell^-\bar{\nu}$, and signal components, respectively, where H_u represents higher-mass non-charm states. For the π modes, the fine crosshatch shows the vector $\to \pi$ cross-feed and the single hatch the $\pi \to \pi$ cross-feed. For the vector modes, the fine cross-hatch shows the $\pi \to$ vector cross-feed and the single hatch shows the vector $\to$ vector cross-feed. The arrows in the lepton-momentum histograms show the cuts on lepton momentum. From Ref. [5].

As in any $\bar{B} \to X_u\ell^-\bar{\nu}$ analysis, there are large backgrounds from $\bar{B} \to X_c\ell^-\bar{\nu}$. These and other backgrounds are incorporated into a joint fit in the $(\Delta E, m_B)$ plane for the five modes $B^- \to \pi^0\ell^-\bar{\nu}$, $\bar{B}^0 \to \pi^+\ell^-\bar{\nu}$, $B^- \to \rho^0\ell^-\bar{\nu}$, $\bar{B}^0 \to \rho^+\ell^-\bar{\nu}$, and $B^- \to \omega\ell^-\bar{\nu}$. For the ρ and ω modes, the $M(\pi\pi)$ and $M(\pi^+\pi^-\pi^0)$ distributions are also included in the fit. Because there are enormous $\bar{B} \to X_c\ell^-\bar{\nu}$ backgrounds, except for relatively high lepton momenta, leptons are required to have $p_\ell >$ 1.5 GeV/c for the $\pi\ell^-\bar{\nu}$ modes and $p_\ell >$ 2.0 GeV/c for $\rho\ell^-\bar{\nu}$ modes. These and other cuts introduce a model dependence into the branching fractions, because theoretical models must be used to extrapolate the rate over the full phase space. Figure 48 shows the projections of the fit onto m_B, ΔE, and lepton momentum. Small but significant signals are evident for both $\bar{B} \to \pi\ell^-\bar{\nu}$ and $\bar{B} \to \rho\ell^-\bar{\nu}$. (The charged and neutral modes are constrained in the fit by the isospin relation given in Eq. 7.89.)

Figure 49 shows the ρ signal in the $\pi\pi$ mass distribution. No significant signal is seen in $\omega\ell^-\bar{\nu}$, but the efficiency is lower in this channel. Figure 50 lists the branching fractions obtained using various models to determine the detection efficiencies. The efficiencies depend on the *shapes* of the distributions from the models, *not on their absolute normalizations.* The CLEO II results can be used to test the various predictions for the ratio $\Gamma(\bar{B} \to \rho\ell^-\bar{\nu})/\Gamma(\bar{B} \to \pi\ell^-\bar{\nu})$; the Körner-Schuler model is only consistent with the measurement at the 0.5% level, and it is not used in the subsequent averages over models, which give

$$\begin{aligned} B(\bar{B}^0 \to \pi^+\ell^-\bar{\nu}) &= (1.8 \pm 0.4 \pm 0.3 \pm 0.2) \times 10^{-4} \\ B(\bar{B}^0 \to \rho^+\ell^-\bar{\nu}) &= (2.5 \pm 0.4^{+0.5}_{-0.7} \pm 0.5) \times 10^{-4}, \end{aligned} \tag{7.94}$$

where the errors are statistical, systematic, and the estimated model dependence, respectively.

The vector-to-pseudoscalar ratio can be extracted from the fits, although the results are again model dependent. The value averaged over the different models studied is

$$\frac{B(\bar{B}^0 \to \rho^+\ell^-\bar{\nu})}{B(\bar{B}^0 \to \pi^+\ell^-\bar{\nu})} = 1.4^{+0.6}_{-0.4} \pm 0.3 \pm 0.4, \tag{7.95}$$

where the first error is statistical, the second systematic, and the third reflects the model dependence. This result is an indication that the vector-to-pseudoscalar ratio may be lower here than for the $b \to c$ modes.

Figure 51 shows the values of $|V_{ub}|$ extracted from the CLEO II measurements and the various models. In contrast to the measurements of branching fractions, $|V_{ub}|$ does depend on the absolute normalization of rates predicted by the models. For each model, the value of $|V_{ub}|$ is obtained by constraining the ρ/π ratio to the value predicted by that model. A final value [5] for $|V_{ub}|$ is then calculated by averaging over several models and explicitly incorporating an uncertainty due to the model dependence:

$$|V_{ub}| = (3.3 \pm 0.2^{+0.3}_{-0.4} \pm 0.7) \times 10^{-3}, \tag{7.96}$$

where the uncertainties are statistical, systematic, and the estimated model dependence, respectively. It is quite encouraging that this result is consistent with the value from the inclusive endpoint spectrum

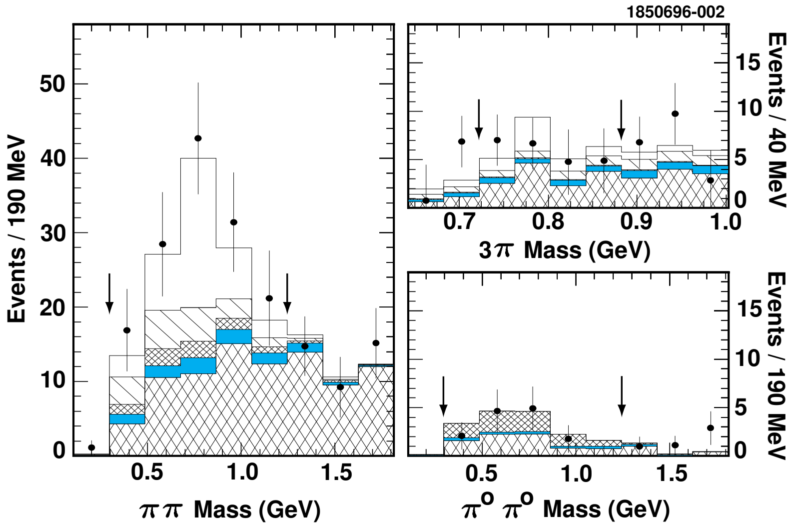

Fig. 49. CLEO II analysis of $\bar{B} \to \rho\ell^-\bar{\nu}$. The histograms show the reconstructed mass distributions for $\rho \to \pi\pi$ (left), $\omega \to 3\pi$ (top right), and for $\pi^0\pi^0$ (bottom right; no signal expected) in the $(M_{m\ell\nu}, \Delta E)$ signal bin. The arrows indicate the mass ranges included in the fit. From Ref. [5].

analysis, $|V_{ub}| = (3.1 \pm 0.8) \times 10^{-3}$. There is certainly a long way to go in determining a precise value for $|V_{ub}|$, and with larger data samples there will be both detailed studies of the kinematic distributions for $\bar{B} \to \pi\ell^-\bar{\nu}$ and $\bar{B} \to \rho\ell^-\bar{\nu}$ and measurements of additional modes.

8. Hadronic Decays, Lifetimes, and Rare Decays

8.1. Hadronic Decays

The decays of B and D mesons into final states consisting only of hadrons are called nonleptonic or hadronic decays. I will use the latter term, even though it is considered imprecise by some people! These modes are much more complicated than leptonic or semileptonic decays, because all of the particles involved can interact strongly. Furthermore, there is no rigorous way even to parametrize the effects of the strong interaction in terms of form factors. Nevertheless, there are many aspects of hadronic bottom and charm decays that can be understood, and there are situations in which quantitative predictions are possible.

Here are some of the key questions that relate to these modes:

- Can we construct any framework that allows us to think about

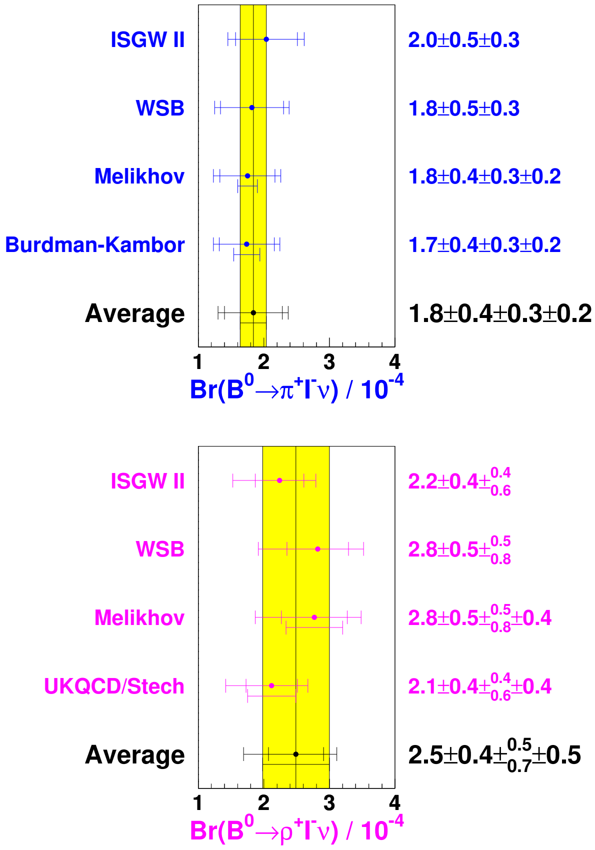

Fig. 50. CLEO II branching fractions for $\bar{B}^0 \to \rho^+\ell^-\bar{\nu}$ and $\bar{B}^0 \to \pi^+\ell^-\bar{\nu}$. The model dependence arises because the detection efficiency depends on the predicted kinematic distributions for lepton energy and other variables. Figure provided by L. Gibbons.

hadronic decays? Can we explain the patterns that appear in values of measured B branching fractions?

- What role do interference effects play in hadronic decays?
- What role do final-state interactions play in hadronic decays?
- What are the inclusive properties of hadronic decays? For example, what is the mean number of c and $\bar{c}$ quarks produced per B decay? What does the inclusive D^* momentum spectrum look like?
- How can we explain the striking observation that $\tau(D^+)/\tau(D^0) \simeq 2.5$, whereas $\tau(B^+)/\tau(B^0) \simeq 1$? In the spectator model, where the D^+ and D^0 lifetimes are essentially determined by the decay rate of the charm quark alone, this result is quite unexpected. A related question is whether the large lifetime ratio is due to an enhancement of the D^0

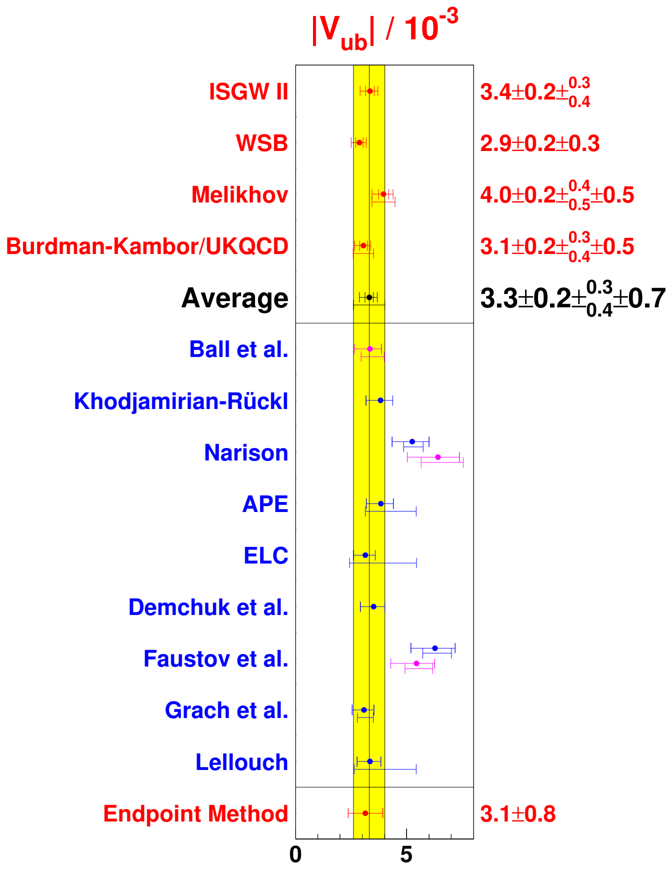

Fig. 51. Values of $|V_{ub}|$ extracted from the CLEO II measurements of $\bar{B} \to \rho\ell^-\bar{\nu}$ and $\bar{B} \to \pi\ell^-\bar{\nu}$. Model dependence enters mainly in relating the overall decay rate to $|V_{ub}|$, but also in determining the detection efficiencies, which depend on the predicted kinematic distributions. The value of $|V_{ub}|$ extracted from the analysis of the inclusive lepton spectrum endpoint region is also shown, and it is consistent with the results from the exclusive analyses. Figure provided by L. Gibbons.

decay rate or to a suppression of the D^+ decay rate.

Some useful review articles on hadronic decays are Browder *et al.* [112] and Neubert and Stech [113], and Neubert *et al.* [114], all of which contain extensive references. The early paper of Bauer, Stech, and Wirbel [115] was among the first to use factorization to make systematic predictions for two-body charm and bottom decays.

Let's begin by trying to make sense of some of the data on exclusive hadronic B decays. Table 17 lists some branching fractions for a selected set of two-body modes. Most of the decays listed involve D or

Table 17

Branching fractions for some hadronic B^- and $\bar{B}^0$ decays. The $D^{(*)}\pi$ and $D^{(*)}\rho$ values are from recent CLEO II measurements [117,118]. One more significant figure is quoted in the references, and a detailed breakdown of contributions to the uncertainties is given. The uncertainties are somewhat correlated due to common D and D^* branching fractions. The $J/\psi K^{(*)}$ branching fractions are from the 1997 Particle Data Book [4]. All confidence levels are at 90%. This table does not list all branching fractions with measured non-zero values; in particular, two-body decays with other charmonium systems ($J/\psi(2S)$, $\chi_{c1}(1P)$) have been observed. What is the $a_1^-(1260)$? It's a very broad ($\Gamma \approx 400$ MeV) isovector ($I = 1$) state with $\ell = 1$ orbital excitation and $J^P = 1^+$.

$\bar{B}^0$ decay	BR (%)	B^- decay	BR (%)
$D^+\pi^-$	0.25 ± 0.04	$D^0\pi^-$	0.47 ± 0.04
$D^{*+}\pi^-$	0.23 ± 0.03	$D^{*0}\pi^-$	0.39 ± 0.06
$D^+\rho^-$	0.79 ± 0.14	$D^0\rho^-$	0.92 ± 0.11
$D^{*+}\rho^-$	0.73 ± 0.10	$D^{*0}\rho^-$	1.28 ± 0.19
$D^0\pi^0$	< 0.01		
$D^{*0}\pi^0$	< 0.04		
$D^0\rho^0$	< 0.04		
$D^{*0}\rho^0$	< 0.06		
$D^+a_1^-$	0.83 ± 0.17	$D^0a_1^-$	0.89 ± 0.15
$D^{*+}a_1^-$	1.16 ± 0.20	$D^{*0}a_1^-$	1.60 ± 0.35
$J/\psi\bar{K}^0$	0.09 ± 0.02	$J/\psi K^-$	0.10 ± 0.01
$J/\psi\bar{K}^{*0}(892)$	0.15 ± 0.02	$J/\psi K^{*-}(892)$	0.17 ± 0.04

D^* mesons and proceed through the dominant $b \to c$ transition. Examine these data, make comparisons, and write down any interesting conclusions or conjectures you might have. Note that a comparison of $\bar{B}^0$ and B^- branching fractions is equivalent to a comparison of decay rates to a good approximation, because the lifetimes of these particles are very nearly the same. You might also find it useful to draw a few Feynman diagrams, but don't attempt any elaborate calculations! The CLEO II signals for the $D^*\pi$, $D^*\rho$, and D^*a_1 modes are shown in Fig. 52.

Here are some observations:

(i) All of the branching fractions are less than 2%.

(ii) $B^0 \to X^0 Y^0 / B^0 \to X^+ Y^-$ comparison:

$$\frac{B(\bar{B}^0 \to D^0 \pi^0)}{B(\bar{B}^0 \to D^+ \pi^-)} \ll 1 \qquad \frac{B(\bar{B}^0 \to D^{*0} \pi^0)}{B(\bar{B}^0 \to D^{*+} \pi^-)} \ll 1$$

(iii) $D^* \pi / D \pi$ comparison:

$$\frac{B(\bar{B}^0 \to D^{*+} \pi^-)}{B(\bar{B}^0 \to D^+ \pi^-)} \approx 1 \qquad \frac{B(B^- \to D^{*0} \pi^-)}{B(B^- \to D^0 \pi^-)} \approx 1$$

(iv) $D^* \rho / D \rho$ comparison:

$$\frac{B(\bar{B}^0 \to D^{*+} \rho^-)}{B(\bar{B}^0 \to D^+ \rho^-)} \approx 1 \qquad \frac{B(B^- \to D^{*0} \rho^-)}{B(B^- \to D^0 \rho^-)} \approx 1$$

(v) $D^{(*)} \rho / D \pi$ comparisons:

$$\frac{B(\bar{B}^0 \to D^+ \rho^-)}{B(\bar{B}^0 \to D^+ \pi^-)} \approx 3 \qquad \frac{B(B^- \to D^0 \rho^-)}{B(B^- \to D^0 \pi^-)} \approx 2$$

$$\frac{B(\bar{B}^0 \to D^{*+} \rho^-)}{B(\bar{B}^0 \to D^{*+} \pi^-)} \approx 3 \qquad \frac{B(B^- \to D^{*0} \rho^-)}{B(B^- \to D^{*0} \pi^-)} \approx 3$$

(vi) B^- / B^0 comparisons:

$$\frac{B(B^- \to D^0 \pi^-)}{B(\bar{B}^0 \to D^+ \pi^-)} > 1 \qquad \frac{B(B^- \to D^{*0} \pi^-)}{B(\bar{B}^0 \to D^{*+} \pi^-)} > 1$$

$$\frac{B(B^- \to D^0 \rho^-)}{B(\bar{B}^0 \to D^+ \rho^-)} > 1 \qquad \frac{B(B^- \to D^{*0} \rho^-)}{B(\bar{B}^0 \to D^{*+} \rho^-)} > 1$$

(vii) The only observed $\bar{B}^0$ decays to neutral+neutral final states involve $c\bar{c}$ mesons.

The first observation, that all of the branching fractions are below 2%, tells us that even many of the most "natural" two-body hadronic B decays have small rates. (Of all B decays, the largest branching fraction for an exclusive mode is $B(\bar{B} \to D^* \ell^- \bar{\nu}) \approx 5\%$.) We can contrast this observation with the situation in D decays, where there are some modes with very substantial branching fractions, such as $B(D^0 \to K^- \rho^+) = (10.7 \pm 1.0)\%$ and $B(D^+ \to \bar{K}^0 \rho^+) = (6.6 \pm 2.5)\%$. Thus, two-body modes are much more dominant in D decays than in B decays. We also

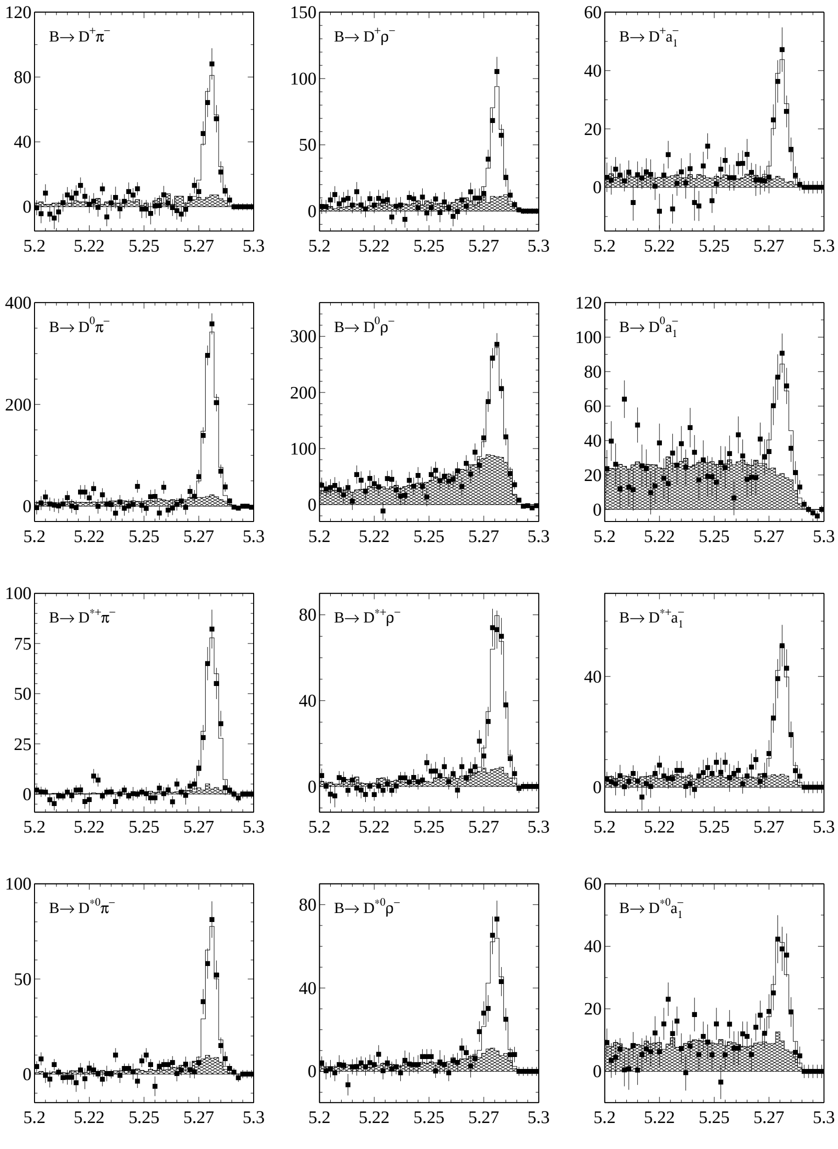

Fig. 52. CLEO II studies of B decays to exclusive hadronic final states. The distributions show the beam-energy constrained B mass reconstructed in various final states with a D or D^* meson and and a light meson π, ρ, or a_1.

see that the inclusive D^{*+} momentum spectrum in B decays, shown in Fig. 53, is very broad, with no visible narrow peaks corresponding to two-body processes.

The second observation compares $\bar{B}^0$ decays to neutral+neutral

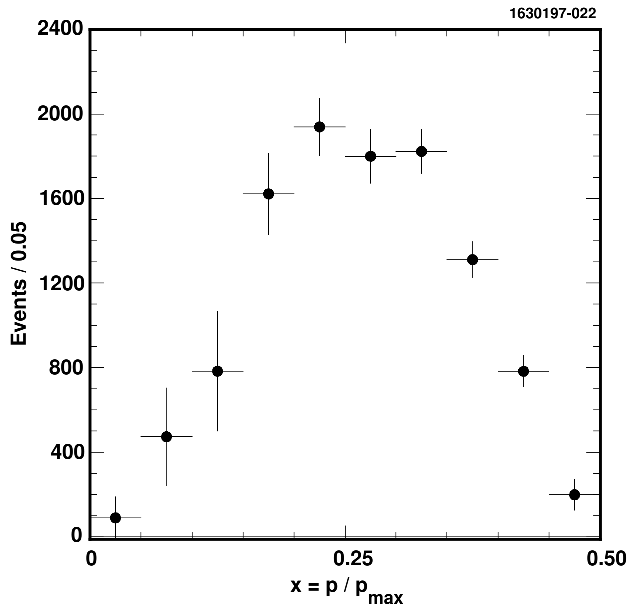

Fig. 53. CLEO II measurement of the inclusive D^{*+} spectrum in B decay. The scaled momentum variable is defined as $x = p/p_{\max}$, $p_{\max} = 4.950$ GeV/c.

(X^0Y^0) final states with decays to charged+charged (X^+Y^-) final states. It is clear that the X^0Y^0 modes are strongly suppressed: none of the $\bar{B}^0 \to D^{(*)0}\pi^0$ or $\bar{B}^0 \to D^{(*)0}\rho^0$ modes have even been observed yet, and the limits are at least an order of magnitude below the X^+Y^- branching fractions. The only observed X^0Y^0 modes involve $c\bar{c}$ bound states. Contrast these results with $B(K_s^0 \to \pi^+\pi^-)/B(K_s^0 \to \pi^0\pi^0) \approx 2$, or with $B(D^0 \to K^-\pi^+) = (3.83 \pm 0.12)\%$ and $B(D^0 \to \bar{K}^0\pi^0) = (2.11 \pm 0.21)\%$.

Figure 54 compares the external and internal spectator diagrams for $\bar{B}^0$ and B^- decay. In $\bar{B}^0$ decay, the external spectator diagram leads to the X^+Y^- final states, while the internal spectator diagram leads to the X^0Y^0 final states. The data therefore indicate that the internal spectator diagram is highly suppressed relative to the external spectator. This observation makes the contrast with K and D decays even more interesting. Internal spectator diagrams in B decay are often said to be color suppressed, since the quarks from the W decay, which are produced as a color-singlet system, do not in general have the correct colors to form color-singlet systems with the other quarks in the process. For B^- decay, the two types of diagrams can lead to the same final state X^0Y^-, so interference effects can occur.

The third observation notes that the $D^*\pi$ final state doesn't get

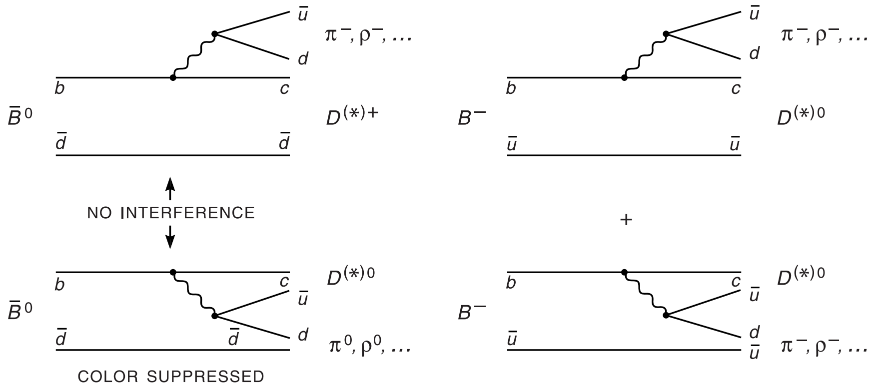

Fig. 54. Comparison of $\bar{B}^0$ and B^- external and internal spectator decays. For $\bar{B}^0$ decay, the two types of processes lead to distinct final states X^-Y^+ and X^0Y^0, which therefore do not interfere. For B^- decay, the two types of diagrams both lead to X^0Y^- final states, and the decay rate is therefore sensitive to interference effects.

any more rate than $D\pi$. This fact is not very surprising, given that the D^* is forced by angular momentum conservation to have helicity zero, so there are no additional helicities that can be populated. In addition, the D and D^* masses and wave functions are quite similar: since the charm quark mass is large, the spin is nearly decoupled from the dynamics of the system. (Of course, the D and D^* masses aren't exactly the same—this measures the size of a $1/m_c$ correction to the heavy-quark symmetry limit.)

The next observation is more interesting: it compares the rates for $D^*\rho$ with $D\rho$ final states. Since the $D^*\rho$ state can now have three possible helicity configurations and still conserve angular momentum, there is now the mystery as to why the $D^*\rho/D\rho$ ratios aren't larger! To complicate matters a little, I have listed decays of the type $\bar{B} \to D^{(*)}D_s^{-(*)}$ in Table 18. In this case, the $D^*D_s^{*-}$ modes do have a higher rate than the DD_s^-, $D^*D_s^-$, or DD_s^{*-} decays. This suggests that the momenta of the final-state particles are relevant, and that the vector-meson helicities in low-momentum and high-momentum decays are populated differently. We will discuss these points below when we compare the polarization of the daughter vector meson in hadronic decay with that in semileptonic decay.

In the fifth observation, we substitute a ρ for a π, keeping everything else the same. The $D^*\rho/D^*\pi$ ratios are around three. This result cannot be due to the ρ having more spin states: we see the effect even in $D\rho/D\pi$, and our previous comparison of $D^*\rho/D\rho$ showed that the extra spin states don't increase the rate by much anyway. The effect is

Table 18

Branching fractions for two-body hadronic B^- and $\bar{B}^0$ decays to final states with D_s^* mesons. The values are from the 1997 Particle Data Book [4] (www edition).

$\bar{B}^0$ decay	BR (%)	B^- decay	BR (%)
$D^+D_s^-$	0.80 ± 0.30	$D^0D_s^-$	1.3 ± 0.4
$D^{*+}D_s^-$	0.96 ± 0.34	$D^{*0}D_s^-$	1.2 ± 0.5
$D^+D_s^{*-}$	1.0 ± 0.5	$D^0D_s^{*-}$	0.9 ± 0.4
$D^{*+}D_s^{*-}$	2.0 ± 0.7	$D^{*0}D_s^{*-}$	2.7 ± 1.0

due in large part to the difference in the decay constants of the ρ and the π. In the external spectator diagrams, which give the dominant contributions, the quarks that feed into the ρ and π are produced at a point from the W decay. The amplitudes for the quarks to overlap in space within a ρ or π are proportional to f_ρ and f_π, respectively. We therefore expect the rates to be roughly in the ratio

$$\frac{f_\rho^2}{f_\pi^2} = \left(\frac{208 \text{ MeV}}{131 \text{ MeV}}\right)^2 \approx 2.5. \tag{8.1}$$

Next, we noted that all of the X^0Y^- branching fractions are larger than the corresponding X^+Y^- branching fractions. We have seen that X^0Y^- modes get contributions from both the external and internal spectator diagrams. However, from the fact that $\bar{B}^0 \to X^0Y^0$ modes have such small branching fractions, it would seem likely that a significant boost to the X^0Y^- rate could only come from the interference term. This argument suggests that the interference is constructive, in contrast to D^+ decays, where it is destructive.

Finally, of the internal spectator processes, the only ones that are observed so far involve $c\bar{c}$ systems. We can tentatively attribute this in part to the large decay constant of the J/ψ: $f_{J/\psi} \simeq 400$ MeV. (See Table 8.)

Although it is not possible to make precise calculations for hadronic decays, the factorization hypothesis provides a framework for understanding many of the observed features of two-body modes and even for making some quantitative predictions. In the factorization approach, one writes the decay amplitude as the product of two currents, in analogy to semileptonic decay. The effects of strong interactions are divided into two categories: (1) short-distance, hard-gluon effects parametrized by the coefficient a_1 for the external spectator diagram and a_2 for the internal (color-suppressed) spectator diagram and (2)

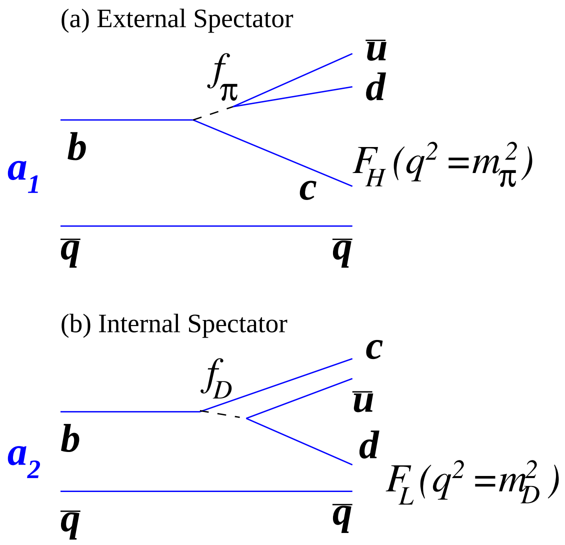

Fig. 55. Spectator diagrams for B decays with (a) an external W and (b) an internal W. The QCD hard-gluon corrections are parametrized by the coefficients a_1 and a_2, while nonperturbative effects are described, in our $B \to D\pi$ example, by the decay constant f_π or f_D and the form factor $F_H(q^2 = m_\pi^2)$ or $F_L(q^2 = m_D^2)$.

long-distance, soft-gluon effects, which are parametrized by decay constants and form factors. The elements used in the factorization description are shown in Fig. 55. Final-state interactions between the daughter hadrons are ignored in the factorization picture. It is, however, possible to parametrize these effects and to use data to constrain the parameters to some extent.

In Fig. 55(a) the $\bar{u}d$ system from the W decay is produced at a point, so that the appropriate meson decay constant, which measures the overlap of the quark anti-quark pair, parametrizes the amplitude to produce the meson. To be definite, we take this meson to be a pion. The daughter charm quark recoiling at the lower W vertex, however, must bind together with the spectator quark. The physics of this process is very similar to the hadronic transition in semileptonic decay discussed earlier, and it is described by the appropriate form factor evaluated at $q^2 = m_\pi^2$. The lower the q^2 value, the higher the recoil velocity, and, in general, the lower the amplitude for producing the meson from the daughter quark and the spectator quark. Thus, for the external spectator diagram example, the non-perturbative QCD physics is described by the pion decay constant f_π and a "heavy-to-heavy" ($B \to X_c$) form factor $F_H(q^2 = m_\pi^2)$.

Consider now the internal spectator diagram, shown in Fig. 55b.

Because the W has such a short range compared with the size of a hadron, the c and the $\bar{u}$ are still effectively produced at the same point, and the relevant decay constant is f_D instead of f_π. It is the daughter d quark that now must bind with the spectator, so there is now a "heavy-to-light" ($B \to X_u$) form factor, which I denote by $F_L(q^2 = m_D^2)$.

For a_1-type decays with large daughter-hadron recoil velocity (i.e., decays at low q^2), one might expect factorization to be a good approximation from the following argument, due to Bjorken [119]. The $q\bar{q}$ pair produced in the W decay is formed at a point as a color singlet, and, for low q^2 processes, the pair moves out of the decaying hadron at high velocity in a collinear fashion. Thus, the pair looks like a very small color dipole that gradually grows to the size of a meson. The pair will not form a meson, however, until it moves a distance $\approx \gamma c\tau_h$, where τ_h is a typical hadronization time in the rest frame, $\tau_h \sim 1$ fm/c. This distance can be quite large; for example $\gamma c\tau_h \approx 16$ fm for the pion in $\bar{B} \to D\pi$ decay. Since this distance is much larger than the size of the decaying meson, the $q\bar{q}$ pair can escape from the cloud of quarks and gluons without significantly interacting with it.

For a $\bar{B}^0$ decay, the external and internal diagrams lead to different final states (X^+Y^- and X^0Y^0), whereas in B^- decay two $\bar{u}$ quarks can be present in the final state, which means that the same X^-Y^0 final state can be reached in two ways. Thus, we have

$$
\begin{aligned}
&\bar{B}^0(b\bar{d}) \to X^+Y^- : \ \Gamma \propto |a_1 f_\pi F_H|^2 \\
&\bar{B}^0(b\bar{d}) \to X^0Y^0 : \ \Gamma \propto |a_2 f_D F_L|^2 \\
&B^-(b\bar{u}) \to X^-Y^0 : \Gamma \propto |a_1 f_\pi F_H + a_2 f_D F_L|^2
\end{aligned}
\tag{8.2}
$$

This pattern is illustrated in Fig. 56, Fig. 57, and Fig. 58.

The factorization picture can be put on a more solid foundation by relating a_1 and a_2 to a set of strong-interaction parameters that can be calculated or at least estimated from QCD. Here I will give only a short summary of the theory underlying factorization-based predictions; for an excellent review, see Neubert and Stech [113], which I will follow in the discussion below. The task is to separate the amplitude into parts that can be identified with (1) hard-gluon effects and (2) soft-gluon interactions, which can then be described in terms of decay constants and form factors. An important question is where to draw the dividing line between soft and hard gluons, the so-called factorization scale μ_f. Given that decay constants and form factors describe the interactions of $q\bar{q}$ systems that remain bound together, the hard gluons are considered to be those that can rearrange the quarks into different hadrons. This

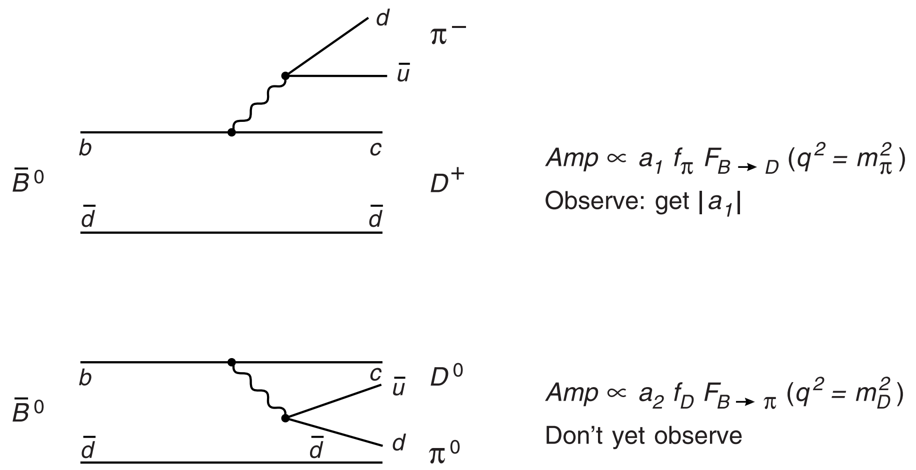

Fig. 56. External (upper figure) and internal (lower figure) spectator diagrams for hadronic decay of a $\bar{B}^0$ meson.

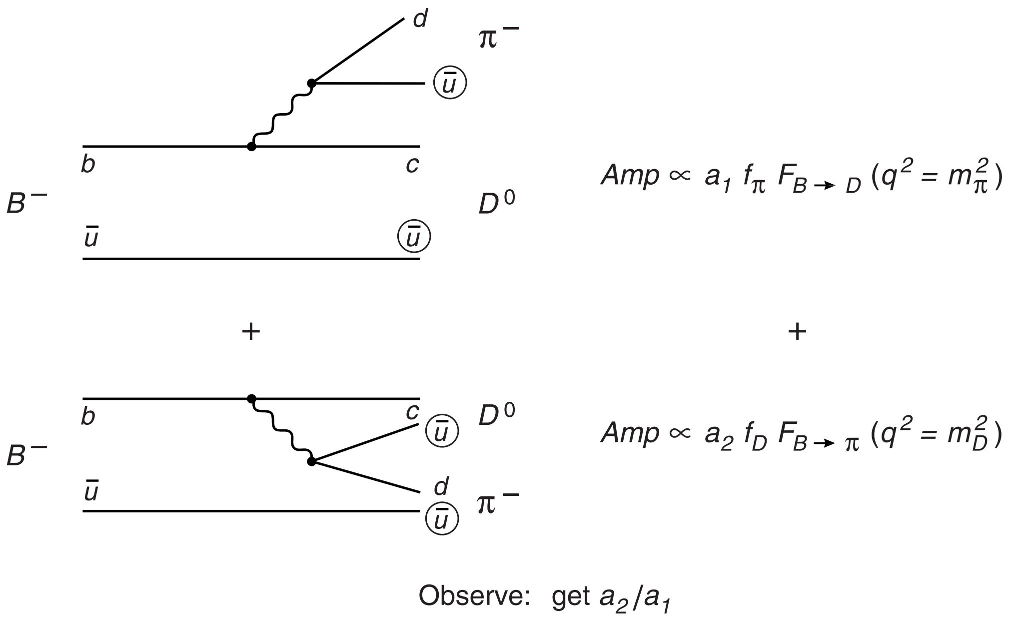

Fig. 57. External (upper figure) and internal (lower figure) spectator diagrams for hadronic decay of a B^- meson.

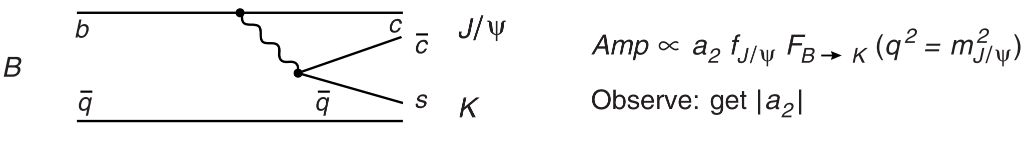

Fig. 58. B decay via color-suppressed internal spectator diagram to a $c\bar{c}$ meson. At present, the only observed internal spectator processes are of this type.

scale is at some level process dependent: if there is a large energy release in the decay, it is harder to rearrange the quarks, and the factorization scale is higher.

We now focus on $b \to c\bar{u}d$ decays, following the analysis of Neubert and Stech. The hard-gluon corrections down to a scale μ can be summed using the renormalization-group equation, which leads to an effective hamiltonian

$$H_{\text{eff}}(b \to c\bar{u}d) = \frac{G_F}{\sqrt{2}} V_{cb} V_{ud}^* \left(c_1(\mu)(\bar{d}u)(\bar{c}b) + c_2(\mu)(\bar{c}u)(\bar{d}b) \right). \quad (8.3)$$

The Wilson coefficients $c_1(\mu)$ and $c_2(\mu)$ describe the hard-gluon effects and at the scale $\mu = m_b$ have the values

$$c_1(m_b) \approx 1.13 \qquad c_2(m_b) \approx -0.29 \quad (8.4)$$

in next-to-leading order. The expression $(\bar{c}b)$ is short-hand for a $V - A$ color-singlet current. The matrix elements of the four-quark operators $(\bar{d}u)(\bar{c}b)$ and $(\bar{c}u)(\bar{d}b)$ must be somehow related to the decay constants and form factors. It it is not obvious how this is to be done, however, because the latter are matrix elements of two-quark operators. For $B^0 \to D\pi$ decay, the amplitudes are written

$$\begin{aligned} A(\bar{B}^0 \to D^+\pi^-) &= \frac{G_F}{\sqrt{2}} V_{cb} V_{ud}^* a_1 \mathcal{F}_{(BD)\pi} \\ A(\bar{B}^0 \to D^0\pi^0) &= \frac{G_F}{\sqrt{2}} V_{cb} V_{ud}^* a_2 \mathcal{F}_{(B\pi)D}, \end{aligned} \quad (8.5)$$

where $\mathcal{F}_{(BD)\pi}$ and $\mathcal{F}_{(B\pi)D}$ are the so-called factorizable contributions:

$$\begin{aligned} \mathcal{F}_{(BD)\pi} &= \langle \pi^- | (\bar{d}u) | 0 \rangle \langle D^+ | (\bar{c}b) | \bar{B}^0 \rangle \\ \mathcal{F}_{(B\pi)D} &= \langle D^0 | (\bar{c}u) | 0 \rangle \langle \pi^0 | (\bar{d}b) | \bar{B}^0 \rangle. \end{aligned} \quad (8.6)$$

The first matrix element on the right-hand side of each of these equations is related to a decay constant (f_π or f_D), while the second is related to a form factor ($B \to D$ or $B \to \pi$). The physics connected with a_1 and a_2 is quite complicated, since these coefficients are defined so as to make Eq. 8.5 exact:

$$\begin{aligned} a_1 &= \left(c_1(\mu) + \frac{c_2(\mu)}{N_c} \right) \left[1 + \varepsilon_1^{(BD)\pi}(\mu) \right] + c_2(\mu) \varepsilon_8^{(BD)\pi}(\mu) \\ a_2 &= \left(c_2(\mu) + \frac{c_1(\mu)}{N_c} \right) \left[1 + \varepsilon_1^{(B\pi)D}(\mu) \right] + c_1(\mu) \varepsilon_8^{(B\pi)D}(\mu), \end{aligned} \quad (8.7)$$

where $N_c = 3$ is the number of colors. Non-factorizable contributions from currents with color-singlet and octet structure are parametrized by the coefficients $\varepsilon_1 = \mathcal{O}(1/N_c^2)$ and $\varepsilon_8 = \mathcal{O}(1/N_c)$. While $|\varepsilon_1| \ll 1$, ε_8 cannot be neglected relative to other terms of order $1/N_c$. Recalling that $\mathcal{O}(c_2) = 1/N_c$, we have

$$\begin{aligned} a_1 &= c_1(m_b) + \mathcal{O}(1/N_c^2) \\ a_2 &= c_2(m_b) + \zeta c_1(m_b) + \mathcal{O}(1/N_c^2), \end{aligned} \tag{8.8}$$

where $\zeta = 1/N_c + \varepsilon_8(m_b)$. Since ε_8 cannot at present be calculated, the strategy is to use measured branching fractions to extract a_1 and a_2 for as many different decays as possible and to see if consistent values are obtained. In principle, ε_8 is process dependent, but its size and variation are empirical questions.

Using measured branching fractions for hadronic B decays, one can extract the coefficients a_1 and a_2 arising from hard-gluon effects. This procedure requires knowledge of both decay constants and form factors. As discussed earlier, our knowledge of these quantities is far from perfect, especially in the case of the form factors for heavy-to-light transitions. Compared with the state of our understanding of hadronic decays, however, form factor predictions might be regarded as reasonably trustworthy, but it is important to remember that there is more uncertainty in calculations made within the factorization framework than is often explicitly stated.

One interesting wrinkle occurs in decays to final states with two pseudoscalars. The amplitude for $B \to D\pi$ is

$$\begin{aligned} A(\bar{B}^0 \to D^+\pi^-) &= -\frac{G_F}{\sqrt{2}} V_{cb} V_{ud}^* a_1 \langle \pi^- | (\bar{d}u)_A | 0 \rangle \langle D^+ | (\bar{c}b)_V | \bar{B}^0 \rangle \\ &= -\frac{G_F}{\sqrt{2}} V_{cb} V_{ud}^* a_1 (-i f_\pi q_\mu) \\ &\quad \times \{ F_1^{B\to D}(q^2) \left[(p+p')^\mu - \frac{m_B^2 - m_D^2}{q^2} q^\mu \right] \\ &\quad + F_0^{B\to D}(q^2) \frac{m_B^2 - m_D^2}{q^2} q^\mu \}, \end{aligned} \tag{8.9}$$

where $q = p - p'$. When the two currents are contracted, the term proportional to $F_1^{B\to D}(q^2)$ vanishes, giving

$$A(\bar{B}^0 \to D^+\pi^-) = -i \frac{G_F}{\sqrt{2}} V_{cb} V_{ud}^* (m_B^2 - m_D^2) a_1 f_\pi F_0^{B\to D}(q^2 = m_\pi^2).$$

$$(8.10)$$

The form factor that enters here is precisely the one for which there is almost no sensitivity in semileptonic decay, where its contribution vanishes in the limit of zero lepton mass! (See Sec. 7.6 and 7.7.) In practice, this is not a serious problem. In the present example,

$$F_0^{B\to D}(q^2 = m_\pi^2) \simeq F_0^{B\to D}(0) = F_1^{B\to D}(0), \tag{8.11}$$

where the relation between $F_0^{B\to D}(0) = F_1^{B\to D}(0)$ is discussed after Eq. 7.39. We can regard $F_1^{B\to D}(0)$ as an approximately known quantity, given that $|V_{cb}|$ can be determined from other decays. In addition, HQET can be used to provide relations to form factors that have been probed experimentally. As I have already mentioned, however, factorization predictions involving heavy-to-light form factors do have to make assumptions that have not been tested by experiment.

In B^- decays, there is sensitivity to a_2/a_1 through the interference term. Some predictions from Neubert *et al.* [114] are

$$\begin{aligned}
R_1 &= \frac{B(B^- \to D^0\pi^-)}{B(\bar{B}^0 \to D^+\pi^-)} = (1 + 1.23a_2/a_1)^2 \\
R_2 &= \frac{B(B^- \to D^0\rho^-)}{B(\bar{B}^0 \to D^+\rho^-)} = (1 + 0.66a_2/a_1)^2 \\
R_3 &= \frac{B(B^- \to D^{*0}\pi^-)}{B(\bar{B}^0 \to D^{*+}\pi^-)} = (1 + 1.29a_2/a_1)^2 \\
R_4 &= \frac{B(B^- \to D^{*0}\rho^-)}{B(\bar{B}^0 \to D^{*+}\rho^-)} = (1 + 0.75a_2/a_1)^2.
\end{aligned} \tag{8.12}$$

In a recent CLEO II analysis [117], the models of Deandrea *et al.* [121] and the BSWII model of Neubert *et al.* [113] were used to extract a_1 and a_2 from the measured branching fractions. Table 19 lists some of the predictions of these models, and Table 20 lists the values of a_1 and a_2 extracted from an overall fit to the data. Three features stand out:

- Both a_1 and a_2 are measured with good precision; however, the errors do not reflect the full theoretical uncertainties.
- $a_1 \approx 1$, as expected from QCD predictions.
- $a_2 \approx 0.2$ is substantially smaller, as expected. The sign of a_2/a_1 is positive, corresponding to constructive interference between the external and internal spectator diagrams.

It is important to check that the values extracted for a_1 and a_2 are consistent from mode to mode. Using $B \to \psi K^{(*)}$ decays, one can

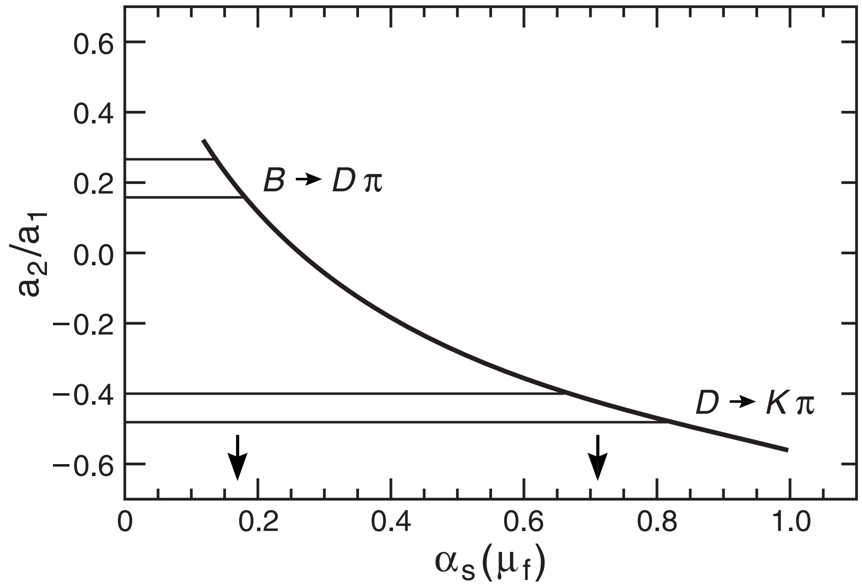

Fig. 59. The ratio of a_2/a_1 as a function of the running coupling constant $\alpha_s(\mu_f)$ evaluated at the factorization scale. The bands indicate the phenomenological values of a_2/a_1 extracted from $B \to D\pi$ and $D \to K\pi$ decays. From Neubert [116]. Used with permission.

extract [112]

$$|a_2| = 0.23 \pm 0.01 \pm 0.01. \tag{8.13}$$

Similar values are obtained in Ref. [113], which also quotes $\zeta = 0.45 \pm 0.05$ and $\varepsilon_8(m_b) = 0.12 \pm 0.05$.

The situation in charm decays is much more complicated. The data on charm decays show that unless final-state interactions are taken into account factorization predictions by themselves do not yield consistent results. Browder, Honscheid, and Pedrini [112] use $D \to K\pi$, $D \to K\rho$ and other modes to obtain

$$a_1(D) = 1.10 \pm 0.03 \qquad a_2(D) = -0.50 \pm 0.03. \tag{8.14}$$

Although the errors do not take into account all of the uncertainties, it is clear that the sign of a_2/a_1 is negative in D decays and positive in B decays. This effect can be explained [113] as a consequence of the running of $\alpha_s(\mu_f)$, since the factorization scale μ_f is lower in D than in B decays, leading to a much larger value of the strong coupling constant. The relation between the running of α_s and a_2/a_1 is shown in Fig. 59. The presence of destructive interference, together with the predominance of two-body decays, explains the long D^+ lifetime.

While factorization appears to have some validity, many people regard it with a great deal of skepticism, given the complexity of hadronic

Table 19

Predictions for two-body B decays in factorization-based models. The predictions of the models were slightly modified, as described in Ref. [117], to take into account more recent values of the input parameters.

B Decay Mode	B BSWII	B CDDFGN
$D^+\pi^-$	$0.25a_1^2$	$0.26a_1^2$
$D^{*+}\pi^-$	$0.24a_1^2$	$0.26a_1^2$
$D^+\rho^-$	$0.59a_1^2$	$0.58a_1^2$
$D^{*+}\rho^-$	$0.67a_1^2$	$0.77a_1^2$
$D^0\pi^-$	$0.25(a_1+1.2a_2)^2$	$0.26(a_1+1.2a_2)^2$
$D^{*0}\pi^-$	$0.24(a_1+1.3a_2)^2$	$0.26(a_1+1.7a_2)^2$
$D^0\rho^-$	$0.63(a_1+0.66a_2)^2$	$0.58(a_1+0.5a_2)^2$
$D^{*0}\rho^-$	$0.67(a_1^2+0.64a_2^2+1.5a_1a_2)$	$0.77(a_1^2+0.69a_2^2+1.4a_1a_2)$

Table 20

Values of a_1 and a_2 extracted from fitting the BSWII and CDDFGN models to CLEO II measurements of $D^*\pi$ and $D^*\rho$ branching fractions. The values are from Ref. [117]. The stated errors do not include any uncertainty associated with the form factors.

Model	$\lvert a_1\rvert$	a_2/a_1	χ^2/dof
CDDFGN	$0.95\pm0.03\pm0.04\pm0.02$	$0.23\pm0.04\pm0.02\pm0.02$	20.3/6
BSWII	$0.99\pm0.03\pm0.04\pm0.02$	$0.26\pm0.04\pm0.03\pm0.02$	9.1/6

processes. Most of the results discussed above are from two-body decays that have a large energy release (or low q^2), where we would expect factorization to work best. It is perhaps not too surprising that, among these modes, the values of a_1 and a_2 are consistent. It is important to make as many quantitative tests of factorization as possible, and to determine when it begins to break down. (We know that in D decays factorization without including final-state interactions is inadequate to describe the data.) One approach to testing factorization is to compare the decay rate for a hadronic mode with the rate at the same value of q^2 for a semileptonic decay. From the Dalitz plot for $\bar{B}\to D^*\ell^-\bar{\nu}$ shown in Fig. 25, it is clear that $q^2=m_\pi^2$, $q^2=m_\rho^2$, and $q^2=m_{a_1}^2$ all correspond to the low q^2 region of phase space, where the D^* polarization is mostly longitudinal. For $q^2=m_{D_s}^2$ we have moved to about the mid position of the q^2 range. For $B\to D^{(*)}P$ decays, where P is a pseudoscalar meson, one can define [113] the ratio

$$R_P^{(*)}=\frac{\Gamma(\bar{B}\to D^{(*)}P)}{d\Gamma(\bar{B}\to D^{(*)}\ell^-\bar{\nu})/dq^2|_{q^2=m_P^2}}$$

Table 21
Values of a_1 extracted from a comparison of hadronic and semileptonic B decays. The consistency of these values is an indication of whether factorization provides a good description of the hadronic decays.

Mode	a_1
$\bar{B}^0 \to D^+\pi^-$	0.92 ± 0.10
$\bar{B}^0 \to D^+\rho^-$	0.97 ± 0.13
$\bar{B}^0 \to D^{*+}\pi^-$	0.96 ± 0.10
$\bar{B}^0 \to D^{*+}\rho^-$	0.92 ± 0.12
$\bar{B}^0 \to D^{*+}a_1^-$	1.1 ± 0.13
$\bar{B}^0 \to D^{(*)+}D_s^{(*)-}$	1.24 ± 0.40

$$= 6\pi^2 f_P^2\, a_1^2 |V_{ij}|^2 X_P^{(*)}(q^2 = m_P^2). \tag{8.15}$$

The quantities X_P and X_P^* are for DP and D^*P decays, respectively, and are equal to the squares of the ratios of form factors for hadronic and semileptonic decay (The ratio is defined precisely in Neubert *et al.* [113].) In most cases, $X_P^{(*)}$ is very close to one. For $B \to D^*V$ decays, the corresponding ratios X_V and X_V^* are exactly unity.

The ratio on the upper line of Eq. 8.15 can be evaluated from experiment, while the lower line ($\simeq 6\pi^2 f_p^2 a_1^2 |V_{ij}|^2$) can be calculated from theory, the comparison giving a test of whether factorization is valid. The constant $a_1 \approx 1$ can be calculated from QCD, as discussed above, but I prefer to use Eq. 8.15 to extract a_1 for different decay modes and then to check whether the resulting values are consistent with each other and the prediction.

Table 21 shows the values of a_1 for a set of $\bar{B}^0$ decay modes that can be compared with $\bar{B}^0 \to D^+\ell^-\bar{\nu}$ and $\bar{B}^0 \to D^{*+}\ell^-\bar{\nu}$. The agreement among these values is reasonably good, indicating that at the low values of q^2 (fast recoil) at which these hadronic decays occur, factorization provides a good description of the process. The data for the comparison with $\bar{B} \to D\ell^-\bar{\nu}$ are taken from the CLEO [101], while the $\bar{B} \to D^*\ell^-\bar{\nu}$ comparison is made using combined CLEO and ARGUS data compiled in Browder *et al.* [112]. The data for the $\bar{B}^0 \to D^{(*)+}D_s^{(*)-}$ are from CLEO [122] and assume $f_{D_s} = f_{D_s^*}$.

We can also compare the polarization of the D^* in the hadronic decay $\bar{B}^0 \to D^{*+}\rho^-$ with that in the semileptonic decay $\bar{B}^0 \to D^{*+}\ell^-\bar{\nu}$, measured at the same value of q^2. In a semileptonic decay at low q^2, the lepton and antineutrino are nearly collinear, so their net spin along their direction of motion is zero. Since the B has spin zero, the recoiling meson must also have helicity zero. In the factorization picture, the quark-antiquark pair from the W would behave like the lepton-antineutrino system, so that the ρ^- (or D^{*+}) is expected to be almost completely longitudinally polarized. This explains why $B(B \to D^*\rho) \approx B(B \to D\rho)$. An update [123] of CLEO II measurement of the $\bar{B} \to D^*\ell^-\bar{\nu}$ form factors gives $(\Gamma_L/\Gamma)_{q^2=m_\rho^2} = (91 \pm 1.3 \pm 0.6)\%$. For $\bar{B}^0 \to D^{*+}\rho^-$, CLEO obtains [124] $\Gamma_L/\Gamma = (93{\pm}5{\pm}5)\%$, a very similar value. It will be interesting to make this comparison at higher q^2, for example, when there are enough events in $\bar{B} \to D^* D_s^{*-}$ to measure the angular distributions.

We have considered the relatively small slice of B decays that correspond to two-body or quasi-two-body modes with easily reconstructed final states. There are many other important topics in hadronic decays, including the observation of $B \to D^{(*)}D^{(*)}K$ modes [125], that I cannot cover here.

I will conclude this section with a list of some inclusive properties of B decays, Table 22. The information in the table can be used to compute the average number of c or $\bar{c}$ quarks produced per B decay (charmonium states count twice). The value measured by CLEO [126], $\langle n_c \rangle = 1.10 \pm 0.05$, can be used along with the semileptonic branching fraction to test our understanding of the hadronic rate. Historically, theorists have had an extremely difficult time obtaining a value of the semileptonic branching fraction $\mathcal{B}_{\rm SL}$ that is as low as the measured value (see Sec. 7.4). Bigi *et al.* argued that $\mathcal{B}_{\rm SL}$ must be greater than 12.5%; if measurements yielded a lower value, this could be an indication either that the *perturbative* QCD corrections to the semileptonic rate were surprisingly large or that there was new physics involved. This issue is related to the value of n_c because a larger $B \to c\bar{c}X$ rate would increase n_c and lower $\mathcal{B}_{\rm SL}$. Recent analyses of this problem have therefore focussed on understanding both of these quantities together. For a recent review, see Drell [103].

8.2. Lifetimes

The most striking overall feature of b-hadron lifetimes is how similar they are, in contrast with those for charm hadrons. I will not discuss charm lifetimes in any detail, but it is worth recalling a few of the measured values, which are listed in Table 23. Charm lifetimes lie

Table 22
CLEO II measurements [126] of inclusive properties of B meson decays.

Mode	Branching Fraction
$B \to D^0 X$	$0.636 \pm 0.014 \pm 0.019 \pm 0.018$
$B \to D^+ X$	$0.235 \pm 0.009 \pm 0.009 \pm 0.024$
$B \to D^{*0} X$	$0.247 \pm 0.012 \pm 0.018 \pm 0.018$
$B \to D^{*+} X$	$0.239 \pm 0.015 \pm 0.014 \pm 0.009$
$\bar{B} \to D^0 X + \bar{B} \to D^+ X$	0.871 ± 0.035
$\bar{B} \to D_s X$	0.118 ± 0.031
$\bar{B} \to \Lambda_c X$	0.039 ± 0.020
$\bar{B} \to \Xi_c^+ X$	$0.008 \pm -.005$
$\bar{B} \to \Xi_c^0 X$	0.012 ± 0.009
$2 \times \mathcal{B}(\bar{B} \to \text{Charmonia}X)$	0.054 ± 0.007
$\langle n_c \rangle$	1.10 ± 0.05

roughly in the range 0.1 ps to 1 ps; even though considerable, this range is still much less than that in the kaon system, where

$$\frac{\tau(K_L^0)}{\tau(K_S^0)} \approx \frac{52 \text{ ps}}{0.089 \text{ ps}} \approx 580 \qquad \frac{\tau(K^+)}{\tau(K_S^0)} \approx \frac{12 \text{ ps}}{0.089 \text{ ps}} \approx 140. \tag{8.16}$$

In the early days of charm physics, many people expected $\tau(D^0)$ and $\tau(D^+)$ to be very similar. It was argued that the lifetime of the charm quark should essentially determine the lifetime of the hadron, with the other quarks acting as spectators. Initially, the lifetime ratio $\tau(D^+)/\tau(D^0)$ was inferred from the ratio of semileptonic branching fractions. In the 1980s, high-statistics, fixed-target charm experiments at Fermilab nailed down the individual lifetimes using direct decay-length measurements. With the installation of a new silicon-strip vertex detector, the CLEO experiment should soon be competitive in this area as well. From Table 23, we see the uncertainties on the D lifetimes are now quite small. Although the lifetimes are roughly similar, we see that $\tau(D^0) \approx \tau(D_s) \approx 0.4\tau(D^+)$. This observation suggests that it is the D^+ lifetime that is in some sense anomalous; as discussed in the previous section, there is also good evidence that destructive interference in hadronic D^+ decays suppresses its rate. The b-quark, however, is sufficiently heavy that b hadrons begin to fulfill the old expectation that the lifetimes should be nearly equal.

Lifetimes of b-hadrons have been measured by the LEP experiments and SLD using $Z \to b\bar{b}$ and by the CDF experiment, which uses $p\bar{p} \to b\bar{b}X$. Figure 60 lists the averages computed by the LEP B

Table 23
A summary of lifetimes for ground-state charm hadrons. The values are averages from the 1997 Particle Data Group update [4].

Particle	$\tau/10^{-12}$ s
D^+ $(c\bar{u})$	1.057 ± 0.015
D^0 $(c\bar{d})$	0.415 ± 0.004
D_s^+ $(c\bar{s})$	0.467 ± 0.017
Λ_c^+ (cud)	0.206 ± 0.012
Ξ_c^+ (csu)	$0.35^{+0.07}_{-0.04}$
Ξ_c^0 (csd)	$0.098^{+0.023}_{-0.015}$
Ω_c^+ (css)	0.064 ± 0.020

Lifetime Working Group [127]. Their averages take into account the many sources of correlated experimental error, such as assumed fragmentation models, decay models, and branching fractions. Individual measurements of $\bar{B}^0$ and B^- lifetimes are reaching an impressive precision, with systematic errors as small as ± 0.02 ps (CDF), and total errors as small as ± 0.06 ps (DELPHI). There are substantial improvements in the lifetime measurements for both the B_s and Λ_b, but here the event samples are much smaller and more data are needed to obtain precise values. Before considering these measurements, we look at some of the theoretical predictions.

Predictions for ratios of b-hadron lifetimes are based on the heavy-quark $(1/m_Q)$ expansion and have been made by many theorists. I will give only a couple of examples here. A recent review of inclusive b-hadron predictions based on the heavy-quark expansion was given by Mannel [128]. Neubert [129] gives the following estimates for the lifetime ratios:

$$\frac{\tau(B^-)}{\tau(B^0)} = 1 + \mathcal{O}(1/m_b^3),$$
$$\frac{\tau(B_s)}{\tau(B^0)} = (1.00 \pm 0.01) + \mathcal{O}(1/m_b^3),$$
$$\frac{\tau(\Lambda_b)}{\tau(B^0)} \simeq 0.98 + \mathcal{O}(1/m_b^3), \tag{8.17}$$

where the estimate for $\tau(\Lambda_b)/\tau(B^0)$ includes corrections that arise at order $1/m_b^2$. Although these ratios might appear very close to unity,

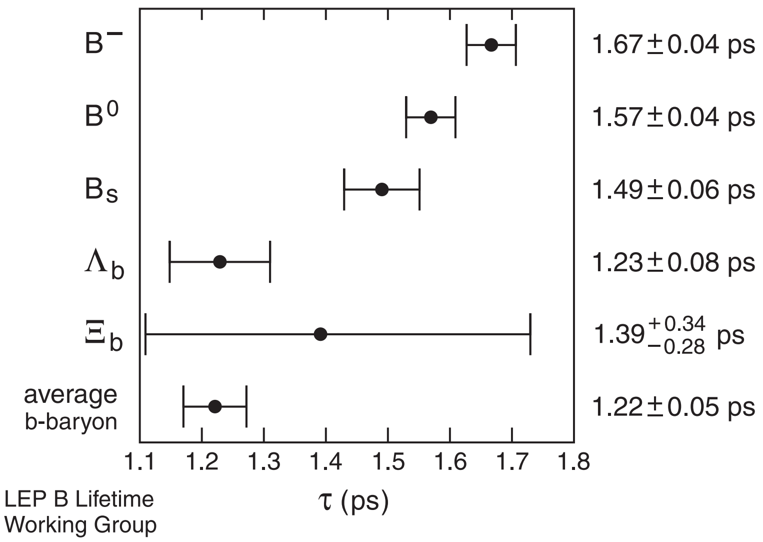

Fig. 60. Summary of b-hadron lifetimes. The averages, current as of Oct. 1997. were calculated by the LEP B Lifetime Working Group [127] and take into account correlated systematic errors among the measurements. Figure redrawn and used with permission.

Neubert argues that the $1/m_b^3$ corrections to $\tau(B^-)/\tau(B^0)$ might be large (due to phase-space enhancement of effects involving the spectator quark), and he concludes that theoretical uncertainties allow a lifetime ratio in the range $0.8 < \tau(B^-)/\tau(B^0) < 1.2$. This subject is controversial, and other theorists have placed tighter contraints on this ratio. For example, Bigi [130] concludes that the B^- lifetime should be longer than the B^0 lifetime:

$$\frac{\tau(B^-)}{\tau(B^0)} \simeq 1 + 0.05 \cdot \frac{f_B^2}{(200\ \mathrm{MeV})^2}. \tag{8.18}$$

There is more consensus on $\tau(B_s)/\tau(B^0)$, which is expected to be unity up to corrections of order 1%. Theoretical estimates for $\tau_{\Lambda_b}/\tau_{B^0}$ are typically in the range 0.9 to 1.0.

Lifetime measurements can be grouped into three broad categories, corresponding to the use of semileptonic decays, fully reconstructed hadronic decays, and inclusive methods such as topological vertexing. The main advantages of using semileptonic decays, such as $\bar{B} \to D^{(*)}\ell^-(X)\bar{\nu}$, are the large branching fractions, the presence of the lepton, and good vertex determination. There are, however, significant disadvantages. Because there is always at least one missing particle, the neutrino, it is generally not possible to reconstruct a B mass peak. As a consequence, it can be difficult to determine whether

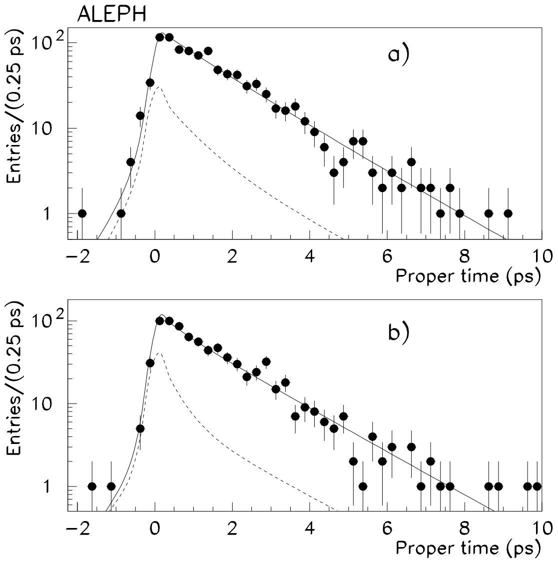

Fig. 61. Proper time distribution for the ALEPH measurement of $\tau(B^-)$ and $\tau(B^0)$ using semileptonic B decay. The points with errors show the data for (a) $D^{*+}\ell^-$ events and (b) $D^0\ell^-$ events, which correspond mainly to the B^0 and B^- decays. The dashed curves represent the background contribution, and the solid curves show the total fit.

there are additional missing particles, especially neutrals. The neutrino and other missing particles degrade the B momentum resolution and hence reduce the precision of the proper decay time measurement. In addition, missing charged particles hinder the clean separation of $\bar{B}^0$ and B^- samples. Figure 61 shows the proper time distributions from ALEPH [131] for $D^{*+}\ell^-$ and $D^0\ell^-$ samples, which would ideally correspond to $\bar{B}^0$ and B^- decays. In reality, the $D^{*+}\ell^-$ sample is $(87 \pm 4)\%$ pure, and the $D^0\ell^-$ is $(75 \pm 5)\%$ pure, so these distributions are fit simultaneously. A model is needed to account for possible feed-down contributions from various $D^{**}\ell^-\bar{\nu}$ modes. In spite of these complications, ALEPH achieves a very good systematic error on these measurements: $\tau_{B^0} = (1.61 \pm 0.07 \pm 0.04)$ ps and $\tau_{B^-} = (1.58 \pm 0.09 \pm 0.04)$ ps. DELPHI [132] reports a very precise result $\tau(B^0) = (1.532 \pm 0.041 \pm 0.040)$ ps based on a study of $\bar{B}^0 \to D^{*+}X\ell^-\bar{\nu}$ decays. Their measurement uses a method in which the $D^{*+} \to D^0\pi^+$ decay is reconstructed inclusively, leading to a sample of ≈ 3500 decays.

The second method for determining b-hadron lifetimes uses fully reconstructed, exclusive hadronic decays, and the analyses are usually much simpler than those using semileptonic modes. A b-hadron mass peak is observed, whose sidebands can be used to study the lifetime distribution of the background. Since all particles are observed, the decay vertex and the b-hadron momentum are well determined, and the conversion to proper lifetime is very straightforward. The only disadvantage is that the event samples are typically smaller than those for semileptonic decay. In hadron colliders, however, a sufficiently large number of B mesons is produced for decays to final states with J/ψ's to provide a competitive method for measuring lifetimes. Figure 62 shows the reconstructed B^+ mass from CDF [133] for the final states $J/\psi K^+$, $J/\psi K^{*+}$, $\psi(2S)K^+$, and $\psi(2S)K^{*+}$. The upper and lower histogram in the figure show the data before and after the proper decay length cut $c\tau > 100$ μm. This cut is not actually used for the lifetime fit, but it demonstrates that the background is concentrated at short proper lifetimes. Figure 63 shows the distribution of proper decay lengths in the signal region (upper histogram) and in the B mass sidebands (lower histogram), together with the fits to the data. This measurement yields the value $\tau(B^+) = (1.68 \pm 0.07 \pm 0.02)$ ps; the result for the B^0 lifetime is $\tau(B^0) = (1.58 \pm 0.09 \pm 0.02)$ ps. In my view, these very small systematic errors, which are related to the considerations discussed above, demonstrate that hadronic decays are significantly better than semileptonic modes for lifetime measurements, assuming that enough events are available.

The third method for measuring b hadron lifetimes makes use of topological vertexing, in which the B meson charge is determined from the total charge of the tracks associated with the decay vertex. The SLD results are [134]

$$\begin{aligned} \tau(B^-) &= (1.698 \pm 0.040 \pm 0.046) \text{ ps} \\ \tau(B^0) &= (1.581 \pm 0.043 \pm 0.061) \text{ ps}. \end{aligned} \tag{8.19}$$

The measurement errors here are comparable to those of many of the LEP and CDF results, despite a much smaller event sample, 200,000 hadronic Z decays. This is due not only to the inclusive nature of the method, but also to the advantages of the SLC accelerator, with its very small diameter beams, small radius beampipe, and electron beam polarization.

To compare the B^0 and B^- lifetimes, it is best to calculate the lifetime ratio for each experiment, so that many systematics cancel, and then to compute the average of the individual lifetime ratios. The average computed by the LEP B Lifetime Working Group is

$$\tau(B^-)/\tau(B^0) = 1.07 \pm 0.04. \tag{8.20}$$

This value is certainly consistent with unity, but it is not sufficiently

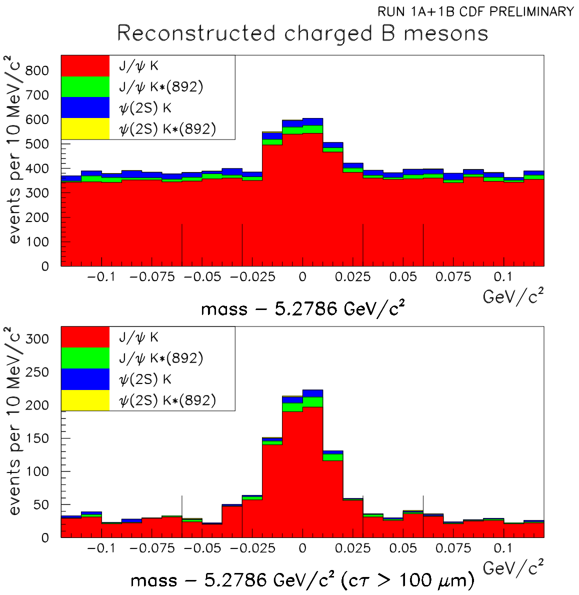

Fig. 62. CDF measurement of $\tau(B^+)$. The upper histogram (a) shows the invariant mass distributions for B^+ candidates in the $J/\psi K^+$, $J/\psi K^{*+}$, $\psi(2S)K^+$ and $\psi(2S)K^{*+}$ final states; (b) shows the same distributions after the cut $c\tau > 100$ μm. Figure used with permission.

precise to rule out a lifetime difference at the 10% level. The positive sign of a_2/a_1, however, would indicate that $\tau(B^-)/\tau(B^0) < 1$. As other B^- decay modes are observed, it will be interesting to see if the interference is constructive or destructive.

The uncertainties in B_s lifetime measurements are much larger than those for the $\bar{B}^0$ and B^-, due to smaller event samples and larger combinatorial backgrounds. Most of the measurements use the semileptonic decay $B_s \to D_s^+ X \ell^- \bar{\nu}$ and reconstruct the D_s^+ decay in one or more modes, although some use an inclusive D_s^+ signal or a D_s^+ with an associated hadron. The average lifetime from measurements based on these modes is

$$\tau(B_s) = 1.49 \pm 0.06 \text{ ps}, \tag{8.21}$$

consistent with the B^0 and B^- lifetimes.

Because the B_s^0 and $\bar{B}_s^0$ can oscillate into one another, the two mass eigenstates are expected to differ somewhat in their masses and lifetimes. Theoretical estimates indicate that the difference in decay widths may be as large as $\Delta\Gamma/\Gamma \approx 15\%$ [135]. CDF [136] has reconstructed 58 ± 8 events in the decay $B_s \to J/\psi\phi$, which is expected to be predominantly CP even, in contrast to the $D_s^+ \ell^- X$ final state, which

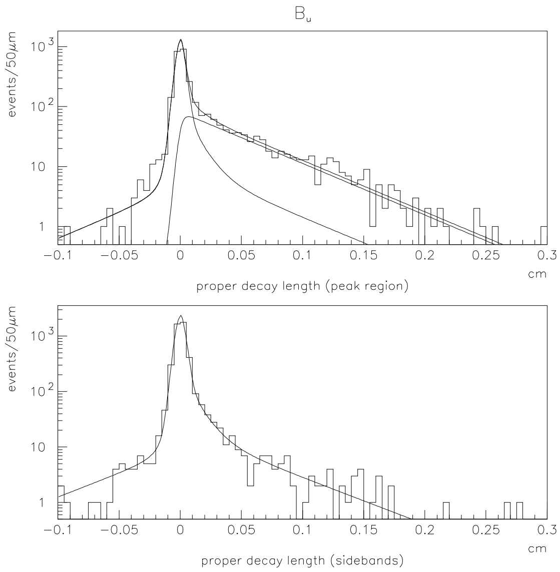

Fig. 63. CDF measurement of $\tau(B^+)$. The upper histogram shows the proper decay length distribution for events in the B mass peak; the lower histogram shows the distribution for events in the B mass sidebands. Figure used with permission.

is expected to be an equal mixture of CP even and CP odd. The result from $B_s \to J/\psi\phi$, $\tau(B_s) = 1.34^{+0.23}_{-0.19} \pm 0.05$ ps, is not yet sufficiently precise to address this issue, but future measurements with more data should be extremely interesting.

The measured values of b-baryon lifetimes are systematically lower than those for B mesons. These analyses are performed using a variety of methods that select different compositions of b baryons, whose production fractions at the Z or at the Fermilab collider are not well known. (In fact, some papers use the symbol Λ_b to denote a generic b-baryon, but I use Λ_b^0 to denote the $I = 0$ *bud* ground state baryon.) Measurements of the Λ_b^0 lifetime generally use $\Lambda_c^{\pm}\ell^{\mp}$ correlations to select events from the decay $\Lambda_b^0 \to \Lambda_c^+ X \ell^- \bar{\nu}$. By fully reconstructing the $\Lambda_c^+ \to pK^-\pi^+$ decay and using kinematic cuts, one can obtain a high purity sample of $\Lambda_b^0 \to \Lambda_c^+ \ell^- \bar{\nu}$ decays. Alternatively, one can obtain larger event samples by using the inclusive decay $\Lambda_c^+ \to \Lambda X$ and searching for $\Lambda\ell^-$ or even $p\ell^-$ combinations. These methods, however, have a lower purity of Λ_b^0 baryons, since, for example, there can be background from $\Xi_b \to \Xi_c \ell^- \bar{\nu}$, $\Xi_c \to \Lambda X$.

By including measurements that use $\Lambda\ell^-$ and $p\ell^-$ correlations, the LEP B Lifetime Working Group obtains the average $\tau(b\text{−baryon}) =$

(1.21 ± 0.06) ps. This low value is difficult to accomodate in calculations based on the $1/m_Q$ expansion, which predict $\tau(\Lambda_b)/\tau(B^-)$ to be in the range 0.9 to 1.0.

OPAL [137] has measured the ratio $R_{\Lambda\ell} = B(b\text{−baryon} \to \Lambda\ell X)/B(b\text{−baryon} \to \Lambda X)$, which should be a good approximation to the average b baryon semileptonic branching fraction. They obtain $R_{\Lambda\ell} = (6.8 \pm 1.3 \pm 1.0)\%$, which is consistent with the expectation based on the shorter b-baryon lifetime and the assumption of equal semileptonic widths of B mesons and b baryons.

In spite of a tremendous effort, there remain basic questions on b-hadron lifetimes, all of which call for more precision:

- How similar are the B^0, B^-, B_s lifetimes?
- Are the b-baryon lifetimes really significantly lower than those of the mesons?
- Do the B_s mass eigenstates have significantly different lifetimes?

The CDF experiment should be able to contribute much to answering these questions as it obtains more data.

8.3. Rare decays

With B data samples of over 10^6 events, experiments have now achieved sensitivities to branching fractions in the range 10^{-4} to 10^{-5}, opening up new types of processes for study. Several new modes were recently discovered by CLEO, and it is likely that many more will be found in the next few years. The study of rare decays has therefore become an exciting and rapidly developing area of B physics. There are important rare processes to search for in charm decays as well. Because charm particles have Cabibbo-favored $c \to s$ decays, however, rare modes tend to have smaller branching fractions, and it is more difficult to achieve a comparable sensitivity to exotic processes than it is in B decays. Lingel, Skwarnicki, and Smith [138] have written a review of rare decays from an experimental perspective; recent theoretical reviews include those by Buras and Fleischer [12] and Ali [139].

In this section, we consider three types of rare decays:

- Hadronic decays resulting from $b \to u$ transitions. These are very similar to the hadronic decays discussed in Sec. 8.1 but are highly suppressed due to the factor $|V_{ub}|^2$.
- Hadronic decays resulting from penguin processes. Sometimes called gluonic penguins, these decays involve the emission and reabsorption of a W, resulting in a $b \to Q(+2/3) \to s$ or $b \to Q(+2/3) \to d$ transition, where $Q(+2/3)$ is u, c, or t.

• Radiative penguin decays. These processes also involve the emission and reabsorption of a W, but a photon is radiated from one of the charged particles. Radiative penguins with real photons, such as $B \to K^*\gamma$, have been discovered. The photon can also be virtual, materializing into a e^+e^- or $\mu^+\mu^-$ pair. At present, experiments do not have sufficient sensitivity to observe these decays.

Many rare hadronic decays, such as $B \to \pi\pi$ and $B \to K\pi$, can proceed either through a $b \to u$ spectator diagram or through a gluonic penguin, as shown in Fig. 64. In a gluonic penguin, a $b \to d$ or $b \to s$ transition occurs through a virtual loop containing a W and either a t, c, or u quark, with the radiation of a gluon. The dominant contribution is expected to arise from the t-quark intermediate state, but effects from the c quark are not necessarily negligible. Buras and Fleischer [12] discuss this point in detail.

The gluonic penguins are of interest not only as one-loop processes, but also because they are relevant to studies of CP violation. We will see in Sec. 9 that CP violation can occur in a number of different ways, all of which require interference between at least two amplitudes. CP violation can result from interference between tree and penguin diagrams, for example, giving a difference in rate between $\bar{B}^0 \to K^-\pi^+$ and $B^0 \to K^+\pi^-$. Another method for studying CP violation can be applied when both $\bar{B}^0$ and B^0 decay into the same final state f. Then, interference between $B^0 \to f$ and $B^0 \to \bar{B}^0 \to f$ can produce a CP asymmetry. In this case it is quite undesirable to have amplitudes with different CKM factors contributing to the decay, because the measurement becomes sensitive to poorly-known strong-interaction phases. The term "penguin pollution" is used to describe this problem. It is amazing how quickly a fascinating new process can become a problem for the next set of measurements!

A simple argument gives a rough idea of the possible relative contribution of the tree and penguin amplitudes in $B \to \pi\pi$ and $B \to K\pi$. Assuming that the t-quark dominates the loop, the penguin contribution to $\bar{B}^0 \to \pi^+\pi^-$ is suppressed relative to that for $\bar{B}^0 \to K^-\pi^+$ by $|V_{td}/V_{ts}|^2 = \mathcal{O}(\lambda^2)$ in the rate, where $\lambda \simeq 0.22$ is the sine of the Cabibbo angle. (The same conclusion holds when there is a c-quark in the intermediate state.) Furthermore, the tree contribution to $\bar{B}^0 \to K^-\pi^+$ is suppressed relative to that for $\bar{B}^0 \to \pi^+\pi^-$ by a factor $|V_{us}/V_{ud}|^2 \simeq \lambda^2$ in the rate. By itself, all this tells us is that the tree diagram contributes more to $\pi\pi$ than to $K\pi$ and the penguin contributes more to $K\pi$ than to $\pi\pi$.

Now, suppose that $B(\bar{B}^0 \to \pi^+\pi^-) \approx B(\bar{B}^0 \to K^-\pi^+)$, as is crudely

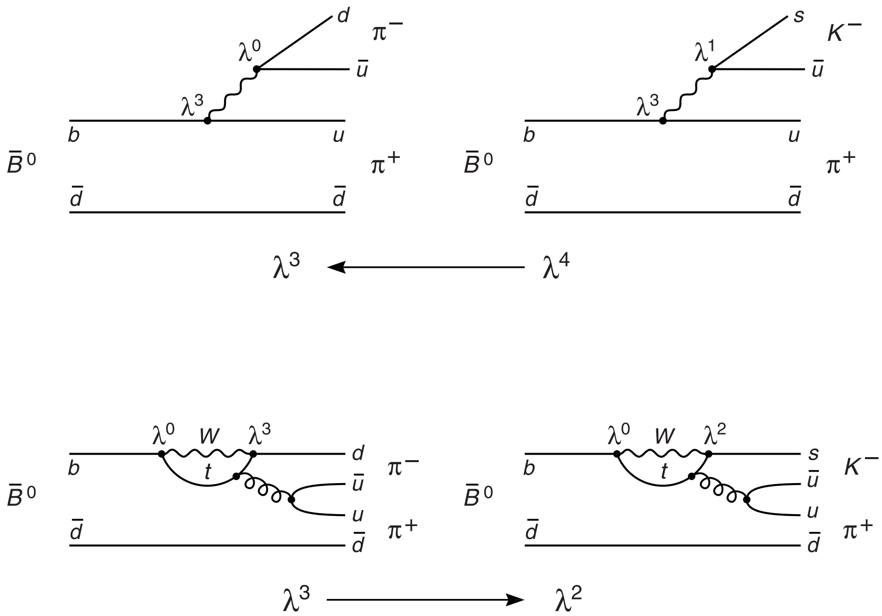

Fig. 64. Diagrams for $\bar{B}^0 \to \pi^+\pi^-$ and $\bar{B}^0 \to K^-\pi^+$. Both modes have contributions from tree $b \to u$ and penguin processes. The figure shows the dependence of each amplitude on $\lambda = \sin\theta_C$, as determined from the Wolfenstein parametrization of the CKM matrix. Simple power counting shows that the tree process should contribute more to $\bar{B}^0 \to \pi^+\pi^-$ than to $\bar{B}^0 \to K^-\pi^+$, while the penguin process (with intermediate t or c quarks) should contribute more to $\bar{B}^0 \to K^-\pi^+$ than to $\bar{B}^0 \to \pi^+\pi^-$. Both the tree and penguin contributions to $\bar{B}^0 \to \pi^+\pi^-$ are $\mathcal{O}(\lambda^3)$. In a scenario where $B(\bar{B}^0 \to K^-\pi^+) \approx B(\bar{B}^0 \to \pi^+\pi^-)$, we could conclude that $\bar{B}^0 \to K^-\pi^+$ was predominantly penguin and that $\bar{B}^0 \to \pi^+\pi^-$ was predominantly a tree process. That is, the upper-left and lower-right diagrams must dominate. For, if the $\bar{B}^0 \to K^-\pi^+$ were mainly a tree process (upper-right diagram, $\mathcal{O}(\lambda)^4$), then the $\bar{B}^0 \to \pi^+\pi^-$ tree contribution (upper left, $\mathcal{O}(\lambda^3)$) would be even larger, and we would observe $B(\bar{B}^0 \to \pi^+\pi^-) > B(\bar{B}^0 \to K^-\pi^+)$. Similarly, if $\bar{B}^0 \to \pi^+\pi^-$ were mainly penguin (lower-left, $\mathcal{O}(\lambda^3)$), then $\bar{B}^0 \to K^-\pi^+$ penguin contribution (lower right, $\mathcal{O}(\lambda^2)$) would be even larger. Current data have very large statistical uncertainties but suggest that the penguin amplitude may be somewhat larger than expected, increasing the $\bar{B}^0 \to K^-\pi^+$ rate and producing "penguin pollution" in $\bar{B}^0 \to \pi^+\pi^-$.

indicated by experiment. Then our CKM argument implies that $\bar{B}^0 \to K^-\pi^+$ must be mainly penguin, or else the $\pi^+\pi^-/K^-\pi^+$ ratio would be larger. Furthermore, even if all of the $\bar{B}^0 \to K^-\pi^+$ rate were penguin, the (assumed) near equality of the branching fractions implies that the penguin contribution to $\bar{B}^0 \to \pi^+\pi^-$ must be fairly small, since this contribution is suppressed by λ^2 in the rate relative to the penguin contribution to $\bar{B}^0 \to K^-\pi^+$.

The dominant background in most CLEO measurements of rare hadronic decay modes is due to continuum processes, which can produce high-momentum tracks. In the analyses, great effort is required

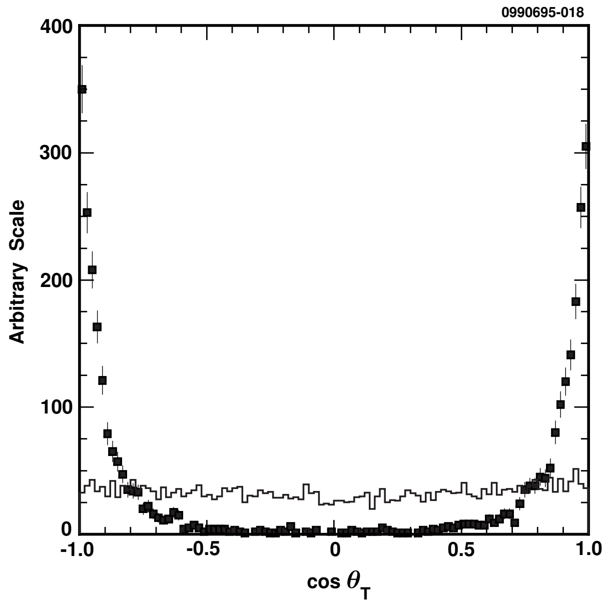

Fig. 65. CLEO II distribution of the $\cos\theta_T$ variable for $\bar{B}^0 \to \pi^+\pi^-$ (histogram) and for continuum background (solid squares). The signal distribution is taken from a Monte Carlo simulation.

to suppress this background. Figure 65 shows one powerful variable that is used for this purpose. We define θ_T as the polar angle between the thrust axis of the B candidate tracks (both charged and neutral) and the thrust axis of all the remaining tracks in the event. In (jetlike) continuum events, these axes tend to be highly correlated, resulting in peaks at $\cos\theta_T = \pm 1$, while for the more spherical $\Upsilon(4S) \to B\bar{B}$ events the axes are essentially uncorrelated, resulting in a uniform distribution.

Experimentally, it can be quite difficult to distinguish between $\bar{B}^0 \to \pi^+\pi^-$ and $\bar{B}^0 \to K^-\pi^+$, because the daughter hadrons have momenta $p \approx 2.6$ GeV/c. In CLEO, the dE/dx separation between kaons and pions at this momentum is only 1.7σ. Until recently, both CLEO and the LEP experiments have only been able to report measurements of the sum of the two modes. Table 24 lists a set of new CLEO II measurements [140], based on a sample of 3.3 million $B\bar{B}$ pairs, of $\bar{B} \to \pi\pi$, $\bar{B} \to K\pi$, and $\bar{B} \to KK$ modes in various charge states. The $B^0 \to \pi^+\pi^-$ significance, at 2.2σ, is still not sufficiently large to claim a signal, but the $\bar{B}^0 \to K^-\pi^+$ mode has a 5.6σ significance and has a branching fraction of $(1.5 \pm 0.5) \times 10^{-5}$. Figure 66 shows some of the signals. The quoted significance is based on a careful

Table 24
CLEO II branching fractions ($\mathcal{B}$) and theoretical predictions for $B \to K\pi$, $B \to \pi\pi$, and $B \to KK$. N_S is the number of signal events. The quoted significance (Sig.) is statistical only. $\mathcal{E}$ is the detection efficiency. The errors on $\mathcal{B}$ are statistical, fit systematics, and efficiency systematics respectively. The symbol h^+ represents either a π^+ or a K^+. The results are based on 3.3 million $\Upsilon(4S) \to B\bar{B}$ decays. From Ref. [140], which contains references to the theoretical predictions. Following standard practice, conjugate modes are included; that is, each branching fraction is the average over the indicated final state and its conjugate.

Mode	N_S	Sig./σ	$\mathcal{E}(\%)$	$\mathcal{B}/10^{-5}$	Theory $\mathcal{B}/10^{-5}$
$\pi^+\pi^-$	$9.9^{+6.0}_{-5.1}$	2.2	44 ± 3	< 1.5	$0.8 - 2.6$
$\pi^+\pi^0$	$11.3^{+6.3}_{-5.2}$	2.8	37 ± 3	< 2.0	$0.4 - 2.0$
$\pi^0\pi^0$	$2.7^{+2.7}_{-1.7}$	2.4	29 ± 3	< 0.93	$0.006 - 0.1$
$K^+\pi^-$	$21.6^{+6.8}_{-6.0}$	5.6	44 ± 3	$1.5^{+0.5}_{-0.4} \pm 0.1 \pm 0.1$	$0.7 - 2.4$
$K^+\pi^0$	$8.7^{+5.3}_{-4.2}$	2.7	37 ± 3	< 1.6	$0.3 - 1.3$
$K^0\pi^+$	$9.2^{+4.3}_{-3.8}$	3.2	12 ± 1	$2.3^{+1.1}_{-1.0} \pm 0.3 \pm 0.2$	$0.8 - 1.5$
$K^0\pi^0$	$4.1^{+3.1}_{-2.4}$	2.2	8 ± 1	< 4.1	$0.3 - 0.8$
K^+K^-	$0.0^{+1.3}_{-0.0}$	0.0	44 ± 3	< 0.43	–
$K^+\bar{K}^0$	$0.6^{+3.8}_{-0.6}$	0.2	12 ± 1	< 2.1	$0.07 - 0.13$
$K^0\bar{K}^0$	0	-	5 ± 1	< 1.7	$0.07 - 0.12$
$h^+\pi^0$	$20.0^{+6.8}_{-5.9}$	5.5	37 ± 3	$1.6^{+0.6}_{-0.5} \pm 0.3 \pm 0.2$	-

analysis of the joint $\pi^+\pi^-$-$K^-\pi^+$ likelihood function, which is shown, along with those for other modes, in Fig. 67.

The $\bar{B}^0 \to \pi^+\pi^-$ branching fraction is of great interest because this mode can be used to measure the CKM angle α. Using the measured branching fraction for $\bar{B}^0 \to \pi^+\ell^-\bar{\nu} = (1.8 \pm 0.4 \pm 0.3 \pm 0.2) \times 10^{-4}$, together with the factorization hypothesis, one can estimate [140] $B(\bar{B}^0 \to \pi^+\pi^-) = (1.2 \pm 0.4) \times 10^{-5}$, very close to $B(\bar{B}^0 \to K^-\pi^+) \approx 1.5 \times 10^{-5}$ given in Table 24. The central value of the fit to the data, $B(\bar{B}^0 \to \pi^+\pi^-) = (0.7 \pm 0.4) \times 10^{-5}$, is consistent with the factorization-model prediction. It has been said that the $\bar{B}^0 \to \pi^+\pi^-$ branching fraction is turning out to be lower than expected, but at this point the uncertainties are too large to draw any strong conclusion.

Table 24 also shows that there is a significant signal for $B^- \to \bar{K}^0\pi^-$ (or $B^+ \to K^0\pi^+$). In Fig. 68 we see that the penguin diagram produces the appropriate set of quarks for this decay, $s\bar{d}d\bar{u}$, while the tree diagram produces $s\bar{u}u\bar{u}$. We might conclude that there can be absolutely no tree contribution, in which case this signal would represent the first unambiguous observation of a gluonic penguin process. In principle, however, final-state interactions could convert the $u\bar{u}$ system in the

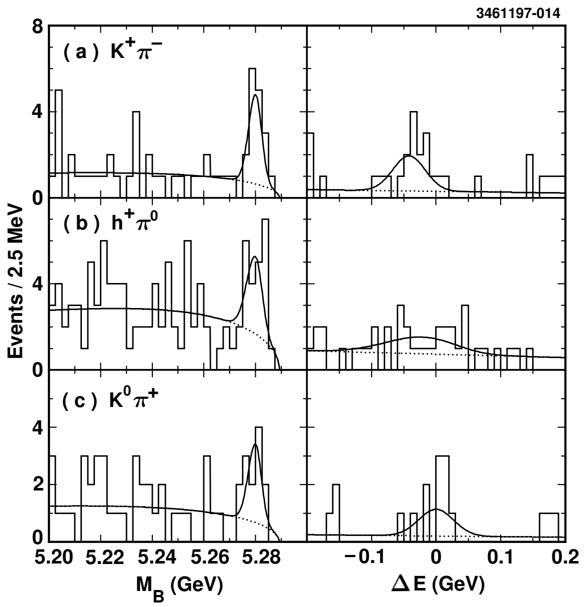

Fig. 66. CLEO II observation of (a) $B^0 \to K^+\pi^-$, (b) $B^+ \to h^+\pi^0$ (h^+ is either a π^+ or a K^+), and (c) $B^+ \to K^0\pi^+$. The solid curves show the scaled projections of the total likelihood fit, while the dotted curves show the continuum background component in each channel. The ΔE distributions are calculated assuming $\bar{B}^0 \to \pi^+\pi^-$, and the signal ΔE distribution for $\bar{B}^0 \to K^-\pi^+$ is centered at -42 MeV. This kinematic distribution gives a 1.6σ separation between $B^- \to K^-\pi^+$ and $\bar{B}^0 \to \pi^+\pi^-$.

tree diagram into a $d\bar{d}$ pair. To the extent that final-state interactions are likely to be small, the original conclusion still holds. Furthermore, the amplitude for the tree diagram is $\mathcal{O}(\lambda^4)$, while that for the penguin is $\mathcal{O}(\lambda^2)$, making it extremely unlikely that the tree contribution could be significant.

A number of other rare B decay modes have now been observed. The most striking are $B^+ \to \eta' K^+$ and $B^0 \to \eta' K^0$, whose branching fractions [141] are listed in Table 25. Although the branching fractions have large uncertainties, their large values suggest that something interesting might be going on. Figure 69 shows that there are several diagrams that may contribute to these modes. CLEO has also searched for two-body B decays with ϕ or ω mesons. The $\phi K^{(*)}$ modes have no tree contributions, while the $\omega K^{(*)}$ modes can have both penguin and tree contributions. A significant signal for $B^+ \to \omega K^+$ is listed in Table 25.

Radiative penguins are processes in which the effective flavor-changing-neutral-current transition is accompanied by the emission of a photon rather than a gluon. Although these are electromagnetic de-

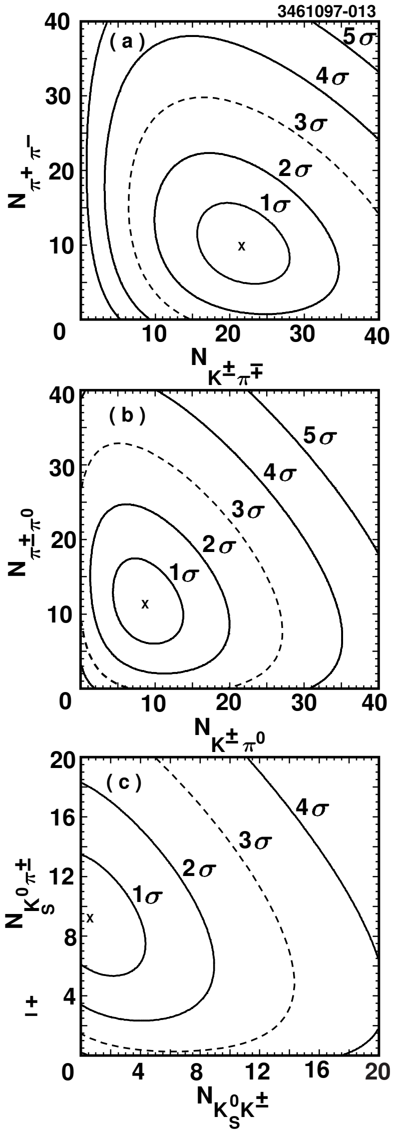

Fig. 67. Likelihood contours for the CLEO II $B \to \pi\pi$, $B \to K\pi$, and $B \to KK$ analyses. The best fit results are marked with an x.

cays, strong-interaction effects are extremely important, giving a large enhancement in the rate. There has been a heroic theoretical effort to calculate the standard-model prediction to next-to-leading order in QCD; this work involved many groups and was completed in 1996. A review with references is given by Buras and Fleischer [12]. At the same time, there have been intensive experimental investigations. Currently the branching fraction for the exclusive decay $B \to K^*\gamma$ has been mea-

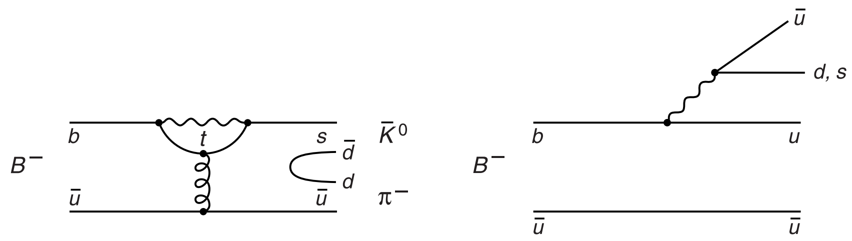

Fig. 68. The decay $B^- \to \bar{K}^0\pi^-$ has a penguin contribution (left). The tree diagram (right) does not contain a $\bar{d}$ quark and therefore cannot directly produce a $\bar{K}^0$. In principle, final-state interactions (which are expected to be small) could convert the $u\bar{u}$ pair produced in the tree diagram into a $d\bar{d}$ pair, and a $\bar{K}^0\pi^-$ system could be produced. In addition, the amplitude for the tree diagram is $\mathcal{O}(\lambda^4)$, while that for the penguin is $\mathcal{O}(\lambda^2)$.

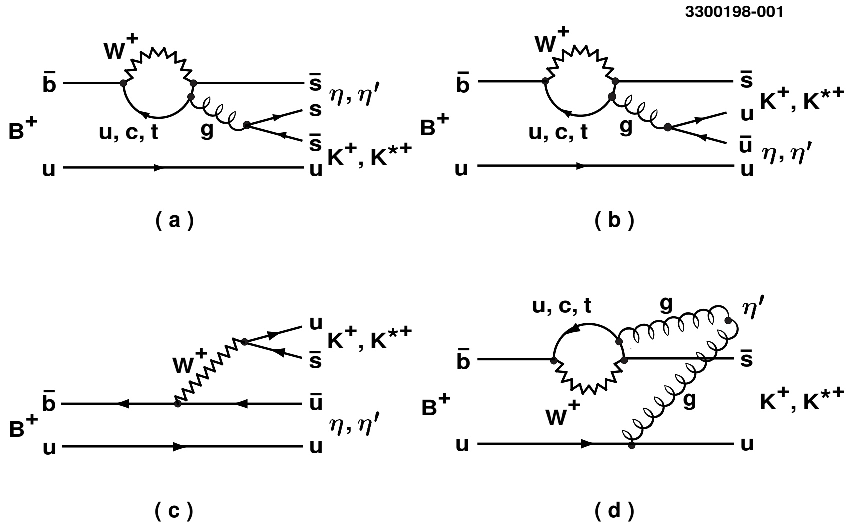

Fig. 69. Diagrams that can contribute to $B^+ \to \eta^{(\prime)}K^{(*)}$: (a) and (b) show two internal penguin processes, (c) shows an external spectator diagram, and (d) shows a flavor-singlet penguin. Constructive interference among these processes may account for the large observed rate for $B \to \eta' K$.

sured by CLEO, and that for the inclusive $b \to s\gamma$ process has been measured by both CLEO and ALEPH.

Figure 70 shows the standard-model diagrams for $\bar{B} \to K^*\gamma$ and $\bar{B} \to \rho\gamma$. Part of the interest in these decays comes from the possibility that, besides the W, other charged particles such as charged Higgs bosons could appear in the loop. There are a host of predictions from extended versions of the standard model with extra Higgs doublets, from SUSY models, and from models with composite W bosons.

Historically, the first signal for an electromagnetic penguin came

Table 25

CLEO II results on selected rare hadronic B decays. The symbol h^+ represents either a π^+ or a K^+. The results are based on 3.3 million $\Upsilon(4S) \to B\bar{B}$ decays. These results, as well as references to the theoretical predictions, are given in Ref. [141] and Ref. [142].

Mode	N_S	$\mathcal{E}(\%)$	$\mathcal{B}/10^{-5}$	Theory $\mathcal{B}/10^{-5}$
$B^+ \to \eta' K^+$			$6.5^{+1.5}_{-1.4} \pm 0.9$	$0.7 - 4.1$
$B^0 \to \eta' K^0$			$4.7^{+2.7}_{-2.0} \pm 0.9$	$0.9 - 3.3$
$B^+ \to \eta'_{\eta\pi\pi} K^+$	$11.2^{+4.1}_{-3.4}$	30	$6.7^{+2.5}_{-2.1} \pm 0.8$	
$B^+ \to \eta'_{\rho\gamma} K^+$	$19.6^{+6.6}_{-5.7}$	28	$7.0^{+2.4}_{-2.1} \pm 0.9$	
$B^+ \to \eta'_{5\pi} K^+$	$2.3^{+2.2}_{-1.5}$	17	$4.2^{+4.0}_{-2.7} \pm 1.4$	
$B^0 \to \eta'_{\eta\pi\pi} K^0$	$1.4^{+1.7}_{-1.0}$	23	$3.1^{+3.7}_{-2.1} \pm 0.6$	
$B^0 \to \eta'_{\rho\gamma} K^0$	$5.7^{+3.7}_{-2.8}$	27	$6.2^{+4.0}_{-3.0} \pm 1.2$	
$B^+ \to \omega K^+$	$12.2^{+5.5}_{-4.5}$	28	$1.5^{+0.7}_{-0.6} \pm 0.2$	$0.1 - 0.7$
$B^0 \to \omega K^0$	$2.3^{+2.4}_{-1.5}$	15	< 5.7	$0.1 - 0.4$
$B^+ \to \omega \pi^+$	$9.2^{+5.3}_{-4.3}$	29	< 2.3	$0.1 - 0.7$
$B^+ \to \omega h^+$	$21.4^{+6.5}_{-5.6}$	29	$2.5^{+0.8}_{-0.7} \pm 0.3$	
$B^0 \to \omega \pi^0$	$2.4^{+2.9}_{-1.8}$	24	< 1.4	$0.01 - 1.2$
$B^+ \to \phi K^+$	$0.0^{+0.8}_{-0.0}$	47	< 0.5	$0.07 - 1.6$
$B^0 \to \phi K^0$	$1.9^{+2.0}_{-1.2}$	32	< 3.1	$0.07 - 1.3$
$B^+ \to \phi \pi^+$	$0.0^{+0.9}_{-0.0}$	49	< 0.5	$\ll 0.1$
$B^+ \to \phi \pi^0$	$0.0^{+0.6}_{-0.0}$	31	< 0.5	$\ll 0.1$

Table 26

CLEO II upper limits (90% C.L.) for B decays to $\rho\pi$, $K\rho$, and $K^*\pi$. The results are based on 3.3 million $\Upsilon(4S) \to B\bar{B}$ decays. From Ref. [143], which also contains references to the theoretical predictions.

Mode	$\mathcal{E}(\%)$	$\mathcal{B}/10^{-5}$	Theory $\mathcal{B}/10^{-5}$
$B^0 \to \pi^\pm \rho^\mp$	5.3 ± 1.1	< 8.8	$1.9 - 8.8$
$B^0 \to \pi^0 \rho^0$	6.4 ± 1.3	< 1.8	$0.07 - 0.23$
$B^+ \to \pi^+ \rho^0$	7.1 ± 1.4	< 5.8	$0.0 - 1.4$
$B^+ \to K^+ \rho^-$	5.6 ± 1.1	< 3.3	$0.0 - 0.2$
$B^0 \to K^0 \rho^0$	2.7 ± 0.4	< 3.0	$0.004 - 0.04$
$B^+ \to K^+ \rho^0$	7.4 ± 1.5	< 1.4	$0.01 - 0.06$
$B^+ \to K^0 \rho^+$	2.2 ± 0.3	< 6.4	$0 - 0.03$
$B^0 \to K^{*+} \pi^-$		< 6.7	$0.1 - 1.9$
$B^0 \to K^{*0} \pi^0$		< 2.0	$0.3 - 0.5$
$B^+ \to K^{*+} \pi^0$		< 8.0	$0.05 - 0.9$
$B^+ \to K^{*0} \pi^+$		< 3.9	$0.6 - 0.9$

from a CLEO analysis [144] of the exclusive decay $B \to K^*\gamma$. Why look for $K^*\gamma$ rather than $K\gamma$? The answer is simple: $B \to K\gamma$ violates

Table 27

CLEO II $B \to K^*\gamma$ results. N_S is the number of signal events, $\mathcal{E}$ is the efficiency, and $\mathcal{B}$ is the branching fraction.

Final state	N_S	$\mathcal{E}(\%)$	$\mathcal{B}/10^{-5}$
$K^{*0}(K^+\pi^-)\gamma$	$24.2^{+6.1}_{-5.6}$	22.3 ± 2.0	$4.2^{+1.1}_{-1.0} \pm 0.4$
$K^{*0}(K^0\pi^0)\gamma$	$2.8^{+2.0}_{-1.5}$	1.8 ± 0.2	$6.1^{+4.2}_{-3.3} \pm 0.8$
$K^{*-}(K^0\pi^-)\gamma$	$6.3^{+3.0}_{-2.5}$	5.7 ± 0.6	$4.3^{+2.1}_{-1.7} \pm 0.5$
$K^{*-}(K^-\pi^0)\gamma$	$4.6^{+4.4}_{-3.0}$	6.9 ± 0.7	$2.6^{+2.5}_{-1.7} \pm 0.3$
Combined $K^*\gamma$			$4.2 \pm 0.8 \pm 0.6$

conservation of angular momentum, since the K cannot cancel the photon's helicity, and there can be no orbital angular momentum projection along the decay axis. An updated version of the original analysis, with 2.6 million $\Upsilon(4S) \to B\bar{B}$ events was later performed [145]. The result is

$$B(\bar{B} \to K^*\gamma) = (4.2 \pm 0.8 \pm 0.6) \times 10^{-5}. \tag{8.22}$$

The signal is observed in four final states: $B^0 \to K^{*0}\gamma$ with $K^{*0} \to K^+\pi^-$ or $K^{*0} \to K^0\pi^0$ and $B^- \to K^{*-}\gamma$ with $K^{*-} \to K^0\pi^-$ or $K^{*-} \to K^-\pi^0$. A comparison of the yields and efficiencies of these modes is given in Table 27.

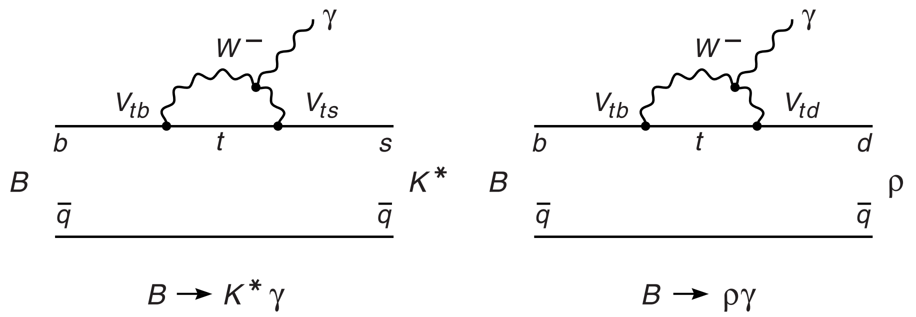

Fig. 70. Diagrams for the radiative penguin decays $\bar{B} \to K^*\gamma$ (left) and $\bar{B} \to \rho\gamma$ (right).

The measurement of the inclusive $B \to X_s\gamma$ branching fraction has been performed by both CLEO and ALEPH. Here X_s represents any kinematically accessible final state containing a strange particle. It is remarkable that such an analysis is even possible, given the huge number of photons from π^0's. The large value of the photon energies, $\sim$ 2.0 GeV to $\sim$ 2.7 GeV, is a significant help. From a theoretical perspective, this measurement is much more valuable than that for

$B \to K^*\gamma$, which is harder to predict since one must understand the hadronization into a particular final state, rather than summing over all final states. The standard-model prediction, including next-to-leading-order QCD corrections, gives [139]

$$B(\bar{B} \to X_s\gamma) = (3.5 \pm 0.3) \times 10^{-4}. \tag{8.23}$$

The relatively small uncertainty on this quantity represents a major achievement. The prediction is scaled to the measured semileptonic rate and uses unitarity of the CKM matrix to determine $|V_{ts}|$.

Two essentially independent measurements were performed in CLEO. The first analysis was based on the photon-energy spectrum and event-shape cuts, while the second also attempted to explicitly reconstruct the X_s system into final states $(K^\pm/K^0)n\pi$, where $n = 1-4$ and at most one π^0 was allowed. Figure 71 shows the photon-energy spectrum from the second analysis, which has a significant excess of events over the predicted background. Figure 72 shows the distribution of the X_s masses recoiling against the photon. A peak is observed at the K^* mass, as well as a broader bump above about 1.1 GeV, where there are many high-mass strange states. Together the two CLEO II inclusive analyses give [146]

$$B(B \to X_s\gamma) = (2.32 \pm 0.57 \pm 0.35) \times 10^{-4}. \tag{8.24}$$

This result is based on a sample of 2.6×10^6 $\Upsilon(4S) \to B\bar{B}$ events. An ALEPH analysis [147] using 0.6×10^6 $Z \to b\bar{b}$ events gives

$$B(b \to s\gamma) = (3.11 \pm 0.80 \pm 0.72) \times 10^{-4}. \tag{8.25}$$

Both of these results are consistent with the standard-model prediction given above, and they provide a powerful constraint on parameters in theories beyond the standard-model.

9. CP Violation and Oscillations

Fundamental symmetries and symmetry breaking are central issues in particle physics. The three symmetry operators C, P, and T produce discrete transformations:

$$\begin{aligned} &C:\ a \leftrightarrow \bar{a}\ (\bar{a} \text{ is the antiparticle of } a) \\ &P:\ \mathbf{x} \to -\mathbf{x}\ (\text{parity inversion of spatial coordinates}) \\ &T:\ t \to -t\ (\text{motion or “time” reversal}). \end{aligned} \tag{9.1}$$

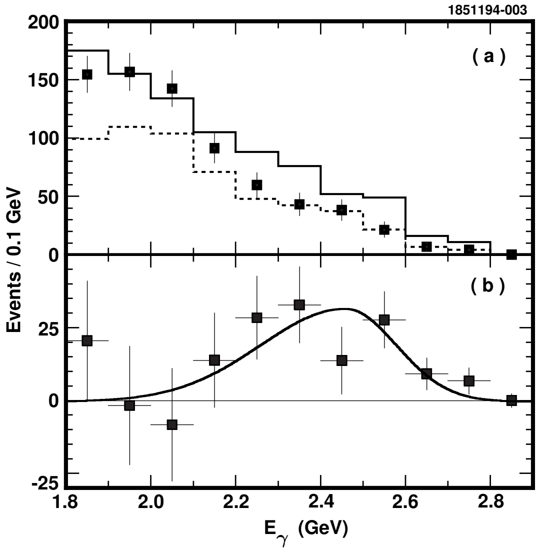

Fig. 71. CLEO II photon-energy spectrum from $\bar{B} \to X_s\gamma$ analysis. (a) shows the $\Upsilon(4S)$ data (solid histogram), the scaled off-resonance data (dashed histogram), and the sum of scaled off-resonance and the background from $\Upsilon(4S)$ (squares with error bars). (b) shows the backgound-subtracted data (squares with error bars) and the Monte Carlo prediction for the shape of the $\bar{B} \to X_s\gamma$ signal (solid curve).

These transformations play a special role in our understanding and classification of particle interactions. The famous CPT theorem states that all relativistic quantum-field theories must possess symmetry under the combined CPT operation, so that CP violation implies a compensating T violation. Both effects have now been observed in neutral K decays [148], while no CPT violation is seen.

CP violation was discovered [149] at the Brookhaven Alternating Gradient Synchrotron (AGS) in 1964, well before there was a theoretical framework, let alone a prediction, to guide experimentalists. Christenson, Cronin, Fitch, and Turlay observed the decay $K_L^0 \to \pi^+\pi^-$ with a branching fraction of $(2.0 \pm 0.4) \times 10^{-3}$. If CP were conserved, this decay would be forbidden, as discussed later in this section. I particularly recommend the articles by Cronin [150] and Fitch [151] in *Reviews of Modern Physics*, which contain their Nobel Prize lectures. Fitch notes that

> ...Professor Cronin and I are being honored for a purely experimental discovery, a discovery for which there were no precursive indications, either theoretical or experimental. It is a discovery

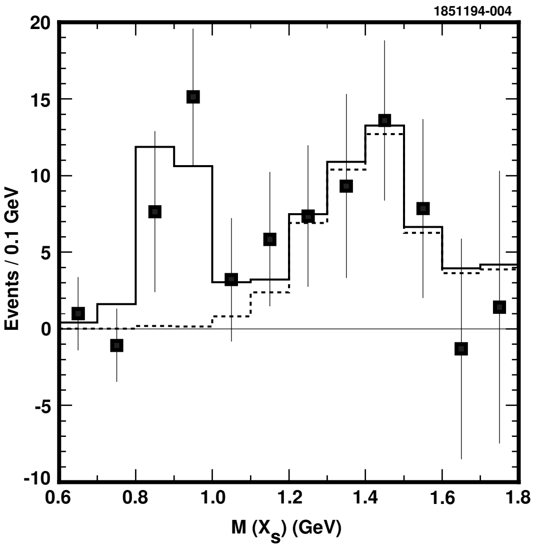

Fig. 72. CLEO II inclusive analysis of $\bar{B} \to X_s\gamma$: the apparent distribution of $M(X_s)$. The squares with error bars represent the background-subtracted data, not corrected for efficiency or cross-feed; the solid histogram shows the fit to the Monte-Carlo-based distributions; and the dotted histogram shows the component of the fit from resonances other than $K^*(892)$.

> for which after more than 16 years years there is no satisfactory accounting.

CP violation was not easy for everyone to swallow, and there was a lot of healthy skepticism regarding the measurement. Cronin recalls the 1964 International Conference on High Energy Physics at Dubna:

> As the session neared a close, one of my Soviet colleagues suggested that, perhaps, the effect was due to regeneration of short-lived K mesons (K_S) in a fly unfortunately trapped in the helium bag. We did a quick "back of the envelope" estimate of the density of the fly necessary to produce the effect. The density required was far in excess of uranium.

The experimental result withstood all scrutiny, but the source of CP violation remained a mystery. We now do have a *possible* explanation for CP violation, namely, interference effects that are sensitive to the phase in the CKM matrix (Sec. 3). The CKM matrix in turn originates in the electroweak-symmetry-breaking physics of the Higgs sector, and it is intimately related to quark masses. There are many ways for this

CP-violating phase to manifest itself experimentally, and several major new experiments will begin to test the CKM framework using B decays. These experiments will be able to measure *CP-odd observables* (or CP asymmetries), which vanish if there is no CP violation. In the CKM framework, the amplitudes of CP-violating processes are proportional to the area of the unitarity triangle. We have already obtained some important constraints on these quantities by measuring the lengths of the sides of the unitarity triangle (Sec. 3 and Sec. 7). If the new measurements are not compatible with the CKM framework, they will open the door to physics beyond the standard model.

Cronin concludes his article with the statement

> ... the effect is telling us that at some tiny level there is a fundamental asymmetry between matter and antimatter, and it is also telling us that at some tiny level interactions will show an asymmetry under the reversal of time. We know that improvements in detector technology and quality of accelerators will permit even more sensitive experiments in coming decades. We are hopeful, then, that at some epoch, perhaps distant, this cryptic message from nature will be deciphered.

The following sections describe the next stage in our effort to decipher the message.

9.1. Introduction to CP violation

CP violation is a deep and fascinating subject, but it is not always easy to see through the formalism to the simplicity of the underlying physics. I will try to present a coherent picture of the different types of CP violation, and I will discuss CP violation in K^0 decays to a certain extent. In these lectures, however, I will only be able to scratch the surface of the subject. There are many excellent papers and books on CP violation, and I have listed some of them in the references. I have found the discussions of Buras and Fleischer [12], Fleischer [152], Kayser [9], Leader and Predazzi [153], Nakada [154], Nelson [155], Nir [156], Nir and Quinn [157], Bigi and Sanda [158], and Sanda [159] to be particularly useful. A careful discussion of CP violation in the neutral kaon system is given in the book on weak interactions by Marshak, Riazuddin, and Ryan [160]. A much more recent review of this topic is given by Winstein and Wolfenstein [161].

The parity operator P is a unitary operator ($P^{-1} = P^\dagger$) that reverses the sign of spatial coordinates: $\mathbf{r} \to -\mathbf{r}$. If a particle a has four-momentum $p = (E, \mathbf{p})$ and helicity λ, the transformation is

$$P|a(p, \lambda)\rangle = \eta_P |a(\tilde{p}, -\lambda)\rangle, \tag{9.2}$$

where $\tilde{p} = (E, -\mathbf{p})$. Parity reverses the momentum direction but not the spin direction; the helicity $\lambda = \mathbf{s} \cdot \hat{\mathbf{p}}$ therefore reverses sign under parity. Since P is defined such that $P^2 = 1$, we have $P = P^{-1} = P^\dagger$.

From unitarity, we have

$$1 = \langle a|a\rangle = \langle a|P^\dagger P|a\rangle = \eta_P^* \eta_P \langle a_P|a_P\rangle = \eta_P^* \eta_P, \tag{9.3}$$

where $|a_P\rangle$ is the parity-transformed version of $|a\rangle$. This result implies that $\eta_P = \exp(i\theta_P)$. Moreover, we can use $P^2 = 1$ to show that $\eta_P = \pm 1$:

$$|a\rangle = P^2 |a\rangle = \eta_P P |a_P\rangle = \eta_P^2 |a\rangle, \tag{9.4}$$

so that $\eta_P^2 = 1$ and $\eta_P = \pm 1$.

Charge conjugation (C) is a unitary operator that changes particle to antiparticle and vice-versa. Its name is somewhat misleading, because it reverses not only electric charge, but also other quantum numbers such as color ($R \to \bar{R}$). It has no effect on momentum, spin direction, or helicity:

$$C|a(p, \lambda)\rangle = \eta_C |\bar{a}(p, \lambda)\rangle, \tag{9.5}$$

where $\bar{a}$ is the antiparticle of a and η_C is a phase factor. Like P, C is defined such that $C^2 = 1$, so that $C = C^{-1} = C^\dagger$.

We can let C operate twice on a particle $|a\rangle$ and use $C^2 = 1$:

$$|a\rangle = C^2 |a\rangle = \eta_C(a) C |\bar{a}\rangle = \eta_C(a) \eta_C(\bar{a}) |a\rangle, \tag{9.6}$$

so that $\eta_C(a)\eta_C(\bar{a}) = 1$. Since η_C must be a phase factor as a consequence of unitarity, this implies

$$\eta_C(a) = e^{i\theta_C} \qquad \eta_C(\bar{a}) = \eta_C(a)^* = e^{-i\theta_C}. \tag{9.7}$$

If $|a\rangle$ is an eigenstate of C, $\eta_C(a) = \eta_C(\bar{a}) = \pm 1$.

The combined effect of C and P is

$$CP|a(p, \lambda)\rangle = \eta_{CP} |\bar{a}(\tilde{p}, -\lambda)\rangle, \tag{9.8}$$

where $\eta_{CP} = \eta_C \eta_P$. From the properties of C and P, it is easy to show that $(CP)^{-1} = (CP)^\dagger = CP$.

Suppose that $|i\rangle$ and $|f\rangle$ are arbitrary states. They can be multiparticle states, for example, and they may have definite orbital angular momentum rather than definite linear momentum. If CP is conserved, $[CP, H] = 0$ and we have

$$\begin{aligned} \langle f|H|i\rangle &= \langle |(CP)^\dagger (CP) H (CP)^\dagger (CP)|i\rangle \\ &= \langle f|(CP)^\dagger H (CP)|i\rangle, \end{aligned} \tag{9.9}$$

so that if both $|f\rangle$ and $|i\rangle$ are eigenstates of CP,

$$\langle f|H|i\rangle = \eta_{CP}(f)\eta_{CP}(i)\langle f|H|i\rangle. \tag{9.10}$$

This relation implies either that the CP eigenvalues are the same or that the amplitude is zero (*i.e.*, the transition is forbidden).

What if CP is conserved but the states are not eigenstates of CP? Let's consider the decay $a \to b + c$ and analyze the amplitudes for transitions between states of definite linear momentum and helicity. Then

$$\begin{aligned} &\langle b(p_b, \lambda_b), c(p_c, \lambda_c)|H|a(p_a, \lambda_a)\rangle \\ &= \langle b(p_b, \lambda_b), c(p_c, \lambda_c)|(CP)^\dagger (CP) H (CP)^\dagger (CP)|a(p_a, \lambda_a)\rangle \\ &= \eta^*_{CP}(b)\eta^*_{CP}(c)\eta_{CP}(a)\langle \bar{b}(\tilde{p}_b, -\lambda_b), \bar{c}(\tilde{p}_c, -\lambda_c)|H|\bar{a}(\tilde{p}_a, -\lambda_a)\rangle \end{aligned} \tag{9.11}$$

where $p_a = (E_a, \mathbf{p}_a)$ and $\tilde{p}_a = (E_a, -\mathbf{p}_a)$, etc. The matrix element on the right-hand side of Eq. 9.11 is the amplitude for the transition between the CP-transformed versions of the original states. We see, therefore, that due to the factor $\eta^*_{CP}(b)\eta^*_{CP}(c)\eta_{CP}(a)$, CP conservation does not quite imply that the original and CP transformed amplitudes are the same, although their magnitudes are. In general, it is important to keep track of whether the states are labeled by definite linear momenta or orbital angular momenta. It can't be both! When we consider a state at rest, it generally means that we are discussing an intrinsic property such as the intrinsic parity η_P of the state, and labels such as momentum and helicity are suppressed.

We will often focus on processes involving a pseudoscalar meson P^0 that is distinct from its CP-conjugate particle $\bar{P}^0$. Neither P^0 nor $\bar{P}^0$ is an eigenstate of CP. A standard phase *convention* is to define

$$\begin{aligned} CP|P^0\rangle &= -|\bar{P}^0\rangle \\ CP|\bar{P}^0\rangle &= -|P^0\rangle. \end{aligned} \tag{9.12}$$

Although this convention is natural and can be convenient, I will try to keep nearly all of my presentation independent of any particular phase convention. This approach helps to reduce confusion between what is and what is not a physically meaningful phase. In fact, we have the freedom to redefine the phases such that [156]

$$|(P^0)'\rangle = e^{-i\zeta}|P^0\rangle \qquad |(\bar{P}^0)'\rangle = e^{+i\zeta}|\bar{P}^0\rangle. \tag{9.13}$$

This freedom is a consequence of flavor conservation in the strong and electromagnetic interactions, which are used to define the quantum numbers of P^0. Flavor conservation means that the interactions are invariant under global $U(1)$ symmetry, so we can redefine the particle phases, as long as we do it in a consistent manner.

Let's consider a simple example of $K^0 \to \pi\pi$ decay, keeping the arbitrary phase throughout the discussion. Since the $\pi\pi$ system is either $\pi^+\pi^-$ or $\pi^0\pi^0$ in a definite state of orbital angular momentum ($\ell = 0$), it is an eigenstate of CP with eigenvalue equal to one. For the $\pi^+\pi^-$ system, for example, $\eta_{CP}(\pi^+\pi^-) = (\eta_P)^2\eta_C\eta_C^*(-1)^\ell = 1$.

The action of CP on $|K^0\rangle$ and $|\bar{K}^0\rangle$ is given by

$$CP|K^0\rangle = e^{2i\theta_{CP}}|\bar{K}^0\rangle \qquad CP|\bar{K}^0\rangle = e^{-2i\theta_{CP}}|K^0\rangle, \tag{9.14}$$

where θ_{CP} is an arbitrary phase. (The factor of 2 in the exponent is not in any way fundamental but corresponds to a common usage.) Let's assume that CP is conserved in K^0 decays. Then

$$\begin{aligned} A_{2\pi} &= \langle 2\pi|H|K^0\rangle \\ &= \langle 2\pi|(CP)^\dagger(CP)H(CP)^\dagger(CP)|K^0\rangle \\ &= e^{2i\theta_{CP}}\langle 2\pi|H|\bar{K}^0\rangle \\ &= e^{2i\theta_{CP}}\bar{A}_{2\pi}, \end{aligned} \tag{9.15}$$

where we have used $\eta_{CP}(\pi\pi) = 1$ and $(CP)H(CP)^\dagger = H$. It is easy to show that the (orthogonal) states

$$\begin{aligned} |K_{CP=+1}\rangle &= \frac{1}{\sqrt{2}}(|K^0\rangle + e^{i2\theta_{CP}}|\bar{K}^0\rangle) \\ |K_{CP=-1}\rangle &= \frac{1}{\sqrt{2}}(|K^0\rangle - e^{i2\theta_{CP}}|\bar{K}^0\rangle), \end{aligned} \tag{9.16}$$

are eigenstates of CP with eigenvalues $+1$ and -1, respectively. Then

$$\begin{aligned} A_{2\pi}^{\pm} &= \langle 2\pi|H|K_{CP=\pm 1}\rangle \\ &= \frac{1}{\sqrt{2}}\left[\langle 2\pi|H|K^0\rangle \pm \langle 2\pi|H|\bar{K}^0\rangle e^{i2\theta_{CP}}\right] \\ &= \frac{1}{\sqrt{2}}\left[A_{2\pi} \pm \bar{A}_{2\pi}e^{i2\theta_{CP}}\right] \end{aligned}$$

$$= \frac{1}{\sqrt{2}}\left[A_{2\pi} \pm A_{2\pi}e^{-i2\theta_{CP}}e^{i2\theta_{CP}}\right]$$
$$= \frac{1}{\sqrt{2}}A_{2\pi}(1 \pm 1), \tag{9.17}$$

where the relation between $A_{2\pi}$ and $\bar{A}_{2\pi}$ is defined in Eq. 9.15. Thus, if CP is conserved, the CP-odd eigenstate cannot decay into 2π. In performing the corresponding experiment to search for CP violation, it is crucial to be able to define the type of kaon that is decaying. We will encounter the general issue of "tagging" the initial state throughout the discussion of CP violation and mixing.

9.2. CP violation and cosmology

In 1967, Sakharov [162] noted that CP violation has an important connection to cosmology, because it is one of three conditions necessary to generate an asymmetry between the number of baryons and antibaryons in the universe and therefore to explain the preponderance of matter over antimatter that we observe today. It is considered unlikely by some theorists that sources of CP violation accessible in B physics, such as the CKM matrix, are responsible for this effect, and the relation of upcoming experiments to cosmological issues may be overstated. It is nevertheless interesting to see what role CP violation plays in generating a baryon-number asymmetry, and we will now examine this issue.

Consider a hypothetical particle X, which has decay modes to final states labeled $Y_i(\Delta B_i)$, where ΔB_i is the difference between the baryon numbers of Y_i and X. If X has no baryon number, then ΔB_i is just the baryon number of Y_i, and any mode with $\Delta B_i \neq 0$ violates baryon number. The universe is assumed initially to be in thermal equilibrium at some temperature, with equal numbers of X and $\bar{X}$ particles. (In thermal equilibrium, all states with the same energy must be equally populated.) Baryon-number violation is a necessary condition for generating a baryon-number asymmetry, but it is not sufficient. Why not?

It is easy to show that, starting with equal numbers of X and $\bar{X}$ particles, *baryon number violation in X decay would be exactly cancelled by an opposite-sign baryon-number violation in $\bar{X}$ decay, if either CP or C were conserved.* Let X and $\bar{X}$ decay with branching fractions

$$f_i = B(X \to Y_i(\Delta B_i))$$
$$\bar{f}_i = B(\bar{X} \to \bar{Y}_i(-\Delta B_i)). \tag{9.18}$$

The net baryon number resulting from these decays is

$$\begin{aligned} B_{\rm net} &\propto \sum_i B(X \to Y_i(\Delta B_i)) \cdot \Delta B_i + \sum_i B(\bar{X} \to \bar{Y}_i(-\Delta B_i)) \cdot (-\Delta B_i) \\ &\propto \sum_i (f_i - \bar{f}_i)\Delta B_i. \end{aligned} \tag{9.19}$$

Thus, $B_{\rm net} \neq 0$ implies that there must be a decay mode that has both baryon number violation ($\Delta B_i \neq 0$) and a difference in the partial widths f_i and $\bar{f}_i$. Baryon-number violation by itself is not sufficient.

Equality of f_i and $\bar{f}_i$ can be guaranteed either by C conservation or CP conservation: either of these symmetries relates the particle decay process to the antiparticle decay process. For C, the helicities are unchanged, while for CP they are reversed. However, we are simply counting the number of baryons regardless of their spin states, so either C or CP invariance implies that the populations of Y_i and $\bar{Y}_i$ will be the same. Thus, to violate baryon number we need to violate *both C and CP*. If both symmetries are broken, then the one with the smaller symmetry violation will determine the baryon-number asymmetry. In the weak interactions, C is violated to a much greater extent than CP, so if weak processes were the source of the baryon-number asymmetry, it would be the extent of CP violation that would determine the size of the asymmetry.

One more condition is necessary to generate a baryon-number asymmetry: departure from thermal equilibrium. If the system is in thermal equilibrium, all states with the same energy will be equally populated, so particle and antiparticle populations will be the same. (Thermal equilibrium means that, crudely speaking, there is an infinite amount of time, at least compared to the time scales of the processes under consideration.) Thus, we have Sakharov's famous three conditions for generating a baryon-number asymmetry in the early universe:

(i) baryon-number violation

(ii) C and CP violation

(iii) departure from thermal equilibrium.

The CP-violating mechanism operative in the early universe may well have no relation to the CP asymmetries in K or B decays. As particle physicists, we shouldn't apologize even if it doesn't—what we observe will be important enough! It is fair to say, however, that studies of these processes can be regarded as a necessary first step in a long quest to understand the broader issues and implications of CP violation.

A CP-violating phase factor can manifest itself in several ways:

- CP violation in decay,
- CP violation in mixing,
- CP violation in the interference between mixing and decay.

In the following sections we will consider each of these in turn.

9.3. CP violation in decay ("direct" CP violation)

Conceptually, one of the simplest ways to study CP violation is to compare the decay rates $\Gamma(P \to f)$ with $\Gamma(\bar{P} \to \bar{f})$, where P is a pseudoscalar meson and f and $\bar{f}$ are CP-conjugate final states. One can also study direct CP violation by comparing the Dalitz plots for P and $\bar{P}$ decays, but here we will sum over all kinematic configurations, so the particle states will not carry momentum labels. We define the action of the CP operator on the states $|P\rangle$ and $|f\rangle$ by

$$\begin{aligned} CP|P\rangle &= e^{2i\theta(P)}|\bar{P}\rangle \\ CP|f\rangle &= e^{2i\theta(f)}|\bar{f}\rangle, \end{aligned} \tag{9.20}$$

where the values of the phases are convention dependent. Given the large number of things that P can represent, I should emphasize that $\exp 2i\theta(P)$ is the intrinsic CP phase factor associated with the pseudoscalar particle P.

We can determine a simple condition that determines whether CP is conserved or violated in a decay process. Let's assume that CP is conserved: $[H, CP] = 0$. We can then write the amplitude $A \equiv A(P \to f)$ for the $P \to f$ decay as *

$$\begin{aligned} A = \langle f|H|P\rangle &= \langle f|(CP)^\dagger (CP)H(CP)^\dagger (CP)|P\rangle \\ &= \langle \bar{f}|(CP)H(CP)^\dagger|\bar{P}\rangle \cdot e^{2i(\theta(P)-\theta(f))} \\ &= \langle \bar{f}|H|\bar{P}\rangle \cdot e^{2i(\theta(P)-\theta(f))} \\ &= \bar{A} \cdot e^{2i(\theta(P)-\theta(f))}, \end{aligned} \tag{9.21}$$

where

$$\bar{A} \equiv A(\bar{P} \to \bar{f}) = \langle \bar{f}|H|\bar{P}\rangle \tag{9.22}$$

* I am using the symbol $\langle f|H|P\rangle$ somewhat loosely here. Strictly speaking, the amplitude $A(P \to f)$ is given by the matrix element of the *transition operator*, and I have just written the first-order term of the perturbation expansion. For our purposes, the distinction is not important.

is the amplitude for the CP-conjugate process. Thus, *CP conservation* implies $|\bar{A}/A| = |\exp[-2i(\theta(P) - \theta(f))]| = 1$, independent of phase convention, so that

$$\left|\frac{\bar{A}}{A}\right| \neq 1 \qquad CP \text{ violation in decay.} \tag{9.23}$$

If this condition is met, the rates $\Gamma(P \to f)$ and $\Gamma(\bar{P} \to \bar{f})$ will be different, which we can express as an asymmetry:

$$\mathcal{A} = \frac{\Gamma(P \to f) - \Gamma(\bar{P} \to \bar{f})}{\Gamma(P \to f) + \Gamma(\bar{P} \to \bar{f})} \tag{9.24}$$

In the standard model, CP-conjugate amplitudes differ from the original amplitude at most by a phase factor. As a consequence, *if only a single amplitude contributes to a given decay process, there cannot be an observable CP asymmetry.*

We now suppose that there is more than one amplitude A_j, and that each amplitude has an associated CP-violating phase:

$$\begin{aligned} A &= \langle f|H|P\rangle = \sum_j A_j = \sum_j a_j e^{i\phi_j} \\ \bar{A} &= \langle \bar{f}|H|\bar{P}\rangle = e^{-2i(\theta(P)-\theta(f))} \sum_j a_j e^{-i\phi_j}. \end{aligned} \tag{9.25}$$

This equation is similar to Eq. 9.21, except that there are phases that change sign under CP. These so-called weak phases can be phases from the CKM matrix, but they could also be due to new physics. In general, the coefficients a_j will be of the form

$$a_j = |a_j| e^{i\delta_j}, \tag{9.26}$$

where the δ_j are non-CP-violating phases that can arise, for example, from strong final-state interactions. The δ_j are often called strong phases: they do not change sign under CP. Let us first assume that all such phases δ_j are zero. Then

$$\begin{aligned} \left|\frac{\bar{A}}{A}\right| &= \left|\frac{\sum_j |a_j| e^{-i\phi_j}}{\sum_j |a_j| e^{i\phi_j}}\right| \\ &= \left|\frac{\sum_j |a_j| \cos\phi_j - i \sum_j |a_j| \sin\phi_j}{\sum_j |a_j| \cos\phi_j + i \sum_j |a_j| \sin\phi_j}\right| \\ &= 1. \end{aligned} \tag{9.27}$$

Simply put, the numerator is just the complex conjugate of the denominator, so the magnitudes of the amplitudes are the same. This situation is shown in Fig. 73a for the case of two interfering amplitudes. Thus, the presence of CP-violating phases, even if there is more than one amplitude, is not sufficient to produce a CP asymmetry. We now allow for the possibility that there are non-zero strong phases δ_j in the amplitudes. We can rewrite our result as

$$\begin{aligned}\left|\frac{\bar{A}}{A}\right| &= \left|\frac{\sum_j |a_j| e^{i(\delta_j-\phi_j)}}{\sum_j |a_j| e^{i(\delta_j+\phi_j)}}\right| \\ &= \left|\frac{\sum_j |a_j|\cos(\delta_j-\phi_j) + i\sum_j |a_j|\sin(\delta_j-\phi_j)}{\sum_j |a_j|\cos(\delta_j+\phi_j) + i\sum_j |a_j|\sin(\delta_j+\phi_j)}\right| \\ &\neq 1.\end{aligned} \tag{9.28}$$

An alternative way to express the result is

$$|\bar{A}|^2 - |A|^2 = 2\sum_{i,j} |a_i||a_j| \sin(\phi_i-\phi_j)\sin(\delta_i-\delta_j). \tag{9.29}$$

Usually, we are just concerned with two amplitudes, in which case the asymmetry is

$$\mathcal{A} = \frac{|\bar{A}|^2 - |A|^2}{|\bar{A}|^2 + |A|^2} = \frac{2|a_1||a_2|\sin(\delta_1-\delta_2)\sin(\phi_1-\phi_2)}{|a_1|^2+|a_2|^2+|a_1||a_2|\cos(\delta_1-\delta_2)\cos(\phi_1-\phi_2)} \tag{9.30}$$

Examples showing the interaction of the strong and weak phases are shown in Fig. 73b and Fig. 73c.

These results have important implications. We can observe CP-violating effects by comparing $\Gamma(P\to f)$ with $\Gamma(\bar{P}\to\bar{f})$ only if there are *both* CP-violating *and* non-CP-violating phases. In fact, this may well be the way in which CP violation is discovered in the B system. For example, one could compare $\Gamma(\bar{B}^0\to K^-\pi^+)$ with $\Gamma(B^0\to K^+\pi^-)$. These decays have both tree and penguin contributions, which have different weak (and presumably different strong) phases. Unfortunately, it is not possible at present to calculate the strong phases. Although observation of direct CP violation in B decays would be very important, the value of the weak phase would be ambiguous. In general, to obtain a large CP asymmetry, we need two interfering amplitudes that are roughly equal in magnitude. By studying the interference between mixing and decay, we can achieve this situation. Furthermore, the uncertainties associated with strong interaction effects can be eliminated if there is only one amplitude for the direct decay, and one can then extract precise CKM phase information.

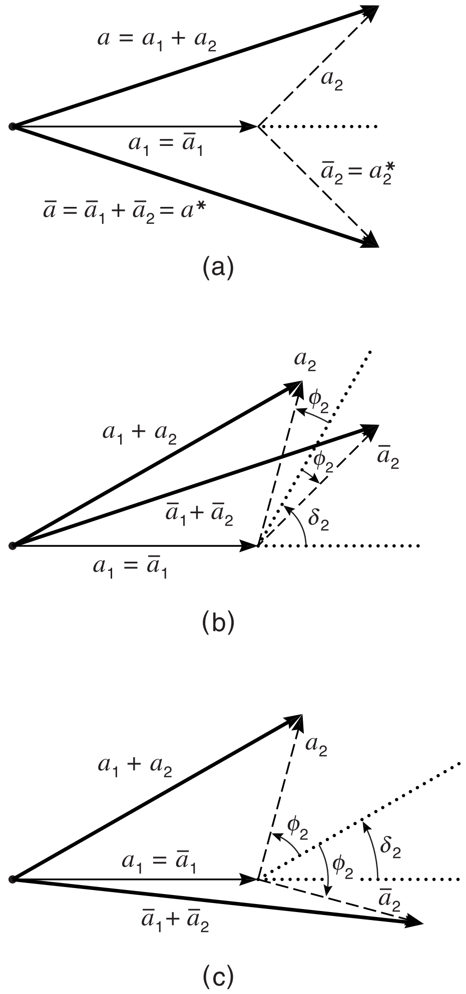

Fig. 73. Amplitudes a_1 and a_2 in direct CP violation. The amplitudes for the conjugate process are $\bar{a}_1$ and $\bar{a}_2$. In (a), there is a relative weak phase between a_2 and a_1, but no relative strong phase. In this case, the CP-conjugate amplitude $\bar{a} = \bar{a}_1 + \bar{a}_2$ has the same magnitude as the original amplitude a, and there is no CP asymmetry. In (b) and (c), there is both a relative weak and a relative strong phase between a_2 and a_1. The magnitudes of $\bar{a}$ and a now differ, giving a CP asymmetry.

An example of what can be done with direct CP violation is the Fleischer-Mannel bound [163,15,164], which is based on an analysis of branching fractions for the various charged and neutral $B \to K\pi$ modes. Here I briefly summarize the argument; full details and discussion of the many (controversial) assumptions are contained in the references. We have seen in Sec. 8.3 that the decay $B^0 \to \pi^- K^+$ has both penguin and tree contributions, while, to a good approximation,

$B^+ \to \pi^+ K^0$ is entirely a penguin process. Furthermore, the penguin amplitudes for these processes should be essentially identical, since the corresponding decays differ only in the isospin of the spectator quark. We can therefore write the decay rates as

$$\begin{aligned} &\Gamma(B^0 \to \pi^- K^+) \propto |A_P - A_T e^{-i\gamma} e^{i\delta}|^2 \\ &\Gamma(\bar{B}^0 \to \pi^+ K^-) \propto |A_P - A_T e^{i\gamma} e^{i\delta}|^2 \\ &\Gamma(B^+ \to \pi^+ K^0) = \Gamma(B^- \to \pi^- \bar{K}^0) \propto |A_P|^2, \end{aligned} \tag{9.31}$$

where A_P and A_T contain no CKM phases and δ is the relative strong phase shift between the penguin and tree processes. As we have seen, CLEO has reported the average branching fraction for $B^0 \to \pi^- K^+$ and $\bar{B}^0 \to \pi^+ K^-$. We therefore compute

$$\frac{\Gamma(B^0 \to \pi^- K^+) + \Gamma(\bar{B}^0 \to \pi^+ K^-)}{2} \propto |A_P|^2 (1 - 2r\cos\gamma\cos\delta + r^2), \tag{9.32}$$

where $r = A_T/A_P$. Thus, we can compute

$$R \equiv \frac{\Gamma(B_d \to \pi^\mp K^\pm)}{\Gamma(B^\pm \to \pi^\pm K)} = 1 - 2r\cos\gamma\cos\delta + r^2. \tag{9.33}$$

The minimum value of R as a function of r is attained when $r = \cos\delta\cos\gamma$ and is given by

$$R \geq 1 - \cos^2\gamma\cos^2\delta \geq \sin^2\gamma. \tag{9.34}$$

Assuming that $\sin^2\gamma < 1$ we have a constraint in the $\rho - \eta$ plane:

$$\sin^2\gamma = \frac{\eta^2}{\rho^2 + \eta^2} \leq R. \tag{9.35}$$

Current data yield $R = 0.65 \pm 0.40$, which suggests that there may be a useful constraint once the experimental uncertainties are reduced with more data and if various theoretical issues are resolved.

There has been a tremendous experimental effort [161,148] to detect direct CP violation in $K \to \pi\pi$ decays. In general, a two-pion system can have isospin $I = 0, 1$, or 2. Bose symmetry, however, requires that the overall wave function of the $\pi\pi$ system be symmetric, and since angular momentum conservation in $K \to \pi\pi$ requires $\ell = 0$, the isospin wave function must be symmetric. As a consequence, only $I = 0$ and $I = 2$ are allowed. The strong interactions conserve isospin, and for each of these channels there are separate phase shifts δ_0 and δ_2 due to final-state interactions:

$$\langle(\pi\pi)_{I=0}|H|K^0\rangle = a_0 e^{i\delta_0} \qquad \langle(\pi\pi)_{I=2}|H|K^0\rangle = a_2 e^{i\delta_2}, \tag{9.36}$$

where $\delta_{0,2}$ are the strong phase shifts. The amplitudes a_0 and a_2 contain the weak phases θ_0 and θ_2:

$$a_0 = |a_0|e^{i\theta_0} \qquad a_2 = |a_2|e^{i\theta_2}. \tag{9.37}$$

Direct CP violation is then characterized by the parameter

$$\varepsilon' = \frac{i}{\sqrt{2}} \operatorname{Im}\left(\frac{a_2}{a_0}\right) e^{i(\delta_2-\delta_0)}, \tag{9.38}$$

where $(\delta_2 - \delta_0) \approx -\pi/4$. (There are a number of slightly different definitions of ϵ' in the literature.) You might wonder whether it is possible for the weak interactions to produce the pions in both $I = 0$ and $I = 2$ states. This is indeed possible for the standard spectator diagram, as well as certain electroweak penguin diagrams. In gluonic penguin diagrams, only $I = 0$ is allowed: when a $u\bar{u}$ or $d\bar{d}$ pair is produced by a gluon, the pair must have $I = 0$. In principle, these quarks can then combine with the other final-state quarks to give total isospin $I = 0$ or $I = 1$, but Bose symmetry excludes $I = 1$.

Direct CP violation in K^0 decays can be studied by comparing the ratios

$$\eta_{+-} \equiv \frac{A(K_L^0 \to \pi^+\pi^-)}{A(K_S^0 \to \pi^+\pi^-)} \qquad \eta_{00} \equiv \frac{A(K_L^0 \to \pi^0\pi^0)}{A(K_S^0 \to \pi^0\pi^0)}. \tag{9.39}$$

Since $\pi^+\pi^-$ and $\pi^0\pi^0$ are different mixtures of the $I = 0$ and $I = 2$ states, comparison of η_{+-} and η_{00} is sensitive to direct CP violation. If CP violation in the $K^0\bar{K}^0$ system is due to state mixing only, the final state is irrelevant and $\eta_{+-} = \eta_{00}$. Using great care to control systematic errors, two experiments have measured the "double ratio"

$$\left|\frac{\eta_{00}}{\eta_{+-}}\right|^2 = \left|\frac{A(K_L^0 \to \pi^0\pi^0)}{A(K_S^0 \to \pi^0\pi^0)}\right|^2 \Big/ \left|\frac{A(K_L^0 \to \pi^+\pi^-)}{A(K_S^0 \to \pi^+\pi^-)}\right|^2 \approx 1 - 6\operatorname{Re}\frac{\varepsilon'}{\varepsilon}. \tag{9.40}$$

Note that the measurement of direct CP violation is related to $\operatorname{Re}\varepsilon'/\varepsilon \propto \sin(\theta_2 - \theta_0)\sin(\delta_2 - \delta_0)$, which vanishes if either the weak or the strong phases are equal. The results are

$$\begin{aligned} \operatorname{Re}\varepsilon'/\varepsilon &= (23 \pm 3.6 \pm 5.4) \times 10^{-4} \qquad \text{NA31} \\ \operatorname{Re}\varepsilon'/\varepsilon &= (7.4 \pm 5.2 \pm 2.9) \times 10^{-4} \qquad \text{E731}. \end{aligned} \tag{9.41}$$

The NA31 result indicate a small amount of direct CP violation in K^0 decays, but the uncertainties are too large to draw a definite conclusion.

New measurements from NA48 at CERN and KTeV at Fermilab should help to clarify the situation.

The calculation of ε'/ε is extraordinarily difficult due to the large number of processes involved and the presence of long-distance strong-interaction effects. Predicted values are in the range 10^{-4} to a few times 10^{-3}. Observation of a non-zero value, however, would establish that the observed CP violation could not be attributed entirely to a new $\Delta S = 2$ ($s\bar{d} \to \bar{s}d$) Fermi-type interaction (the "superweak hypothesis"), which would produce CP violation in mixing but not in decay.

9.4. CP violation in mixing ("indirect" CP violation)

The spontaneous oscillation of a particle into its antiparticle, often called mixing, provides a remarkable example of quantum-mechanical behavior. Mixing does not necessarily mean that there will be CP violation, but it does provide interfering amplitudes that can potentially produce CP violation. CP violation in neutral-K decays is largely if not entirely attributable to interfering amplitudes introduced through the mixing process. Using the $B^0\bar{B}^0$ system, we can extract clean information on certain CP-violating phases by exploiting the interference between mixing and decay amplitudes.

In this section we consider how CP violation can be manifested in the mixing of two pseudoscalar mesons, P^0 and $\bar{P}^0$, which could represent $K^0\bar{K}^0$, $D^0\bar{D}^0$, $B^0\bar{B}^0$, or $B_s\bar{B}_s$. While large mixing effects have been observed in both the $K^0\bar{K}^0$ and $B^0\bar{B}^0$ systems, $D^0\bar{D}^0$ mixing has not been observed. Due to approximate GIM cancellations, the mixing rate predicted within the standard model is expected to be quite low. Furthermore, $D^0\bar{D}^0$ mixing may well be sensitive to new physics, and it is a key topic for the charm physics program. We will see that, in contrast, $B_s\bar{B}_s$ oscillations are expected to be quite rapid, so that extremely good time resolution is required to observe them. In practice, this implies that one needs excellent resolution on decay length and high-statistics data samples. Searches for $B_s\bar{B}_s$ oscillations have so far only produced limits.

The standard formalism for mixing is based on a time-dependent perturbation-theory analysis of a two-state system, $|P^0\rangle$ and $|\bar{P}^0\rangle$, together with a continuum of states $|f\rangle$ into which the particles P^0 and $\bar{P}^0$ can decay. The total hamiltonian is written

$$H = H_0 + H_w, \tag{9.42}$$

where H_0 contains the strong and electromagnetic interactions, and H_w contains the weak interactions that induce $P^0 \leftrightarrow \bar{P}^0$, $P^0 \to f$, and $\bar{P}^0 \to f$ transitions. The basis states $|P^0\rangle$, $|\bar{P}^0\rangle$, and $|f\rangle$ are eigenstates of H_0:

$$\begin{aligned} H_0|P^0\rangle &= m_0|P^0\rangle \\ H_0|\bar{P}^0\rangle &= m_0|\bar{P}^0\rangle \\ H_0|f\rangle &= E_f|f\rangle, \end{aligned} \tag{9.43}$$

and any state in the space can be written as

$$\Psi(t) = a(t)|P^0\rangle + b(t)|\bar{P}^0\rangle + \sum_f c_f(t)|f\rangle. \tag{9.44}$$

As the system evolves, P^0 and $\bar{P}^0$ decay, so that probability moves into the states $|f\rangle$. However, the standard formalism recasts Eq. 9.42 and Eq. 9.44 into an equivalent form

$$\mathbf{H}\begin{pmatrix} a(t) \\ b(t) \end{pmatrix} = \begin{pmatrix} H_{11} & H_{12} \\ H_{21} & H_{22} \end{pmatrix}\begin{pmatrix} a(t) \\ b(t) \end{pmatrix} = i\frac{\partial}{\partial t}\begin{pmatrix} a(t) \\ b(t) \end{pmatrix} \tag{9.45}$$

in which $|f\rangle$ does not explicitly appear. The new effective hamiltonian matrix $\mathbf{H}$ is not hermitian, since we are only considering a projection onto the state space spanned by $|P^0\rangle$ and $|\bar{P}^0\rangle$.

The form of $\mathbf{H}$ is constrained by CPT symmetry, which implies [160, 153] that the matrix can be written

$$\begin{aligned} \mathbf{H} = \begin{pmatrix} H_{11} & H_{12} \\ H_{21} & H_{22} \end{pmatrix} &= \begin{pmatrix} M - \frac{i}{2}\Gamma & M_{12} - \frac{i}{2}\Gamma_{12} \\ M_{12}^* - \frac{i}{2}\Gamma_{12}^* & M - \frac{i}{2}\Gamma \end{pmatrix} \\ &= \begin{pmatrix} M & M_{12} \\ M_{12}^* & M \end{pmatrix} - \frac{i}{2}\begin{pmatrix} \Gamma & \Gamma_{12} \\ \Gamma_{12}^* & \Gamma \end{pmatrix} \\ &= \mathbf{M} - \frac{i}{2}\Gamma. \end{aligned} \tag{9.46}$$

Note that $H_{11} = H_{22}$, $M_{21} = M_{12}^*$, and $\Gamma_{21} = \Gamma_{12}^*$, but $H_{21} \neq H_{12}^*$. The equality of the diagonal elements is simply the usual result that the masses of a particle and its antiparticle are the same, as are their lifetimes. The matrix $\mathbf{M}$ is called the mass matrix, and $\mathbf{\Gamma}$ is called the decay matrix. The perturbation-theory analysis shows that, to second order, their elements are given by

$$\begin{aligned} M_{ij} &= m_0\delta_{ij} + \langle i|H_w|j\rangle + \mathcal{P}\sum_f \frac{\langle i|H_w|f\rangle\langle f|H_w|j\rangle}{m_0 - E_f} \\ \Gamma_{ij} &= 2\pi\sum_f \langle i|H_w|f\rangle\langle f|H_w|j\rangle\delta(m_0 - E_f), \end{aligned} \tag{9.47}$$

where $\mathcal{P}$ denotes the principal value prescription for performing the sum over intermediate states, avoiding states for which $m_0 = E_f$. The term $\langle i|H_w|j\rangle$ corresponds to a $\Delta S = 2$ non-standard-model interaction of the type discussed in connection with ε'.

I will not derive these results here, but it may be useful to note the behavior of the energy denominator that appears in perturbation theory:

$$\lim_{\epsilon\to 0^+} \frac{1}{(m_0 - E_f) + i\epsilon} = \lim_{\epsilon\to 0^+} \left[\frac{m_0 - E_f}{(m_0 - E_f)^2 + \epsilon^2} - i\frac{\epsilon}{(m_0 - E_f)^2 + \epsilon^2}\right]$$
$$= \mathcal{P}\left(\frac{1}{m_0 - E_f}\right) - i\pi\delta(m_0 - E_f). \tag{9.48}$$

The principal value, like the δ-function, only has meaning when used in performing an integral. It's not hard to convince yourself that these results are plausible. Since the real term is odd in $x = m_0 - E_f$ (plot it!), it deletes the contribution at $x = 0$ and therefore gives the "principal part" of the integral (you integrate up to $x = 0$ and then beyond it, but don't include $x = 0$). The imaginary part is even in $x = m_0 - E_f$. If you plot $\epsilon/(x^2 + \epsilon^2)$, you will see that it tends to $\delta(x)$ as $\epsilon \to 0$.

We will not specifically use the results in Eq. 9.47 for calculations, but they provide insight into the origin of the terms in the mass and decay matrices by relating them to particular classes of physical processes. Recalling that $1 = P^0$ and $2 = \bar{P}^0$, we note that:

• The diagonal elements M of the mass matrix are dominated by the eigenvalue m_0 of the unperturbed hamiltonian H_0, which contains information on the quark masses and the strong interactions that bind the quarks into the mesons.

• The off-diagonal elements of the *mass matrix*, M_{12} and M_{21}, are, in the standard model, due to second order weak transitions $\bar{P}^0 \leftrightarrow P^0$ and $P^0 \leftrightarrow \bar{P}^0$ respectively, via *virtual* (off-shell) intermediate states. The fact that these states must be virtual is enforced by the principal-value prescription, which means that in the sum over intermediate states $|f\rangle$, those states with $m_0 = E_f$ are excluded.

• The diagonal elements Γ of the decay matrix are due to all allowed decays $P^0 \to f$ and $\bar{P}^0 \to \bar{f}$. These states are on shell due to the factor $\delta(m_0 - E_f)$.

• The off-diagonal elements of the decay matrix, Γ_{12} and Γ_{21}, are due to transitions $\bar{P}^0 \to f \to P^0$ and $P^0 \to f \to \bar{P}^0$, where f is again an on-shell intermediate state, that is, one into which both P^0 and $\bar{P}^0$ can decay.

The term $\langle i|H_w|j\rangle$ is zero in the standard model, since $\Delta S = 2$, $\Delta C = 2$, or $\Delta B = 2$ processes do not occur in first order. The so-called superweak model postulates a new interaction that permits such processes in first order. It has not been ruled out experimentally that such an interaction is in fact responsible for the CP violation observed in the $K^0\bar{K}^0$ system!

It is very simple to solve the eigenvalue problem for this system. The hamiltonian matrix can be written

$$\mathbf{H} = H_{11}\begin{pmatrix} 1 & 0 \\ 0 & 1 \end{pmatrix} + \begin{pmatrix} 0 & H_{12} \\ H_{21} & 0 \end{pmatrix} = H_{11}\mathbf{1} + \mathbf{K} \tag{9.49}$$

where $\mathbf{1}$ is the 2×2 unit matrix and $\mathbf{K}$ is an off-diagonal matrix. Thus, the eigenvectors of $\mathbf{K}$ will also be eigenvectors of $\mathbf{H}$. We write the eigenvectors in the form

$$\begin{aligned} |P_+\rangle &= \frac{1}{\sqrt{|p|^2 + |q|^2}}\left(p|P^0\rangle + q|\bar{P}^0\rangle\right) \\ |P_-\rangle &= \frac{1}{\sqrt{|p|^2 + |q|^2}}\left(p|P^0\rangle - q|\bar{P}^0\rangle\right). \end{aligned} \tag{9.50}$$

Solving

$$\begin{pmatrix} 0 & H_{12} \\ H_{21} & 0 \end{pmatrix}\begin{pmatrix} p \\ q \end{pmatrix} = \mu\begin{pmatrix} p \\ q \end{pmatrix}, \tag{9.51}$$

we find that

$$\left(\frac{q}{p}\right)^2 = \frac{H_{21}}{H_{12}} \qquad \mu^2 = H_{12}H_{21}, \tag{9.52}$$

so that the eigenvalues of $\mathbf{H}$ are

$$\mu_\pm = H_{11} \pm (H_{12}H_{21})^{1/2} = M_\pm - \frac{i}{2}\Gamma_\pm, \tag{9.53}$$

where $M_\pm$ and $\Gamma_\pm$ are by definition real quantities:

$$\begin{aligned} M_\pm &= \mathrm{Re}\,\mu_\pm = M \pm \mathrm{Re}(H_{12}H_{21})^{1/2} \\ \Gamma_\pm &= \Gamma \mp 2\,\mathrm{Im}(H_{12}H_{21})^{1/2}. \end{aligned} \tag{9.54}$$

Due to the square root, the signs ($\pm$) of the eigenvalues do not necessarily map onto the same signs in the state vectors. We will discuss this point further below (see Eq. 9.73). In many presentations of this subject, the mass eigenstates are labeled with subscripts L or H to indicate that one has been chosen as the lighter and one the heavier mass state. For now, we will simply keep the subscripts $\pm$ according to the sign of the coefficient of q.

From Eq. 9.50 and Eq. 9.52, we see that the eigenvectors of **K** and **H** are specified by:

$$\alpha \equiv \frac{q}{p} = \left(\frac{H_{21}}{H_{12}}\right)^{1/2} = \left(\frac{M_{12}^* - \frac{i}{2}\Gamma_{12}^*}{M_{12} - \frac{i}{2}\Gamma_{12}}\right)^{1/2} \tag{9.55}$$

This quantity will appear many times in our discussion of CP violation.

It is important not to confuse the $M_\pm$ and $\Gamma_\pm$ with M_{12} and Γ_{12} appearing in **H**. However, we would expect that the off-diagonal elements of **H** determine the mass and width splittings between the eigenstates, and this is indeed the case. From Eq. 9.54 we can see that

$$\begin{aligned} \Delta M = M_- - M_+ &= -2\,\mathrm{Re}(H_{12}H_{21})^{1/2} \\ \Delta\Gamma = \Gamma_- - \Gamma_+ &= 4\,\mathrm{Im}(H_{12}H_{21})^{1/2}. \end{aligned} \tag{9.56}$$

Furthermore, we will see below that if CP is conserved, then $|\Delta\Gamma| = 2\Gamma_{12}$ and $|\Delta M| = 2M_{12}$.

In Sec. 9.5 we will see that for the case of the $B^0\bar{B}^0$ system, $H_{12} \simeq M_{12}$ and $H_{21} \simeq M_{12}^*$ due to the complete dominance of the $t\bar{t}$ intermediate state in all mixing transitions. As a consequence, $H_{12}H_{21} \simeq |M_{12}|^2$ is nearly real, and there is a mass splitting ΔM but very little difference $\Delta\Gamma$ in the widths.

In all of this formalism, it is easy to lose track of the key question: what is the condition for CP violation in mixing? To find the answer, we need first to define the action of the CP operator on $|P^0\rangle$ and $|\bar{P}^0\rangle$. We work in an arbitrary phase convention where

$$\begin{aligned} CP|P^0\rangle &= e^{2i\theta_{CP}}|\bar{P}^0\rangle \\ CP|\bar{P}^0\rangle &= e^{-2i\theta_{CP}}|P^0\rangle. \end{aligned} \tag{9.57}$$

In the subspace spanned by $|P^0\rangle$ and $|\bar{P}^0\rangle$ we can therefore write the matrix representation of CP operator as

$$\mathbf{CP} = \begin{pmatrix} 0 & e^{-2i\theta_{CP}} \\ e^{2i\theta_{CP}} & 0 \end{pmatrix}. \tag{9.58}$$

If CP is conserved, then $[CP, H] = 0$ or $(CP)^{-1}H(CP) = H$. Let's write out the matrix version of this statement. Since **CP** commutes with the identity matrix, we need only calculate

$$(\mathbf{CP})^{-1}\mathbf{K}(\mathbf{CP})$$
$$= \begin{pmatrix} 0 & e^{-2i\theta_{CP}} \\ e^{2i\theta_{CP}} & 0 \end{pmatrix} \begin{pmatrix} 0 & H_{12} \\ H_{21} & 0 \end{pmatrix} \begin{pmatrix} 0 & e^{-2i\theta_{CP}} \\ e^{2i\theta_{CP}} & 0 \end{pmatrix}$$

$$= \begin{pmatrix} 0 & e^{-4i\theta_{CP}}(M_{12}^* - \frac{i}{2}\Gamma_{12}^*) \\ e^{4i\theta_{CP}}(M_{12} - \frac{i}{2}\Gamma_{12}) & 0 \end{pmatrix}$$

$$\stackrel{?}{=} \begin{pmatrix} 0 & M_{12} - \frac{i}{2}\Gamma_{12} \\ M_{12}^* - \frac{i}{2}\Gamma_{12}^* & 0 \end{pmatrix}, \qquad (9.59)$$

where the last line holds only if $(\mathbf{CP})^{-1}\mathbf{H}(\mathbf{CP}) = \mathbf{H}$. Thus, if $[CP, H] = 0$, then

$$e^{4i\theta_{CP}}(M_{12} - \frac{i}{2}\Gamma_{12}) = (M_{12}^* - \frac{i}{2}\Gamma_{12}^*), \qquad (9.60)$$

so that $\alpha = q/p$ must be a pure phase factor directly related to the CP phases of $|P^0\rangle$ and $|\bar{P}^0\rangle$. From Eq. 9.55 and Eq. 9.60, we have in this case

$$\alpha = e^{i(2\theta_{CP}+n\pi)}, \qquad (9.61)$$

where n is an integer. When we define our mass eigenstates in Eq. 9.77 below, we will take n even so that, in the limit of no CP violation,

$$\alpha = e^{2i\theta_{CP}}, \qquad (9.62)$$

and the sign of the coefficient of α will be the CP eigenvalue. Equation 9.60 implies that

$$\left|\frac{M_{12}^* - \frac{i}{2}\Gamma_{12}^*}{M_{12} - \frac{i}{2}\Gamma_{12}}\right| = \left|e^{4i\theta_{CP}}\right| = 1. \qquad (9.63)$$

The condition for CP violation can be written

$$|\alpha|^2 = \left|\frac{q}{p}\right|^2 = \left|\frac{H_{21}}{H_{12}}\right| = \left|\frac{M_{12}^* - \frac{i}{2}\Gamma_{12}^*}{M_{12} - \frac{i}{2}\Gamma_{12}}\right| \neq 1 \qquad CP \textbf{ violation in mixing.}$$

$$(9.64)$$

It may help to remember that H_{21} is simply the amplitude for a $P^0 \to \bar{P}^0$ transition while H_{12} is the amplitude for a $\bar{P}^0 \to P^0$ transition. If the magnitudes of these quantities are different, we have an asymmetry between the behavior of matter and antimatter. Yet another way to understand the condition for CP violation is to write

$$M_{12} = |M_{12}| \exp(i\theta_{M_{12}})$$
$$\Gamma_{12} = |\Gamma_{12}| \exp(i\theta_{\Gamma_{12}}) \qquad (9.65)$$

and then to substitute these expressions into the definition of α (Eq. 9.55). After some algebra, one finds

$$\frac{q}{p} = \left[\frac{4|M_{12}|^2 e^{-2i(\theta_{M_{12}}-\theta_{\Gamma_{12}})} + |\Gamma_{12}|^2}{4|M_{12}|^2 + |\Gamma_{12}|^2 - 4|M_{12}||\Gamma_{12}|\sin(\theta_{M_{12}} - \theta_{\Gamma_{12}})}\right]^{1/2} e^{-i\theta_{\Gamma_{12}}} e^{-im\pi}$$

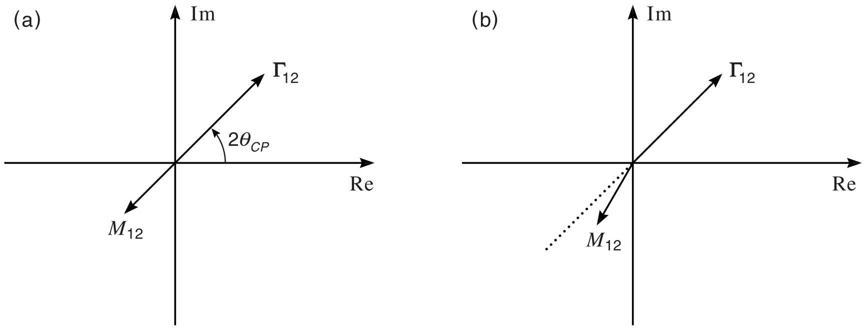

Fig. 74. CP violation in mixing. In (a) the amplitudes M_{12} and Γ_{12} are collinear, so that $\mathrm{Im}(M_{12}\Gamma^*_{12}) = 0$, and there is no CP asymmetry. The overall orientation of M_{12} and Γ_{12}, however, depends on phase convention. In (b), M_{12} and Γ_{12} point in different directions, producing a CP asymmetry.

(9.66)

where the factor $e^{-im\pi}$ (m integer) has again been used to indicate that there are two possible solutions. Inspection of this result shows that α will be a pure phase factor if

$$\theta_{M_{12}} = \theta_{\Gamma_{12}} + n'\pi, \tag{9.67}$$

where n' is yet another integer. If M_{12} and Γ_{12} are not collinear in the complex plane there will be CP violation in mixing. But that is not the only way to make $|\alpha| = 1$. If either $M_{12} = 0$ or $\Gamma_{12} = 0$, we would also have $|\alpha| = 1$. These conditions can be stated as

$$\begin{aligned} \mathrm{Im}(M_{12}\Gamma^*_{12}) &= |M_{12}||\Gamma_{12}|\,\mathrm{Im}\,e^{i(\theta_{M_{12}}-\theta_{\Gamma_{12}})} \\ &= |M_{12}||\Gamma_{12}|\sin(\theta_{M_{12}} - \theta_{\Gamma_{12}}) \\ &\neq 0 \qquad CP \textbf{ violation in mixing.} \end{aligned} \tag{9.68}$$

This condition contains the analog of the requirement that (1) $\sin(\phi_i - \phi_j) \neq 0$ in the formula for a direct CP violating asymmetry (Eq. 9.29) and (2) there must be at least two interfering amplitudes. Figure 74 shows situations that correspond to CP conservation and CP violation in mixing.

The condition stated in Eq. 9.68 is remarkably simple, given the complexity of all the intermediate states that can play a role in mixing. It would seem that a myriad of interference effects could take place even within the set of on-shell (or off-shell) transitions to produce a CP asymmetry. Yet Eq. 9.68 seems to be telling us that there is something special about the mass and decay matrices. There cannot be CP asymmetry in mixing unless the magnitudes of both M_{12} and

Γ_{12} are nonzero. At the end of this section I will try to explain why this is!

When $[CP, H] = 0$, M_{12} and Γ_{12} point either in the same or opposite direction. The phases of M_{12} and Γ_{12}, however, depend on convention, since

$$\arg\left(\frac{q}{p}\right) = -(\theta_{\Gamma_{12}} + m\pi) = 2\theta_{CP} + n\pi. \tag{9.69}$$

Using all of these phase relations we have

$$\begin{aligned} \theta_{M_{12}} &= -2\theta_{CP} - (n + m - n')\pi \\ \theta_{\Gamma_{12}} &= -2\theta_{CP} - (n + m)\pi. \end{aligned} \tag{9.70}$$

Thus, when CP is conserved in mixing,

$$\begin{aligned} M_{12} - i\frac{\Gamma_{12}}{2} &= \left[|M_{12}| - \frac{i}{2}(-1)^{n'}|\Gamma_{12}|\right] e^{[i(-2\theta_{CP}-(n+m-n')\pi)]} \\ M_{12}^* - i\frac{\Gamma_{12}^*}{2} &= \left[|M_{12}| - \frac{i}{2}(-1)^{n'}|\Gamma_{12}|\right] e^{[-i(-2\theta_{CP}-(n+m-n')\pi)]}. \end{aligned} \tag{9.71}$$

Since $H_{12}H_{21}$ enters directly into expressions for measurable quantities, it must be independent of phase convention:

$$H_{12}H_{21} = (|M_{12}| - \frac{i}{2}(-1)^{n'}|\Gamma_{12}|)^2, \tag{9.72}$$

and the mass and width splittings are given by

$$\begin{aligned} \Delta M &= \pm 2|M_{12}| \\ \Delta\Gamma &= \pm(-1)^{n'} 2|\Gamma_{12}|. \end{aligned} \tag{9.73}$$

The sign ambiguities and the factor $(-1)^{n'}$ permit either the CP even or odd state to be the heavier one, and either to have a longer lifetime, leading to four possibilities. The appropriate signs can be determined from data or in principle from a detailed theoretical calculation. Since CP violation in mixing is very small in all cases, these results for the splittings are valid to a good approximation.

Other useful expressions related to α that are valid even when CP is not conserved are

$$|\alpha|^2 = \left|\frac{q}{p}\right|^2 = \left[\frac{|M_{12}|^2 + \frac{1}{4}|\Gamma_{12}|^2 + \mathrm{Im}(M_{12}\Gamma_{12}^*)}{|M_{12}|^2 + \frac{1}{4}|\Gamma_{12}|^2 - \mathrm{Im}(M_{12}\Gamma_{12}^*)}\right]^{\frac{1}{2}} \tag{9.74}$$

and

$$\frac{|p|^2 - |q|^2}{|p|^2 + |q|^2} = \frac{\mathrm{Im}(M_{12}^*\Gamma_{12})}{|M_{12}|^2 + \frac{1}{4}|\Gamma_{12}|^2 + \frac{1}{4}((\Delta M)^2 + \frac{1}{4}(\Delta\Gamma)^2)}, \tag{9.75}$$

where we have used

$$|\Delta M - \frac{i}{2}\Delta\Gamma|^2 = (\Delta M)^2 + \frac{1}{4}(\Delta\Gamma)^2$$
$$= 4\sqrt{(|M_{12}|^2 + \frac{1}{4}|\Gamma_{12}|^2)^2 - (\mathrm{Im}(\Gamma_{12}^* M_{12}))^2}. \qquad (9.76)$$

Again, a non-zero value of $\mathrm{Im}(M_{12}\Gamma_{12}^*)$ *or* $|\alpha| \neq 1$ *signals* CP *violation in mixing.*

Now that we have identified the (phase-convention-independent) criterion for CP violation in mixing, we can analyze the effect of CP violation on the time-evolution of the $P^0\bar{P}^0$ system. The normalized eigenstates of **H**—the mass eigenstates—are

$$|P_+^0\rangle = \frac{1}{\sqrt{1+|\alpha|^2}}(|P^0\rangle + \alpha|\bar{P}^0\rangle)$$
$$|P_-^0\rangle = \frac{1}{\sqrt{1+|\alpha|^2}}(|P^0\rangle - \alpha|\bar{P}^0\rangle). \qquad (9.77)$$

Actually, α by itself does not completely specify the eigenstates in Eq. 9.50, because it only contains the relative phase of q/p. The states in Eq. 9.77 in principle could have an overall phase factor $\exp(i\theta_p)$, where θ_p is the phase of p. Since there is no physics connected with this overall phase factor, we will set it to unity from now on. This is not equivalent to choosing a CP phase convention, because that phase is opposite for $|P^0\rangle$ and $|\bar{P}^0\rangle$. We also note that, in many treatments, one of these mass eigenstates is selected to be the heavier than the other, and they are labelled with subscripts H (heavy) or L (light).

An alternative formulation for the coefficients in the mass eigenstates is sometimes used, especially for the neutral kaon system:

$$|K_S^0\rangle = \frac{1}{\sqrt{2}}\frac{1}{\sqrt{1+|\bar{\epsilon}|^2}}\left[(1+\bar{\epsilon})|K^0\rangle + (1-\bar{\epsilon})|\bar{K}^0\rangle\right]$$
$$|K_L^0\rangle = \frac{1}{\sqrt{2}}\frac{1}{\sqrt{1+|\bar{\epsilon}|^2}}\left[(1+\bar{\epsilon})|K^0\rangle - (1-\bar{\epsilon})|\bar{K}^0\rangle\right] \qquad (9.78)$$

where the bar over the ϵ is meant to emphasize that $\bar{\epsilon}$ is a phase-convention-dependent quantity. By comparing the two ways to write the ratio q/p we can relate α and $\bar{\epsilon}$

$$\alpha = \frac{1-\bar{\epsilon}}{1+\bar{\epsilon}} \qquad \bar{\epsilon} = \frac{1-\alpha}{1+\alpha}. \qquad (9.79)$$

Although the two forms have the same q/p, in Eq. 9.78 the coefficient of $|K^0\rangle$ is not real, but the overall phase freedom is used instead to set $\mathrm{Im}\, q = -\mathrm{Im}\, p$.

If CP is violated in mixing, the mass eigenstates are not orthogonal, since

$$\langle P_-^0 | P_+^0 \rangle = \frac{|p|^2 - |q|^2}{|p|^2 + |q|^2} = \frac{1 - |\alpha|^2}{1 + |\alpha|^2}. \tag{9.80}$$

If $[CP, H] = 0$, α is just $\exp(2i\theta_{CP})$, so that these states become the CP eigenstates that we constructed in Eq. 9.16, which, in our notation for a general pseudoscalar particle, are

$$\begin{aligned} |P^0_{CP=+1}\rangle &= \frac{1}{\sqrt{2}}(|P^0\rangle + e^{2i\theta_{CP}}|\bar{P}^0\rangle) \\ |P^0_{CP=-1}\rangle &= \frac{1}{\sqrt{2}}(|P^0\rangle - e^{2i\theta_{CP}}|\bar{P}^0\rangle). \end{aligned} \tag{9.81}$$

Note that if one adopts the natural convention that $CP|P^0\rangle = -|\bar{P}^0\rangle$ and $CP|\bar{P}^0\rangle = -|P^0\rangle$, then $\exp(2i\theta_{CP}) = -1$.

Although this relentless series of relations among different basis states can be mind-numbing, it's useful to express the mass eigenstates in terms of the CP eigenstates:

$$\begin{aligned} |P_+^0\rangle &= \frac{1}{\sqrt{2}} \frac{1}{\sqrt{1+|\alpha|^2}} (1 + \alpha e^{-2i\theta_{CP}}) \left[|P^0_{CP=+1}\rangle + \frac{(1 - \alpha e^{-2i\theta_{CP}})}{(1 + \alpha e^{-2i\theta_{CP}})} |P^0_{CP=-1}\rangle \right] \\ |P_-^0\rangle &= \frac{1}{\sqrt{2}} \frac{1}{\sqrt{1+|\alpha|^2}} (1 + \alpha e^{-2i\theta_{CP}}) \left[\frac{(1 - \alpha e^{-2i\theta_{CP}})}{(1 + \alpha e^{-2i\theta_{CP}})} |P^0_{CP=+1}\rangle + |P^0_{CP=-1}\rangle \right] \end{aligned} \tag{9.82}$$

You can check that when CP is conserved, these formulas behave as expected: the mass eigenstates become CP eigenstates.

Because $|P_+^0\rangle$ and $|P_-^0\rangle$ are eigenstates of $\mathbf{H}$, their time-dependence is extremely simple:

$$\begin{aligned} |P_+^0(t)\rangle &= P_+(0) e^{-i\mu_+ t} |P_+^0\rangle \\ &= \frac{1}{\sqrt{1+|\alpha|^2}} P_+(0) e^{-i(M_+ + \frac{i}{2}\Gamma_+)t} (|P^0\rangle + \alpha|\bar{P}^0\rangle) \\ |P_-^0(t)\rangle &= P_-(0) e^{-i\mu_- t} |P_-^0\rangle \\ &= \frac{1}{\sqrt{1+|\alpha|^2}} P_-(0) e^{-i(M_- + \frac{i}{2}\Gamma_-)t} (|P^0\rangle - \alpha|\bar{P}^0\rangle), \end{aligned} \tag{9.83}$$

where $P_+(0)$ and $P_-(0)$ are the amplitudes at $t = 0$.

To determine the time dependence of the flavor eigenstates, we express them in terms of the mass eigenstates:

$$|P^0\rangle = \frac{1}{2}\sqrt{1+|\alpha|^2}(|P^0_+\rangle + |P^0_-\rangle)$$
$$|\bar{P}^0\rangle = \frac{\sqrt{1+|\alpha|^2}}{2\alpha}(|P^0_+\rangle - |P^0_-\rangle) \tag{9.84}$$

The time dependence of states that are initially $|P^0\rangle$ or $|\bar{P}^0\rangle$ is therefore

$$|P^0(t)\rangle = \frac{1}{2}\sqrt{1+|\alpha|^2}\left(|P^0_+\rangle e^{-i(M_+ + \frac{i}{2}\Gamma_+)t} + |P^0_-\rangle e^{-i(M_- + \frac{i}{2}\Gamma_-)t}\right)$$
$$|\bar{P}^0(t)\rangle = \frac{\sqrt{1+|\alpha|^2}}{2\alpha}\left(|P^0_+\rangle e^{-i(M_+ + \frac{i}{2}\Gamma_+)t} - |P^0_-\rangle e^{-i(M_- + \frac{i}{2}\Gamma_-)t}\right). \tag{9.85}$$

Finally, we obtain the time evolution of the states that are produced as flavor eigenstates, expressed in the flavor-eigenstate basis:

$$|P^0(t)\rangle = f_+(t)|P^0\rangle + \alpha f_-(t)|\bar{P}^0\rangle$$
$$|\bar{P}^0(t)\rangle = \frac{1}{\alpha}f_-(t)|P^0\rangle + f_+(t)|\bar{P}^0\rangle, \tag{9.86}$$

where

$$f_+(t) = \frac{1}{2}\left(e^{-iM_+t}e^{-\Gamma_+t/2} + e^{-iM_-t}e^{-\Gamma_-t/2}\right)$$
$$f_-(t) = \frac{1}{2}\left(e^{-iM_+t}e^{-\Gamma_+t/2} - e^{-iM_-t}e^{-\Gamma_-t/2}\right). \tag{9.87}$$

These expressions are general and can be used as a starting point to analyze any of the neutral meson systems with oscillations. We can now calculate the mixing probabilities as a function of time:

$$\text{Prob}(P^0 \text{ at } t|P^0 \text{ at } t=0) = \frac{1}{4}\left[e^{-\Gamma_+t} + e^{-\Gamma_-t} + 2e^{-\Gamma t}\cos(\Delta M t)\right]$$
$$\text{Prob}(\bar{P}^0 \text{ at } t|P^0 \text{ at } t=0) = \frac{1}{4}|\alpha|^2\left[e^{-\Gamma_+t} + e^{-\Gamma_-t} - 2e^{-\Gamma t}\cos(\Delta M t)\right]$$
$$\text{Prob}(P^0 \text{ at } t|\bar{P}^0 \text{ at } t=0) = \frac{1}{4|\alpha|^2}\left[e^{-\Gamma_+t} + e^{-\Gamma_-t} - 2e^{-\Gamma t}\cos(\Delta M t)\right]$$
$$\text{Prob}(\bar{P}^0 \text{ at } t|\bar{P}^0 \text{ at } t=0) = \frac{1}{4}\left[e^{-\Gamma_+t} + e^{-\Gamma_-t} + 2e^{-\Gamma t}\cos(\Delta M t)\right], \tag{9.88}$$

where

$$\Delta M = M_- - M_+ \qquad \Gamma = \frac{1}{2}(\Gamma_+ + \Gamma_-).$$

These expressions behave as expected for $t = 0$: $|P^0(t = 0)\rangle$ has not yet developed any $|\bar{P}^0\rangle$ component, and $|\bar{P}^0(t = 0)\rangle$ has not yet developed any $|P^0\rangle$ component. We are accustomed to the survival probability of a particle being an exponential. For $|\alpha|^2 = 1$,

$$\text{Prob}(P^0 \text{ at } t|P^0 \text{ at } t = 0) + \text{Prob}(\bar{P}^0 \text{ at } t|P^0 \text{ at } t = 0) = \frac{1}{2}\left[e^{-\Gamma_+ t} + e^{-\Gamma_- t}\right]. \tag{9.89}$$

That is, the total probability to survive either as a P^0 or a $\bar{P}^0$ is the sum of two exponentials. If CP is violated, this probability *isn't even* the sum of two exponentials, since the oscillating term is present.

In the $B^0\bar{B}^0$ system, there is essentially no lifetime splitting, so $\Gamma_+ = \Gamma_- = \Gamma$, and the oscillating term can be written

$$\cos(\Delta M t) = \cos(\frac{\Delta M}{\Gamma}\frac{t}{\tau}). \tag{9.90}$$

Thus, the quantity $\Delta M/\Gamma$ characterizes the mixing rate when we measure time in units of proper lifetime.

We can also see that if $|\alpha|^2 \neq 1$

$$\text{Prob}(P^0 \to \bar{P}^0) \neq \text{Prob}(\bar{P}^0 \to P^0). \tag{9.91}$$

If $|\alpha| < 1$, we get less $\bar{P}^0$ than P^0 because

$$|\alpha| = |H_{21}/H_{12}| = |\langle\bar{P}^0|H|P^0\rangle/\langle P^0|H|\bar{P}^0\rangle|. \tag{9.92}$$

The equality of the $P^0(t) \to P^0$ and $\bar{P}^0(t) \to \bar{P}^0$ probabilities is a consequence of CPT symmetry. Figure 75 shows the behavior of the formulas in Eq. 9.88 for the neutral kaon system. As discussed in Sec. 9.5 the lifetimes of the mass eigenstates are very different: $\tau_L \approx$ 52 ns and $\tau_s = 0.09$ ns.

Before leaving this section, I would like to discuss why it is that the condition for CP violation in mixing, $\text{Im}(M_{12}\Gamma_{12}^*) \neq 0$, is so remarkably simple. What is magic about the mass and decay matrices? After all, CP violation is generated by the interference between different amplitudes, and there can be many amplitudes with on-shell intermediate states (why can't these interfere with each other, producing CP violation?) and many amplitudes for off-shell intermediate states (why can't these interfere with each other producing CP violation?). The statement $\text{Im}(M_{12}\Gamma_{12}^*) \neq 0$ is saying that CP violation in mixing can only

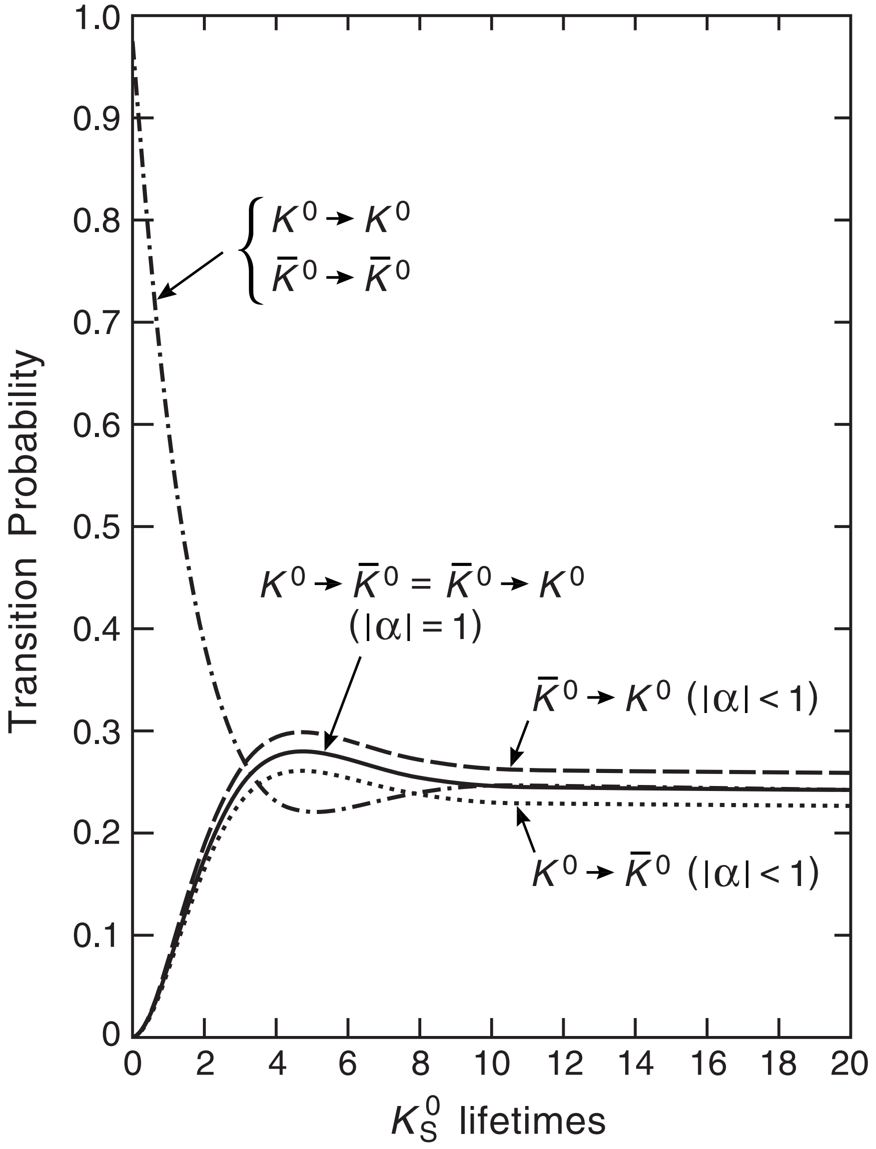

Fig. 75. Time evolution of particles initially tagged as a K^0 and $\bar{K}^0$. The probabilities for $K^0 \to K^0$ and $\bar{K}^0 \to \bar{K}^0$ are equal, as required by CPT symmetry. For $|\alpha| \neq 1$, however, there is a difference between $K^0 \to \bar{K}^0$ and $\bar{K}^0 \to K^0$. The CP asymmetry is seen as the difference between the dashed line and the dotted line, and it was generated with $|\alpha| = 0.967$, corresponding to an asymmetry about ten times the actual size ($|\alpha| = 0.9967$). The curves appear to reach an essentially flat asymptote; this is because $\tau_L \gg \tau_S$ and the scale only extends out to twenty K_S^0 lifetimes.

originate in the interference between the total amplitude via on-shell intermediate states and the total amplitude for off-shell intermediate states!

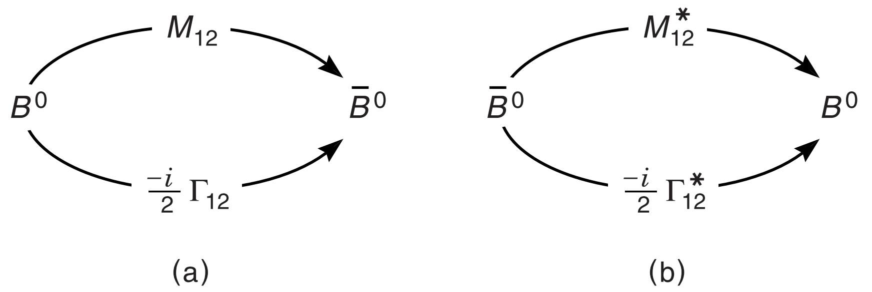

Fig. 76. CP violation in mixing. The interference occurs between the set of amplitudes with virtual intermediate states (M_{12}) and on-shell intermediate states (Γ_{12}). The factor $-i = \exp(-i\pi/2)$ plays the role of the strong-phase factor $\exp[i(\delta_i - \delta_j)]$ in direct CP violation: it doesn't change sign for the CP-conjugate amplitude.

To resolve this question, consider Fig. 76, which shows how CP violation in mixing is generated. Keep in mind that we are comparing H_{12} and H_{21}:

$$\begin{aligned} H_{12} &= \langle P^0|H|\bar{P}^0\rangle = \langle P^0|M|\bar{P}^0\rangle - \frac{i}{2}\langle P^0|\Gamma|\bar{P}^0\rangle \\ &= M_{12} - \frac{i}{2}\Gamma_{12} \\ H_{21} &= \langle \bar{P}^0|H|P^0\rangle = \langle \bar{P}^0|M|P^0\rangle - \frac{i}{2}\langle \bar{P}^0|\Gamma|P^0\rangle \\ &= M_{21} - \frac{i}{2}\Gamma_{21} = M_{12}^* - \frac{i}{2}\Gamma_{12}^*. \end{aligned} \tag{9.93}$$

Figure 76a shows the two amplitudes that contribute to $P^0 \to \bar{P}^0$; Fig. 76b shows the analogous amplitudes that contribute to $\bar{P}^0 \to P^0$. Each of these amplitudes is actually a bundle of the amplitudes for various intermediate states, but by itself, neither bundle can produce CP violation. Thus, if there are only off-shell intermediate states, such as $t\bar{t}$, there can be no CP violation in mixing, no matter what CKM phases are present in amplitudes, because CPT invariance guarantees that $M_{21} = M_{12}^*$ [153]. Without an amplitude from on-shell intermediate states (Γ_{12}) the rates for $P^0 \to \bar{P}^0$ and $\bar{P}^0 \to P^0$ would be equal. Similarly, because $\Gamma_{21} = \Gamma_{12}^*$, mixing via on-shell intermediate states alone cannot produce CP violation. The factor of $-i = \exp(-i\pi/2)$ that multiplies both $\Gamma_{12}/2$ and $\Gamma_{12}^*/2$ comes from the coefficient of the δ-function in Eq. 9.48 that defines the on-shell intermediate states. It is this i that plays the role that strong phases play in direct CP violation: it has the same sign in the CP-conjugate amplitude, while both M_{12} and Γ_{12} are complex-conjugated.

9.5. Phenomenology of mixing

The formalism presented in the previous section applies equally well to $K^0\bar{K}^0$, $D^0\bar{D}^0$, $B^0\bar{B}^0$, or $B_s\bar{B}_s$ oscillations. Differences in the detailed physics, however, lead to approximations and results that are different for each case. In this section, we examine the specifics of the phenomenology and review some of the mixing measurements.

The $K^0\bar{K}^0$ system is characterized by a huge lifetime splitting between the two mass eigenstates:

$$\frac{\tau(K_L^0)}{\tau(K_S^0)} \simeq \frac{52 \text{ ns}}{0.09 \text{ ns}} \simeq \frac{15.5 \text{ m}}{2.7 \text{ cm}} \simeq 580. \tag{9.94}$$

The origin of this splitting is simple. CP violation in $K^0\bar{K}^0$ mixing is a very small effect, so to a good approximation, the physical mass eigenstate K_S^0 corresponds to the CP-even eigenstate and K_L^0 corresponds to the CP-odd eigenstate. Note that the *mass eigenstates* $K_S^0 = K_+^0$ and $K_L^0 = K_-^0$ are given by Eq. 9.77. We have already seen in Eq. 9.17 that the CP-odd state cannot decay into 2π. Thus, the K_L^0 essentially has only four significant decay modes: $\pi^0\pi^0\pi^0$ (21.1%), $\pi^+\pi^-\pi^0$ (12.6%), $\pi^\pm\mu^\mp\nu$ (27.2%), and $\pi^\pm e^\mp\nu$ (38.8%), all of which are dramatically suppressed by three-body phase space. In contrast, the K_s^0 has decays $K_S^0 \to \pi^+\pi^-$ and $K_S^0 \to \pi^0\pi^0$, which account for nearly all of its decay rate. (The approximate ratio $\Gamma(K_S^0 \to \pi^+\pi^-)/\Gamma(K_S^0 \to \pi^0\pi^0) \approx 2$ is a consequence of the $\Delta I = 1/2$ rule.)

For the neutral kaon system, the mass and width splittings are comparable

$$\begin{aligned}\Delta\Gamma &= \Gamma_- - \Gamma_+ = \Gamma_{K_L^0} - \Gamma_{K_S^0} \approx -\Gamma_{K_S^0} \approx -10^{-10} \text{ s}^{-1}\\ \Delta M &= M_- - M_+ = M_{K_L^0} - M_{K_S^0} = (0.5304 \pm 0.0014) \times 10^{10} \text{ s}^{-1}\end{aligned} \tag{9.95}$$

where the mass difference corresponds to about 3.5 μeV. (Remember that the subscripts $\pm$ here are not CP eigenvalues, but the eigenvalues the states would have if CP violation were turned off.) Thus,

$$\Delta\Gamma \approx -2\Delta M. \tag{9.96}$$

The lifetime splitting has important implications for experiments, since it means that any neutral-kaon beam evolves over distance into an essentially pure K_L^0 beam. As a consequence, it is possible to know that the particles under study are K_L^0s without identifying a correlated particle, which would provide a "tag." Since the K_L^0 is an eigenstate of $\mathbf{H}$, it remains a K_L^0 unless a K_S^0 component is regenerated by an interaction with matter, which introduces different amplitudes for the K^0 and $\bar{K}^0$ pieces of the K_L^0 wave function.

Because $K^0(\bar{s}d) \to \pi^-\ell^+\nu$ but $\bar{K}^0(s\bar{d}) \to \pi^+\ell^-\bar{\nu}$, semileptonic decays can be used to monitor the K^0 and $\bar{K}^0$ content of the state. From Eq. 9.83,

$$\begin{aligned}
\delta &\equiv \frac{\Gamma(K_L^0 \to \pi^-\ell^+\nu) - \Gamma(K_L^0 \to \pi^+\ell^-\nu)}{\Gamma(K_L^0 \to \pi^-\ell^+\nu) + \Gamma(K_L^0 \to \pi^+\ell^-\nu)} \\
&= \frac{|\langle K^0|K_L^0\rangle|^2 - |\langle \bar{K}^0|K_L^0\rangle|^2}{|\langle K^0|K_L^0\rangle|^2 + |\langle \bar{K}^0|K_L^0\rangle|^2} \\
&= \frac{1-|\alpha|^2}{1+|\alpha|^2} = \langle K_L^0|K_S^0\rangle \\
&= (3.27 \pm 0.12) \times 10^{-3}.
\end{aligned} \tag{9.97}$$

This value demonstrates that CP-violation is present in $K^0\bar{K}^0$ mixing, but that it is a small effect. We can use it to measure the size of $|\alpha|$:

$$|\alpha| \simeq 1 - \delta \simeq 0.9967. \tag{9.98}$$

We can summarize this by saying that $K_L^0 \sim (K^0 - \alpha\bar{K}^0)$ semileptonic decays have slightly more positively-charged than negatively-charged leptons, due to a slight excess of K^0 over $\bar{K}^0$.

T. D. Lee has presented [165] some interesting observations regarding the charge asymmetry in Eq. 9.97. Before meeting each other, the representatives of two civilizations from different parts of the universe decide that it would be prudent to determine whether their definitions of matter and antimatter were the same. The spectroscopy of their atoms would be identical, even if the atoms of one civilization were made from antiprotons and positrons. However, they could use the decays of the longer-lived neutral kaon to determine whether direct contact would result in their mutual annihilation. From the asymmetry in Eq. 9.97, the civilizations could establish a sign-convention for charge: the lepton that is produced more often could be called positively charged, and they could compare this charge to that of their atomic nuclei. Note that a decay that violates parity or charge-conjugation only, such as $\pi^+ \to \mu^+\nu_\mu$ would not be adequate for this purpose. You could say that a positively charged muon was predominantly helicity $+1/2$, but then the civilizatons would have to find some way to establish a common convention for handedness. A way around this would be to communicate with polarized light signals, definining a handedness convention by a direct handshake. However, if unpolarized light were used, then an analysis based on CP violation would be required.

Another method for studying mixing effects in the $K^0\bar{K}^0$ system has been used by the CPLEAR experiment at CERN. In this experiment, $p\bar{p}$ collisions at rest can produce neutral kaons in association with charged kaons:

$$\begin{aligned} p\bar{p}\ (\text{at rest}) &\to K^-\pi^+K^0 \qquad (2\times 10^{-3}) \\ &\to K^+\pi^-\bar{K}^0 \qquad (2\times 10^{-3}). \end{aligned} \tag{9.99}$$

Thus, by selecting these processes and using their charge correlations, one can determine whether the neutral kaon is produced as a K^0 or a $\bar{K}^0$.

The picture for the $B^0\bar{B}^0$ system is different in many respects. To generate Γ_{12} and hence $\Delta\Gamma$, we need modes with large rates that both B^0 and $\bar{B}^0$ can decay into. These supply the on-shell intermediate states in the mixing amplitude. Since $b\to c$ and $\bar{b}\to\bar{c}$ usually lead to different sets of quarks in B^0 and $\bar{B}^0$ decay, the rate into such common modes is expected to be small. Both B^0 and $\bar{B}^0$ can decay into $u\bar{u}d\bar{d}$ systems, but these involve highly suppressed $b\to u$ transitions. There are also common states with $c\bar{c}d\bar{d}$ quark content, such as $D^*\bar{D}^*$ and $J/\psi K^*$; both of these are Cabibbo suppressed and the latter is color suppressed. Finally, there are common states with quark content $c\bar{u}d\bar{d}$ or $\bar{c}ud\bar{d}$. In this case, either the B^0 or $\bar{B}^0$ decay must involve a $b\to u$ transition and the other one is Cabibbo suppressed. The amplitudes for these processes enter into the mixing diagram with different signs, so there will even be some cancellation. Thus, $\Delta\Gamma$ and Γ_{12} are both expected to be very small, and in our mixing formulas we can set $\Delta\Gamma = 0$. (This conclusion is supported by a direct calculation of Γ_{12} in the standard model, whose result is given below.)

It is interesting that in the $B_s\bar{B}_s$ system, $\Delta\Gamma$ can be significant because both B_s and $\bar{B}_s$ can decay into the Cabibbo-favored final states with quark content $c\bar{c}s\bar{s}$. As a consequence the lifetime splitting between the two B_s mass eigenstates could be $\sim 15\%$ [135].

The mass difference in the $B^0\bar{B}^0$ system, on the other hand, is generated by mixing amplitudes with off-shell intermediate states. In the standard model, these amplitudes are completely dominated by the box diagrams with $t\bar{t}$. The standard-model prediction for ΔM is [12]

$$M_{12} = \frac{G_F^2 M_W^2 \eta_B m_B B_B f_B^2}{12\pi^2}(V_{td}^* V_{tb})^2 S_0(x_t) e^{i(\pi - 2\theta_{CP}(B^0))}, \tag{9.100}$$

where $x_t = m_t^2/m_W^2$, f_B is the B-meson decay constant, B_B is the B-meson bag constant, η_B parametrizes (calculable) QCD corrections, and

$$S_0(x_t) = \frac{4x_t - 11x_t^2 + x_t^3}{4(1-x_t)^2} - \frac{3x_t^3 \ln x_t}{2(1-x_t)^3}. \tag{9.101}$$

For large x_t, $S_0(x_t) \propto x_t$, so

$$\left|\frac{\Gamma_{12}}{M_{12}}\right| = \mathcal{O}(m_b^2/m_t^2) \ll 1. \tag{9.102}$$

It is therefore useful to write $\alpha = q/p$ in a form appropriate for small Γ_{12}/M_{12}:

$$\alpha \simeq \left[1 + \frac{|\Gamma_{12}|}{2|M_{12}|}\sin(\theta_{M_{12}} - \theta_{\Gamma_{12}})\right] e^{-i(\theta_{M_{12}} - \theta_{\Gamma_{12}} + n'\pi)}. \tag{9.103}$$

The mass dependence of the term $\sin(\theta_{M_{12}} - \theta_{\Gamma_{12}}) \propto (m_c/m_b)^2$ is given in Buras and Fleischer [12]. Thus, CP-violation in $B^0\bar{B}^0$ mixing is proportional to $(m_b/m_t)^2(m_c/m_b)^2 = (m_c/m_t)^2 = \mathcal{O}(10^{-4})$.

Since the lifetime splitting is negligible between the neutral-B mass eigenstates, the state of the B at the initial time cannot be determined by letting one component decay away. Instead the initial state must be tagged by identifying a particle whose flavor is correlated with that of the B. We can again use semileptonic decays to determine whether the B is a B^0 or $\bar{B}^0$ at the decay time. We can therefore measure the asymmetry

$$\begin{aligned}\mathcal{A}_{CP} &= \frac{\Gamma(B^0(t) \to \ell^-\bar{\nu}X) - \Gamma(\bar{B}^0(t) \to \ell^+\nu X)}{\Gamma(B^0(t) \to \ell^-\bar{\nu}X) + \Gamma(\bar{B}^0(t) \to \ell^+\nu X)} \\ &= \frac{|\langle\bar{B}^0|B^0(t)\rangle|^2 - |\langle B^0|\bar{B}^0(t)\rangle|^2}{|\langle\bar{B}^0|B^0(t)\rangle|^2 + |\langle B^0|\bar{B}^0(t)\rangle|^2} \\ &= \frac{|\alpha|^2 - \frac{1}{|\alpha|^2}}{|\alpha|^2 + \frac{1}{|\alpha|^2}} = \frac{|\alpha|^4 - 1}{|\alpha|^4 + 1}.\end{aligned} \tag{9.104}$$

This result has a different form than the asymmetry we wrote down for the K_L^0 (Eq. 9.97) because here we are not starting with a mass eigenstate. Because Γ_{12} is very small for $B^0\bar{B}^0$ mixing, α is given, to a good approximation, by

$$\alpha = \frac{q}{p} \simeq \sqrt{\frac{M_{12}^*}{M_{12}}}, \tag{9.105}$$

which implies that $|\alpha| = 1$ to a good approximation. Even though α carries a non-trivial CKM phase, CP violation in mixing alone has no sensitivity to it. This is because $\Gamma_{12} = 0$, so that α is a pure phase factor, and the CP asymmetry in Eq. 9.104 vanishes. We will return to Eq. 9.105 in the following section, when we discuss CP violation in the interference between mixing and decay. That type of interference is sensitive to the phase of α. Using $|\alpha| = 1$ and $\Gamma_+ = \Gamma_- = \Gamma$ in Eq. 9.88, we can obtain formulas for the $B^0\bar{B}^0$ mixing probabilities as a function of time:

$$\begin{aligned}\text{Prob}(B^0 \text{ at } t|B^0 \text{ at } t=0) &= \text{Prob}(\bar{B}^0 \text{ at } t|\bar{B}^0 \text{ at } t=0)\\ &= \frac{1}{2}e^{-\Gamma t}\left[1+\cos(\Delta M t)\right]\\ \text{Prob}(\bar{B}^0 \text{ at } t|B^0 \text{ at } t=0) &= \text{Prob}(B^0 \text{ at } t|\bar{B}^0 \text{ at } t=0)\\ &= \frac{1}{2}e^{-\Gamma t}\left[1-\cos(\Delta M t)\right].\end{aligned} \tag{9.106}$$

The rate for $B_s\bar{B}_s$ mixing is expected to be much higher than that for the $B^0\bar{B}^0$ system. In each case, ΔM is dominated by the $t\bar{t}$ intermediate state, so that the relevant CKM factors are

$$\Delta M_d \propto (V_{tb}V_{td}^*)^2 \qquad \Delta M_s \propto (V_{tb}V_{ts}^*)^2, \tag{9.107}$$

while the other factors are similar for the two cases. Figure 77 shows calculated curves for B_d and B_s mixing, where the current experimental lower limit on ΔM_s is used in the latter case.

The predicted values of ΔM for both $B_d\bar{B}_d$ ($= B^0\bar{B}^0$) and $B_s\bar{B}_s$ mixing are given in Buras and Fleischer [12]:

$$\begin{aligned}\Delta M_d &= 0.50\ \text{ps}^{-1}\cdot\left[\frac{\sqrt{B_{B_d}}f_{B_d}}{200\ \text{MeV}}\right]^2\left[\frac{\bar{m}_t(m_t)}{170\ \text{GeV}}\right]^{1.52}\left[\frac{|V_{td}|}{8.8\times10^{-3}}\right]^2\left[\frac{\eta_B}{0.55}\right]\\ \Delta M_s &= 15.1\ \text{ps}^{-1}\cdot\left[\frac{\sqrt{B_{B_s}}f_{B_s}}{240\ \text{MeV}}\right]^2\left[\frac{\bar{m}_t(m_t)}{170\ \text{GeV}}\right]^{1.52}\left[\frac{|V_{ts}|}{0.040}\right]^2\left[\frac{\eta_B}{0.55}\right].\end{aligned} \tag{9.108}$$

The experimental results on $B^0\bar{B}^0$ and $B_s\bar{B}_s$ mixing were recently reviewed by Schune [166], who described the advantages and disadvantages of various techniques and reported an average of LEP, SLD, and CDF experiments. These experiments measure the time dependence of mixing (Eq. 9.106) using high-precision vertex detectors to measure the B decay distance, which is then converted into the proper decay

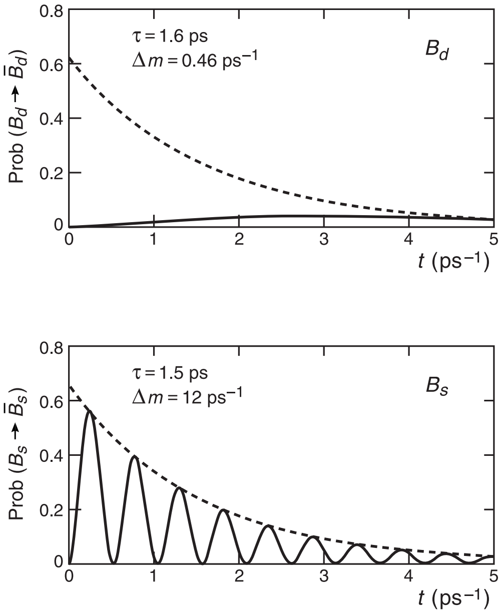

Fig. 77. The mixing probabilities (solid lines) for B_s and B_d mesons as a function of time. The dashed lines show the exponential decays. The value of Δm used for the B_d is essentially the world average value; the value for the B_s is slightly above the current lower limit.

time using the measured B momentum. The world average value for ΔM_d calculated by the LEP B Oscillations Working Group is

$$\Delta M_d = (0.472 \pm 0.018)\ \mathrm{ps}^{-1}. \tag{9.109}$$

Measurements of ΔM_d have become a major industry: 22 values are included in this average!

Measurements of $B_s\bar{B}_s$ mixing have so far only yielded the lower limit

$$\Delta M_s > 10.2\ \mathrm{ps}^{-1} \quad (95\%\ \mathrm{C.L.}). \tag{9.110}$$

Mixing in the $B^0\bar{B}^0$ system is sufficiently slow that it is also possible to measure it using time-integrated rates for opposite-sign and like-sign dilepton rates in the process $\Upsilon(4S) \to B^0\bar{B}^0$. The mixing probability can be expressed in terms of the parameter χ:

$$\begin{aligned}\chi &= \frac{\int_0^{+\infty} \mathcal{P}_{B^0\to\bar{B}^0}(t)dt}{\int_0^{+\infty} \mathcal{P}_{B^0\to\bar{B}^0}(t)dt + \int_0^{+\infty} \mathcal{P}_{B^0\to B^0}(t)dt}\\ &= \frac{(\Delta M/\Gamma)^2}{2(1+(\Delta M/\Gamma)^2)},\end{aligned} \tag{9.111}$$

where $\mathcal{P}_{B^0\to\bar{B}^0}(t)$ is the probability for a meson initially tagged as a B^0 to be found at time t as a $\bar{B}^0$. This technique works well for the $B^0\bar{B}^0$ system, where $\Delta M/\Gamma = \Delta M\tau \simeq 0.75$ is not too large, giving $\chi \simeq 0.2$. The measurement compares the yield of like-sign dilepton events, which are mainly due to mixing, to the yield of opposite-sign dilepton events, which are unmixed. Considerable care is required, because the like-sign sample has a contribution from secondary leptons from charm decays. In addition, the contribution from $\Upsilon(4S) \to B^+B^-$ decays must be accounted for. Nevertheless, this method has produced precise results, and it was the method used by ARGUS for the discovery of $B^0\bar{B}^0$ mixing [167]. We will see in the following section that when a B^0 and $\bar{B}^0$ are produced at the $\Upsilon(4S)$, their time evolution is correlated: until one or the other particle decays, their oscillations cannot produce a B^0B^0 or $\bar{B}^0\bar{B}^0$ system.

For large ΔM, the B-meson oscillates many times before it decays, so that χ approaches 1/2. Thus, for $B_s\bar{B}_s$ mixing, a measurement of the time-integrated mixing rate has little sensitivity to ΔM_s, and it is essential to use high-precision vertex detectors to measure the time dependence of the oscillation directly. The process $Z \to b\bar{b}$ is well-suited for this purpose due to the long b-hadron decay length, about 3 mm. The measurement must provide three pieces of information:

(i) The flavor of the B meson when it was produced is obtained by measurement of the other b hadron in the event. The effects of mistagging are significant and must be corrected for.

(ii) The flavor of the B meson when it decays is determined from semileptonic decay, either inclusive or semi-inclusive.

(iii) To determine the proper decay time, one measures the decay length, which requires knowledge of both the primary (Z decay) vertex position and the B decay vertex. To convert the decay length into the proper decay time, the B momentum must be measured. Since a semileptonic decay is used to reconstruct the B, there is some uncertainty associated with the neutrino momentum.

It is interesting to examine how the uncertainty on the proper decay time t depends on measured quantitities. Using $L = (p/m)ct$, it is easy to show that the uncertainty is given by

$$\sigma_t = \sqrt{\left(\frac{\sigma_L M}{p}\right)^2 + t^2\left(\frac{\sigma_p}{p}\right)^2}, \tag{9.112}$$

where σ_L is the uncertainty on the decay length, p is the momentum, σ_p is the uncertainty on the momentum. For large t, the uncertainty on the momentum, which gives the boost to the rest frame, gives the dominant contribution.

The effects of decay-length resolution and mistagging, called dilution, are shown in Fig. 78 for the separate cases of B_d and B_s mixing. The dilution is simply

$$\eta = \frac{N_{B^0,\ \text{incorr. tagged}}}{N_{B^0,\ \text{corr. tagged}}}. \tag{9.113}$$

The effects on B_s oscillation measurements are dramatic. Prospects appear to be good for measurements of B_s mixing in hadron-collider experiments.

9.6. CP violation due to interference between mixing and decay

As we have seen, CP-violating effects require interfering amplitudes in order that the weak phases can be manifest in the asymmetry between rates. As shown earlier (Fig. 2), these amplitudes can be supplied by

(i) Direct decay $B^0 \to f$, where f is a final state that both B^0 and $\bar{B}^0$ can decay into;

(ii) $B^0 \to \bar{B}^0$ mixing followed by $\bar{B}^0 \to f$.

Both the B^0 and $\bar{B}^0$ must be able to decay into f, which can be a CP eigenstate f_{CP} (*e.g.*, $\pi^+\pi^-$ or D^+D^-) but need not be (*e.g.*, $D^{*+}\pi^-$). Using the "gold-plated" decay $B^0 \to J/\psi K_S^0$, one can measure $\sin 2\beta$ with virtually no uncertainties due to strong-interaction effects. In other cases, such as $B^0 \to \pi^+\pi^-$, the situation is more complicated due to the simultaneous presence of direct CP violation, with the attendant strong phases, and CP violation due to interference between mixing and decay. As we will see, this mode will be used to extract $\sin 2\alpha$, but it remains to be seen how the uncertainties due to strong phases will be sorted out. In any case, the method of using interference between mixing and decay to a CP eigenstate is very powerful, because the interfering amplitudes are of comparable size and the asymmetries can be very large.

We start with the general mixing formulas, which we repeat here (with $P^0 = B^0$) for convenience

$$\begin{aligned} |B^0(t)\rangle &= f_+(t)|B^0\rangle + \alpha f_-(t)|\bar{B}^0\rangle \\ |\bar{B}^0(t)\rangle &= \frac{1}{\alpha} f_-(t)|B^0\rangle + f_+(t)|\bar{B}^0\rangle, \end{aligned} \tag{9.114}$$

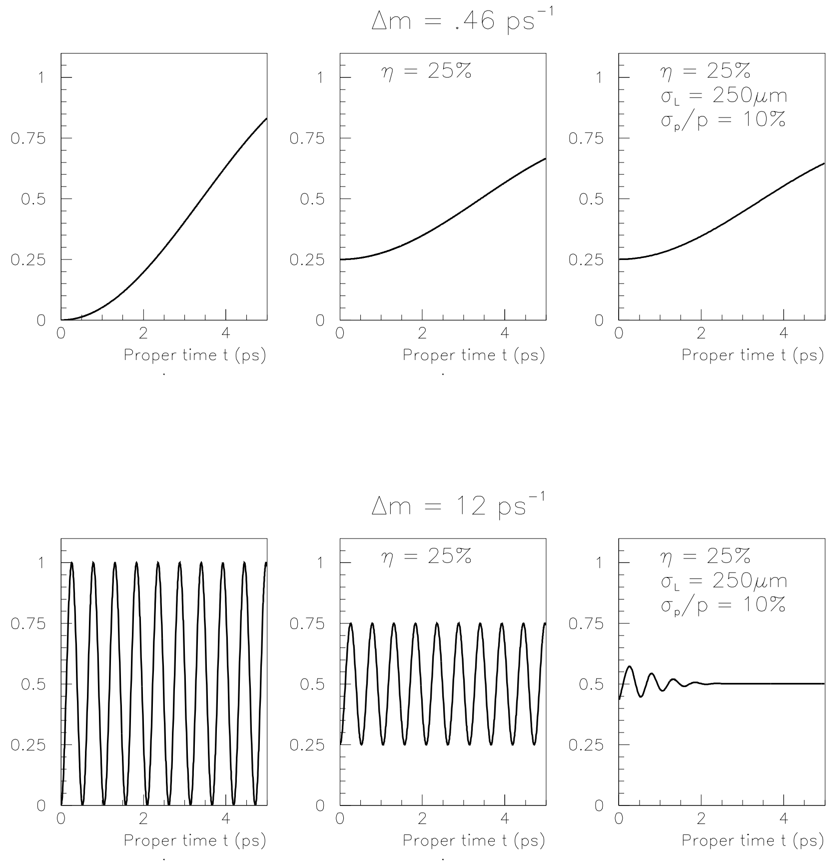

Fig. 78. The effects of decay-length resolution and dilution (mistagging) on B_d and B_s oscillation measurements. Figure provided by M.-H. Schune.

where

$$
\begin{aligned}
f_+(t) &= \frac{1}{2}\left(e^{-iM_+t}e^{-\Gamma_+t/2} + e^{-iM_-t}e^{-\Gamma_-t/2}\right) \\
f_-(t) &= \frac{1}{2}\left(e^{-iM_+t}e^{-\Gamma_+t/2} - e^{-iM_-t}e^{-\Gamma_-t/2}\right).
\end{aligned}
\tag{9.115}
$$

Recall that $|B^0(t)\rangle$ is the state that at $t=0$ is pure $|B^0\rangle$ and $|\bar{B}^0(t)\rangle$ is the state that at $t=0$ is pure $|\bar{B}^0\rangle$; the time evolution of the system, however, mixes in their antiparticles. The states $|B^0(t)\rangle$ and $|\bar{B}^0(t)\rangle$ are sometimes labeled $|B^0_{\rm phys}(t)\rangle$ and $|\bar{B}^0_{\rm phys}(t)\rangle$ to emphasize that they are not purely $|B^0\rangle$ or $|\bar{B}^0\rangle$.

As discussed in the previous section, for $B^0\bar{B}^0$ mixing, we can assume

$$\frac{\Delta\Gamma}{\Gamma} \ll 1. \tag{9.116}$$

The coefficients $f_+(t)$ and $f_-(t)$ can then be written

$$\begin{aligned}
f_+(t) &= \frac{1}{2}\left(e^{-iM_+t}e^{-\Gamma_+t/2} + e^{-iM_-t}e^{-\Gamma_-t/2}\right) \\
&= \frac{1}{2}e^{-i\frac{1}{2}(M_++M_-)t}\left(e^{-i\frac{1}{2}(M_+-M_-)t}e^{-\Gamma_+t/2} + e^{i\frac{1}{2}(M_+-M_-)t}e^{-\Gamma_-t/2}\right) \\
&= e^{-iMt}e^{-\frac{\Gamma}{2}t}\cos\frac{\Delta Mt}{2}
\end{aligned} \tag{9.117}$$

and

$$\begin{aligned}
f_-(t) &= \frac{1}{2}\left(e^{-iM_+t}e^{-\Gamma_+t/2} - e^{-iM_-t}e^{-\Gamma_-t/2}\right) \\
&= ie^{-iMt}e^{-\frac{\Gamma}{2}t}\sin\frac{\Delta Mt}{2},
\end{aligned} \tag{9.118}$$

where

$$M = \frac{1}{2}(M_+ + M_-), \qquad \Delta M = M_- - M_+, \qquad \Gamma = \Gamma_+ = \Gamma_- \tag{9.119}$$

The factor of i in Eq. 9.118 is crucial. It is associated with the mixing amplitude and plays the role of the strong phase factor ($i = \exp(i\pi/2)$) in our discussion.

Recall that the subscripts ($\pm$) on M refer to the sign of the coefficient of $\alpha|\bar{B}^0\rangle$ in Eq. 9.77. We now assume that $M_- = M_H$ and $M_+ = M_L$, where M_H and M_L are the masses of the heavier and lighter mass eigenstates, respectively. Thus, $\Delta M = M_- - M_+ = M_H - M_L > 0$. The time dependence of states $|B^0(t)\rangle$ and $|\bar{B}^0(t)\rangle$ that at $t = 0$ are $|B^0\rangle$ and $|\bar{B}^0\rangle$, is therefore

$$\begin{aligned}
|B^0(t)\rangle &= e^{-\frac{\Gamma}{2}t}e^{-iMt}\left(\cos\frac{\Delta Mt}{2}|B^0\rangle + i\alpha\sin\frac{\Delta Mt}{2}|\bar{B}^0\rangle\right) \\
|\bar{B}^0(t)\rangle &= e^{-\frac{\Gamma}{2}t}e^{-iMt}\left((i/\alpha)\sin\frac{\Delta Mt}{2}|B^0\rangle + \cos\frac{\Delta Mt}{2}|\bar{B}^0\rangle\right).
\end{aligned} \tag{9.120}$$

We now let these states decay into a common final state $|f_{CP}\rangle$, which we take to be a CP eigenstate with eigenvalue $\eta_{CP}(f) = \pm 1$. The amplitude for $B^0(t) \to f_{CP}$ is given by

$$\langle f_{CP}|H|B^0(t)\rangle = e^{-\frac{1}{2}\Gamma t}e^{-iMt} \times \left(\langle f_{CP}|H|B^0\rangle \cos\frac{\Delta Mt}{2} + i\alpha\langle f_{CP}|H|\bar{B}^0\rangle \sin\frac{\Delta Mt}{2}\right), \tag{9.121}$$

while that for $\bar{B}^0(t) \to f_{CP}$ is

$$\langle f_{CP}|H|\bar{B}^0(t)\rangle = e^{-\frac{1}{2}\Gamma t}e^{-iMt} \times \left(\langle f_{CP}|H|B^0\rangle(i/\alpha) \sin\frac{\Delta Mt}{2} + \langle f_{CP}|H|\bar{B}^0\rangle \cos\frac{\Delta Mt}{2}\right). \tag{9.122}$$

In these two equations, we see explicitly the two amplitudes whose interference can produce a CP asymmetry. We next write these equations in terms of a ratio of amplitudes

$$\lambda \equiv \alpha \cdot \frac{\langle f_{CP}|H|\bar{B}^0\rangle}{\langle f_{CP}|H|B^0\rangle} = \sqrt{\frac{M_{12}^* - \frac{i}{2}\Gamma_{12}^*}{M_{12} - \frac{i}{2}\Gamma_{12}}} \cdot \frac{\langle f_{CP}|H|\bar{B}^0\rangle}{\langle f_{CP}|H|B^0\rangle}. \tag{9.123}$$

This quantity plays a key role in determining whether there is a CP asymmetry, as we will show below.

The amplitude for $B^0(t) \to f_{CP}$ is

$$\langle f_{CP}|H|B^0(t)\rangle = e^{-\frac{1}{2}\Gamma t}e^{-iMt}\langle f_{CP}|H|B^0\rangle \times \left(\cos\frac{\Delta Mt}{2} + i\alpha\frac{\langle f_{CP}|H|\bar{B}^0\rangle}{\langle f_{CP}|H|B^0\rangle} \sin\frac{\Delta Mt}{2}\right), \tag{9.124}$$

and that for $\bar{B}^0(t) \to f_{CP}$

$$\langle f_{CP}|H|\bar{B}^0(t)\rangle = e^{-\frac{1}{2}\Gamma t}e^{-iMt}\langle f_{CP}|H|B^0\rangle(i/\alpha) \times \left(\sin\frac{\Delta Mt}{2} - i\alpha\frac{\langle f_{CP}|H|\bar{B}^0\rangle}{\langle f_{CP}|H|B^0\rangle} \cos\frac{\Delta Mt}{2}\right). \tag{9.125}$$

If the initial state at $t = 0$ is $|B^0\rangle$, the probability to produce $|f_{CP}\rangle$ at time t is therefore

$$|\langle f_{CP}|\, H\, |B^0(t)\rangle|^2 = e^{-\Gamma t}|\langle f_{CP}|H|B^0\rangle|^2 \cdot\ (\cos^2\frac{\Delta Mt}{2} + |\lambda|^2 \sin^2\frac{\Delta Mt}{2} - \operatorname{Im}\lambda \cdot 2\cos\frac{\Delta Mt}{2} \sin\frac{\Delta Mt}{2})$$

$$
\begin{aligned}
&= e^{-\Gamma t}|\langle f_{CP}|H|B^0\rangle|^2 \cdot [\frac{1}{2}(1+|\lambda|^2) \\
&\quad + \frac{1}{2}(1-|\lambda|^2)\cos\Delta M t - \mathrm{Im}\,\lambda \cdot \sin\Delta M t], \qquad (9.126)
\end{aligned}
$$

while the probability to produce $|f_{CP}\rangle$ at time t starting from $|\bar{B}^0\rangle$ at time $t=0$ is

$$
\begin{aligned}
|\langle f_{CP}|\, H\, |\bar{B}^0(t)\rangle|^2 &= e^{-\Gamma t}\left|\frac{1}{\alpha}\right|^2 |\langle f_{CP}|H|B^0\rangle|^2 \\
&\quad \cdot \ (|\lambda|^2\cos^2\frac{\Delta M t}{2} + \sin^2\frac{\Delta M t}{2} + \mathrm{Im}\,\lambda \cdot 2\cos\frac{\Delta M t}{2}\sin\frac{\Delta M t}{2}) \\
&= e^{-\Gamma t}\left|\frac{1}{\alpha}\right|^2 |\langle f_{CP}|H|B^0\rangle|^2 \cdot [\frac{1}{2}(1+|\lambda|^2) \\
&\quad - \frac{1}{2}(1-|\lambda|^2)\cos\Delta M t + \mathrm{Im}\,\lambda \cdot \sin\Delta M t]. \qquad (9.127)
\end{aligned}
$$

We now use the fact that $\Gamma_{12} \simeq 0$, and that (see Eq. 9.100)

$$
\begin{aligned}
M_{12} &= a(V_{tb}V_{td}^*)^2 e^{-2i\theta_{CP}} \\
M_{12}^* &= a(V_{tb}^*V_{td})^2 e^{+2i\theta_{CP}}, \qquad (9.128)
\end{aligned}
$$

where a is a real constant. Thus,

$$
\begin{aligned}
\alpha &= \sqrt{\frac{M_{12}^*}{M_{12}}} = \frac{V_{tb}^*V_{td}}{V_{tb}V_{td}^*} e^{2i\theta_{CP}} \\
&= e^{2i\phi_M(B^0)} e^{2i\theta_{CP}(B^0)} \qquad B^0\bar{B}^0 \text{ mixing}, \qquad (9.129)
\end{aligned}
$$

where the last expression defines the mixing phase $\phi_M(B^0)$. The first important consequence of this result is that $|\alpha| = |1/\alpha| = 1$. Below, we will evaluate λ for various cases and show that it has no dependence on phase-convention. We note that for $B_s\bar{B}_s$ mixing, α is given by

$$
\begin{aligned}
\alpha(B_s) &= \frac{V_{tb}^*V_{ts}}{V_{tb}V_{ts}^*} e^{2i\theta_{CP}(B_s)} \\
&= e^{2i\phi_M(B_s)} e^{2i\theta_{CP}(B_s)} \qquad B_s\bar{B}_s \text{ mixing}. \qquad (9.130)
\end{aligned}
$$

We can now calculate the time-dependent CP asymmetry

$$
\begin{aligned}
\mathcal{A}_{CP}(t) &= \frac{|\langle f_{CP}|H|B^0(t)\rangle|^2 - |\langle f_{CP}|H|\bar{B}^0(t)\rangle|^2}{|\langle f_{CP}|H|B^0(t)\rangle|^2 + |\langle f_{CP}|H|\bar{B}^0(t)\rangle|^2} \\
&= \frac{(1-|\lambda|^2)\cos\Delta M t - 2\,\mathrm{Im}\,\lambda \sin\Delta M t}{1+|\lambda|^2}, \qquad (9.131)
\end{aligned}
$$

which is one of the key results in the analysis. Incidentally, to compute the so-called time-integrated asymmetry, you should not integrate this expression. Instead, compute the asymmetry between the time-integrated rates (see below).

To evaluate λ, we use

$$\begin{aligned}\langle f_{CP}|H|\bar{B}^0\rangle &= \langle f_{CP}|(CP)^\dagger(CP)H(CP)^\dagger(CP)|\bar{B}^0\rangle \\ &= \eta_{CP}(f)e^{-2i\theta_{CP}}\langle f_{CP}|(CP)H(CP)^\dagger|B^0\rangle.\end{aligned} \tag{9.132}$$

Two rather different types of situations can emerge at this point, depending on whether the direct decay to f_{CP} is dominated by a single amplitude. If this is the case, then

$$\begin{aligned}\langle f_{CP}|H|B^0\rangle &= |a|e^{i(\delta+\phi_D)} \\ \langle f_{CP}|(CP)H(CP)^\dagger|B^0\rangle &= |a|e^{i(\delta-\phi_D)},\end{aligned} \tag{9.133}$$

where $e^{i\delta}$ is, as usual, a strong (CP-conserving) phase factor and $e^{i\phi_D}$ is the weak phase factor that we want to extract from the measurement. (The second of these two equations is discussed in the Appendix.) Thus,

$$\langle f_{CP}|H|\bar{B}^0\rangle = \eta_{CP}(f)e^{-2i\theta_{CP}}|a|e^{i(\delta-\phi_D)}. \tag{9.134}$$

Putting the pieces together we have

$$\lambda = \frac{V_{tb}^*V_{td}}{V_{tb}V_{td}^*}\eta_{CP}(f)e^{-2i\phi_D} = \eta_{CP}(f)e^{2i(\phi_M(B^0)-\phi_D)} \tag{9.135}$$

where the two phase-convention dependent factors have cancelled. In this important case (a single weak phase in the decay amplitude),

$$|\lambda| = 1, \tag{9.136}$$

so that the term in Eq. 9.131 proportional to $\cos\Delta Mt$ does not contribute. This term in effect measures direct CP violation and would be present if two processes with different CKM and strong phases contributed significantly to the decay. Assuming $|\lambda| = 1$ in Eq. 9.126 and Eq. 9.127, we obtain the remarkably simple results

$$\begin{aligned}|\langle f_{CP}|H|B^0(t)\rangle|^2 &= e^{-\Gamma t}|\langle f_{CP}|H|B^0\rangle|^2\cdot\Big[1-\mathrm{Im}\,\lambda\cdot\sin\Delta Mt\Big] \\ |\langle f_{CP}|H|\bar{B}^0(t)\rangle|^2 &= e^{-\Gamma t}|\langle f_{CP}|H|B^0\rangle|^2\cdot\Big[1+\mathrm{Im}\,\lambda\cdot\sin\Delta Mt\Big],\end{aligned} \tag{9.137}$$

which give the asymmetry

$$\mathcal{A}_{CP}(t) = -\operatorname{Im}\lambda \cdot \sin \Delta M t. \tag{9.138}$$

Let's continue with the assumption that only one diagram contributes to the direct weak decay, or more precisely, that all of the contributing processes have the same weak phase. Since a $\bar{B}^0$ meson contains a b quark, the CKM factors associated with tree diagrams give

$$\begin{aligned} e^{-2i\phi_D} &= \frac{V_{cb}V_{cs}^*}{V_{cb}^*V_{cs}} \qquad b \to c\bar{c}s \\ e^{-2i\phi_D} &= \frac{V_{cb}V_{cd}^*}{V_{cb}^*V_{cd}} \qquad b \to c\bar{c}d \\ e^{-2i\phi_D} &= \frac{V_{ub}V_{ud}^*}{V_{ub}^*V_{ud}} \qquad b \to u\bar{u}d. \end{aligned} \tag{9.139}$$

Each of these quantities gives the orientation in of a quantity $V_{ij}V_{ik}^*$ in the complex plane. This orientation depends on the CKM phase convention, but the angle *between* two such quantities does not. For $\bar{B}^0 \to \pi^+\pi^-$ we have

$$\begin{aligned} \lambda &= \frac{V_{tb}^*V_{td}}{V_{tb}V_{td}^*} \cdot e^{-2i\phi_D} \\ &= \frac{V_{tb}^*V_{td}}{V_{tb}V_{td}^*} \cdot \frac{V_{ub}V_{ud}^*}{V_{ub}^*V_{ud}} = e^{2i\alpha}, \end{aligned} \tag{9.140}$$

which implies that

$$\operatorname{Im}\lambda = \sin(2\alpha). \tag{9.141}$$

Now consider the D^+D^- final state. Using Eq. 3.40 we have

$$\lambda = \frac{V_{tb}^*V_{td}}{V_{tb}V_{td}^*} \cdot \frac{V_{cb}V_{cd}^*}{V_{cb}^*V_{cd}} = e^{-2i\beta}, \tag{9.142}$$

or

$$\operatorname{Im}\lambda = -\sin 2\beta. \tag{9.143}$$

If all of the CKM factors in these equations become too mesmerizing, just look at the CKM triangle in Fig. 3. The pairs $V_{ub}^*V_{ud}$, $-V_{cb}^*V_{cd}$, and $V_{tb}^*V_{td}$ are simply the complex numbers representing the directed sides of the triangle. Thus, their orientation in the complex plane depends on the choice of CKM phase convention. As discussed in Sec. 3, a different choice of quark phase will result in a rotation of the triangle. However, if z_1 and z_2 represent any two of the directed sides of the triangle, the quantity $z_1 z_2^* = |z_1||z_2| \exp[i(\theta_2 - \theta_1)]$ measures the convention-independent area (see the discussion at the end of Sec. 3). Similarly, $(z_1/z_1^*)(z_2^*/z_2) = \exp[2i(\theta_2 - \theta_1)]$ gives a convention-independent measure that governs the size of the asymmetries in the case of interference between mixing and decay.

We next consider the decay $\bar{B}^0 \to J/\psi K_S^0$. To a very good approximation, we regard the K_s^0 as a CP eigenstate with eigenvalue $+1$, so the CP eigenvalue of the final state is $CP(J/\psi K_S^0) = -1$. We have to be careful, because $\bar{B}^0 \to J/\psi \bar{K}^0$ but $B^0 \to J/\psi K^0$. To reach the common final state, the K^0's must mix, introducing an additional phase difference between the two processes. Since λ gives the ratio $\bar{B}^0/B^0$, the required additional factor is

$$\alpha_K = \frac{V_{cs} V_{cd}^*}{V_{cs}^* V_{cd}} \tag{9.144}$$

and

$$\begin{aligned} \lambda &= (-1) \frac{V_{tb}^* V_{td}}{V_{tb} V_{td}^*} \cdot \frac{V_{cb} V_{cs}^*}{V_{cb}^* V_{cs}} \cdot \frac{V_{cs} V_{cd}^*}{V_{cs}^* V_{cd}} \\ &= -e^{-2i\beta} \end{aligned} \tag{9.145}$$

so that

$$\operatorname{Im} \lambda = \sin 2\beta. \tag{9.146}$$

The extraordinary feature of these results is that we have been able to express measurable CP asymmetries directly in terms of CKM quantities, without knowledge of hadronic matrix elements. This simplicity is compromised in the cases where additional amplitudes contribute, since a dependence on strong phases is introduced. Most importantly from an experimental perspective, the asymmetries can be quite large, since the angles of the unitarity triangle are not all near 0 or $\pi/2$ and the magnitudes of the interfering amplitudes are comparable in size. Figure 79 shows the decay rates vs. time for B mesons initially tagged as B^0 or $\bar{B}^0$. The decay rates are non-exponential (Eq. 9.137), a characteristic of CP violation. The figure also shows the associated CP asymmetry, which has a sinusoidal time dependence (Eq. 9.138).

Before proceeding, I would like to write the decay amplitudes in a form that we can easily relate to a simple graphical analysis. Again specializing to the case of a single direct-decay amplitude, and using Eq. 9.129, Eq. 9.133, and Eq. 9.134

$$\alpha = e^{2i\phi_M(B^0)} e^{2i\theta_{CP}(B^0)}$$

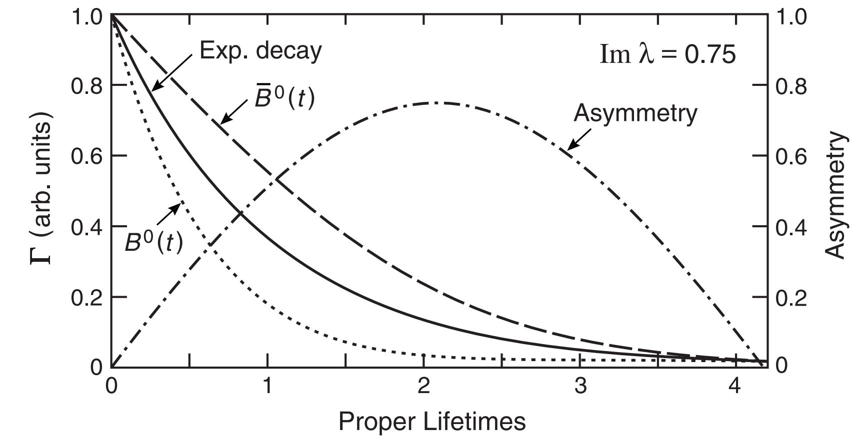

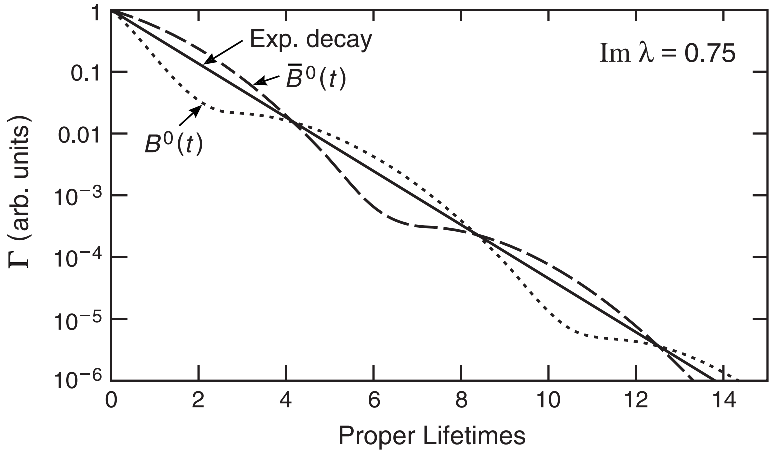

Fig. 79. CP asymmetry for neutral B mesons resulting from the interference between mixing and decay. The upper plot shows the decay rates as a function of proper lifetime for $\Gamma(B^0(t) \to f_{CP})$ and $\Gamma(\bar{B}^0(t) \to f_{CP})$, where $B^0(t)$ is tagged as a B^0 at $t = 0$ and $\bar{B}^0(t)$ is tagged as a $\bar{B}^0$ at $t = 0$. The asymmetry is a sinusoidal function of time, reaching a maximum value equal to $\mathrm{Im}\,\lambda$. The lower plot shows the decay rates on a logarithmic scale. The main point is that the size of the CP asymmetries in B decays can be very large; this is a consequence of the fact that all three sides of the corresponding unitarity triangle have lengths of order λ^3, giving large interior angles ϕ_i and hence large values of $\mathrm{Im}\,\lambda = \sin 2\phi_i$. The value $\mathrm{Im}\,\lambda = 0.75$ is a plausible value for $\sin 2\beta$.

$$\begin{aligned} \langle f_{CP}|H|B^0\rangle &= |a|e^{i(\delta+\phi_D)} \\ \langle f_{CP}|H|\bar{B}^0\rangle &= \eta_{CP}(f)e^{-2i\theta_{CP}(B^0)}|a|e^{i(\delta-\phi_D)} \end{aligned} \tag{9.147}$$

in Eq. 9.121 and Eq. 9.122 we have

$$\begin{aligned} \langle f_{CP}|H|B^0(t)\rangle = |a|e^{-\frac{1}{2}\Gamma t}e^{-iMt}e^{i(\delta+\phi_D)} \\ \times \left(\cos\frac{\Delta Mt}{2} + i\eta_{CP}(f)e^{2i(\phi_M-\phi_D)}\sin\frac{\Delta Mt}{2}\right), \end{aligned}$$

(9.148)

and

$$\langle f_{CP}|H|\bar{B}^0(t)\rangle = |a|\eta_{CP}(f)e^{-\frac{1}{2}\Gamma t}e^{-iMt}e^{i\delta}e^{-i(2\theta_{CP}(B^0)+\phi_D)} \times \left(\cos\frac{\Delta Mt}{2} + i\eta_{CP}(f)e^{-2i(\phi_M-\phi_D)}\sin\frac{\Delta Mt}{2}\right). \tag{9.149}$$

Note that the strong phase factor $\exp(i\delta)$ is common to all the amplitudes, so it factors out and has no effect on observable quantities. The phase $i = \exp(i\pi/2)$ from mixing fills the role played by the strong phase in direct CP violation: it is not conjugated in going from $B^0(t)$ to $\bar{B}^0(t)$ decay. The weak phase, which is conjugated, is given by $2(\phi_M - \phi_D)$. The complicated hadronic effects in mixing have neatly divided out in α, since mixing is completely dominated by off-shell processes and $H_{12} = M_{12}$ has the same magnitude as $H_{21} = M_{21} = M_{12}^*$. The two interfering amplitudes have similar magnitudes, allowing for large CP-violating asymmetries. Figure 80 shows the amplitudes schematically, and Figure 81 shows a graphical construction of the amplitudes as a function of time.

We again see that CP violation produces a nonexponential decay probability

$$\begin{aligned}|A(B^0(t) \to f_{CP})|^2 &= |a|^2e^{-\Gamma t}\left[1 - \eta_{CP}(f)\sin(\Delta Mt)\sin 2(\phi_M - \phi_D)\right]\\ |A(\bar{B}^0(t) \to f_{CP})|^2 &= |a|^2e^{-\Gamma t}\left[1 + \eta_{CP}(f)\sin(\Delta Mt)\sin 2(\phi_M - \phi_D)\right].\end{aligned} \tag{9.150}$$

We have already computed the CP asymmetry as a function of time. Note that the asymmetry between the time-integrated rates is given by

$$\begin{aligned}\mathcal{A}_{CP} &\equiv \frac{\int_0^\infty(|A(B^0(t) \to f_{CP})|^2 - |A(\bar{B}^0(t) \to f_{CP})|^2)}{\int_0^\infty(|A(B^0(t) \to f_{CP})|^2 + |A(\bar{B}^0(t) \to f_{CP})|^2)}\\ &= -\eta_{CP}(f)\frac{x}{1+x^2}\sin[2(\phi_M - \phi_D)],\\ &= -\eta_{CP}(f)(0.48)\sin[2(\phi_M - \phi_D)],\end{aligned} \tag{9.151}$$

where $x = \frac{\Delta M}{\Gamma}$. This time-integrated asymmetry can be measured in a hadron-collider experiment such as LHC-B or BTeV, but not in $e^+e^- \to \Upsilon(4S)$ experiments, as we will now see.

For experiments that produce $B^0\bar{B}^0$ pairs using the decay $\Upsilon(4S) \to B^0\bar{B}^0$, there are important tagging considerations arising from the

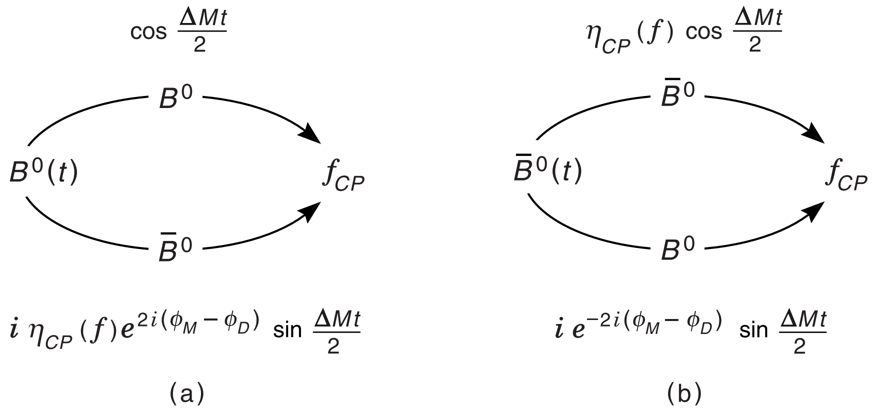

Fig. 80. Amplitudes contributing to the interference between mixing and decay to a CP eigenstate f_{CP} in the $B^0\bar{B}^0$ system. For simplicity, most of the relative phases have been attached to the $\sin(\Delta M t/2)$ term. The overall exponential decay factors have been omitted.

$C = -1$ quantum number of the $\Upsilon(4S)$. Since the strong and electromagnetic interactions conserve C, the $B^0\bar{B}^0$ system must also have $C = -1$. We can write the overall wave-function of this system as

$$|\Psi(t_1, t_2)\rangle_{C=\pm 1} = \frac{1}{\sqrt{2}}(|B^0(t_1); \mathbf{p}\rangle|\bar{B}^0(t_2); -\mathbf{p}\rangle \pm |\bar{B}^0(t_1); \mathbf{p}\rangle|B^0(t_2); -\mathbf{p}\rangle) \tag{9.152}$$

for $C = \pm 1$ states. We have specified a particular momentum direction for the B mesons; the actual wave function for the final state is a superposition of such two-particle plane wave states with a weighting factor $d^1_{\pm 1,0}(\theta) \propto \sin\theta$, (no $d^1_{0,0}(\theta)$ due to helicity conservation—see Sec. 7.2), which gives the $dN/d\cos\theta \propto \sin^2\theta$ angular distribution. Substituting the expressions for $|B^0(t)\rangle$ and $|\bar{B}^0(t)\rangle$ from Eq. 9.114, we obtain

$$\begin{aligned}
|\Psi(t_1, t_2)\ \rangle_{\ C=\pm 1} \\
= \frac{1}{\sqrt{2}}\{ \ &\tfrac{1}{\alpha}\,[f_+(t_1)f_-(t_2) \pm f_-(t_1)f_+(t_2)]|B^0; \mathbf{p}\rangle|B^0; -\mathbf{p}\rangle \\
&+ [f_+(t_1)f_+(t_2) \pm f_-(t_1)f_-(t_2)]|B^0; \mathbf{p}\rangle|\bar{B}^0; -\mathbf{p}\rangle \\
&+ [f_-(t_1)f_-(t_2) \pm f_+(t_1)f_+(t_2)]|\bar{B}^0; \mathbf{p}\rangle|B^0; -\mathbf{p}\rangle \\
&+ \alpha\,[f_-(t_1)f_+(t_2) \pm f_+(t_1)f_-(t_2)]|\bar{B}^0; \mathbf{p}\rangle|\bar{B}^0; -\mathbf{p}\rangle\}
\end{aligned} \tag{9.153}$$

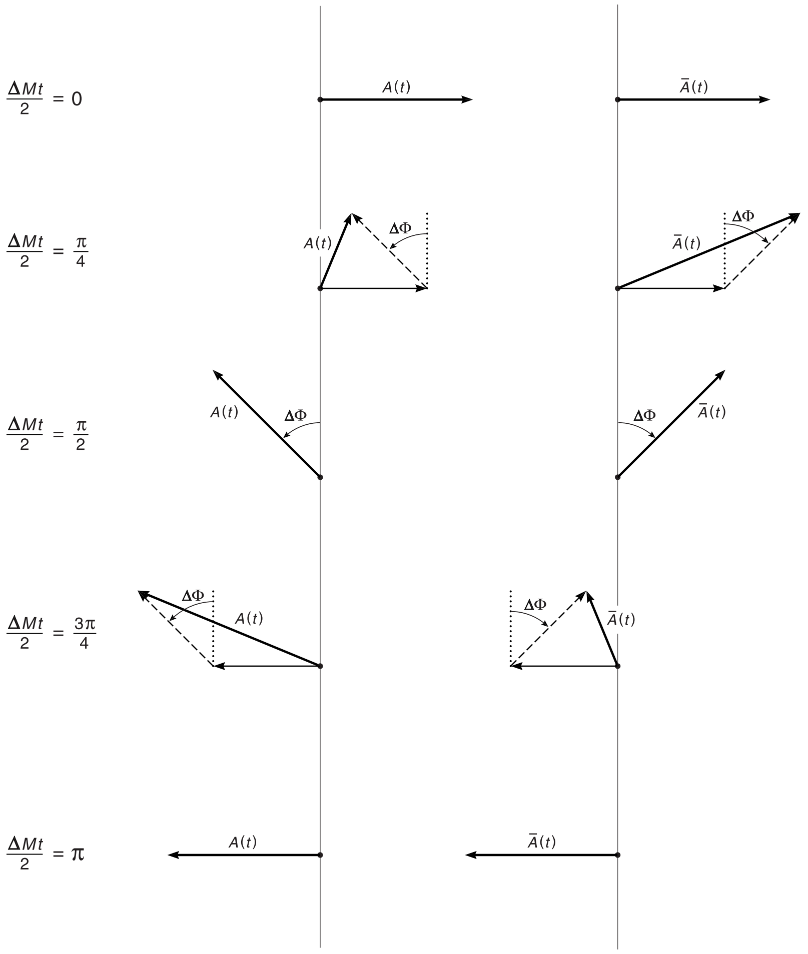

Fig. 81. Graphical analysis of the amplitudes contributing to the interference between mixing and decay in the $B^0\bar{B}^0$ system, as a function of time. The amplitudes correspond to those in Fig. 80, except the exponential decay factors have been ignored for clarity. (These factors would rapidly shrink the triangles in the figure.) The triangles on the left correspond to decays $B^0(t) \to f_{CP}$, while those on the right correspond to $\bar{B}^0(t) \to f_{CP}$. In each case, the vectors in the horizontal direction (real axis) correspond to the $\cos(\Delta Mt/2)$ term. To display the $\sin(\Delta Mt/2)$ term, we begin with the "strong phase" $i = \exp(i\pi/2)$ associated with mixing. This phase factor is oriented vertically on the page, along the imaginary axis. The weak phase factor $\exp(i\Delta\Phi) \equiv \exp[\pm 2i(\phi_M - \phi_D)]$ rotates either counterclockwise or clockwise with respect to this axis, depending on whether we are considering $B^0(t)$ or $\bar{B}^0(t)$. Note that the $B^0(t)$ or $\bar{B}^0(t)$ amplitudes at time $\Delta Mt/2 = \pi/4$ have different magnitudes, as do those at $\Delta Mt/2 = 3\pi/4$. At $\Delta Mt/2 = \pi/2$, the amplitudes have different orientations but their magnitudes are the same.

We substitute the results for $f_+(t)$ (Eq. 9.117) and $f_-(t)$ (Eq. 9.118), which gives

$$|\Psi(t_1, t_2)\rangle_{C=-1} = \frac{1}{\sqrt{2}} e^{-iM(t_1+t_2)} e^{-\frac{\Gamma}{2}(t_1+t_2)}$$

$$\cdot\ [\cos(\frac{\Delta M}{2}(t_1 - t_2))\left(|B^0;\mathbf{p}\rangle|\bar{B}^0;-\mathbf{p}\rangle - |\bar{B}^0;\mathbf{p}\rangle|B^0;-\mathbf{p}\rangle\right)$$
$$-i\sin(\frac{\Delta M}{2}(t_1 - t_2))\left(\frac{1}{\alpha}|B^0;\mathbf{p}\rangle|B^0;-\mathbf{p}\rangle - \alpha|\bar{B}^0;\mathbf{p}\rangle|\bar{B}^0;-\mathbf{p}\rangle\right)] \tag{9.154}$$

For $t_1 = t_2$, the sine terms vanish, so only $|B^0;\mathbf{p}\rangle|\bar{B}^0;-\mathbf{p}\rangle$ or $|\bar{B}^0;\mathbf{p}\rangle|B^0;-\mathbf{p}\rangle$ terms contribute to the $C = -1$ wave function. This means that the two B mesons evolve coherently and, until one of them decays, one of them is a B^0 and the other one a $\bar{B}^0$. If one B decays into a mode that tags its flavor as, say, a $\bar{B}^0$ at time $t = t_1$, then the other one is a B^0 at that instant t_0, and it evolves from that time onward as $|B^0(t - t_0)\rangle$.

We can project the state vector $|\Psi(t_1, t_2)\rangle$ onto a state $|f_{CP}(t_1), f_{\rm tag}(t_2)_{\bar{B}^0}\rangle$. One B meson decays at time t_1 into a CP eigenstate, while the other decays at time t_2 into a state that tags it as a $\bar{B}^0$. The tagging final state could be $\bar{B}^0 \to D^{*+}\ell^-\bar{\nu}$ or another semileptonic mode. This calculation gives

$$|\langle f_{CP}(t_1), f_{\rm TAG}(t_2)_{\bar{B}^0} \mid H|\Psi(t_1,t_2)\rangle|^2 = \frac{1}{2}e^{-\Gamma(t_1+t_2)}|\bar{A}_{\rm TAG}|^2|A_{f_{CP}}|^2$$
$$\cdot\{\frac{1}{2}(1+|\lambda|^2) - \frac{1}{2}(1-|\lambda|^2)\cos[\Delta M(t_1 - t_2)]$$
$$-\,{\rm Im}\,\lambda\cdot\sin[\Delta M(t_1 - t_2)]\}. \tag{9.155}$$

This result is essentially the same as that in Eq. 9.127, but the correlations due to tagging at the $\Upsilon(4S)$ have been taken into account. It is evident that the corresponding asymmetry can be either positive or negative, depending on the sign of $t_1 - t_2 = t_{CP} - t_{\rm TAG}$. If the time of the tag is not known relative to the time of the decay to the CP eigenstate, no asymmetry will be observed, since there will be a cancellation of the asymmetry for $t_1 - t_2 > 0$ with that for $t_1 - t_2 < 0$. As a consequence, it is crucial to perform the asymmetry measurement as a function of the time $t_1 - t_2$.

Measurements of CP violation at the $\Upsilon(4S)$ using the interference between mixing and decay must therefore accomplish three main tasks:
• Determine the flavor of one of the neutral B mesons directly from its decay products (*e.g.*, semileptonic decay).
• Reconstruct the other B meson in a state that both $\bar{B}^0$ and B^0 can decay into. In the simplest case, this state is an eigenstate of CP, but it is not essential that this be the case.
• Measure the time difference, $\Delta t = t_1 - t_2$, between the two decays.

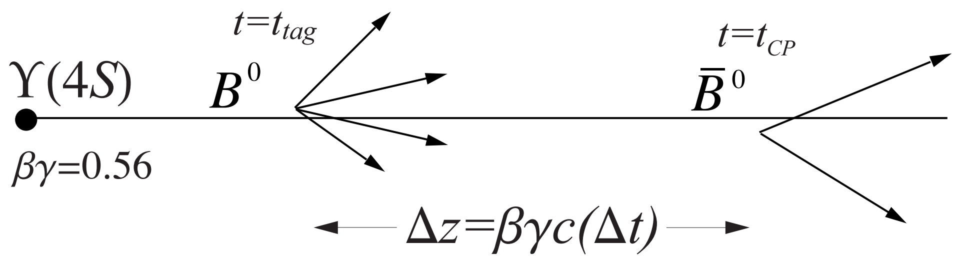

Fig. 82. CP Asymmetry measurement as a function of B vertex separation. At the PEP-II and KEKB asymmetric-energy e^+e^- colliders, the $\Upsilon(4S)$ is boosted, resulting in a typical separation of the B decay vertices of $\Delta z \approx 260$ μm. (The typical transverse momentum of the B mesons is much smaller than their longitudinal momentum.) One B^0 is reconstructed in a state that tags its flavor; the other is reconstructed in a CP eigenstate. In the case shown, $t_{\rm TAG} < t_{CP}$. Since one B meson is determined to be a B^0 at time $t = t_{\rm TAG}$, the other one is known to be at $\bar{B}^0$ at that time. Due to mixing, this other B meson can be either a B^0 or a $\bar{B}^0$ when it decays into the CP eigenstate f_{CP}. The boost allows the CP asymmetry to be measured as a function of the difference of the two decay times. This element of the measurement is essential, because at the $\Upsilon(4S)$ the time-integrated asymmetry vanishes.

These times are actually the proper times, but the B mesons move slowly in the $\Upsilon(4S)$ rest frame, so this is not an important consideration.

Figure 82 shows how the measurement of the decay time difference Δt is performed. Because the B mesons are boosted along the z axis, the decay time difference translates into a difference $\Delta z = \beta\gamma c\Delta t$ in decay positions along the z (beam) axis. The mean separation for $\beta\gamma = 0.56$ is $\langle z\rangle \approx 260$ μm. This distance scale is measurable with silicon vertex detectors placed just outside the beampipe, as shown in Fig. 83 (view transverse to the beam axis) and Fig. 84 (view along the beam axis).

The requirement that one neutral B meson be flavor tagged with a relatively high efficiency also places demanding requirements on the detector. Leptons of sufficiently high momentum from semileptonic B decay are mostly primary and provide one straight-forward way to tag the flavor. A second method uses charged kaons from the $B \to D \to K$ decay sequence. Neither of these methods is perfect, and there is an associated mistagging probability.

One B meson must also be reconstructed in a CP eigenstate, and it is desirable to use as many modes as possible. For $B^0 \to \pi^+\pi^-$ there

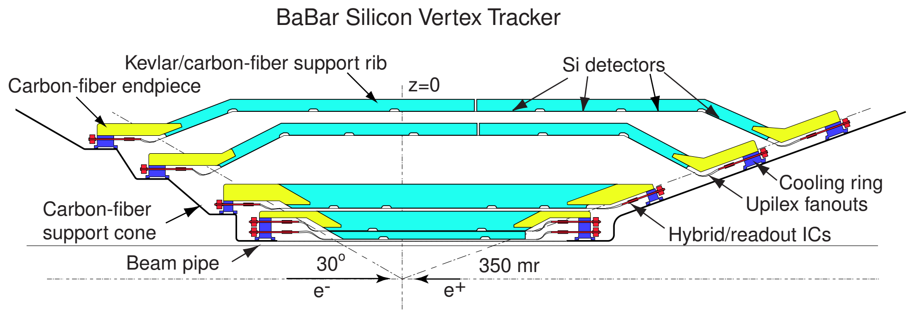

Fig. 83. BaBar silicon vertex tracker (side view). The approximate radii of the layers are 32 mm, 40 mm, 54 mm, 124 mm, and 140 mm. Note the asymmetry of the detector with respect to the interaction point. The modules are mounted to cooling rings on the carbon-fiber support cones. The region within the cones is occupied by the B1 dipole magnets shown in Fig. 7. Flexible upilex fanouts allow the hybrid readout circuits to be mounted at an angle with respect to the silicon detectors, thereby keeping the readout electronics out of the tracking volume.

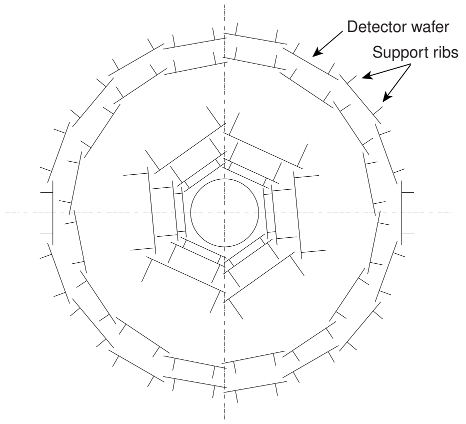

Fig. 84. BaBar silicon vertex tracker (cross section in xy plane).

is background from $B^0 \to K^-\pi^+$. To cleanly separate these modes, it is very helpful to have good particle ID capability at high momentum, which has led to innovative new approaches to particle ID.

A useful summary of the statistical requirements of the CP asymmetry measurements using the interference between mixing and decay has been presented by Cassel [168]. The number of $\bar{\Upsilon}(4S) \to B\bar{B}$ events required to observe an asymmetry a in a final state f with branching fraction $\mathcal{B}_f = B(B \to f)$ and detection efficiency ϵ_f is

$$N_{B\bar{B}} = \frac{s^2}{2 f_0 \mathcal{B}_f \epsilon_f \epsilon_{\text{tag}} d^2(x_d) a^2} \frac{S+B}{S}, \tag{9.156}$$

where $s = a/\sigma_a$ is the statistical significance, S/B is the ratio of the number of signal to background events, and $f_0 \simeq 0.5$ is the fraction of $B^0\bar{B}^0$ events in $\Upsilon(4S)$ decays. The dependence on tagging arises from the quantity

$$\epsilon_{\text{tag}} = \mathcal{B}_{\text{tag}} \epsilon_{\text{tag}} (1 - 2w)^2, \tag{9.157}$$

where $\mathcal{B}_{\text{tag}}$ is the branching fraction for the tagging mode, ϵ_{tag} is the efficiency for the tagging mode, w is the fraction of wrong tags to total tags, and $d(x_d)$ is a dilution factor that accounts for the loss in asymmetry due to fitting the time distributions. Although the CP asymmetries in B decay can be large, the modes that are common to B^0 and $\bar{B}^0$ have small branching fractions, so an enormous amount of data will be required to obtain measurements of good precision. The next generation of experiments is expected to acquire over 30×10^6 $\Upsilon(4S) \to B\bar{B}$ events per year, leading to a precision on $\sin 2\beta$ of better than about 0.1.

This discussion of CP violation is far from comprehensive, and an enormous amount of work and thought is going into figuring how to exploit all of the information that will be available in forthcoming experiments. In particular, the complications caused by penguin processes in $B \to \pi\pi$ and the difficulty of measuring $\sin 2\gamma$ have led to many creative, if not entirely successful methods for dealing with these issues. (For a recent review see Fleischer [152].)

The program of measuring and understanding CP asymmetries in B decays will be a major part of the high-energy physics effort for at least the next decade. Although B physics has matured enormously since the discovery of the first B meson events in 1983, the expanse of uncharted territory remains vast. There remain key unanswered questions in charm physics as well, such as the rate for $D^0\bar{D}^0$ mixing. Heavy-quark physics will offer many opportunities and challenges, and there will be a great deal of excitement as the pieces of the puzzle are collected and the overall picture emerges.

10. Acknowledgements

It is a pleasure to thank the vast number of people who helped in the preparation of these lectures. My colleagues at UCSB, Claudio Campagnari, Michael Witherell, Rollin Morrison, Steve Giddings, Harry Nelson, and Bob Sugar helped with many valuable comments, suggestions, and ideas. I would like to especially thank Natalia Kuznetsova, a UCSB graduate student, who did an extraordinary amount of work checking the text and equations.

Many other colleagues helped by generously providing information and figures. I'm sure I won't remember all of them, but they include Patricia Ball, Elliot Bloom, Tom Browder, Patricia Burchat, Lucia Di Ciaccio, Jonathan Flynn, Lawrence Gibbons, Joseph Kroll, David Lange, Matthias Neubert, Alex Nippe, Ritchie Patterson, Anders Ryd, Marie-Hélène Schune, Jim Smith, Noel Stanton, Sheldon Stone, Ed Thorndike, Jim Wiss, and Renata Zaliznyak. My colleagues in CLEO have, over the years, given me all sorts of ideas and information that has made its way into this paper. Dorothy McLaren at UCSB drew many of the original figures; her hard work contributed greatly to this paper. I would also like to thank the organizers and staff at Les Houches, in particular Rajan Gupta, for putting together a superb school in a beautiful and congenial setting. Finally, I want to thank Patricia Metropolis for valuable editorial assitance and Kate Metropolis for her help and encouragement in countless ways, and especially for her belief that this paper would one day be finished. I would like to thank Daniel Richman for many useful conversations.

11. Appendix 1: Remarks on Hadronic Currents, Form Factors, and Decay Constants

In this appendix, I will derive some of the results regarding hadronic currents that are used in the text. For example, in leptonic decay of a pseudoscalar particle P, only the matrix element of the axial-vector part of the current operator contributes (Eq. 6.2), while in a semileptonic decay $P \to P'\ell\nu$, where P and P' are both pseudoscalars only the matrix element of the vector part contributes (Eq. 7.39). In $P \to V\ell\nu$ decay, where V is a vector meson, there are contributions from both the vector and axial-vector parts of the current (Eq. 7.47).

We first consider the hadronic current that enters into the semileptonic decay $P \to P'\ell\nu$. The S-matrix element is

$$S_{fi} = -i \int d^4x d^4y J^{\mu}_{\rm had}(x) W_{\mu\nu}(x-y) J^{\nu}_{\rm lep}(y), \tag{11.1}$$

where

$$J^\mu_{\rm had}(x) = \frac{-ig}{2\sqrt{2}} V_{Qq'} \langle P'(p')|H^\mu(x)|P(p)\rangle \tag{11.2}$$

is the hadronic current, $W_{\mu\nu}(x-y)$ is the W-boson propagator, and $J^\nu_{\rm lep}(y)$ is the leptonic current. The hadronic current has the well-known $V-A$ form:

$$\langle P'(p')|H^\mu(x)|P(p)\rangle = \langle P'(p')|\bar{\psi}_{q'}(x)\gamma^\mu(1-\gamma_5)\psi_Q(x)|P(p)\rangle. \tag{11.3}$$

To avoid getting hopelessly confused, it is useful to remember what the objects in the hadronic current actually are. In particular, $\psi_Q(x)$ annihilates Q or creates $\bar{Q}$, but it also contains the spinors appropriate for fermions and antifermions. There are also spinors associated with $\psi_{q'}$, so that the product $\bar{\psi}_{q'}(x)\gamma^\mu(1-\gamma_5)\psi_Q(x)$ has no remaining spinor structure—it consists only of particle creation and annihilation operators and functions of the space-time coordinate x. The standard procedure is to use translational invariance to remove this coordinate dependence. Let $\hat{P}$ be the four-momentum operator. Then

$$H^\mu(x) = e^{i\hat{P}\cdot x} H^\mu(0) e^{-i\hat{P}\cdot x}. \tag{11.4}$$

We next substitute this expression into Eq. 11.3, letting the momentum operators act on the states to the left and right, to obtain

$$\langle P'(p')|H^\mu(x)|P(p)\rangle = e^{i(p-p')\cdot x}\langle P'(p')|\bar{\psi}_{q'}(0)\gamma^\mu(1-\gamma_5)\psi_Q(0)|P(p)\rangle. \tag{11.5}$$

When integrated along with similar terms from the leptonic current, the exponentials become part of the overall four-momentum-conserving δ-function. We can now work with the current evaluated at $x=0$. Let Π be the parity operator. (We use a different symbol here than in the text to avoid confusion with the momentum operator $\hat{P}$.) Since Π is unitary, $\Pi\Pi^\dagger = 1$. We can relate the hadronic current to its parity-transformed version:

$$\begin{aligned}\langle P'(p')|H^\mu(0)|P(p)\rangle &= \langle P'(p')|\bar{\psi}_{q'}(0)\gamma^\mu(1-\gamma_5)\psi_Q(0)|P(p)\rangle \\ &= \langle P'(p')|\Pi^\dagger\Pi\bar{\psi}_{q'}(0)\gamma^\mu(1-\gamma_5)\psi_Q(0)\Pi^\dagger\Pi|P(p)\rangle \\ &= \eta(P')\eta(P)\langle P'(\tilde{p}')|\Pi\bar{\psi}_{q'}(0)\gamma^\mu(1-\gamma_5)\psi_Q(0)\Pi^\dagger|P(\tilde{p})\rangle,\end{aligned} \tag{11.6}$$

where $\eta(P)$ and $\eta(P')$ are the intrinsic parities of the particles P and P', respectively, and

$$p^\mu = (E, \mathbf{p}) \qquad \tilde{p}^\mu = (E, -\mathbf{p})$$

$$p'^{\mu} = (E', \mathbf{p}') \qquad \tilde{p}'^{\mu} = (E', -\mathbf{p}'). \tag{11.7}$$

The particle states must be labeled with linear momenta because we want to parametrize the currents in terms of simple functions of these momenta. We now use the transformation properties of the vector and axial-vector currents under parity:

$$\begin{aligned} \Pi\bar{\psi}_{q'}(0)\gamma^{\mu}\psi_{Q}(0)\Pi^{\dagger} &= a^{\mu}_{\nu}\bar{\psi}_{q'}(0)\gamma^{\nu}\psi_{Q}(0) \\ \Pi\bar{\psi}_{q'}(0)\gamma^{\mu}\gamma^{5}\psi_{Q}(0)\Pi^{\dagger} &= -a^{\mu}_{\nu}\bar{\psi}_{q'}(0)\gamma^{\nu}\gamma_{5}\psi_{Q}(0), \end{aligned} \tag{11.8}$$

where a^{μ}_{ν} is a matrix with the elements $(1, -1, -1, -1)$ along the diagonal and zeros off the diagonal. The relations in Eq. 11.8 simply say that, under parity, the spatial components (only) of a vector change sign, while the timelike component (only) of an axial-vector quantity changes sign. Note in particular that

$$\tilde{p}^{\mu} = a^{\mu}_{\nu}p^{\nu}. \tag{11.9}$$

Using the expressions for the transformed currents in Eq. 11.6, we obtain

$$\langle P'(p')|H^{\mu}(0)|P(p)\rangle = \eta(P)\eta(P')a^{\mu}_{\nu}\langle P'(\tilde{p}')|\bar{\psi}_{q'}(0)\gamma^{\nu}(1+\gamma_5)\psi_Q(0)|P(\tilde{p})\rangle. \tag{11.10}$$

There are only two linearly independent four-vectors available in the current, which we choose to be $p+p'$ and $p-p'$. We can therefore write

$$\begin{aligned} \langle P'(p')|\bar{\psi}_{q'}(0)\gamma^{\mu}\psi_Q(0)|P(p)\rangle = f^V_+(q^2)(p+p')^{\mu} \\ + f^V_-(q^2)(p-p')^{\mu}, \end{aligned} \tag{11.11}$$

and

$$\begin{aligned} \langle P'(p')|\bar{\psi}_{q'}(0)\gamma^{\mu}\gamma_5\psi_Q(0)|P(p)\rangle = f^A_+(q^2)(p+p')^{\mu} \\ + f^A_-(q^2)(p-p')^{\mu}. \end{aligned} \tag{11.12}$$

The functions $f^{V,A}_+(q^2)$ and $f^{V,A}_-(q^2)$ must be Lorentz-invariant, so they can depend only on $q^2 = (p-p')^2$ as well as m^2_P and $m^2_{P'}$. (The quantity $(p+p')^2$ can be expressed in terms of these quantities.) We will show that $f^A_+(q^2) = f^A_-(q^2) = 0$, which is equivalent to the statement that only the matrix element of the vector current contributes. Using $\tilde{q}^2 = (\tilde{p}-\tilde{p}')^2 = q^2$, the expression on the right-hand side of Eq. 11.10 can be expressed in terms of form factors:

$$\begin{aligned} \langle P'(\tilde{p}')|\bar{\psi}_{q'}(0)\gamma^{\nu}(1+\gamma_5)\psi_Q(0)|P(\tilde{p})\rangle = f^V_+(q^2)(\tilde{p}+\tilde{p}')^{\nu} + f^V_-(q^2)(\tilde{p}-\tilde{p}')^{\nu} \\ f^A_+(q^2)(\tilde{p}+\tilde{p}')^{\nu} + f^A_-(q^2)(\tilde{p}-\tilde{p}')^{\nu} \end{aligned} \tag{11.13}$$

We substitute this expression into Eq. 11.10 to obtain

$$\langle P'(p')|H^\mu(0)|P(p)\rangle = \eta(P)\eta(P')a^\mu_\nu[f^V_+(q^2)(\tilde{p}+\tilde{p}')^\nu + f^V_-(q^2)(\tilde{p}-\tilde{p}')^\nu + f^A_+(q^2)(\tilde{p}+\tilde{p}')^\nu + f^A_-(q^2)(\tilde{p}-\tilde{p}')^\nu] \tag{11.14}$$

or

$$\langle P'(p')|H^\mu(0)|P(p)\rangle = \eta(P)\eta(P')[f^V_+(q^2)(p+p')^\mu + f^V_-(q^2)(p-p')^\mu + f^A_+(q^2)(p+p')^\mu + f^A_-(q^2)(p-p')^\mu] \tag{11.15}$$

But the original definition of $H^\mu(0)$, given in the first line of Eq. 11.6 has a $V-A$ structure, so that

$$\langle P'(p')|H^\mu(0)|P(p)\rangle = [f^V_+(q^2)(p+p')^\mu + f^V_-(q^2)(p-p')^\mu - f^A_+(q^2)(p+p')^\mu - f^A_-(q^2)(p-p')^\mu]. \tag{11.16}$$

By comparing Eq. 11.15 with Eq. 11.16, we conclude that

$$f^A_+(q^2) = f^A_-(q^2) = 0. \tag{11.17}$$

Thus, the only terms that contribute are those from Eq. 11.11.

A similar analysis can be used for leptonic decays. Here the hadronic current is

$$\begin{aligned}\langle 0|H^\mu(0)|M_{Q\bar{q}}(p)\rangle &= \langle 0|\bar{\psi}_q(0)\gamma^\mu(1-\gamma_5)\psi_Q(0)|M_{Q\bar{q}}(p)\rangle \\ &= \langle 0|\Pi^\dagger\Pi\bar{\psi}_q(0)\gamma^\mu(1-\gamma_5)\psi_Q(0)\Pi^\dagger\Pi|M_{Q\bar{q}}(p)\rangle \\ &= \eta(M_{Q\bar{q}})\langle 0|\Pi\bar{\psi}_q(0)\gamma^\mu(1-\gamma_5)\psi_Q(0)\Pi^\dagger|M_{Q\bar{q}}(\tilde{p})\rangle\end{aligned} \tag{11.18}$$

where $|0\rangle$ represents the vacuum state. Since the momentum of the meson is the only available four-vector in the hadronic current, we can write

$$\begin{aligned}\langle 0|\bar{\psi}_q(0)\gamma^\mu\psi_Q(0)|M_{Q\bar{q}}(p)\rangle &= if^V_M p^\mu \\ \langle 0|\bar{\psi}_q(0)\gamma^\mu\gamma_5\psi_Q(0)|M_{Q\bar{q}}(p)\rangle &= if^A_M p^\mu.\end{aligned} \tag{11.19}$$

Using the transformation properties of the vector and axial-vector currents, Eq. 11.8, we have

$$\begin{aligned}\langle 0|H^\mu(0)|M_{Q\bar{q}}(p)\rangle &= \eta(M_{Q\bar{q}})a^\mu_\nu\langle 0|\bar{\psi}_q(0)\gamma^\nu(1+\gamma_5)\psi_Q(0)|M_{Q\bar{q}}(\tilde{p})\rangle \\ &= i\eta(M_{Q\bar{q}})a^\mu_\nu\left[f^V_M + f^A_M\right]\tilde{p}^\nu \\ &= i\left[-f^V_M - f^A_M\right]p^\mu\end{aligned} \tag{11.20}$$

But the original form of the current can be written

$$\langle 0|H^\mu(0)|M_{Q\bar{q}}(p)\rangle = i\left[f_M^V - f_M^A\right]p^\mu \tag{11.21}$$

so we must have $f_M^V = 0$, and the nonzero contribution comes from the matrix element of the axial-vector current.

12. Appendix 2: Remarks on CP-Conjugate Amplitudes

In Sec. 9, we required the relationship between the two amplitudes $\langle\bar{f}|H|\bar{B}^0\rangle$ and $\langle f|H|B^0\rangle$. We can write

$$\begin{aligned}\langle\bar{f}|H|\bar{B}^0\rangle &= \langle\bar{f}|(CP)^\dagger(CP)H(CP)^\dagger(CP)|\bar{B}^0\rangle\\ &= e^{-2i(\theta_{CP}(B)-\theta_{CP}(f)}\langle f|(CP)H(CP)^\dagger|B^0\rangle,\end{aligned} \tag{12.1}$$

where we have used

$$\begin{aligned}CP|\bar{B}^0\rangle &= e^{-2i\theta_{CP}(B)}|B^0\rangle\\ CP|\bar{f}\rangle &= e^{-2i\theta_{CP}(f)}|f\rangle.\end{aligned} \tag{12.2}$$

If $|f\rangle$ is a CP eigenstate, then replace $\exp[-2i\theta_{CP}(f)]$ with $\eta_{CP}(f) = \pm 1$. We will consider the amplitude for a single weak process, the tree diagram, in $B \to \pi\pi$ or $B \to \rho\pi$. The relevant part of the weak hamiltonian (ignoring the strong interactions) is

$$H = \frac{G_F}{\sqrt{2}}[V_{ub}V_{ud}^*(\bar{\psi}_d\Gamma^\mu\psi_u)(\bar{\psi}_u\Gamma_\mu\psi_b) + V_{ub}^*V_{ud}(\bar{\psi}_u\Gamma^\mu\psi_d)(\bar{\psi}_b\Gamma_\mu\psi_u)], \tag{12.3}$$

where $\Gamma^\mu = \gamma^\mu(1-\gamma_5)$. We now compute

$$\begin{aligned}(CP)H(CP)^{-1} = \frac{G_F}{\sqrt{2}}&[V_{ub}V_{ud}^*(\bar{\psi}_u\Gamma^\mu\psi_d)(\bar{\psi}_b\Gamma_\mu\psi_u)\\ &+V_{ub}^*V_{ud}(\bar{\psi}_d\Gamma^\mu\psi_u)(\bar{\psi}_u\Gamma_\mu\psi_b)].\end{aligned} \tag{12.4}$$

(Several steps were skipped here!) The operator responsible for B^0 decay must destroy a $\bar{b}$ quark, so that

$$\langle f|(CP)H(CP)^\dagger|B^0\rangle = \frac{G_F}{\sqrt{2}}V_{ub}V_{ud}^*\langle f|(\bar{\psi}_u\Gamma^\mu\psi_d)(\bar{\psi}_b\Gamma_\mu\psi_u)|B^0\rangle \tag{12.5}$$

while

$$\langle f|H|B^0\rangle = \frac{G_F}{\sqrt{2}}V_{ub}^*V_{ud}\langle f|(\bar{\psi}_u\Gamma^\mu\psi_d)(\bar{\psi}_b\Gamma_\mu\psi_u)|B^0\rangle. \tag{12.6}$$

Thus,

$$\langle \bar{f}|H|\bar{B}^0\rangle = e^{-2i(\theta_{CP}(B)-\theta_{CP}(f)}\frac{\langle f|(CP)H(CP)^\dagger|B^0\rangle}{\langle f|H|B^0\rangle}\langle f|H|B^0\rangle. \tag{12.7}$$

Using Eq. 12.5 and Eq. 12.6 in Eq. 12.7, we find

$$\langle \bar{f}|H|\bar{B}^0\rangle = e^{-2i(\theta_{CP}(B)-\theta_{CP}(f))}\frac{V_{ub}V_{ud}^*}{V_{ub}^*V_{ud}}\langle f|H|B^0\rangle, \tag{12.8}$$

which relates the amplitude for a particular process with that for the CP-conjugate particles.

References

[1] J.D. Richman and P.R. Burchat, Rev. Mod. Phys. **67**, 893 (1995).
[2] J.D. Richman, in *Proceedings of the 28th International Conference on High Energy Physics*, Warsaw, 25–31 July, 1996, eds. Z. Ajduk and A. K. Wroblewski, p. 143 (World Scientific, Singapore, 1997); preprint hep-ex/9701014.
[3] C. Jarlskog, in *CP Violation, Advanced Series on Directions in High Energy Physics–Vol. 3*, edited by C. Jarlskog (World Scientific, Singapore, 1989), p. 3.
[4] The 1997 Review of Particle Physics (WWW edition), http://pdg.lbl.gov/.
[5] J.P. Alexander, Phys. Rev. Lett. **77**, 5000 (1996).
[6] A. P. Heinson, invited talk at the Second International Conference on B Physics and CP Violation, Honolulu, March 24-27, 1997; preprint hep-ex/9707026.
[7] M. Kobayashi and T. Maskawa, Prog. Theor. Phys. **49**, 652 (1973).
[8] O. Nachtmann, *Elementary Particle Physics* (Springer-Verlag, Berlin), (1990).
[9] B. Kayser, to be published the *Proceedings of the Summer School in High Energy Physics and Cosmology*, held at ICTP, Trieste, 1995; preprint hep-ph/9702264.
[10] L. Wolfenstein, Phys. Rev. Lett. **51**, 1945 (1983).
[11] A. Buras, to be published in *Proceedings of the 7th International Symposium on Heavy Flavor Physics, Santa Barbara, California, 1997*, edited by C. Campagnari (World Scientific, Singapore, 1998); preprint hep-ph/9711217.
[12] A. J. Buras and R. Fleischer, in *Heavy Flavours II* (World Scientific, Singapore, 1997), edited by A. J. Buras and M. Lindner; preprint hep-ph/9704376.
[13] L. L. Chau and W. Y. Keung, Phys. Rev. Lett. **53**, 1802 (1984).
[14] T. Inami and C.S. Lim, Prog. Theor. Phys. **65**, 297 (1981); Erratum: **65**, 1772 (1982).
[15] Y. Grossman, Y. Nir, S. Plaszczynski, and M.-H. Schune, Nucl. Phys. B **511**, 69 (1998); preprint hep-ph/9709288.
[16] The CESR storage ring is described in http://www.lns.cornell.edu/public/lab-info/cesr.html.
[17] BaBar Collaboration, *BaBar Technical Design Report*, SLAC-R-95-457 (1995).
[18] Belle Collaboration, *A Study of CP Violation in B Meson Decays: Technical Design Report*, KEK Report 95-1 (1995).
[19] CLEO Collaboration, *The CLEO III Detector: Design and Physics Goals*, http://www.lns.cornell.edu/public/CLEO/CLEO3/CLEO3.html (1994).
[20] L. Chaussard, talk presented at the International Europhysics Conference on High Energy Physics, 19–26 August 1997, Jerusalem.

[21] J. Kroll, to be published in *Proceedings of the 7th International Symposium on Heavy Flavor Physics, Santa Barbara, California, 1997*, edited by C. Campagnari (World Scientific, Singapore, 1998).
[22] J. A. Appel, Ann. Rev. Nucl. Part. Sci. **42**, 367 (1992).
[23] S. Behrends, *et al.*, Phys. Rev. Lett. **50**, 881 (1983).
[24] R. N. Cahn and G. Goldhaber, *The Experimental Foundations of Particle Physics* (Cambridge University Press, Cambridge, 1989), p. 365.
[25] S. Stone, in proceedings of *Twenty Beautiful Years of Bottom Physics Symposium*, Chicago, IL, 1997.
[26] R. M. Baltrusaitis *et al.* (Mark III Collab.), Phys. Rev. Lett. **56**, 2140 (1986).
[27] J. Adler *et al.* (Mark III Collab.), Phys. Rev. Lett. **60**, 89 (1988).
[28] B. Niczyporuk, representing the Crystal Ball Collaboration, in *Proceedings of the 12th SLAC Summer Institute on Particle Physics, Stanford, California, 1984*, edited by P. McDonough, SLAC Report No. 281, 513 (1985).
[29] E. D. Bloom, in proceedings of the *5th Topical Workshop on Proton-Antiproton Collider Physics, Aosta, 1985*, ed. by M. Greco (World Scientific, Singapore, 1985), p. 722.
[30] E. D. Bloom, private communication.
[31] M. Paulini, in *Proceedings of the Joint International Lepton-Photon Symposium & Europhysics Conference on High Energy Physics, Geneva, Switzerland, 1991*, edited by S. Hegarty, K. Potter, and E. Quercigh (World Scientific, Singapore, 1992), p. 592.
[32] A. Bean *et al.* (CLEO Collab.), Phys. Rev. Lett. **70**, 2681 (1993).
[33] S. Adler *et al.* (E787 Collab.), Phys. Rev. Lett. **79**, 2204 (1997); preprint hep-ex/9708031.
[34] J. L. Rosner, Phys. Rev. D **42**, 3732 (1990).
[35] M. Neubert and B. Stech, to appear in *Heavy Flavours, 2nd edition*, edited by A. J. Buras and M. Lindner (World Scientific, Singapore); preprint hep-ph/9705292.
[36] M. Neubert, Phys. Reports **245**, 259 (1994).
[37] K. Kodama *et al.* (E653 Collab.), Phys. Lett. B **382**, 299 (1996); preprint hep-ex 9606017.
[38] M. Chadha *et al.* (CLEO Collab.), submitted to Phys. Rev. D, CLEO preprint 97-28, hep-ex/9712010.
[39] S. Aoki *et al.* (WA75), Prog. Theor. Phys. **89**, 131 (1993).
[40] J.Z. Bai *et al.* (BES), Phys. Rev. Lett. **74**, 4599 (1995).
[41] M. Acciarri *et al.* (L3 Collab.), Phys. Lett. B **396**, 327 (1997).
[42] F. Parodi (DELPHI Collab.), paper submitted to the International Europhysics Conference on High Energy Physics, 19–26 August 1997, Jerusalem, HEP97 #455, DELPHI 97-105 CONF 87.
[43] A. Nippe, to be published in *Proceedings of the 7th International Symposium on Heavy Flavor Physics, Santa Barbara, California, 1997*, edited by C. Campagnari (World Scientific, Singapore, 1998).
[44] D. Atwood, G. Eilam, and A. Soni, Mod. Phys. Lett. **11**, 1061 (1996).
[45] T. Browder *et al.* (CLEO Collab.), Phys. Rev. D **56**, 11 (1997).
[46] C. Bernard, to be published in *Proceedings of the 7th International Symposium on Heavy Flavor Physics, Santa Barbara, California, 1997*, edited by C. Campagnari (World Scientific, Singapore, 1998).
[47] R. Sugar, private communication; C. Bernard *et al.* (MILC Collab.), to be published.
[48] A. Ali Khan *et al.* hep-lat/9801038, to be published in Phys. Lett. B.
[49] J. E. Duboscq *et al.* (CLEO Collab.), Phys. Rev. Lett. **76**, 3898 (1996).
[50] M. Jacob and G. C. Wick, Ann. Phys. (N.Y.) **7**, 404 (1959).
[51] J. D. Richman, Caltech preprint CALT-68-1148, unpublished.

[52] E. V. Shuryak, Nucl. Phys. B **93**, 134 (1980).
[53] S. Nussinov and W. Wetzel, Phys. Rev. D **36**, 130 (1987).
[54] M. B. Voloshin and M.A. Shifman, Yad. Fiz. **45**, 463 (1987), [Sov. J. Nucl. Phys. **45**, 292 (1987).]
[55] M. B. Voloshin and M.A. Shifman, Yad. Fiz. **47**, 801 (1988) [Sov. J. Nucl. Phys. **47**, 511 (1988).]
[56] N. Isgur and M. B. Wise, Phys. Lett. B **232**, 113 (1989).
[57] N. Isgur and M. B. Wise, Phys. Lett. B **237**, 527 (1990).
[58] E. Eichten and B. Hill, Phys. Lett. B **234**, 511 (1990).
[59] E. Eichten and B. Hill, Phys. Lett. B **243**, 427 (1990).
[60] A. F. Falk, H. Georgi, B. Grinstein, and M. B. Wise, Nucl. Phys. B **343**, 1 (1990).
[61] B. Grinstein, Nucl. Phys. B **339**, 253 (1990).
[62] H. Georgi, Phys. Lett. B **240**, 447 (1990).
[63] M. Wise, in *Proceedings of the 5th International Symposium on Heavy Flavour Physics, Montreal, Canada, July 6-10, 1993,* edited by D. I. Britton, D. B. MacFarlane, and P. M. Patel (Editions Frontièrs, France), p. 5.
[64] M. Wise, in *Proceedings of the 16th International Symposium on Lepton and Photon Interactions, Ithaca, N.Y., 1993*, AIP Conference Proceedings No. 302, edited by P. Drell and D. Rubin (AIP, New York), p. 253 (1994).
[65] M. Wise, in *Proceedings of Beauty 97*, University of California Los Angeles, October 12-16, 1997; preprint hep-ph/9803247.
[66] I.Bigi, M. Shifman, and N. Uraltsev, in *Ann. Rev. Nucl. Part. Sci.* **47**, 591 (1997); preprint hep-ph/9703290.
[67] B. Grinstein, Lectures presented at the VI Mexican School of Particles and Fields, Villahermosa, Tabasco, Oct. 3–7, 1994; preprint hep-ph/9508227.
[68] T. Mannel, Contribution to the workshop on *Heavy Quark Physics*, December 13 – 16, 1994, Bad Honnef, Germany; preprint hep-ph/9503272.
[69] T. Mannel, talk presented at the workshop *Heavy Quarks at Fixed Target*, St. Goar, Germany, Oct. 3-6, 1996; preprint hep-ph/9611411.
[70] M. Neubert, in *Proceedings of the International Europhysics Conference on High Energy Physics*, Jerusalem, Israel, 19–26 August 1997; preprint hep-ph/9801269.
[71] M. B. Voloshin, M.B., "Topics in Heavy Quark Physics," Lectures presented at the 1994 ITEP Winter School, Feb. 22–March 2, 1994, U. of Minnesota Preprint No. TIP-MINN-94/18-T and UMN-TH-1257-94 (1994).
[72] J. Chay, H. Georgi, and B. Grinstein, Phys. Lett. B **247**, 399 (1990).
[73] I. I. Bigi, B. Blok, M. Shifman, and A. Vainshtein, Phys. Lett. B **323**, 408 (1994).
[74] J. Bartelt *et al.* (CLEO Collab.), CLEO preprint CLEO-CONF-93-19, submitted to the *16th International Symposium on Lepton and Photon Interactions at High Energies,* Cornell University, Ithaca, NY, August, 1993.
[75] D. Besson, in *Proceedings of the 16th International Symposium on Lepton and Photon Interactions at High Energies,* Cornell University, Ithaca, NY, August, 1993; p. 221.
[76] D. Atwood and W. Marciano, Phys. Rev. D **41**, 1736 (1990).
[77] H. Albrecht *et al.* (ARGUS Collab.), Phys. Lett. B **318**, 397 (1993).
[78] B. Barish *et al.* (CLEO Collab.), Phys. Rev. Lett. **76**, 1570 (1996).
[79] L.K. Gibbons, in *Proceedings of the 28th International Conference on High Energy Physics*, Warsaw, 25–31 July, 1996, eds. Z. Ajduk and A. K. Wroblewski, p. 183 (World Scientific, Singapore, 1997).
[80] I. Bigi, N. Uraltsev, and A. Vainshtein, Phys. Lett. B **293**, 430 (1992); **297**, 477(E) (1993).
[81] I. Bigi and N. Uraltsev, Z. Phys. C **62**, 623 (1994).
[82] M. Luke and M. Savage, Phys. Lett. B **321**, 88 (1994).

[83] P. Ball, M. Beneke, and V. M. Braun, Phys. Rev. D **52**, 3929 (1995).
[84] M. Shifman, N. G. Uraltsev, and A. Vainshtein, Phys. Rev. D **51**, 2217 (1995).
[85] J. L. Rosner, in *B Decays*, edited by S. Stone (World Scientific, Singapore, 1992), p. 312.
[86] J. Bartelt *et al.* (CLEO Collab.), Phys. Rev. Lett. **71**, 4111 (1993).
[87] G. Fox and S. Wolfram, Phys. Rev. Lett. **41**, 1581 (1978).
[88] M. Wirbel, B. Stech, and M. Bauer, Z. Phys. C **29**, 637 (1985).
[89] J. G. Körner and G.A. Schuler, Z. Phys. C **46**, 93 (1990).
[90] M. Neubert and V. Rieckert, Nucl. Phys. B **382**, 97 (1992).
[91] A. F. Falk and M. Neubert, Phys. Rev. D **47**, 2965 (1993).
[92] J. G. Körner and G.A. Schuler, Z. Phys. C **38**, 511 (1988); Erratum: C **41**, 690 (1989).
[93] R. Garisto, Phys. Rev. D, **51**, 1107 (1995).
[94] F. J. Gilman and R. L. Singleton, Jr., Phys. Rev. D **41**, 93 (1990).
[95] Z Ligeti, Y. Nir, and M. Neubert, Phys. Rev. D **49**, 1302 (1994).
[96] D. Scora, N. Isgur, B. Grinstein, and M. B. Wise, Phys. Rev. D **39**, 799 (1989).
[97] D. Scora and N. Isgur, Phys. Rev. D **52**, 2783 (1995); preprint hep-ph/9503486.
[98] A. Bean *et al.* (CLEO Collab.), Phys. Lett. B **317**, 647 (1993).
[99] A. Ryd, to be published in *Proceedings of the 7th International Symposium on Heavy Flavor Physics, Santa Barbara, California, 1997*, edited by C .Campagnari (World Scientific, Singapore, 1998).
[100] P. L. Frabetti *et al.* (E687 Collab.), Phys. Lett. B **364**, 127 (1995).
[101] CLEO Collaboration (M. Athanas *et al.*), Phys. Rev. Lett. **79**, 2208 (1997); preprint hep-ex/9705019.
[102] B. Barish *et al.* (CLEO Collab.), Phys. Rev. D **51**, 1014 (1995); preprint hep-ex/9406005.
[103] P. Drell, to be published in *Proceedings of the 18th International Symposium on Lepton - Photon Interactions (LP 97)*, Hamburg, Germany, 28 Jul - 1 Aug 1997; preprint hep-ex/9711020.
[104] J. E. Duboscq *et al.*, Phys. Rev. Lett. **76**, 3898 (1996).
[105] F. Close and A. Wambach, Phys. Lett. B **348**, 207 (1995).
[106] E. M. Aitala *et al.* (E791 Collab.), Phys. Rev. Lett. **80**, 1393 (1998); preprint hep-ph/9710216.
[107] J. Flynn, to be published in *Proceedings of the 7th International Symposium on Heavy Flavor Physics, Santa Barbara, California, 1997*, edited by C .Campagnari (World Scientific, Singapore, 1998); preprint hep-lat/9710080.
[108] A. Anastassov *et al.* (CLEO Collab.), Phys. Rev. Lett. **80**, 4127 (1998); preprint hep-ex/9708035.
[109] P. Ball, to be published in *Proceedings of the 7th International Symposium on Heavy Flavor Physics, Santa Barbara, California, 1997*, edited by C .Campagnari (World Scientific, Singapore, 1998); preprint hep-ph/9709407.
[110] J. L. Diaz-Cruz, G. Lopez Castro, J. H. Munoz, Phys. Rev. D **54**, 2388 (1996); preprint hep-ph/9605344.
[111] G. Lopez Castro, J. H. Munoz, and G. Toledo Sanchez, Phys. Rev. D **56**, 6025 (1997); preprint hep-ph/9709266.
[112] T. Browder, K. Honscheid, and D. Pedrini, in *Annual Review of Nuclear and Particle Science*, Vol. 46 (Annual Reviews, Palo Alto, 1996), 395; preprint hep-ph/9606354.
[113] M. Neubert and B. Stech, to be published in *Heavy Flavours*, 2nd edition, edited by A. J. Buras and M. Lindner, (World Scientific, Singapore), preprint hep-ph/9705292.
[114] M. Neubert, V. Rieckert, B. Stech, and Q.P. Xu, in *Heavy Flavors*, A.J. Buras and H. Linder, eds. (World Scientific, Singapore, 1992), p. 286.

[115] M. Bauer, B. Stech, M. Wirbel, Z. Phys. C **34**, 103 (1987).
[116] M. Neubert, in *Proceedings of the High-Energy Physics Euroconference on Quantum Chromodynamics, Montepelier, France, 3–9 July 1997*; preprint hep-ph/9707368.
[117] B. Barish *et al.* (CLEO Collab.), CLEO CONF 97-01, EPS 97-339, paper submitted to the International Europhysics Conference on High Energy Physics, Jerusalem, Israel, 19–26 August 1997.
[118] CLEO Collaboration (B. Nemati *et al.*). Phys. Rev. D **57**, 5363 (1998); preprint hep-ex/9708033.
[119] J.D. Bjorken, Nucl. Phys. B (Proc. Suppl.) **11**, 325 (1989).
[120] CLEO Collaboration (G. Brandenburg et al.). Phys. Rev. Lett. **80**, 2762 (1998); preprint hep-ex/9706019.
[121] A. Deandrea, N. Di Bartolomeo, R. Gatto, and G. Nardulli, Phys. Lett. B **318**, 549 (1993).
[122] D. Gibaut *et al.*, (CLEO Collab.), Phys. Rev. D **53**, 4734 (1996).
[123] A. Anastassov *et al.* (CLEO Collab.), contributed paper to *The 28th International Conference on High Energy Physics,* Warsaw, Poland, 25-31 July 1996, CLEO-CONF 96-8, ICHEP96 pa 05-079 (1996).
[124] M. S. Alam *et al.* (CLEO Collab.), Phys. Rev. D **50**, 43 (1994).
[125] CLEO Collab., paper submitted to the International Europhysics Conference on High Energy Physics, Jerusalem, Israel, 19–26 August 1997; CLEO CONF 97-26, EPS97-337.
[126] L. Gibbons *et al.* (CLEO Collab.), Phys. Rev. D **56**, 3783 (1997); preprint hep-ex/9703006.
[127] LEP *B* Lifetimes Working Group web page, http://wwwcn.cern.ch/~claires/lepblife.html.
[128] T. Mannel, to be published in *Proceedings of the 7th International Symposium on Heavy Flavor Physics, Santa Barbara, California, 1997*, edited by C. Campagnari (World Scientific, Singapore, 1998).
[129] M. Neubert, Int. J. Mod. Phys. A **11**, 4173 (1996).
[130] I. I. Bigi, preprint hep-ph/9508408; G. Bellini, I. Bigi, and P. J. Dornan, Phys. Rept. **289**, 1 (1997).
[131] D. Buskulic *et al.* (ALEPH Collab.), Zeit. fur Physik C **71**, 31 (1996).
[132] P. Abreu *et al.* (DELPHI Collab.), Zeit. fur Physik C **74**, 19 (1997).
[133] F. Abe *et al.* (CDF Collab.), Phys. Rev. D **57**, 5382 (1998).
[134] K. Abe *et al.* (SLD Collab.), SLAC-PUB-7635, EPS-127 PA05, paper submitted to the International Europhysics Conference on High Energy Physics, Jerusalem, Israel, 19–26 August 1997; see also K. Abe *et al.* (SLD Collab.), Phys. Rev. Lett. **79**,590 (1997).
[135] M. Beneke, G. Buchalla, I. Dunietz, Phys. Rev. D **54**, 4419 (1996); I. Dunietz, Phys. Rev. D **52**, 3048 (1995); I. Dunietz, Phys. Rev. D **52**, 3048 (1996).
[136] F. Abe *et al.* (CDF Collab.), Phys. Rev. Lett. **77**, 1945 (1996).
[137] K. Ackerstaff (OPAL Collab.), Zeit. fur Physik C **74**, 423 (1997).
[138] K. Lingel, T. Skwarnicki, and J. G. Smith, COLO-HEP-395, SLAC-PUB-7796, HEPSY 98-1, to be published in *Annual Reviews of Nuclear and Particle Science.*
[139] A. Ali, to be published in to be published in *Proceedings of the 7th International Symposium on Heavy Flavor Physics, Santa Barbara, California, 1997*, edited by C. Campagnari (World Scientific, Singapore, 1998); preprint hep-ph/9709507.
[140] R. Godang *et al.* (CLEO Collab.), Phys. Rev. Lett. **80**, 3456 (1998); preprint hep-ex/9711010.
[141] B. Behrens *et al.* (CLEO Collab.), Phys. Rev. Lett. **80**, 3710 (1998); preprint hep-ex/9801012.

[142] T. Bergfeld *et al.* (CLEO Collab.), CLNS-97-1537, submitted to Phys. Rev. Lett., preprint hep-ex/9803018.

[143] CLEO Collab., CLEO CONF 97-24, EPS-334.

[144] R. Ammar *et al.* (CLEO Collab.), Phys. Rev. Lett. **71**, 674 (1993).

[145] R. Ammar *et al.* (CLEO Collab.), CLEO CONF 96-05, contributed paper to *The 28th International Conference on High Energy Physics,* Warsaw, Poland (1996).

[146] M. S. Alam *et al.* (CLEO Collab.), Phys. Rev. Lett. **74**, 2885 (1995).

[147] R. Barate *et al.* (ALEPH Collab.), CERN EP/98-044, submitted to Phys. Lett. B.

[148] P. Pavlopoulos, in Proceedings of the Workshop on K Physics, edited by L. Iconomidou-Fayard (Editions Frontieres, France, 1997); M. M. Velasco, to be published in *Proceedings of the 7th International Symposium on Heavy Flavor Physics, Santa Barbara, California, 1997*, edited by C. Campagnari (World Scientific, Singapore, 1998).

[149] J. H. Christenson, J. W. Cronin, V. L. Fitch, and R. Turlay, Phys. Rev. Lett. **13**, 138 (1964).

[150] J. W. Cronin, Rev. Mod. Phys. **53**, 373 (1981).

[151] V. L. Fitch, Rev. Mod. Phys. **53**, 367 (1981).

[152] R. Fleischer, to be published in *Proceedings of the 7th International Symposium on Heavy Flavor Physics, Santa Barbara, California, 1997*, edited by C. Campagnari (World Scientific, Singapore, 1998), preprint hep-ph/9709291; R. Fleischer, Int. J. Mod. Phys. A **12**, 2459 (1997).

[153] E. Leader and E. Predazzi, *An Introduction to Gauge Theories and Modern Particle Physics, Vol. 2* (Cambridge University Press, Cambridge, 1996), p. 12.

[154] T. Nakada, PSI preprint PSI-PR-91-02 (1991).

[155] H. Nelson, in *Proceedings of the Twentieth SLAC Summer Institute on Particle Physics: The Third Family and the Physics of Flavor*, Stanford, Calif., Jul 13-24, 1992, SLAC-412, edited by L. Vassilian.

[156] Y. Nir, in *Proceedings of the Twentieth SLAC Summer Institute on Particle Physics: The Third Family and the Physics of Flavor*, Stanford, Calif., Jul 13-24, 1992, SLAC-412, edited by L. Vassilian.

[157] Y. Nir and H. Quinn, Ann. Rev. Nucl. Part. Sci. **42**, 211 (1992).

[158] I. I. Bigi and A. I. Sanda, Nucl. Phys. B **193**, 85 (1981).

[159] M. H. Schune, to be published in *Proceedings of the 7th International Symposium on Heavy Flavor Physics, Santa Barbara, California, 1997*, edited by C. Campagnari (World Scientific, Singapore, 1998).

[160] R. E. Marshak, Riazuddin, C. P. Ryan, *The Theory of Weak Interactions in Particle Physics* (Wiley, New York, 1969).

[161] B. Winstein and L. Wolfenstein, Rev. Mod. Phys. **65**, 1113 (1993).

[162] A. D. Sakharov, ZhETF Pis. Red. **5**, 32 (1967); JETP Lett. **5**, 24 (1967).

[163] R. Fleischer and T. Mannel, preprint hep-ph/9706261.

[164] M. Neubert, preprint hep-ph/9712224

[165] T. D. Lee, *Particle Physics and Introduction to Field Theory* (Harwood Academic Publishers, Chur, 1981), p. 186.

[166] M. H. Schune, to be published in *Proceedings of the 7th International Symposium on Heavy Flavor Physics, Santa Barbara, California, 1997*, edited by C. Campagnari (World Scientific, Singapore, 1998).

[167] H. Albrecht (ARGUS Collab.), Phys. Lett. B **192**, 245 (1987).

[168] D. Cassel, to be published in the *Proceedings of Frontiers in Contemporary Physics–1997*, Vanderbilt University, Nashville, TN, May 12-16, 1997; Cornell preprint CLNS 97/1538.